Implant Communication Using Intrabody Communication (IBC) Mechanisms

Assefa Kassa TESHOME

(B.Sc., M.Tech. in Electrical Eng'g, M.Eng.(research) in Telecommunications Eng'g.)

College of Engineering and Science
Victoria University Melbourne

A thesis submitted in fulfillment of the requirements for the degree of

Doctor of Philosophy

in

Electrical Engineering

December 2017

Abstract

The current trend in healthcare is the move towards proactive health monitoring and making health one's responsibility. This has seen a proliferation of wearable devices that monitor physical and physiological parameters in real time. However, there is an increasing need to monitor internal body parameters, detect risks and act on them in a timely manner. Implanted medical devices (IMDs) are gaining recent attention due to their capability to provide diagnostic, therapeutic and assistive functionalities. With a projected annual growth of 7.1 % (2016- 2022) the global market share of IMDs is expected to reach 116.3 billion USD by year 2022. In Australia alone, the clinical use of remotely monitored IMDs has risen sharply from 987 (2013-14) to 2269 in just two fiscal years. The increasing demand for ubiquitous and minimally invasive implants is due to the prevalence of chronic disease and growing aging population.

While bio-sensing and implant drug delivery techniques have improved tremendously, implant communication technology has advanced at a slower rate. This poses problems for the new generation of implants such as brain computer interfaces (BCI), controllers for artificial prostheses and bionics which will require higher data rates. Existing IMD communications are mainly enabled through antenna based radio frequency links that rely on electromagnetic (EM) wave propagation at ultra high frequencies (UHF). The Medical Device Radio Communication Services (MedRadio) band (401-406 MHz) and Industrial Scientific and Medical radio (ISM) band (2.4 GHz) are most commonly used. However, the human body has a high attenuation to signals at these high radio frequencies; as a result, transceivers tend to consume high power and require complex circuitry to mitigate channel attenuation effects. Lower RF frequencies (lower attenuation through the body) require larger antenna sizes resulting in larger implant sizes. On the other hand, while inductively coupled techniques use lower frequencies

(lower path loss), they generally have a narrow transmission band and lower data rates. Thus, the race is on to develop new implant data transmission techniques that consume less power yet provide high (acceptably high) data rates. The thesis addresses this challenge by investigating an alternative implant communication technique using intrabody communication (IBC) mechanisms, specifically galvanically coupled IBC (gc-IBC). This communication method utilises the human tissue as a volume conductor for data communications.

In this thesis we began by critically reviewing existing and emerging implant communications technologies. We then proposed and investigated gc-IBC as a new alternative implant communication technology. A novel analytical framework that modeled the human body as a communication channel was proposed. Simulation results were experimentally confirmed by measurements on phantom body solutions. The framework was then extended to analyse a hybrid communication scheme for cortical implants that utilised gc-IBC and the popular inductively coupled data transfer (ic-DT). It was found that for the same frequency range, gc-IBC offers a wider bandwidth for data transmission compared to ic-DT while ic-DT was better for wireless power transfer due to its narrow band characteristic and lower path loss at the resonant frequency. It was also shown that gc-IBC provided 20 dB lower path loss than antenna based RF schemes for the same transmit power. Then, an integrated sensor gc-IBC implant transceiver prototype was designed and developed to characterise and demonstrate the feasibility of implant communication using gc-IBC mechanism. The integration of the sensor into the transmitter was made in a way that minimises transmitter complexity which was crucial to achieve high degree of miniaturisation and low power consumption. Transceiver characterisation experiments were conducted using an automated mechatronic rig that is specifically designed and built for this work. The rig moves the receiver inside the phantom solution in the three axes with respect to the transmitter and is capable of computing the bit error rate (BER) of the reception. The transceiver demonstrated the feasibility of gc-IBC scheme for implants with a BER of 1.1 $\times 10^{-4}$ at signal to noise ratio (SNR) of 8 dB which is better compared to existing uncoded schemes. The gc-IBC channel noise was characterised for the first time as a function of transmission distance and was found to be -118 dB/Watt on average. Future work will focus on extending the framework to model more complex parts e.g.,

organs, channel capacity estimation under different setting, testing different coding schemes to improve transceiver performance and miniaturisation.

I would like to dedicate this thesis to my loving parents
Kassa Teshome and *Yeshi Nigus*.

Declaration

"I, Assefa Kassa Teshome, declare that the PhD thesis entitled 'Implant Communications Using Intrabody Communication (IBC) Mechanism' is no more than 100,000 words in length including quotes and exclusive of tables, figures, appendices, bibliography, references and footnotes. This thesis contains no material that has been submitted previously, in whole or in part, for the award of any other academic degree or diploma. Except where otherwise indicated, this thesis is my own work".

Assefa Kassa TESHOME
12 December 2017

Acknowledgements

"Trust in the Lord with all your heart, and lean not on your own understanding, in all your ways acknowledge Him, and He shall direct your paths." Proverbs 3:5-6. First and foremost, I would like to thank God almighty for his gracious guidance in all my ways.

I would like to extend my sincere gratitude to my supervisor Assoc. Prof. Daniel Lai for his academic mentorship, continued supervision and motivation throughout the journey of my PhD candidature. Thank you Daniel for your advices in academics and in life in general; discussions over our coffee catch ups were very instrumental. Your timely advice and guidance made this work a success.

I would also like to thank Prof. Mike Faulkner for his comments and discussions in some aspects of my work. My thanks go to Miroslav, Greame, David and my colleagues form our research group Kim, Clement, Rui, Johannis and Abdoo for being supportive and cheerful; in particular, I am grateful to Behailu for his friendship, discussion and fun times we had.

Last but not least, I would like to thank my fiancé Senait and my parents Kassa Teshome and Yeshi Nigus for their immense love and support.

Thank you all.

List of Publications

1. **Assefa K Teshome**, Behailu Kibret, and Daniel TH Lai. A Review of Implant Communication Technology in Wireless Body Area Networks (WBAN) : Progress and Challenges. *IEEE Reviews on Biomedical Engineering (preprint)*, DOI:10.1109/RBME.2018.2848228, vol. 12, no. 1, pp. 1—13, 2018.

2. **Assefa K Teshome**, Behailu Kibret, and Daniel TH Lai. Wireless Implant Communications Using the Human Body. *In Encyclopedia of Information Science and Technology*, Fourth Edition, pages 6319-6334. IGI Global, 2018.

3. **Assefa K Teshome**, Behailu Kibret, and Daniel TH Lai. Galvanically coupled intrabody communications for medical implants: A unified analytic model. *IEEE Transactions on Antennas and Propagation*, Vol. 64. No. 7, pp. 2989–3002, 2016.

4. **Assefa K Teshome**, Behailu Kibret, and Daniel TH Lai. Intrabody Communication for Implants in Body Area Network Scenarios. *Intelligent Environments (Workshops)*. pages 544–551, 2016.

5. **Assefa K Teshome**, Behailu Kibret, and Daniel TH Lai. A Hybrid Intrabody Communications for Wireless Cortical Implants. *Submitted to IEEE Transactions on Antennas and Propagation.*

6. **Assefa K Teshome**, Behailu Kibret, and Daniel TH Lai. Integrated Sensor Galvanically Coupled Implant Transceiver : Implementation and Characterisation. *Submitted to IEEE Transactions on Biomedical Engineering.*

7. Behailu Kibret, **Assefa K Teshome**, and Daniel T H Lai, A New Perspective on the Cylindrical Antenna Theory, *IEEE Transactions on Antennas and Propagation*, Vol. 64. No. 7, pp. 2981-2988, 2016.

8. Clement Ogugua Asogwa, **Assefa K Teshome**, Stephen F. Collins and Daniel T. H. Lai, A Circuit Model of Real Time Human Body Hydration, *IEEE Transactions on Biomedical Engineering*, Vol. 63, No. 6, June 2016.

9. Behailu Kibret, **Assefa K Teshome**, and Daniel T H Lai, Analysis of the Human Body as an Antenna for Wireless Implant Communication, *IEEE Transactions on Antennas and Propagation*, Vol. 64. No. 4, 1466-1476, 2016.

10. Pazit Levinger, Daniel Zeina, **Assefa K Teshome**, Elizabeth Skinner, Rezaul Begg, and John Haxby Abbott. "A real time biofeedback using Kinect and Wii to improve gait for post-total knee replacement rehabilitation: a case study report." *Disability and Rehabilitation: Assistive Technology* 11, no. 3 (2016): 251-262.

11. Behailu Kibret, **Assefa K Teshome**, and Daniel T H Lai, Characterizing of the human body as a monopole antenna, *IEEE Transactions on Antennas and Propagation*, Vol. 63, No. 10, 4384-4392, 2015

12. Behailu Kibret, **Assefa K Teshome**, and Daniel T H Lai, Cylindrical antenna theory for the analysis of whole body averaged specific absorption rate, *IEEE Transactions on Antennas and Propagation*, Vol. 63, No. 11, 5224 5229, 2015.

13. Behailu Kibret, **Assefa K Teshome**, and Daniel T H Lai, Human body as antenna and its effect on human body communications, *Progress in Electromagnetics Research*, Vol. 148, 193-207, 2014.

14. Behailu Kibret, **Assefa K Teshome**, and Daniel T H Lai, Analysis of the whole-body averaged specific absorption rate (SAR) for far-field exposure of an isolated human body using cylindrical antenna theory, *Progress in Electromagnetics Research M*, Vol. 38, 103–112, 2014.

Table of contents

List of figures

List of tables

List of Abbreviations

ARQ	Automatic Repeat Request
CSF	Cerebrospinal Fluid
CST	Computer Simulations Technology
DAC	Digital to Analog Converter
dB	deci Bell
DET	Detector
DSP	Digital Signal Processing
DSSS	Direct Sequence Spread Spectrum
DUT	Device Under Test
ECC	Error Control Coding
ASK	Amplitude Shift Keying
EEG	Electroencephalography
EFC	Electric Field Communication
ERP	Effective Radiated Power
ETSI	Europian Telecommunications and Standards Institute
FCC	Federal Communications Commission
FDTD	Finite Difference Time Domain

FEM Finite Element Method

FHSS Frequency Hopping Spread Spectrum

FPGA United Nations

FSDT Frequency Selective Digital Transmission

AWGN Additive White Gaussian Noise

gc-IBC Galvanically Coupled Intrabody Communication

GPU Graphics Processing Unit

HBC Human Body Communications

IBC Intrabody Communications

ic-DT Inductively Coupled Data Transfer

ICNIRP International Commission on Non-Ionizing Radiation Protection

ic-PT Inductively Coupled Power Transfer

IMD Implanted Medical Device

IoT Internet of Things

IP67 Ingress Protection 67

BCC Body Channel Communication

IR Infrared

ISM Industrial Scientific and Medical radio

kHz kilohertz

LBT Listen Before Talk

LED Light Emitting Diode

LFSR Linear Feedback Shift Register

LSB List Significant Bit

LSK Load Shift Keying

LUT Lookup Table

MAC Media Access Control

BER Bit Error Rate

MedRadio Medical Device Radiocommunications Service

MEG Magnetoencephalography

MEMS Microelectromechanical Systems

MHz Megahertz

MICS Medical Implant Communication Service

MSB Most Significant Bit

NB Narrow Band

OOK On-off Keying

OQPSK Orthogonal Quadrature Phase Shift Keying

PHY Physical Layer

BGMs United Nations

PIFA Planar Inverted-F Antenna

PL Path Loss

PRS Pseudo Random Sequence

PSD Power Spectral Density

QPSK Quadrature Phase Shift Keying

RAM Random Access Memory

RF Radio Frequency

RFID Radio Frequency Identification

ROI	Region of Interest
RS	Reed-Solomon
BPSK	Binary Phase Shift Keying
RTL	Register Transfer Level
SAR	Specific Absorption Rate
SNR	Signal to Noise Ratio
SP	Series-Parallel
UHF	Ultra High Frequency
USDT	Ultrasonic Data transfer
USPT	Ultrasonic Power transfer
UWB	Ultra Wide Band
VCO	Voltage Controlled Oscillator
VCSEL	Vertical-Cavity Surface-Emitting Laser
CDR	Clock and Data Recovery
VNA	Vector Network Analyser
WBAN	Wireless Body Area Network
CMOS	Complementary Metal-Oxide-Semiconductor

Chapter 1

Introduction

1.1 Motivation

Since the first pacemaker was implanted in 1958, research in practical use of remotely monitored implanted medical devices (IMDs) has risen to shape the future of health-care monitoring and intervention. The global growth in demand for IMDs is driven by the increasing prevalence of chronic diseases and rising geriatric population, and is fueled by technological advancements in medical diagnostics and engineering [1, 2]. In fact, this growing demand for IMDs or on-body mounted devices that communicate through the human body is not limited to health care but also a number of other applications such as athletic performance monitoring in sports, body-to-body communication for e-commerce and data transfer, security, entertainment and military applications such as long term fatigue and physiological assessment and assistive-prosthesis with brain-machine communication capabilities [1, 3].

However, existing IMD communications are mainly enabled through antenna based radio frequency links that rely on electromagnetic (EM) wave propagation

at very high frequencies in the Medical Device Radio Communication Services (MedRadio) band (401-406 MHz) and Industrial Scientific and Medical radio (ISM) band (2.4 GHz). The human body has a high attenuation to signals at such high frequencies; as a result, transceivers consume high power and require complex features to mitigate channel effects. On the other hand, if the transmission frequency is decreased to reduce attenuation, the IMD would require a larger antenna and hence be difficult to miniaturise.

With a predicted average annual growth of 7.1 % between 2016 and 2022, the market share of IMDs is expected to expand form 72.3 billion USD (year 2016) to 116.3 billion USD (year 2022)[1]. Currently, North America alone comprises half the global market share while Europe and Asia-Pacific region account for most of the remaining half. This figure represents the collective implanted devices such as orthopedic, dental, breast, cardiovascular, intraocular and electronic medical implants for remote monitoring in use today. In Australia alone, the clinical use of remotely monitored IMDs has risen sharply from 987 in the year 2013-14 to 2269 in just two fiscal years [4]. Thus, research and development in IMD technology is timely and of great importance.

Classical medical diagnosis is often limited to biopsy or blood samples taken from patients and analysed in laboratories. However, technological advancements are now enabling implanted devices to provide timely diagnostics and even therapeutic intervention. Low power consumption, miniature size and reliable communication of the IMD with external devices are key features required for long term, minimal invasive and ubiquitous diagnostic, therapeutic and assistive-prosthesis applications. Although bio-sensing and diagnostic technologies have advanced, communication of diagnostic readout implants has not advanced as fast. Currently, implant communication is enabled using the existing power hungry radio wave and inductively coupled communication techniques that are

[1] https://www.alliedmarketresearch.com/implantable-medical-devices-market

difficult to miniaturise. Targeting the requirements listed, existing research in IMD communications focuses on exploring two main venues. First, alternative communication techniques that incur minimal path loss to the transmitted signals so that transceivers consume low power. Secondly, sustainable powering regimes to avoid or minimise battery replacement surgeries. This thesis focuses on emerging communication for medical implants with the potential for low power consumption.

Although antenna based radio frequency (RF) and inductively coupled data transfer (ic-DT) are widely explored techniques so far, several emerging communication techniques are being investigated; these include ultrasonic, optical and molecular intrabody communications. These communication techniques can be used individually as alternative or in an integrated manner complementary to each other. For example, molecular communications enable very short communication channels in the order of micrometers while antenna based RF techniques cover up to a few meters outside the human body. However, these schemes are still under development and most of them are not yet standardised. The only two existing standards to govern implant communications or intrabody communications in general are the Medical Device Radio Communication Services (MedRadio) updated in 2009 and the IEEE Standard 802.15.6 which was released in 2012 as a standard for wireless body area communications. The latter standard includes the existing Medical Implant Communication Services (MICS) band in its Narrow Band (NB) layer. The Human Body Communication (HBC) layer of the IEEE 802.15.6 standard uses the Electric Field Communication (EFC) and promises a low power and inherently secured communication.

This thesis proposes galvanically coupled intrabody communication (gc-IBC) as a new alternative implant communication technology. We derive a novel analytical framework to describe the human body as a communication channel. We then simulated the channel characteristics and substantially confirmed the

model by experiments on phantom solution. The model is extended to analyse a hybrid communication scheme for cortical implants. Finally, results are implemented in a prototype gc-IBC implant transceiver.

1.2 Research Aims

Motivated by the problems stated in Section 1.1, the main aim of this project is to investigate the galvanically coupled intrabody communication mechanism as an alternative solution for medical implant communications.

The specific aims of the research are listed as follows:

(a) The state-of-the-art of implant communication techniques and assess progresses and challenges of existing implant communication technologies were critically reviewed.

(b) Electric field communication for IBC and characterise the factors that affect implant communications using galvanic coupling were investigated.

(c) Novel analytical models, simulations and experimental characterisations of the human body for implant to implant and implant to surface communication channel using the galvanic coupling mechanism were developed.

(d) Factors that determine the limits of miniaturising an implant transmitter in the galvanic coupling setting were investigated.

(e) Hybrid techniques for implant communication by combining different IBC techniques were explored.

(f) Design and implementation of integrated sensor implant transceiver prototype was carried out with two main aims. First, to demonstrate feasibility

of gc-BC transceivers using results from the model and second, to characterise the bit error rate (BER) verses signal-to-noise ratio (SNR). The latter is used to evaluate channel noise as function of communication distance.

1.3 Contributions and Thesis Organisation

The major contribution of this research is to investigate IBC for implant communication and develop a novel miniaturised low-power galvanically coupled implant transmitter. This implant communication technique will be made to comply with the existing standards. This thesis presents the following important contributions as outcomes of our work from the aims:

(a) Critical evaluation of existing and emerging implant communication technologies.

(b) A novel lower bound on implant size for galvanically coupled IBC transceivers.

(c) A novel analytical path loss models and design techniques of galvanically coupled miniaturised implants.

(d) A hybrid implant-to-implant and implant-to-surface communication schemes with analytical models and characterisation.

(e) A prototype sensor integrated galvanically coupled IBC transceiver with noise characterisation.

The rest of the thesis is organised as follows:

- Chapter 2 presents a comprehensive review of the progress, current state-of-the-art and future direction in implant communications. IMDs are designed

mainly for the purpose of diagnostic, therapeutic and assitive applications in heath-care, active living and sports technology. The primary target of IMD design revolves around reliable communication, sustainable power source, high degree of miniaturisation while simultaneously maintaining tissue bio-compatibility and ensuring safe electromagnetic operation with in the appropriate guidelines. In addition to reviewing the state-of-the art, a novel intuitive lower bound on implant size is presented. The role of internet of things (IoT) and big data analysis in implant device networks as a future venue is also presented.

- In chapter 3 we report a novel analytical electromagnetic model framework for implant communication that uses galvanically coupled IBC as an alternative to radio wave based techniques. The model is unified in the sense that it is based on multi-layered ellipsoidal geometry that can be applied to any part of the body (i.e., head, torso, limbs etc.). Our model accurately predicts signal attenuation and influence of tissue layer thicknesses and electromagnetic properties, implant size and depth, and body part geometry. The model is substantially validated by experiments carried out using phantom solutions. The model proves the inherent security and low power consumption of IBC. The model affirms that gc-IBC does not result in electromagnetic radiation outside the human body. It was shown that the path loss of IBC implants is lower compared to their Medical Implant Communication Services (MICS) counterparts.

- Chapter 4 presents a hybrid communication scheme for a cortical implant communication. Cortical and deep brain implants are emerging as popular technologies in human-machine interfaces, bionic prostheses, diagnostics and treatment of neurological ailments. These applications require reliable and low power data communication between implants and an external device. Some cortical implants employ inductively coupled data and power

transfer, while others are enabled by antenna based radio frequency (RF) centered on 401–406 MHz and around 2.4 GHz. This chapter theoretically compares the efficacy of galvanically coupled intrabody communication (gc-IBC) and inductive link for cortical implants in the frequency range 1–10 MHz with implantation depths up to 7 cm. We propose a hybrid integration of gc-IBC and inductive scheme suitable for implant communications. It is shown here that, while inductive coupling is preferred for power transfer, gc-IBC offers wider bandwidth than inductively coupled data transfer and is about 20 dB lower in path loss than antenna based RF schemes.

- Chapter 5 presents a novel gc-IBC prototype transceiver design and implementation. The presented transmitter and receiver are designed with two main objectives. First, to integrate existing capacitive sensors in a simplified way to minimise component count and hence power consumption. Second, as a useful tool to assess the noise characteristics of the gc-IBC channel. A common variable capacitance range of 0-50 pF (as used in glucose sensors) is used to represent sensor data modulated on the carrier. A direct sequence spread spectrum (DSSS) scheme is used to provide noise robust and multiuser capability. A protocol with low overhead is utilised. Various modulation and coding schemes can be integrated with ease as the transceiver is implemented in a modular architecture.

- Chapter 6 presents performance evaluation and noise characterisation of the galvanically coupled implant transceiver designed and implemented in the previous chapter. Two main issues are addressed here. A 3D gantry was designed to enable micro-movements of implants inside phantom body solution prepared to mimic the human body tissue for path loss characterisation. The experimental setup was designed to enable movement of the receiver in three axes with respect to a fixed transmitter location. Both the receiver and the transmitter are inserted inside a phantom solution

that mimics the human muscle tissue. For the characterisation experiment, the receiver was modified to include transmission and error detection. The channel noise is assumed to be a gaussian noise and analytical bit error rate (BER) performance of the transceiver as a function of the signal to noise ratio (SNR) is computed and verified with simulation of the system. Experimental assessment of bit error rate (BER) over communication distance is associated with the theoretical and simulated BER versus signal to noise ratio (SNR) to quantify noise as a function of communication distance. These BER characterisations were also used to derive the relationship of the SNR with distance. Finally, the power spectral density (PSD) of the noise signal was determined to quantify the channel noise for various implantation depth.

- Chapter 7 presents future directions that include extending the presented analytical framework to analyse gc-IBC implant communication scenarios in different body parts; combine the model with further experiments to estimate channel capacity; refine the transceiver by including miniaturisation techniques and improve its reliability by testing different source and channel codes.

Chapter 2

A Review of Implant Communication Technology in Wireless Body Area Networks (WBAN) : Progress and Challenges

Over the past six decades there has been tremendous progress made in the field of medical implant communications. A comprehensive review of the progress, current state-of-the-art and future direction is presented in this chapter. Implanted Medical Devices (IMDs) are designed mainly for the purpose of diagnostic, therapeutic and assistive applications in heath-care, active living and sports technology. The primary target of implanted medical devices (IMDs) design revolve around reliable communications, sustainable power sources, high degree of miniaturisation while maintaining bio-compatibility to surrounding tissues adhering to the human safety limits set by appropriate guidelines. The role of

internet of things (IoT) and intelligent data analysis in implant device networks as future research is presented. Lastly, in addition to reviewing the state-of-the art, a novel intuitive lower bound on implant size is presented.

2.1 Introduction

Since the 1950's, research has sought to address the demand for long-term operation and low power communication for medical implants [5, 6]. Implants are now an integral part of the wireless body area network (WBAN) where different implanted or wearable devices are interconnected via implanted or wearable link sensor nodes as shown in Fig. 2.1. In the WBAN scenario, the defacto implant communication is one where the implanted medical device (IMD) communicates with a wearable data presentation device or a controller located outside the human body and vice versa. In fact, implants also communicate with other implants where an intuitive example is the case of an implanted glucose sensor with an insulin pump [7].

Unlike traditional through-the-air wireless radio frequency (RF) communication, implant communication uses living tissues as part of its transmission channel and hence faces extra challenges. Firstly, the human body is a hostile channel to high frequency electromagnetic signals. To understand the human body's influence to electromagnetic signals several researchers conducted experimental, analytical and simulation-based characterisations. The early work of Gabriel *et al* [8] characterised dielectric properties of different tissues as a function of frequency; this has enabled testing different hypotheses and theories as to how the tissues affect signals at different frequency.

In addition, the invasive nature of implantation surgeries places a stringent miniaturisation requirement and sustainable powering regime for implants, es-

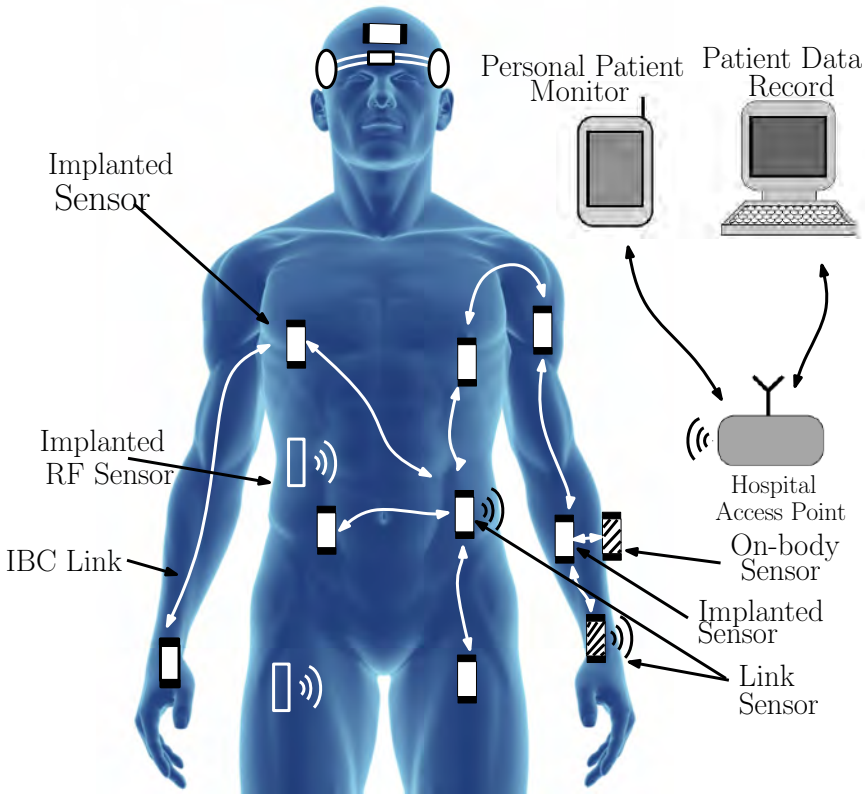

Fig. 2.1 Wireless Body area network. Part of the implanted sensors use RF communication to the external access point; others, use the the HBC mechanism to communicate to the link sensor

pecially for long term duration. As such, proper design and use of electronic medical implants need to take into account the specific application of the device. The data rate required dictates the bandwidth and even the implant communication mechanism. For example, subcutaneous glucose sensor transmitter is implanted just under the skin (depth of 4 mm) with low data rate (of less than 10 kbps [9]) and intermittent transmission while a cochlear implant requires a deeper implantation depth of 2.5 cm with a high data rate of up to 500 kbps in a continuous transmission mode. To this end, different communication mechanisms have been studied and employed; these include inductive coupling between implanted and surface mounted coils[10][11], antenna enabled radio frequency (RF) communication[12], and recently the galvanically and capacitively coupled intra-body communication (IBC)[13]. Other emerging

technologies such as ultrasonic[14][15], optical[16–18] and molecular intrabody communications[19–21] are also being investigated.

Despite the progress made by the research community, there are still challenges and avenues for improvement for reliable implementation. This Chapter reviews the progress and the challenges in implant telecommunications mechanisms for various biomedical applications with respect to the path loss introduced, sustained powering mechanisms, offered bandwidth and device miniaturisation trade-offs. The rest of the chapter is presented as follows; biomedical applications of medical implants are reviewed in Section 2.2. Implants as integral part of the WBAN architecture are discussed in Section 2.3. Existing and emerging implant communication technologies are reviewed in Section 2.4. The major requirements of medical implants with respect to what has been achieved and the challenges posed are discussed in Section 2.5. Finally, our conclusion is given in Section 2.6.

2.2 Biomedical Applications of Implants

The practical application of electronic medical implants date back to the late 1950s where the first heart pacemaker was successfully implanted [1]. Ever since implants have been used in stimulation, sensory (readout) and in closed loop control settings (full implanted operation). The biomedical applications of IMDs can be classified into three broad categories as diagnostics, therapeutic and assistive devices.

Application	Example	Range	Power consumption	frequency	size	data rate	Technology
Diagnostic	Glucose sensor [22]	4 cm	100 μW	38 MHz	9.5 mm × 7 mm × 8 mm	-	icDT
		4 cm	41 mW	2 MHz	9.5 mm × 7 mm × 8 mm	-	icPT
	Oximeter [23]	>1cm	-	1.2 GHz	8–10 mm diameter	-	icDT-usPT
	pH sensors [24]	-	-	915 MHz	-	-	RFID
	gastrointestinal imagery pill	-	-	-	length 18-25 mm diameter 6-12 mm	-	-
Therapeutic	pacemakers[1],	≤12.5 cm	-	-	25.9 mm length	-	-
	nerve and muscle stimulator [25]	5–14 mm	100 mW	5–17 MHz	6.7 mm diameter 8 mm × 8 mm × 0.2 mm	- 4.8kbps	- icPT Stimulation
		5–14 mm	35mW	5–17 MHz	8 mm × 8 mm × 0.2 mm	1.3 Mbps	icDT recording
	deep brain stimulator [26]	7 cm	132 μW	130 Hz	14.5mm diameter 7 cm length	-	-
Assistive Technology	Cochlear implants [27–29]	2.5 cm	574 μW	5, 12, 49 MHz	10–25 mm length	0.5–1 Mbps	Piezoelectric
	bionic vision implants [30, 31]	2 cm	-	5 MHz	9 mm × 9 mm × 2.5 mm	100 kbps	icDT and icPT
	brain computer interfaces	-	-	-	-	-	-
	for prosthetic limbs [32],	-	-	-	-	-	-
	athletic performance monitors	-	-	-	-	-	-

Table 2.1 Summary of biomedical applications of IMDs focussing on comms. Here icDT = Inductively coupled data transfer, RFID = Radio–Frequency Identification, icPT = inductively coupled power transfer, usPT = ultrasonic power transfer

Diagnostic implants measure vital health signs and include devices such as intra-cranial pressure monitors [33, 34], glucose sensors [35], deep brain activity sensors [36], oximeters [37], pH sensors [38], and gastrointestinal imagery pills [39]. The second category, therapeutic IMDs, have been used to treat some form of ailment via electromagnetic stimulation or targeted biochemical intervention according to a pre-calibrated stimulus or controlled closed loop feedback generated by another implanted sensory unit. These IMDs are used in applications such as pacemakers, nerve and muscle stimulator, deep brain stimulator [40], gastric defibrillators [41], targeted drug delivery systems [42]. Finally, assistive IMDs assist sick or even healthy people in improving anatomical and physiological functions. Some examples include cochlear implants [29], bionic vision implants [31], brain computer interfaces for prosthetic limbs [32], and athletic performance monitors. A summary of biomedical applications of implants is presented in Table 2.1. These implants could be either surgically implanted, ingested as a capsule or injected into the particular region of the body. The later two types are minimally invasive. Injectable IMDs are being championed as the future of electronic implants as technology improves miniaturisation.

So far, IMDs are designed for singular applications where communication is restricted between the IMD and external monitoring station either on-body or indoors. However, IMDs could be integrated into a wireless network of implants for more holistic and efficient data transmission. As such, the network of implants can be envisioned as an integral part of internet of things (IoT) for mainly two applications. On one hand, critical medical information could be passed on to patients' physicians and/or next of kin for immediate medical intervention irrespective of where the patient is. On the other hand, diagnostic information from individual patients could be compiled and analysed over time to assist in medical research. However, the later should be done in such way that patient privacy is protected. Although some IMD designs consider privacy and secrecy of

medical data, this calls for a rigorous inclusion of physical and application layers of the implant communication network which increases transmission overhead and reduces bandwidth efficiency.

2.3 Implants in the WBAN Architecture

2.3.1 WBAN and Implants

The Wireless Body Area Network (WBAN) is a subset of the metropolitan area network which is specific to communication around the human body. The general architecture of body area networks, as shown in Fig. 2.1, is that a link node wearable on the surface talks to and listens from the implanted and other surface mounted devices. It then combines and relays the signal to devices external to the body – mainly a monitoring or controlling device on the surface or a few meters away from the body. Another likely scenario is the possibility of two implants talking to each other; for example, a glucose sensor and an insulin pump. To reduce complexity and power consumption it is better to implement advanced security features at the link node rather than each individual implanted or on-body device.

2.3.2 Communication Modalities

Most of the IBC modalities considered in literature are based on the on-body (surface-to-surface) communication where both the transmitter and receiver are worn on the surface of the skin as shown in Fig. 2.2a. This modality, for example, enables ubiquitous communication for wire-free patient vital sign monitoring setups in hospitals. For implant communication as part of the WBAN architecture, we consider two modalities. The first modality is the implant-to-

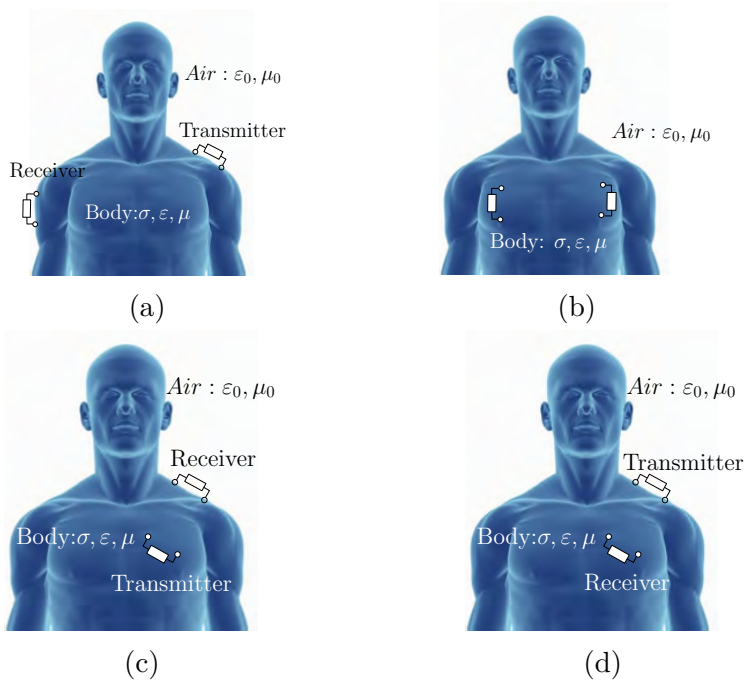

Fig. 2.2 (a) Surface–Surface communication. (b) Implant–Implant communication. (c) Implant–Surface communication. (d) Surface–Implant communication.

implant communication shown in Fig. 2.2b where both the transmitter and receiver are inside the human body. This modality can be used to communicate implants that operate in a closed loop control setting. Besides, implant to implant communication can also serve as information relaying mechanism to cover a long communication distance by chaining implants. The second assumes communication between a transceiver on the surface of the skin and an implant inside human body of given electrical characteristics as shown in Fig. 2.2d (implant- to- surface) and Fig. 2.2c (surface-to-implant). The implant-to-surface implants are used in diagnostic application where a sensed quantity is transmitted to outside the human body. On the other hand, the surface-to-implant modality can be used to with therapeutic and assistive implants to pass stimulation or control signals from the outside to the implant. This modality is also extensively used in wireless powering techniques to transfer power from external sources.

2.4 Implant Communication Technologies

In this section existing and emerging communication technologies are presented. Inductively coupled and antenna based RF technologies have been extensively used to enable communication between implanted and external devices. Other techniques such as intrabody communication that exploit the lossy dielectric nature of the human body, ultrasonic, optical and molecular techniques are emerging as alternative means for implant communication. A summary of implant communication technologies is given in Table 2.2.

2.4.1 Antenna based Radio Frequency (RF) techniques

This technique is employed by IMDs where the transmitted signal is fed to an antenna that radiates RF electromagnetic signals through the human body to an external receiver and vice versa. The external device is wearable on the surface of the body or located some distance away from the human body. Following previous designs and proposals, the antenna based RF communications for implants have been standardised by the Federal Communications Commission (FCC) in 1999.

Medical Device Radiocommunications Service (MedRadio)

In 1999 the medical implants communication system (MICS) was proposed by the FCC and later adopted by the European Telecommunications Standard Institute (ETSI) in 2002. The standard covers the communication between the implant and the controller, and implants within the same body using RF[12].

Technology	Method of propagation	Physical Layer Modulation	Range	Frequency	Standard
Antenna based RF	Radio wave propagation	FSSS, DSSS, QPSK	2 m	401 - 406 MHz, 2.36-2.4 GHz	MedRadio / MICS
Inductively coupled data transfer	Magnetic field (Mutual Inductance)	Load Shift Keying (LSK), Amplitude modulation, OQPSK	a few cm (<4 cm)	1,2,5,10,24,49 MHz	none
IBC - body channel communications	Electric field	FSDT frequency selective spread codes are used to spread the digital signal and select the carrier frequency	body confined (<10 cm for implants)	Galvanic < 10 MHz, Capacitive 21 MHz	IEEE Std. 802.15.6
Molecular Communications	Action potential, Axon propagation, ionic diffusion through junction gap, Hormone diffusion through blood	inter-spike interval codes, discrete binary and frequency coding, neural spike pulse modulation, chemical concentration, hormones as modulated carriers	nm -μm	(0,3 kHz]	none
Optical Communications	infrared propagation	IR Laser diode, VCSEL	mm (mostly subcutaneous <4 mm)	700 nm - 1 mm (300 GHz - 430 THz)	none
Ultrasonic Communications	ultrasonic propagation	OOK, ASK	Several centimeters (≈10 cm)	1-3 MHz	none

Table 2.2 Summary of implant communications technologies

The MICS standard uses the 402 MHz – 405 MHz frequency band with a bandwidth of 300 kHz per channel. This bandwidth is shared for up-link and down-link as the implant operates in full duplex mode, i.e., the sum of the up-link and down-link bandwidth should be 300 kHz. The duplex setting is mandatory because the standard employs a Listen Before Talk (LBT) protocol to prevent the implant from transmitting without the controllers request. The MICS standard is strict in the sense that the power at the band edges needs to be -36 dBm where the maximum power is limited to -16 dBm (25 μW) of Equivalent Radiated Power (ERP). Expansions of the MICS spectrum, initiated by the ETSI in 2004 and by FCC in 2006, led to the inclusion the 401–402 MHz and the 405–406 MHz as wing bands for non-emergency reporting and monitoring applications. Thus, the revised standard released in 2009 was renamed as Medical Device Radiocommunications Service (MedRadio).

It is interesting to observe here that the small bandwidth (300 kHz) is sufficient to support implants like pacemakers that require small data rates; however, does not guarantee the high data rate future requirements of implants (video, audio or networked). Although the MICS band is unlicensed, it is already in use by Meteorological Aids Service for telemetry of weather by weather balloons. As a result, existing MICS implants use several interference mitigation techniques to minimise the impact of meteorological services. Some of the techniques use multiple error correction codes (ECC) and automatic repeat request (ARQ) to overcome impulsive interferences [43]. The proposed error control codes such as BCH code [44] and Reed-Solomon (RS) code [45] employ sophisticated algorithms such as viterbi decoding algorithm. Other mitigation techniques require frequency agile algorithms to choose channels with lowest noise [43]. Thus, MICS implants require a complex transceiver structure. For this reason, the use of MICS is mostly limited to indoors with long polling intervals.

According to ETSI, yet another bandwidth for wideband implant communications is the Industrial Scientific and Medical (ISM) band around 2.4 GHz. In fact, this band is shared by other services like WiFi and BlueTooth. The standard for this band is set to use a Frequency Hopping Spread Spectrum (FHSS) and Direct Sequence Spread Spectrum (DSSS) with a maximum EIRP of 100 μW. The allocated range of frequency for this service is 2.36 GHz – 2.4 GHz.

Miniature Antenna Design

For small implant sizes the resonant frequency of implanted antennas considered fall within the Ultra High Frequency (UHF) band especially from 400 MHz – 2.4 GHz. Different types of antennas have been designed for compact implementation of IMDs at 402 MHz and dual band of 402 MHz/2.4 GHz to comply with the the MedRadio implant communication standard. These include monopole antennas [22] of size $18\times16\times1\text{mm}^3$, dipole antennas[9,32,31] with size ranging from $6\times6\times1.5\text{mm}^3$ to $16.5\times15.7\times1.27\text{mm}^3$, Planar inverted-F antennas (PIFA) [37,34] with sizes $13.5\times15.8\times0.635\text{mm}^3$, patch antennas [23] of sizes $15\times15\times3.81\text{mm}^3$ and cavity slot antennas of size $1.6\times2.8\times4\text{mm}^3$. Several techniques have been used to miniaturise the sizes of these antennas. For example, most dipole and monopole antennas use spiral arms while others use inductive loading and ceramic substrates; some patch, slot and PIFA antennas use stacked and meandered structures.

Several other conformal and non-conformal antennas have been investigated including the human body itself as a lossy monopole antenna [46]. The main challenge with antenna enabled implant communication is that the human body tissues incur increasingly high path loss with frequency. Unlike the air-to-air channel, the lossy dielectric nature of human body (66-70% water) and variable

tissue layers have been shown to drift the designed resonant frequency of the antennas in practice.

For an implant transmitting an electromagnetic field inside the human body, the field strength to penetrate through the transversal tissue layer is an important parameter. The depth at which the electric field is attenuated to $\frac{1}{e}$ of the original value is called skin depth where e is the base of the natural logarithm. The larger the skin depth is the deeper the implant can be installed. However, for MICS, apart from being shared by other popular services, penetration of electric field through the human tissue, i.e., skin depth is less than the corresponding value for lower frequency signals [5]; for example, it is 0.14 m at 20 MHz and 0.028 m at 402 MHz for muscle tissue. The quest for alternative communication mechanisms in and around the human body has led to investigation of other schemes such as the intrabody communication that use the human body as channel.

2.4.2 Inductively Coupled Data Transfer

Inductive data communication between IMDs and wearable devices is achieved via mutual inductance between primary and secondary coils. The current injected into the primary coil induces magnetic flux which in turn induces current in the secondary coil according to the coupling coefficient between the two as shown in Fig. 2.3. In most applications, a narrow band or single sinusoidal power source is used to continuously power the IMD and the IMD uses back telemetry to send sensory recording data back to the external device. This technique has been extensively used for applications that require short range implants such as muscle stimulators, retinal implants, cochlear implants and pacemakers [10, 11]. Different resonance frequencies have been used for inductive data transfer; for

example, 1 MHz [47], 5 and 10 MHz [48], 24 MHz [49] and 49 MHz [27] for the advanced bionics cochlear implant.

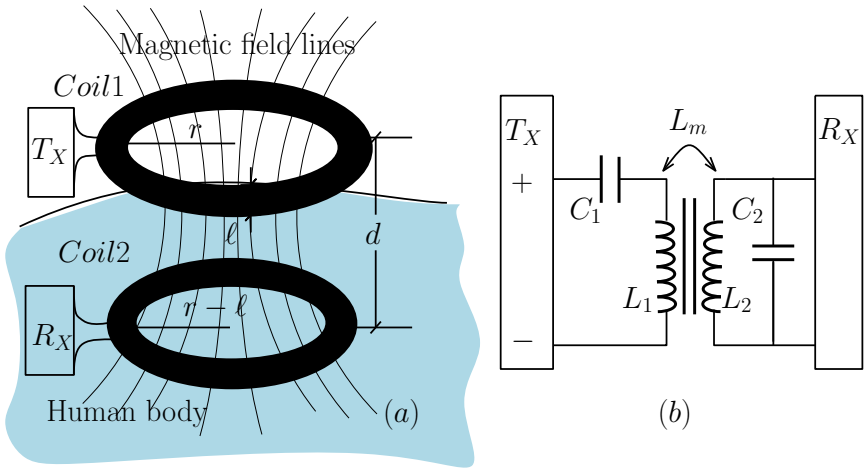

Fig. 2.3 Inductively coupled intrabody communication. (a) conceptual diagram and (b) A series parallel equivalent circuit

The challenges associated with inductively coupled systems is that it offers a small bandwidth (often in hundreds of kbps) when designed for efficient power transfer. To this end, several mitigation techniques have been proposed for wideband communications. These include separating the power and data link coil pairs in orthogonal dual-band arrangement to limit cross talk and using load shift keying (LSK) for data transmission [50–52]. Others use three coil pairs where one pair is used for power transfer and the other two orthogonal pairs are used for bidirectional offset quadrature phase-shift keying (OQPSK) modulation scheme to increase channel use and bandwidth [53, 54]. Recently, emerging solutions promise inductive coupling links with stacked multilayered coils with data rates in Gbits/s [55, 56]. Based on these, Burhan [57] proposed use of multi-layered graphene nano-coils to push the theoretical channel capacity in Tbits/s with operating frequencies in terahertz range. However there is a significant electromagnetic absorption by tissues at such high frequencies and feasibilities are yet to be tested.

Despite its popularity, inductive data transfer has not been standardised. As such, there is no noted inter-operability and integrability of devices based on inductive data transfer with other devices. Selection of operating frequency and physical layer architecture seems rather arbitrary.

2.4.3 Galvanic and Capacitive Coupled Intra-body Communications

In recent years, communication techniques that employ electric field communication (EFC) through human body as a channel have been proposed. These communication mechanisms are interchangeably referred to as human body communication (HBC), or body channel communication (BCC) or intra-body communication (IBC). In this technique, the human body is effectively a volume conductor. It exploits the lossy dielectric nature of the conductive tissue layers to induce a current, and hence a potential distribution, as a result of the electric field caused by the current injected by the transmitter electrode(s). Frequencies ranging from a few hundreds of kilohertz to a few tens of megahertz is a suitable choice for HBC. Such a low frequency signal is expected to penetrate deeper into the tissue layers, thus requiring less power be detected by a receiver on the surface of skin. Moreover, due to a non-conducting free space outside the skin surface, the signal is confined to within the human body.

The concept of IBC was pioneered by Zimmermann in his masters thesis in 1995 [58]. Since then, it has attracted a number of researchers mainly because it promises low power and inherently secured communication as the transmitted signal is confined within the body. Based on the way the current is coupled to the human body, we have two types of intra-body coupling mechanisms - capacitive coupling and galvanic coupling.

Capacitively Coupled IBC

In capacitive coupling, the signal is coupled into the human body via the signal electrode of the transmitter and receiver; a return path is established via the ground electrode through the path outside of the human body as shown in Fig. 2.4. This technique was originally proposed by Zimmermann [58]. Using this scheme, he successfully transmitted a 330 kHz signal with 3 V at 2.4 kbps digital transmission rate consuming 1.5 mW of power.

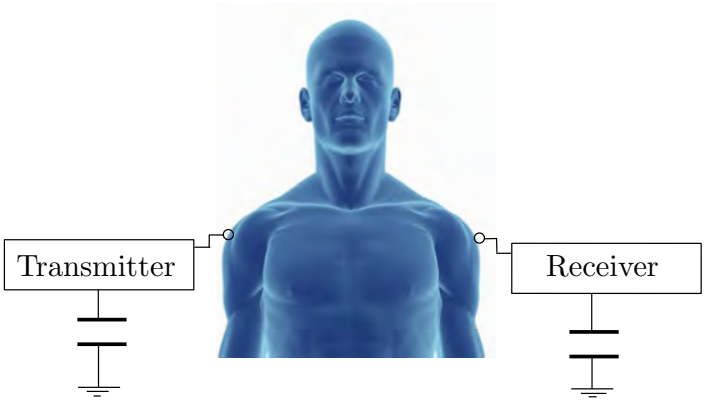

Fig. 2.4 Capacitively coupled intrabody communication

Later, M. Gray [59] developed the capacitive coupling further and designed a system with increased data rate capacity of 2 Mbps at carrier frequency of 100 kHz. He also showed that the noise in IBC is mainly due to circuit noise and interference from environmental EM sources. In 2004, Shinagawa *et al* [60] developed a capacitively coupled IBC system with a half-duplex transmission rate of 10 Mbps; this marked the first practical application of IBC. Then, in 2007, Fujii et al [61] developed a wearable ID key and used FDTD (Finite Difference Time Domain) simulation model for IBC; later that year, Cho *et al* [62] developed a distributed RC circuit model of the human body; they have validated that their model is consistent with human experimentation in the frequency range of 100 kHz – 150 MHz.

From all the studies conducted in capacitively coupled IBC, we can see that it is practically suited for surface-to-surface communication; it cannot be used for implant communication as the return path needs to be established outside the human body.

Galvanically Coupled IBC (gc-IBC)

In galvanic coupling, both the signal and current return electrodes of the transmitter and the receiver are in contact with the human body to couple current differentially as shown in Fig. 2.5. Galvanic coupling IBC was first introduced by Handa in 1997 [63]. This IBC mechanism detects received signal differentially and has inherent common mode rejection capability. Compared to capacitively coupled IBC, the effect by environmental noise outside the body is negligible for galvanic coupled systems. The signal noise is mainly due to differential mode noise. As a result, the system proposed in [63] only used a supply current of 20μA with a power consumption of only 8 μW. Thus, galvanic coupled IBC is a preferred scheme for implant communication.

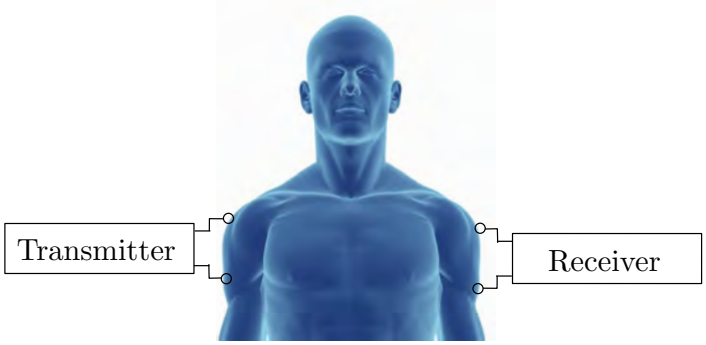

Fig. 2.5 Galvanically coupled intrabody communication

Lindsey et al [64] built a biomedical telemetry system to measure the tension in anterior cruciate ligament after surgery. They implanted a transmitter inside a cadaver and the receiver was on the surface (i.e., implant-to-surface setting).

From their experiment setup, they reported best performance when a current of 3 mA is used at 37 kHz. Following Zimmermann [58], Hadana [63] and Lindsey [64], there has been several developments and research on surface-to-surface intrabody communication system and communication models. However, not much has been done on practical implant communication based on intrabody communication techniques.

In 2005, Hachisuka et al [65] developed a two electrode and four electrode circuit model for the intra-body communication. From their experiments and model predictions, they concluded that the two electrode circuit model performed better than the four electrode model in the kHz and MHz frequency range. The two electrode model can be interpreted as the capacitive coupling and the four electrode model can be interpreted as the galvanic coupling IBC.

In 2011, Song et al [66] developed the four electrode circuit model and derived a transfer function for the galvanic coupled IBC. The model fits the measurement for the 100 kHz – 150 MHz well up to a scale factor. We note here that, most of the models are developed based on the surface-to-surface galvanic coupled setting. For implant communication, it is important to extend these models to include the transversal implant-to-surface communication channel. Wegmuller [67] first studied galvanic coupling for implant-to-implant communication using a simplified Finite Element Method (FEM) simulation model in Comsol Multiphysics software. However, limitations in the models did not explicitly capture the holistic essence of the channel. To this end, recently, we developed an analytical electromagnetic models that captures the variation of potential distribution and path loss as functions of variable number of tissue layers and thicknesses, implant size, depth of implantation transceiver properties in [13] (see Chapter 3)).

IEEE 802.15.6 Wireless Body Area Network (WBAN)

The IEEE 802.15.6 work group was established in 2007 to standardise wireless communication in, on and near the human body - the wireless body area network (WBAN) which was released in 2012 [44]. The IEEE 802.15.6 WBAN standard has three layers the Ultra Wide Band (UWB), the Narrow Band (NB) and the Human body Communication (HBC) layers. Frequencies used in the existing MedRadio standard are included in the Narrow Band specifications of the standard. The 2.4 GHz ISM band is also included in the UWB specification. The standard specifies the HBC to be centered around 21 MHz and uses frequency selective digital transmission (FSDT). Here, frequency selective spread codes are used to spread the digital signal and select the carrier frequency.

Although, HBC is specified mainly for surface to surface communication, works such as [68] [13] and [69] have explored the use, especially, of galvanically coupled IBC for implant communications at frequencies ranging from 100 kHz to 10 MHz. The implant communication channel is very different from the surface-to-surface channel. While the surface to surface channel has a band pass gain characteristic where the gain picks in the region 20-60 MHz, the implant-to-surface communication channel has a low-pass gain characteristics that favours lower frequency transmission for minimal path loss.

Antenna-free miniature implementation, low attenuation and body-confined transmission features of galvanically coupled IBC makes it a good alternative for implant communication. To this end, this Chapter calls for inclusion and proper specification IBC scheme for implant communication. With the advances in diagnostic and health monitoring sensors, the demand for high speed and long term communication continues to grow. Thus, a large number of people are expected to be aided by medical implants (in addition to the existing more than 25 millions of people with implants in the United States alone - estimated in

the early 2000s). Hence, there will be a high risk of interference from implants in different people which was not clearly addressed by the MICS standard. The use of HBC will address the issue of interference in implants in two people as the functional communication is limited to within the body.

2.4.4 Ultrasonic Communications

Ultrasonic communication is enabled by mechanical waves propagating inside the human body as an elastic medium with frequencies above 20 kHz as shown in Fig. 2.6(a). Conversion between electrical and ultrasonic signals is achieved through ultrasonic transducers mainly piezoelectric transducers. In some reports a backscatterng modulation is used to effectively transmit data at a rate of 50 kbps at 1 MHz only consuming 184 μW [14] where on-off keying (OOK) and amplitude shift keying (ASK) modulations are employed. A more involved PHY and MAC protocol that enables a high speed data rate of 700 kbps only consuming 40 μW has been proposed in [15].

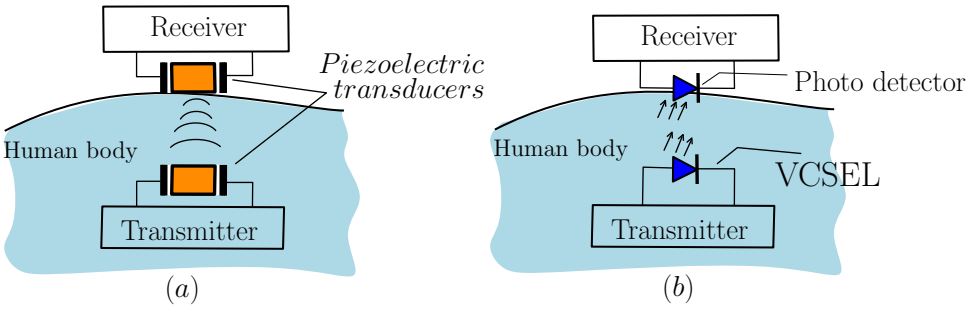

Fig. 2.6 (a) Ultrasonic Implant communication. (b) Optical implant communication using VCSEL.

Although it suffers from high attenuation, this technique is emerging as a valid alternative for short range communications that can be coupled with piezoelectric power scavenging techniques or be powered externally for a backscattering transmission. However, standards have not been adopted to extend its application to integrate with other systems.

2.4.5 Optical Communications

Optical implant communications are enabled by optical propagation of infrared (IR) waves. An implanted transmitter couples electrical signal in to the channel (human body) by converting it into IR signal using a form of laser diode as a transmitter. Often a vertical-cavity-emitting laser (VCSEL) diode is used at the transmitter. When the IR signal is incident, part of it is reflected and the reminder is scattered or absorbed by the human body. IR absorption by the human tissues (especially by skin) is so high that effective communication is limited to millimeters [16] given that the propagation complies to the guidelines set by the International Commission for Non-Ionising Radiation (ICNIRP) [70]. Thus, this communication technique is restricted to transcutaneous or subcutaneous implants. As shown in Fig. 2.6(b), a receiver on the surface of the skin employs a photo detector to convert the IR signal to electrical and proceed with the demodulation and detection of transmitted message. This technique is suitable for operation in the 700 nm - 1 mm (300 GHz-430 THz) band.

For example, Abita *et al* [16] used an 860 nm (348.596 GHz) carrier to transmit an RS-232 data of rate 115.2 kbps. Here, a photonic detector LED PDI-E804 is used over less than 24 mm communication distance where a porcine skin is used as a channel. Although the 24 mm range is an over-estimate for the subcutaneous implants which are often limited to less than 4 mm, the technique at nanometer wave could be used to achieve a much faster data rate up to 50 Mbps as presented in [17] (860 nm, 4 mW power consumption, 4 mm range, VCSEL Tx and PIN Si Photodiode Rx). In a relatively recent work, Mujeeb *et al* [18] proposed an all-optical (optical powering and data transfer) solution for subcutaneous implant communication of distance less than 4 mm. They used the "therapeutic window" of the spectrum which is the near infrared (NIR) band (from about 700 nm to 2500 nm) to obtain a CMOS based optimal optical power and data transfer since this band falls with in the silicon absorption band. As

such, this scheme promises a great deal of miniaturisation with the advances in silicon based technology.

The advantage of optical communication links in the human body is that they are least affected by channel interferences, but suffer from high path loss. Despite being a potential alternative, there is limited work on optical communication for implant communication and integrating it as part of the existing standards.

2.4.6 Molecular Nano-networks and Communications

Molecular communications (MC) refer to biological intrabody communications where the communication between nano-transmitters and nano-receivers is achieved by a combination of chemical and electrical signalling through the channel linking cellular transmitter and receiver. In living bodies, these nano transmitters and receivers (also referred to as nano-machines) are the basic functional units of nano networks that are able to convey simple information [71]. A single pathway in MC ranges in nm–μm distance with small frequencies of 0–3 kHz [72]. These simple nano-machines form a large scale nano-networks where they exchange and cooperate to enable transmission of complex information over an extended distance, e.g., the nervous system capable of interconnecting extremities of the human anatomy. Investigation of MC is motivated to understand the state-of-art mainly for two reasons. These are, to develop bio-inspired nano-networks for applications such as artificial prosthetics and to detect ailments or develop therapeutic interventions such as treatment of neurological ailments and targeted drug delivery when integrated within living organs. Mechanisms of MC are radically different from the conventional signal transmission techniques. Most MCs are enabled by diffusion of molecules while others are enabled by microtubles as channels. In scenarios such as the nervous and cardiovascular systems a combination of electrical and chemical molecules are employed. Analog type

communications are observed in cases where a continuous emission of molecules of varying concentration enables diffusion or variable interspike pulse widths enable electrochemical action potential propagation. Digital communication is observed in the discrete type of chemicals that bind with nanotrasmitter molecules or quantised release time of molecules. The three main nano-networks in human body are the nervous, cardiovascular and endocrine nanonetworks. These networks use a radically different communication paradigm than other traditions wireless communications.

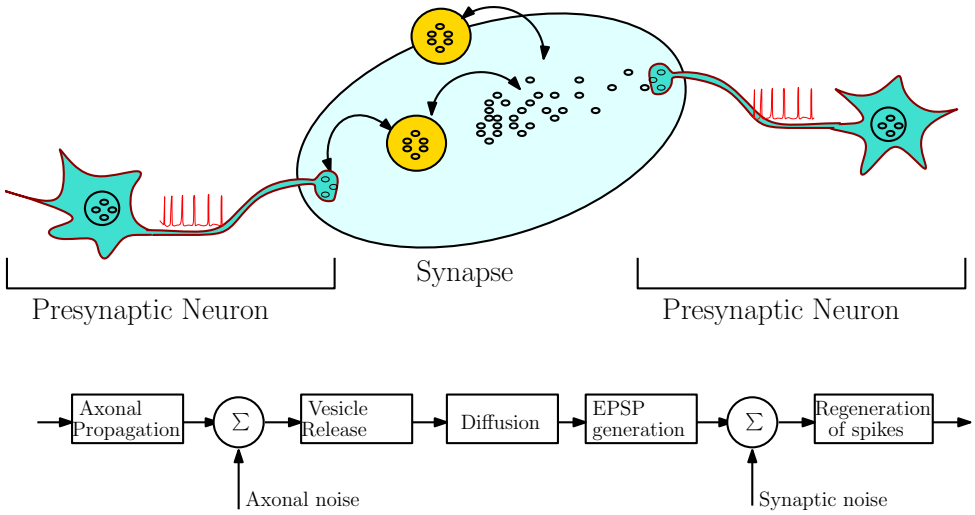

Fig. 2.7 An example molecular communication: Nervous nanonetwork channel [71].

The Nervous nanonetwork (NnN) is an ultralarge network of neurons where information is transmitted between different parts of the body [20]. The fundamental pathway in NnN is one that exists between two nanotransceiver neurons vis presynaptic neuron and postsynaptic neuron. There are two modes of communication to complete the path - Axonal propagation and synaptic propagation [73] as shown in Fig. 2.7. In axonal propagation action potential information is encoded as electrical impulses of variable width and the axon acts as a channel. At the interface membrane of the axon with the synaptic cleft, the propagated action potential induces calcium ions which bind with proteins released through the membrane. The synaptic transmission propagates the neurotransmitter

chemicals via diffusion across the synaptic gap where the rate of diffusion is controlled by the concentration of the chemicals released by the axon (which in turn is proportional to the electrical impulses that propagated the action potential). At the post synaptic end, the diffused proteins are intercepted by special receptors which will extract the ions and inject them through the receiving neuron membrane - synaptic decoding. In the postsynaptic neuron the rate of change of concentration of the ions induces action potential to regenerate the transmitted impulses. This induces a chain that can extend over a long distance. The axonal propagation suffers from axonal noise due to random opening and closing of the ion channel while the synaptic channel suffers from Brownian motion and interference from thousands of neighbouring synapses.

The Cardiovascular nanonetwork is based on the spontaneous action potential created by the cardiac pacemaker cells that are propagated to the cardiomyocytes to create the beating of the heart. It uses connexons as channels in the gap junctions. The connexon is normally closed and opens when it receives the propagated action potential to yield ion transfer in to the gap where diffusion takes over the rest of the way. In Endocrine nanonetworks, hormones are the modulated carries of molecular information. It uses diffusion through the blood. The rate of blood flow is proportional to the data rate and noise is mainly due to Brownian motion of the hormones in the blood.

As communication networks, molecular communications have been modeled as single-input-single-output (SISO) [21] and multiple-input-single-output (MISO) [19] schemes to information theoretically model communications. However, analysis has been limited to simplistic modes and more realistic models with experimental validations are yet to be carried out for complete understanding of these communication techniques.

2.5 Required Features and challenges of Medical Implant Communications

2.5.1 Implant Powering and Power Consumption

The main requirement in implant transceiver design is the low power consumption and a sustained power supply system as the implant is embedded inside the human body. Following the MICS standard, several implant transceivers have been designed and implemented. The most popular MICS implant transceiver is by Bradley [45] of Zarlink Semiconductors. This MICS transceiver consumes less than 5 mA current in the active mode and about 250 nA in the sleep mode at a supply voltage of 2.1–3.5 V; it consumes an average power of 11.5 mW and has a receiver sensitivity of 20 μ V r.m.s. at 400 MHz for a 200 kbps transmission. Microsemi Corporation [74] has also commercialised transceiver, for various MICS telemetry, that has similar features as given in [45]. In 2009 Cho *et al* [75] developed a dual MICS/HBC transceiver consuming a total of 10 mW (2.3 mW for HBC and 8.5 mW for MICS) at a data rate of 50 kbps at the transmitter and 200 kbps at the receiver. Although this transceiver uses less power for MICS than Bradley's [45], the receiver sensitivity is higher at 35 μV_{rms}. The MICS transceiver that consumes the lowest power was developed by Pandey *et al* [76]. At 400 MHz the transceiver consumes 90 μW with an output (transmitted) power of 20 μW (less than the maximum 25 μW set by MICS) with a 200 kbps data rate. The transmitter has an active area less than 200 μ m $\times$ 200 μ m.

Despite this, development of low power implants and sustainable implant powering is still an open problem which has been reviewed in depth by Bazaka *et al* [77]. Single use or rechargeable batteries have been the common power source for implanted medical devices. For example, Medtronic has developed a small

pacemaker a size of vitamin pill, Micra [78] powered by an estimated average 12-year battery life. However, in the case of single use batteries, expensive replacement surgeries are required. To address this challenge, IMDs with rechargeable batteries have been designed to be charged by external power sources. These batteries constitute most of the implant size and impede implant miniaturisation in addition to the risk of adverse bio-compatibility effects[1]. Thus, other powering techniques have been adopted to replace batteries.

Powering techniques that replace batteries can be broadly classified into two; the first being the use of the surface to implant transmitter which transmit a coded power in the form of electromagnetic field to an implant, and the second is the use of electro- and bio- chemical reactions in the body to generate power. With respect to the former, inductively coupled power transfer have been extensively used to power IMDs [79, 80] such as pacemakers, bionic vision[31] and cochlear implants. Here,the primary coil associated with the external power source couples the time harmonic power signal to the secondary coil associated with the IMD via a mutual inductance. External RF electromagnetic sources radiating coded power signals have been used power IMDs where the IMD modulate the message and relay the signal back via backscattering similar to RFIDs[81, 82]. Bio-battery systems using glucose oxidation has been reported to generate a power of 3.4 $\mu W\ cm^{-2}$ – 180 $\mu W\ cm^{-2}$ [77]. Other systems using glucose bio-fuel cells were shown to deliver power density up to 1.3 mW cm^{-2} with an open circuit voltage of 0.95V; by combining two of these cells in series the authors were able to generate 3.25 mW at 1.2 V and an open circuit voltage of 1.8 V. Moreover, electrical power scavenging mechanisms within the body such as human body movement[83, 84], piezoelectric [85], bioelectrical[86] and other biochemical reactions [87, 88] to power IMDs have been investigated. The potential of these techniques render batteryless power source as the future of implant powering.

2.5.2 Miniaturisation and Lower-bound on Implant size

As a foreign object, an implant introduces discomfort to surrounding tissues in addition to requiring invasive surgeries. Thus, light weight and small implant sizes are key features for minimal invasiveness. The size is dependent on electronics, antenna required and battery size. Advancement of the circuit technology ensures a great deal of miniaturisation. The use of batteries is being replaced by betteryless powering regimes. Thus, research on miniaturising implants is focused on antenna sizes. Although low frequency signals experience low path loss, radio wave based RF transmissions are forced to move into the ISM band for miniature micro strip antennas [89, 90]. Helical antenna structures (that can be compacted in small volumes) with circular polarisation have also been used in pill sized ingested implants [91, 92]. The geometry of the antenna determines the frequency of operation and hence does not leave much room for flexibility. In fact, the most reported challenge with microstrip patch antennas at a very high frequency is that a small error in the cut dimensions results in a considerable shift in resonant frequency. Despite this, implant sizes up to 1.4 mm $\times$ 0.905 cm $\times$ 0.945 cm have been designed to operate at 2.4 GHz [93]. Although antennas in GHz frequency partially address the issue of implant size, the human body channel incurs a pthloss of 50-60 dB in a commination distance of 4 cm. Thus, it is worth considering the low frequency IBC techniques with a promise of a better trade-off (i.e., lower path loss and smaller size); this issue of implant size have not been addressed adequately by other researchers.

In general, for galvanically coupled IBC, the larger the intra-electrode distance is the smaller the pathloss will be. Hence, intra-electrode distance can be assumed to be the maximum dimension of the implant. Callejón *et al* [94] developed a simulation model for galvanic coupling IBC as a four port network using a finite element approach to analyse the electric field distribution and current density. Their model and experiments based on human arm on a surface-to-

surface setting showed that path loss decreases as the intra-electrode distance increases. However, this study considered only a few electrode spacing in the surface-to-surface setting and hence needs further work to explain the effect of electrode spacing on implant communication. A trade-off between electrode spacing (intra-electrode) and communication distance (thereby path loss) is an important investigation. To this end, in our previous work [13], we presented analytical and simulation models of IBC for implants that explicitly showed the effect of electrode spacing and tissue layers in pathloss as a function of the communication distance and frequency. Supported by validation experiments, it was shown that galvanically coupled IBC is a feasible means for implant communication. Although smaller electrode spacing incurs larger path loss, the limit up to which this spacing could be reduced (for a required receiver sensitivity) is an important target to consider for implant miniaturisation.

We propose here an intuitive lower bound on the implant size for galvanically coupled IBC. We modeled the galvanic coupled transmitter electrodes as linear dipole antenna sitting inside a lossy dielectric as shown in Fig. 2.2a - 2.2d. The receiver electrodes are also modeled as linear dipole sitting inside the same dielectric and on an air-dielectric boundary to simulate the implant-implant and implant-surface communications respectively.

Considering the implant-to-implant communication scenario given in Fig. 2.2b. Any electromagnetic communication is governed by the set of Maxwell's equation given by

$$\nabla \times \overrightarrow{E} = -\frac{\partial \overrightarrow{B}}{\partial t}, \tag{2.1}$$

$$\nabla \times \overrightarrow{H} = \overrightarrow{J} + \frac{\partial \overrightarrow{D}}{\partial t}, \tag{2.2}$$

$$\nabla \cdot \overrightarrow{B} = 0 \text{ and} \tag{2.3}$$

$$\nabla \cdot \overrightarrow{D} = \rho \tag{2.4}$$

where $\overrightarrow{J}$ and ρ, respectively, are volume current and charge densities that exist in the medium (human body) as time-varying sources. The electric field flux D and the magnetic field density B can be defined in terms of the electric field E and the magnetic field strength H respectively as

$$\overrightarrow{D} = \epsilon \overrightarrow{E}, \text{ and} \tag{2.5}$$

$$\overrightarrow{B} = \mu \overrightarrow{H} \tag{2.6}$$

where ϵ is the permittivity and μ is permeability of the human body as a dielectric material. The relative permittivity (ϵ_r) and conductivity (σ) values as functions of frequency are given in [95]. For muscle tissue, the typical relative permittivity at 21 MHz is $\epsilon_r = 110$. Here $\epsilon = \epsilon_r \epsilon_0$ where $\epsilon_0 = 8.854 \times 10^{-12}$ F/m and $\mu = 4\pi \times 10^{-7}$ H/m. Since the tissue is lossy, i.e., has non-zero conductivity value, we use the complex permittivity $\epsilon' = \epsilon + j\frac{\sigma'}{\omega}$ instead of just the real value to account for the loss. Here, σ is the conductivity of the muscle tissue which is typically 0.6426 S/m at a frequency of f=21 MHz. The variable ω is the angular frequency given as $\omega = 2\pi f$.

Solving Maxwell's equation for the setting given, the electric and magnetic field strength are

$$\overrightarrow{H} = \frac{j\beta Il}{4\pi r}\left(1 + \frac{1}{j\beta r}\right)\sin\theta e^{-j\beta r} a_\phi \tag{2.7}$$

$$\overrightarrow{E} = \frac{\eta Il}{2\pi^2 r}\left(1 + \frac{1}{j\beta r}\right)\cos\theta e^{j\beta r} a_r + \frac{j\beta Il\eta}{4\pi r}\left(1 + \frac{1}{j\beta r} - \frac{1}{\beta^2 r^2}\right)\sin\theta e^{-j\beta r} a_\theta \tag{2.8}$$

where, β is the wave number given by $\beta = \omega\sqrt{(\epsilon'\mu)}$, η is the characteristic impedance of the medium given by $\eta = \sqrt{(\frac{\mu}{\epsilon'})}$, I is the current injected into the transmitting electrode, l is the intra-electrode distance, r is the inter-electrode distance (distance between transmitter and receiver) and θ is the angle the

electrode makes with respect to the vertical axis. The power contained in an electromagnetic field per unit area is given by

$$\overrightarrow{S} = \langle \overrightarrow{E} \times \overrightarrow{H}^{*} \rangle. \tag{2.9}$$

Hence the total power contained by the electromagnetic field can be calculated as

$$P = \oint \overrightarrow{S} \cdot ds. \tag{2.10}$$

Evaluating the power for the maximum power transfer scenario (i.e., matched impedance in the receiver circuit and receiver electrode), the power the receiver detects at a distance r is bounded by

$$P \leq \Re\left\{ \frac{3\eta I^2 l^2}{64\pi r^2} \left(1 - \frac{1}{\beta^2 r^2} + \frac{1}{\beta^4 r^4} \right) \right\} \tag{2.11}$$

Finally, the lower bound on the intra-electrode distance is given by

$$l \geq \Re\left\{ \sqrt{\frac{64\pi r^2 P}{3\eta I^2 \left(1 - \frac{1}{\beta^2 r^2} + \frac{1}{\beta^4 r^4} \right)}} \right\} \tag{2.12}$$

Combining the requirements of MICS and the IEEE 802.15.6 standards, the receiver sensitivity can be set to -92.5 dBm of power. Assuming an input current of 1mA and material properties of the muscle tissue, the lower bound for different frequencies is graphed in Fig. 2.8. In fact, the bound can be computed for different implantation scenarios by considering appropriate tissue characteristics and frequency of operation for analysis purposes.

This lower bound is tight in the sense that it can be achieved with equality. This shows that the implant designs can further be miniaturised to a great extent.

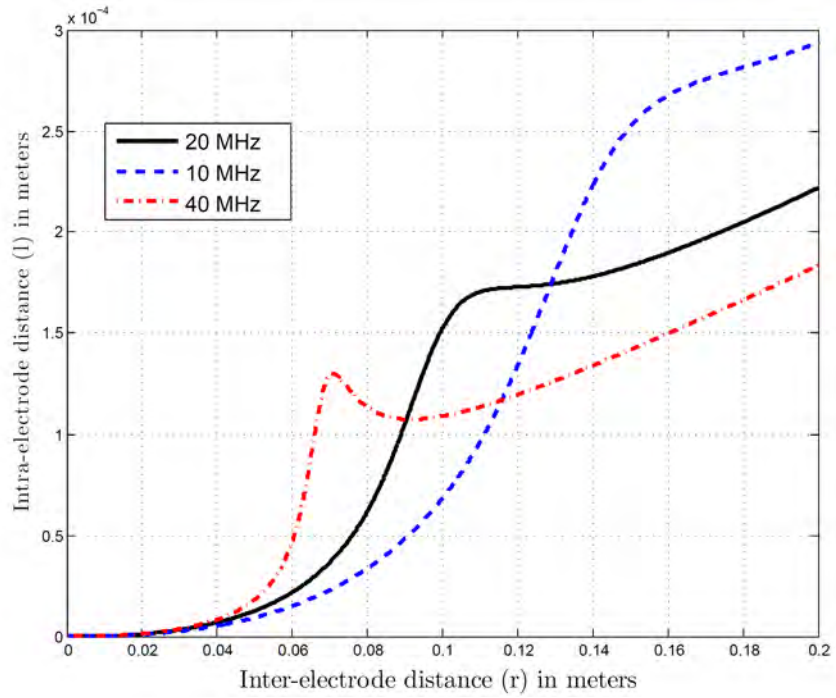

Fig. 2.8 The lower bound on inter-electrode spacing as a function of communication distance.

For example, at 1 mA transmitter current and -92.5 dBm receiver sensitivity we can achieve up to a minimum of 70 μm electrode spacing on a 10 MHz signal for a communication distance of 10 cm. A distance of 10 cm can be considered larger than most practical depths to embed medical implants. Besides, the lower bound shows that lower frequency signals prevail in the near field galvanic coupling setup; while higher frequencies dominate the far-field due to the onset of RF propagation.

2.5.3 Human safety and Bio-compatibility

In addition to design challenges for reliable implant communication, the emanating electromagnetic signal should not exceed the limits for human safety. Moreover, the IMD should be bio-compatible to the surrounding tissue (i.e., inert to its surrounding). With regards to human safety, the International Commission

for Non-Ionising Radiation (ICNIRP) developed a guideline with regards to maximum electric filed, current density, specific absorption rate (SAR) exposures for the general public and occupational settings [70]. To ensure bio-compatibility, encasing the IMD inside steel containers, polymers and/or other superstrates inert to tissues nearby [96, 97]. However latter two are relatively short-lived compared to the desired life span of the IMD. Tissue growth around the device (especially the active region of sensing units) would degrade IMD efficiency over time. Besides, stimulation electrodes (especially in the case of cortical and deep brain implants) have been shown to cause tissue scaring over prolonged usage. To this end, electrode material and geometries that minimise such scarring have been investigated with promising results [98, 99].

2.6 Conclusion

In this chapter we have reviewed progress and challenges in communication and applications of implanted medical devices. We have also presented possible future directions. Electronic medical implants have come a long way since their first application as a pacemaker in late 1950s. Today, IMDs are used in several diagnostic, therapeutic and assitive technologies in health-care and professional sports. The progress has been standardised as MICS in 1999 which later was upgraded to MedRadio services in 2009. Recently, the WBAN standard was also released in 2012 to include non radiating body coupled communications that use the human body as a channel at lower frequencies than considered in MedRadio. These standards has aided the research community and industries like Medtronic and Zarlink to design and develop IMDs with compatible communications circuitry. Although, coordinated effort led to advancement in IMD technology, there are still challenges the research community is targeting to address. These include, reliable and sustainable power sources, implant miniaturisation, bio-

compatibility and human safety. With further advancements and the soaring demand for IMDs, implants per user are envisioned to be interconnected via a wireless network for reliable data transmission to and from the patient to physicians and next of kin even far away. Besides, advancements in the big data analysis can be exploited by compiling data from various patients over time to aid in medical research.

Our review and assessment of the technologies also directed us to further investigate the galvanically coupled IBC scheme as an alternative for implant communication. The motivating features of gc-IBC include, inherently secured body confined communications, use of the loss dielectric nature of the body (and hence predicted low path loss) and especially the achievable miniaturisation bound. Thus, in the next chapters we analytically model, simulate and comparatively analyse the human body as a channel for gc-IBC implant communications. We then design, implement and characterise a novel sensor integrated gc-IBC implant transceiver prototype.

Chapter 3

Galvanically Coupled Intra-body Communications for Medical Implants: A Unified Analytic Model Framework

Electronic health monitoring and diagnostics technology continues to be of great interest in research due to an increasing number of people with chronic diseases. For an improved accuracy and timely diagnosis, implanted electronic medical devices (IMDs) could be surgically inserted inside the human body to for a real-time sensing and transmission of diagnostic information. However, development of effective techniques for communicating the implant with outside world is still an open problem. Existing techniques that rely on propagation of radio wave signals are standardised as the Medical Implant Communication Services (MICS) in the 402–405 MHz frequency range. This was later adopted as Medical Devices Radiocommunications Services (MedRadio) by extending the frequency range to 401–406 MHz. However, the human body has higher attenuation to

signals at high frequency. Intra-body communication (IBC) is a relatively new technique that uses the human body as a channel with lossy dielectric properties for frequencies ranging from a few hundreds of kilohertz to several megahertz. In this chapter, we propose a novel analytical electromagnetic model framework using the galvanically coupled IBC (gc-IBC) as an alternative to radio wave based implant communication. The model is based on multi-layered ellipsoidal geometry that can be applied to any part of the body such as the head, limbs and torso. As such, the model is a unified framework with a wide range of application [13]. The model proves to effectively describe the influence of various tissue layer thicknesses and electromagnetic properties, implant size and depth, and geometry of the body part. Analysis of the model confirms the inherent security and low power consumption of IBC. The path loss incurred by IBC implants is also shown to be lower compared to their MICS counterparts with a promise for further miniaturisation of existing implant sizes.

3.1 Introduction

Fundamental and applied research in electronic health-care monitoring and medical diagnostics technology has drawn a great deal of attention from engineering and medical research community. In fact, it will continue even more so due to an increasing prevalence of chronic diseases [3]. For improved accuracy and timely diagnosis, and hence improve quality of life, sophisticated actuators and biosensors are emerging for various diagnostic applications; for example, glucose sensors for continuous diabetes monitoring [100]. For real-time health care monitoring, these biosensors need to be implanted inside the respective organs and tissues. However, development of effective techniques for communicating the implant with outside world is still an open problem. Over the past decades, a number of techniques for implant communication have been proposed to en-

able implanted medical devices (IMDs); however, existing IMD communication enabled by antenna-based, inductively coupled and wired techniques have been employed in implants such as cardiac pacemakers, deep-brain stimulators, bionic visual and cochlear implants.

The European Telecommunications Standards Institute (ETSI) standardized previous efforts as the MICS standard in 1999. This standard employs wireless communication technique based on radio wave propagation of Radio Frequency (RF) signals with bandwidths of 300 kHz in the 402–405 MHz frequency range [12]. The Federal Communications Commission (FCC) extended the spectrum to the 401–406 MHz range, later in 2009, and renamed the standard as the Medical Device Radiocommunications Service (MedRadio) by combining a core band which is exactly the same as the MICS band and setting wing bands in the 401–402 MHz and 405–406 MHz [101]. In addition, other wideband antenna-based techniques in the gigahertz range and inductively coupled transmission techniques have also been explored; challenges associated and advantages are reviewed in [2, 102, 103]. Implant communication using electromagnetic waves at such high frequencies require transmit signal to travel through different human body tissues incurring a great deal of attenuation. Thus, large transmit power is required resulting in an expensive powering regime with frequent replacement of battery in battery powered implants. Moreover, recommended safe levels of Specific Absorbtion Rate (SAR) are limited by the International Commission on Non-Ionizing Radiation Protection (ICNIRP) guidelines which also limits the maximum electric field, current densities and hence signal transmission power within human tissues[70].

Pioneered by the early works of Zimmermann conducted in 1995 [58], intra-body communications at a much lower frequency compared to their MedRadio counterparts have gained a spotlight in the research community. Relatively recently, in 2012, the IEEE 802.15.6 work group released standards for intra-

body communications. According to the IEEE 802.15.6 standard for wireless body area networks, intra-body communication (IBC) refers to electric field communication (EFC) using the human body as a channel with a lossy dielectric characteristics[104]. This technique is also interchangeably referred to as human body communication (HBC) or body channel communication (BCC). The EFC in IBC is enabled by the induced electric field as a result of electric current injected into the human body via one or two electrodes of the transmitter directly attached to the human body. The signal frequencies used are in the range of hundreds of kilohertz to a few tens of megahertz. The IEEE 802.15.6 standard comprises of three layers where the EFC based IBC technique (mainly for surface to surface communications) is presented in the HBC layer with frequency of operation centred at 21 MHz. The standard also specifies other layers based on radio-wave communication at higher frequencies; the MedRadio band (401–406 MHz) is used in the narrow band (NB) layer and the industrial, scientific and medical (ISM) band (2.4 GHz) used in the ultra-wideband (UWB) layer. In the case of HBC, the signal can be coupled capacitively where only the signal electrode is connected to the human body with the ground electrode left floating [58], or galvanically where both the signal and ground electrodes are connected to human body to inject current differentially[105]. Although the galvanically coupled IBC has a potential to be used in implant communication setting, the standard focuses more on the use of HBC for surface-to-surface communication.

In this work, a novel analytical model framework is proposed for galvanically coupled intra-body communication (gc-IBC) technique to explore its use as an alternative for implant communication. It is crucial that an implanted transmitter inside the human body consumes low power to conserve battery life so as to minimise highly invasive and expensive replacement surgeries. Besides, due to sensitive nature of medical data, it is imperative that security is a paramount requirement of implant communication. To achieve security either

the signal needs to be encrypted at the transmitter or be confined to within the body detectable only by an on-body receiver.

Antenna enabled MICS implant employ propagation of radio waves where the signal is radiated inside and outside the human body. Therefore, it is required that security features be implemented right at the transmitter in order to protect the signal from any adversarial attempts. This, in turn, increases the transmitter complexity requiring power hungry features. Moreover, added features incur further difficulty to miniaturise the transmitter.

HBC is an electric field communication where the human body is effectively used as a volume conductor. Electric field is set by the current injected by the transmitter electrode(s). The lossy dielectric nature of the conductive tissues enables an induced current and hence a potential distribution from the field. At low frequency, the penetration depth of the signal through the tissue layers is expected to be high. Thus, less transmission power is required for the signal to be detected by a receiver on the surface of skin. Moreover, the non conducting free space outside the skin surface ensures the signal to be confined within the human body. Therefore, this communication technique is inherently secure.

Lindsay *et al* [106] used galvanically coupled implant communication between skin surface and a sensor implanted in anterior cruciate ligament of a cadaver in an experimental setting. They have empirically observed a minimum path loss of 37 dB for signals with frequency 2–160 kHz and currents of 1–3 mA at 5 cm distance from the transmitter location. Sun *et al* [107] used a simplified homogenous spherical model and implemented an implant to surface transmitter. They successfully introduced 'x' – shaped electrodes to improve current flow and hence minimise power consumption significantly [108]. However, the discrepancy between the simplified model and the actual measured values show that homogenous models overestimate the measured surface potential which requires

a proper multilayered tissue model. Wegmuler *et al* [68] implemented a finite element method (FEM) simulation of implant–to–implant communication and conducted an experimental test on a homogenous phantom solution. They used signals at 100–500 kHz with current less than 1 μA and found approximately 32 dB loss over 5 cm of transmission distance. Their work reported the predicted dependency of path loss with transmission distance and electrode length. Other mechanisms of implant-able wireless communication and their challenges are also reviewed in [3, 109, 110].

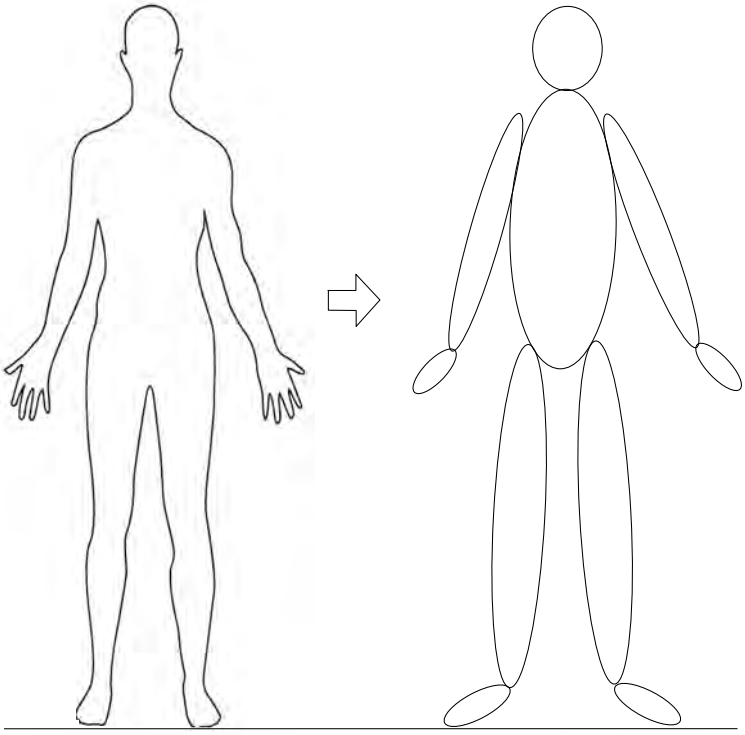

Fig. 3.1 Ellipsoidal approximation of human body

Since it is difficult to conduct in vivo measurements in living humans, to characterise implant communication, experiments have been limited to human cadaver [106] (a different channel due to dry tissues and dead blood cells), anesthetized animals and homogenous body phantom solutions [107]. On the other hand, the existing numerical and analytical models for implant communication are limited to homogenous volumes of simplified geometries [68]. Implant

location directly affects communications due to path loss variation resulting from anthropometric geometries and tissue strata dimensions. Little has been reported on characteristics of different parts of human body as a channel for implant communication. Our proposed model provides an analytical solution to a volume conduction based implant communication scenario for any part of the body modelled by multilayered ellipsoidal geometry.

The reminder of this chapter is organised as follows: section 3.2 motivates and discusses the framework of our model setup while Section 3.3 briefly describes the volume conduction theory and restates the set of Maxwell's equations that govern a galvanically coupled implant communication under quasi-static assumptions. In section 3.4, we define the confocal multilayered ellipsoidal geometry and its symmetry associated with various tissue layers. Later, section 3.5 presents the derivation of electric potential distribution by treating special functions called Lamé's functions in an ellipsoidal coordinate system. Section 3.6 discusses the results in view of potential distribution, path loss and effect of tissue layers; and finally our conclusion is given in section 3.8.

3.2 Model Setup

A number of modeling techniques have been proposed in literature to model the human body as a channel for intrabody communications. Some of these techniques include the two-terminal circuit model [111, 112], four-terminal circuit model [112, 113], finite element approach [68, 69], surface electromagnetic propagation model [114, 115], near-field electromagnetic model [115] and quasi-static electromagnetic model [116]. These models describe various useful aspects of intra-body communication. However, simple geometries that are limited only to specific body parts are used in most of the electromagnetic models used and some fail to capture the multiple tissue layers. On the other hand, circuit

models are generally shortsighted in the sense that the relationship between channel variations and circuit components is not obvious in the transfer functions, although some characterized the channel well in fixed settings.

The analytical electromagnetic model framework presented in this work is motivated by geometries robust enough to capture the multiple tissue layers in a scalable way that can be applied to any part of the body while simple enough to guarantee analytical solutions. Mathematical models of the channel are derived based on the geometry framework to characterise the received signal as a function of the size of the transmitter, transmitter location (depth of implantation), tissue layers of the body part, receiver location and electrode spacing.

By exploring the anatomy of human body further, as shown in Fig. 3.1, it is found that most parts of the human body can be approximately represented by variations of ellipsoidal geometry. A spherical, prolate spheroid, oblate spheroid, or ellipsoid with a dominating semi-axis are several derivatives of an ellipsoidal geometry that can describe various parts of the human body. An ellipsoid geometry close to spherical symmetry can be used to model the human head. An oblate or prolate ellipsoidal geometry can be used to model the torso. In existing electromagnetic models (e.g. [116], [69]), the limbs are often modelled by a cylindrical geometry which can be approximated by an ellipsoid with one dominating semi-axis and other two comparable semi-axes. The largest semi-axis represents the length of the limb, while the other two represent the larger and the shorter radii of the limb; as such, the ellipsoid geometry is more realistic than the cylindrical geometry.

Hence, an electromagnetic model framework that uses a multilayered ellipsoidal geometry to represent the different tissue layers can approximate different body parts by defining the semi-axes lengths according to the average length and radii of the body part. Each tissue layer with varying thickness can be

represented by ellipsoidal shells with an associated complex permittivity and conductivity. As shown in section 3.5, exploiting the symmetric nature of the ellipsoidal geometry and the orthogonal property of the ellipsoidal harmonics greatly simplifies complex analytical expressions that might result otherwise. Ellipsoidal geometry and harmonics have been successfully used in astronomy to analyse gravitational fields in celestial objects in our galaxy [117], and in inverse problems of Electroencephalography (EEG) [118] and Magnetoencephalography (MEG) [119] to localise brain activity sources.

3.3 Volume Conduction Theory for Implant Communication

Volume conduction can be defined as a transmission technique for electric field inside the volume of a lossy dielectric where an electric field is induced by a primary current source; and this field propagates to the receiver by means of an induction current induced in the conductive medium [120]. A galvanically couple IBC transmitter can be viewed as the primary current source inside one (or shared by more) lossy dielectric tissue layers. The total current inside the considered volume (i.e., the sum of primary and induced currents) induces an electric potential distribution inside and on the surface of the body [121]. The IBC receiver could be either another implanted device or a wearable device on the surface of the body that uses its two electrodes to sample the potential difference that exists between the locateions the electrodes are connected to. The considered transmission frequencies do not exceed a few megahertz. At such low frequencies the conductivity and permittivity profiles of human body tissues are such that the electromagnetic signals in the body can be assumed to be quasi-static [116], [122]. Let the electric and magnetic fields be denoted as $\mathbf{E}$ and $\mathbf{B}$ respectively. In quasi-static assumptions the changes of these fields

with time are assumed to be negligible. Hence, the set of Maxwell's equation describing the fields inside the human body can be modified as follows:

$$\begin{aligned} \nabla \times \mathbf{E} &= -\frac{\partial \mathbf{B}}{\partial t} = 0, \\ \nabla \times \mathbf{B} &= \mu J + \mu\epsilon \frac{\partial \mathbf{E}}{\partial t} = \mu J, \\ \nabla \cdot \mathbf{E} &= 0, \\ \nabla \cdot \mathbf{B} &= 0. \end{aligned} \tag{3.1}$$

Where μ is permeability of free space and $\mathbf{J}$ is the net current density in side the volume $[A/m^3]$. Due to the quasi-static assumption, the partial derivatives of the electric and magnetic fields are set to zero (i.e., $\frac{\partial \mathbf{E}}{\partial t} = \frac{\partial \mathbf{B}}{\partial t} = 0$). Here, the electric field $\mathbf{E}$ is

$$\mathbf{E} = -\nabla V, \tag{3.2}$$

where V is the electric potential distribution.

As shown in Fig. 3.2, the gc-IBC implant transmitter is depicted such that its anode and cathode electrodes are used as source and sink for the primary current injected into the tissue volume. The locations of the electrodes in the three dimensional space are denoted by r_1 and the sink by r_2. The current in each of these two points is expressed as point current sources and hence are singularity points for the current density. The source current density $[A/m^3]$ denoted by I_{source} at the source point is expressed as

$$I_{source}(r) = I\delta(r - r_1) \tag{3.3}$$

and the current density at the sink is

$$I_{sink}(r) = -I\delta(r - r_2). \tag{3.4}$$

Here I denotes the primary current $[A]$ injected by the transmitter. Assuming the anode and the cathode electrodes to be the only current source and sinks, the total source current density injected I_{tot}, as a function of point r in space, is given by

$$I_{tot}(r) = I[\delta(r - r_1) - \delta(r - r_2)]. \tag{3.5}$$

While gc-IBC implant communication is desired to operate at comparatively large frequencies (hundreds to a few megahertz), bio-signals (e.g., action potentials) inside the human body exist in frequencies less than 10 kHz [123]. This further supports the assumption that there are no current sources other than the transmitter electrodes.

At the transmitter electrodes, the current distribution creates a current dipole moment acting midway between the anode and cathode electrodes. The dipole moment is denoted by $\mathfrak{M}$ and is given by $\mathfrak{M} = Id$ where $d = |r_1 - r_2|$ is the electrode spacing. Thus, the net primary current source density J^s is

$$J^s(r) = \mathfrak{M}\delta(r - r_0) \tag{3.6}$$

where $r_0 = \frac{r_2+r_1}{2}$ denotes the position midway between the source and sink points at which the current dipole is acting. This source current induces the electric field $\mathbf{E}$ given in (3.2). This electric field in turn induces a current referred to as the induction current. The induction current density denoted by J^i is

$$J^i(r) = \sigma(r)\mathbf{E}(r) \tag{3.7}$$

where $\sigma(r)$ denotes the conductivity of the tissue layer at point r. The total current density J inside the considered volume is then given by

$$\begin{aligned} J(r) &= J^s(r) + J^i(r) \\ &= J^s(r) + \sigma(r)\mathbf{E}(r). \end{aligned} \tag{3.8}$$

It is this total current density J that is responsible for the propagation of the signal from the transmitter to a receiver implanted inside the body or wearable at the surface. The divergence of both sides of (3.8) gives

$$\nabla \cdot J(r) = \nabla \cdot J^s(r) + \nabla \cdot \sigma(r)\mathbf{E}(r). \tag{3.9}$$

In the gc-IBC implant setting, the region external to the human body is taken as non-conducting free space (i.e., $\sigma(r) = 0$). As such, the conduction current vanishes outside the human body and hence is confined to within the body. This can also be stated as no amount of electric current diverges outside the human body. Mathematically, the divergence of the current density $\nabla \cdot J = 0$. As a result, from (3.9) we have

$$-\nabla \cdot \sigma(r)\mathbf{E}(r) = \nabla \cdot J^s(r). \tag{3.10}$$

Substituting (3.2) and (3.6) into (3.10), we have

$$\nabla \cdot \sigma(r)\nabla V(r) = \nabla \cdot \mathfrak{M}\delta(r - r_0). \tag{3.11}$$

From (3.11), it can be seen that the potential distribution follows Poisson's equation inside the tissue layer that contains the implant. On the other hand, for other tissue layers that do not contain the implant, i.e., where J^s vanishes, the potential distribution follows Laplace's equation. Interestingly, from an analytical view point, the primary current propagates through various layers of tissue through the Neumann and Dirichlet boundary conditions at the interfaces between each tissue layers. The Neumann and the Dirichlet boundary conditions for this problem can be interpreted as the continuity of current density and electric potential at each interface.

Equation (3.11) can be used to solve for the potential V by first specifying the geometry and the set of boundary conditions for the problem. The confocal ellipsoidal geometry used to represent tissue layers in the proposed model framework is defined in the following section.

3.4 Ellipsoidal Geometry and Its Symmetry

An ellipsoid is a three dimensional object defined in Cartesian coordinates as [124]

$$\frac{x^2}{\alpha_1^2} + \frac{y^2}{\alpha_2^2} + \frac{z^2}{\alpha_3^2} = 1 \text{ with } \alpha_1 > \alpha_2 > \alpha_3 > 0, \tag{3.12}$$

where α_1, α_2 and α_3 are the semi-axes in the x, y and z directions of the Cartesian coordinate respectively. We use the ellipsoid given in (3.12) as a basis ellipsoid to span confocal ellipsoids; accordingly, for any $\theta \in \mathbb{R}$ such that $\theta > -\alpha_3^2$, confocal layers of ellipsoids can be defined as

$$\frac{x^2}{\alpha_1^2 + \theta} + \frac{y^2}{\alpha_2^2 + \theta} + \frac{z^2}{\alpha_3^2 + \theta} = 1. \tag{3.13}$$

Let h_1, h_2 and h_3 be the differences between squares of the semi-axes (often referred to as semi-axes distances [118])

$$\begin{aligned} h_1^2 &= \alpha_2^2 - \alpha_3^2, \\ h_2^2 &= \alpha_1^2 - \alpha_3^2, \\ h_3^2 &= \alpha_1^2 - \alpha_2^2. \end{aligned} \tag{3.14}$$

For all confocal ellipsoids, we see that h_1, h_2 and h_3 are constant. Substituting $\lambda^2 = \alpha_1^2 + \theta$ and (3.14) in (3.13), the confocal ellipsoidal expression becomes

$$\frac{x^2}{\lambda^2} + \frac{y^2}{\lambda^2 - h_3^2} + \frac{z^2}{\lambda^2 - h_2^2} = 1. \tag{3.15}$$

For fixed x, y and z, (3.15) is a cubic equation in λ^2. If the corresponding three roots λ_1^2, λ_2^2 and λ_3^2 of (3.15) are such that $\lambda_1^2 > h_2^2 > \lambda_2^2 > h_3^2 > \lambda_3^2 > 0$, then $(\lambda_1, \lambda_2, \lambda_3)$ are the ellipsoidal coordinates corresponding to (x, y, z) in the Cartesian coordinate system. Points in the ellipsoidal coordinate system are formed by intersection of an ellipsoid ($\lambda_1 = Constant$), hyperboloid of one sheet ($\lambda_2 = Constant$) and hyperboloid of two sheets ($\lambda_3 = Constant$).

The choice of using confocal ellipsoids to represent various tissue layers reasonably captures the convex interfaces and strict containment of volumes in the hierarchy of tissue layers except for limb joints. As such, interfaces are effectively modeled by one geometry. Besides, use of confocal ellipsoids helps invoke the ellipsoidal symmetry to easily handle parameter changes in the resulting mathematical expressions. For a specific body part, the exterior geometry can be used as a start to determine the semi-axes distances. Then, for each tissue layer, the value of λ (and consequently the semi-axes lengths) only needs to be adjusted according to the thicknesses of the corresponding tissue layer to define different body parts.

While the use of the ellipsoidal coordinate system to represent the implant transceiver location matches the considered setting and simplifies analysis, the Cartesian coordinate system is easy to follow especially in visualising relative distance between transmitter and receiver. The conversion from ellipsoidal coordinates to Cartesian coordinates is given by [117]

$$\begin{aligned} x^2 &= \frac{\lambda_1^2\lambda_2^2\lambda_3^2}{h_2^2h_3^2}, \\ y^2 &= \frac{(\lambda_1^2-h_3^2)(\lambda_2^2-h_3^2)(h_3^2-\lambda_3^2)}{h_1^2h_3^2}, \\ z^2 &= \frac{(\lambda_1^2-h_2^2)(\lambda_2^2-h_2^2)(h_2^2-\lambda_3^2)}{h_1^2h_2^2}. \end{aligned} \tag{3.16}$$

Note here that unless signs are adjusted based on which octant the point falls in the ellipsoidal coordinate, the mapping from ellipsoidal to Cartesian coordinate system is many-to-one.

Consider the scenario where an implant transmitter is implanted inside the muscle tissue layer of human arm where a wearable device on the surface of the skin is used to receive the transmission. In this case, the human arm can be modeled with four confocal ellipsoids defined by $\lambda_1 = \alpha_1^i, \forall i \in \{0,1,2,3\}$ as shown in Fig. 3.2. Here, Fig. 3.2 shows the longitudinal cross-section of the human arm with the four confocal ellipsoidal shells representing skin, fat, muscle and bone tissue layers with conductivities $\sigma_1, \sigma_2, \sigma_3$, and σ_4 respectively. The locations of the anode and the cathode transmitter electrodes are at points r_1 and r_2 respectively. These points are specified in the three dimensions of the Cartesian coordinates system; the corresponding ellipsoidal coordinates can be calculated using (3.16). Similarly, the receiver anode and cathode electrode locations are denoted by r_1' and r_2'. The transmitter injects current I via the anode; the cathode, separated from the anode by an electrode spacing d, is a current sink.

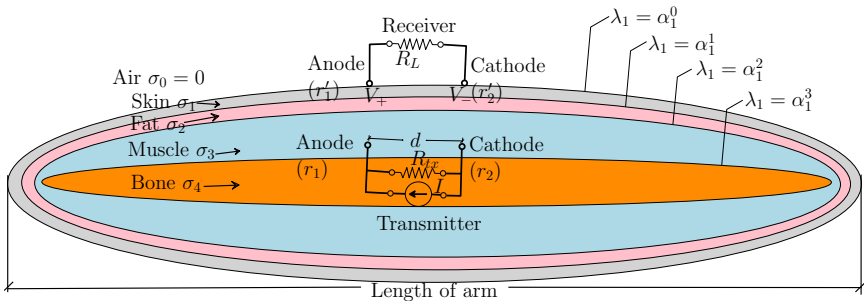

Fig. 3.2 Longitudinal cross-section of multilayered ellipsoidal model of human arm.

Now that the geometric framework of the proposed model is specified, solution to the potential distribution given in equation (3.11) is derived in the following section using this framework.

3.5 Potential Distribution in Multilayered Confocal Ellipsoidal Harmonics

Solving for the electric potential requires solving the poisons equation in multilayered ellipsoidal geometry with the underlying boundary conditions at the interfaces between tissue layers and on the outer surface. Geslowitz *et al* [125] used Green's function to express the potential distribution at the outer surface and Lynn *et al* [126] used a Fredholm type integral equation to solve for potential. However, due to the singularity of the kernel function for the electrostatic fields, analytical solutions do not exist. Hence, a multiple Weilandt deflation is applied to transform the kernel into a nonsingular type and a Jacobian recursive technique is used to find the potential distribution corresponding to the deflated kernel. Applying an appropriate correction factor, the potential distribution for the actual scenario can be computed in a semi-analytic numerical framework. Dechambre [117] and Kutori [118] on the other hand used separation of variables to solve for gravitational and electric fields respectively.

In this work, we use separation of variables in ellipsoidal coordinate systems to solve for the electric potential distribution at the receiver electrodes. Using the confocal ellipsoidal layers, we defined volumes of ellipsoidal shells to model tissue layers. Here, the potential distribution in each tissue layer not containing the transmitting implant (the current source) satisfies a Laplace's equation; whereas, the tissue layer containing the transmitter satisfies a Poisson's equation.

3.5.1 Laplace's Equation in Ellipsoidal Coordinates

Laplace's equation in Cartesian coordinates is given by

$$\frac{\partial^2 V}{\partial x^2} + \frac{\partial^2 V}{\partial y^2} + \frac{\partial^2 V}{\partial z^2} = 0. \tag{3.17}$$

Using (3.16), Laplace's equation in ellipsoidal coordinates is

$$\frac{\partial}{\partial \lambda_1}\left(\frac{H_1}{H_2 H_3}\right)\frac{\partial V}{\partial \lambda_1} + \frac{\partial}{\partial \lambda_2}\left(\frac{H_2}{H_1 H_3}\right)\frac{\partial V}{\partial \lambda_2} + \frac{\partial}{\partial \lambda_3}\left(\frac{H_3}{H_1 H_2}\right)\frac{\partial V}{\partial \lambda_3} = 0, \tag{3.18}$$

where

$$\frac{H_1}{H_2 H_3} = \sqrt{\frac{(\lambda_2^2-\lambda_3^2)^2(\lambda_1^2-h_3^2)(\lambda_1^2-h_2^2)}{(\lambda_2^2-h_3^2)(h_2^2-\lambda_2^2)(h_3^2-\lambda_3^2)(h_2^2-\lambda_3^2)}},$$
$$\frac{H_2}{H_1 H_3} = \sqrt{\frac{(\lambda_1^2-\lambda_3^2)^2(\lambda_2^2-h_3^2)(h_2^2-\lambda_2^2)}{(\lambda_1^2-h_3^2)(\lambda_1^2-h_2^2)(h_3^2-\lambda_3^2)(h_2^2-\lambda_3^2)}},$$
$$\frac{H_3}{H_1 H_2} = \sqrt{\frac{(\lambda_1^2-\lambda_2^2)^2(h_3^2-\lambda_3^2)(h_2^2-\lambda_3^2)}{(\lambda_1^2-h_3^2)(\lambda_1^2-h_2^2)(\lambda_2^2-h_3^2)(h_2^2-\lambda_2^2)}}.$$

To solve (3.18), the method of variable separation is used. In separating the three variables, we are looking for an expression of the potential of the form

$$V(\lambda_1, \lambda_2, \lambda_3) = \mathcal{R}(\lambda_1)\mathcal{M}(\lambda_2)\mathcal{N}(\lambda_3). \tag{3.19}$$

where $\mathcal{R}, \mathcal{M}$ and $\mathcal{N}$ are functions only of λ_1, λ_2 and λ_3 respectively. Due to the fact that $\mathcal{R}, \mathcal{M}$ and $\mathcal{N}$ are functions in each orthogonal axis such solution as (3.19) is known as a normal solution. Substituting (3.19) into (3.18) we can arrive at

$$(\lambda_2^2 - \lambda_3^2)\phi_1(\lambda_1) + (\lambda_1^2 - \lambda_3^2)\phi_2(\lambda_2) + (\lambda_1^2 - \lambda_2^2)\phi_3(\lambda_3) = 0 \tag{3.20}$$

where

$$\begin{aligned}
\phi_1(\lambda_1) &= \frac{\sqrt{(\lambda_1^2 - h_3^2)(\lambda_1^2 - h_2^2)}}{\mathcal{R}(\lambda_1)} \\
&\quad \times \frac{d}{d\lambda_1}\left(\sqrt{(\lambda_1^2 - h_3^2)(\lambda_1^2 - h_2^2)}\frac{d\mathcal{R}}{d\lambda_1}\right), \\
\phi_2(\lambda_2) &= \frac{\sqrt{(\lambda_2^2 - h_3^2)(\lambda_2^2 - h_2^2)}}{\mathcal{M}(\lambda_2)} \\
&\quad \times \frac{d}{d\lambda_1}\left(\sqrt{(\lambda_2^2 - h_3^2)(\lambda_2^2 - h_2^2)}\frac{d\mathcal{M}}{d\lambda_2}\right),
\end{aligned}$$

$$\begin{aligned}
\phi_3(\lambda_3) &= \frac{\sqrt{(h_3^2 - \lambda_3^2)(h_2^2 - \lambda_3^2)}}{\mathcal{N}(\lambda_3)} \\
&\quad \times \frac{d}{d\lambda_1}\left(\sqrt{(h_3^2 - \lambda_3^2)(h_2^2 - \lambda_3^2)}\frac{d\mathcal{N}}{d\lambda_3}\right).
\end{aligned}$$

Here, (3.20) is defined for any triplet $(\lambda_1, \lambda_2, \lambda_3)$ and it can easily be shown that $\phi_i(\lambda_i),\ \forall i \in \{1, 2, 3\}$ has a form $\phi_i(\lambda_i) = H\lambda_i^2 - K$ for some constants H and

K. Substituting this into (3.20), we have

$$(H\lambda_1^2 - K)\mathcal{R}(\lambda_1) = \sqrt{(\lambda_1^2 - h_3^2)(\lambda_1^2 - h_2^2)} \times \frac{d}{d\lambda_1}\left(\sqrt{(\lambda_1^2 - h_3^2)(\lambda_1^2 - h_2^2)}\frac{d\mathcal{R}}{d\lambda_1}\right). \tag{3.21}$$

Equation (3.21) can be rewritten as

$$(\lambda_1^2 - h_3^2)(\lambda_1^2 - h_2^2)\frac{d^2\mathcal{R}(\lambda_1)}{d\lambda_1^2} + \lambda_1(2\lambda_1^2 - h_3^2 - h_2^2)\frac{d\mathcal{R}(\lambda_1)}{d\lambda_1} + (H\lambda_1^2 - K)\mathcal{R}(\lambda_1) = 0. \tag{3.22}$$

The differential equation given in (3.22) is known as Lamé's equation. Similarly, $\mathcal{M}(\lambda_2)$ and $\mathcal{N}(\lambda_3)$ also satisfy the Lamé's equation with respect to λ_2 and λ_3 respectively.

3.5.2 Lamé's Function to Describe Potential in Tissue Layers

Variables H and K used for the separation of variables method can be chosen carefully so that the solutions to Lamé's equation are forced to fall into a set of the possible types of Lamé's functions. Specifically, these functions can be Lamé's function of first kind with degree n and order p (given in Appendix A) denoted by E_n^p. For a given degree n, the order p takes values from the set $\{1, 2, ..., 2n+1\}$ which makes a total of $(2n+1)$ Lamé's function of first kind. Since all of the functions $\mathcal{R}, \mathcal{M}$ and $\mathcal{N}$ satisfy the Lamé's equation and are normal to each other, the product $E_n^p(\lambda_1)E_n^p(\lambda_2)E_n^p(\lambda_3)$ is also a normal solution of (3.18) according to (3.19). This product is denoted by $\mathbb{E}_n^p(\lambda_1, \lambda_2, \lambda_3) = E_n^p(\lambda_1)E_n^p(\lambda_2)E_n^p(\lambda_3)$ and is continuous inside an ellipsoid.

Therefore, inside an ellipsoid with larger semi-axis $\lambda_1 = \alpha_1$, without any current source, the electric potential distribution can be expressed as a linear combination of all possible Lamé's products and is given by

$$V(\lambda_1, \lambda_2, \lambda_3) = \sum_{n=0}^{\infty} \sum_{p=1}^{2n+1} \frac{\beta_n^p}{E_n^p(\alpha_1)} \mathbb{E}_n^p(\lambda_1, \lambda_2, \lambda_3) \tag{3.23}$$

where the coefficients $\frac{\beta_n^p}{E_n^p(\alpha_1)}$ are constant multipliers for each order and degree. Completion of the particular solution requires specifying potential equations and the coefficients in each tissue layer starting from the transmitter all the way up to the receiver. Equation (3.23) is only used to describe the potential for the interior of the ellipsoid. However, we also need an expression for the exterior of the ellipsoid to completely describe the potential distribution. We see that $\lim_{\lambda_1 \to \infty} E_n^p(\lambda_1) = \infty$; however, this contradicts the fact that the potential vanishes at infinity. Therefore, we need to find another Lamé's function $F_n^p(\lambda_1)$ which still is a solution to Lamé's equation but vanishes at infinity. For an elliptic integral $I_n^p(\lambda_1)$ of order n and degree p given by

$$I_n^p(\lambda_1) = \int_{\lambda_1}^{\infty} \frac{dt}{(E_n^p(t))^2 \sqrt{(t^2 - h_2^2)(t^2 - h_3^2)}},$$

a possible choice that satisfies both these requirement is [117]

$$F_n^p(\lambda_1) = (2n+1) E_n^p(\lambda_1) I(\lambda_1),$$

which is known as Lamé's function of second kind. Since $F_n^p(\lambda_1)$ satisfies the Laplace's equation and vanishes at infinity, the exterior potential for $\lambda_1 \geq \alpha_1$ can be expressed as

$$V(\lambda_1, \lambda_2, \lambda_3) = \sum_{n=0}^{\infty} \sum_{p=1}^{2n+1} \frac{\beta_n^p}{F_n^p(\alpha_1)} \mathbb{F}_n^p(\lambda_1, \lambda_2, \lambda_3) \tag{3.24}$$

where $\mathbb{F}_n^p(\lambda_1, \lambda_2, \lambda_3) = F_n^p(\lambda_1)E_n^p(\lambda_2)E_n^p(\lambda_3)$. It can be shown that the products $E_n^p(\lambda_2)E_n^p(\lambda_3)$, referred to as ellipsoidal harmonics, are orthogonal up to a normalisation factor [118]; i.e., over the surface S_λ of an ellipsoid given by $\lambda_1 = \lambda$,

$$\int_{S_\lambda} \frac{E_n^p(\lambda_2)E_n^p(\lambda_3)E_{\acute{n}}^{\acute{p}}(\lambda_2)E_{\acute{n}}^{\acute{p}}(\lambda_3)}{\sqrt{(\lambda^2-\lambda_2^2)(\lambda^2-\lambda_3^2)}}dS = 0, \forall n \neq \acute{n} \text{ or } p \neq \acute{p}$$
$$\text{and } \int_{S_\lambda} \frac{(E_n^p(\lambda_2)E_n^p(\lambda_3))^2}{\sqrt{(\lambda^2-\lambda_2^2)(\lambda^2-\lambda_3^2)}}dS = \gamma_n^p. \tag{3.25}$$

where γ_n^p is the normalisation constant. The orthogonality property in (3.25) is essential in determining the coefficients of the potential in the region which contains the singularity points. Expressions of $E_n^p(\lambda_i)$ and $\gamma_n^p, \forall n \leq 3$ are given in Appendices A and B respectively.

3.5.3 Boundary Conditions and Explicit Potential Distribution

So far, we have the general expressions for the interior and exterior ellipsoidal potentials. In the following we will derive the explicit expression of the potential distribution for the scenario given in Fig. 3.2. There are four tissue layers and air as the external medium. For signals with frequency $\omega = 2\pi f$, the complex permittivity at location r is $\epsilon(r) = \epsilon_r(r)\epsilon_0$, and the complex conductivity $\sigma(r) = i\omega\epsilon_0\epsilon_r(r)$ where ϵ_0 is the permittivity of free space and relative permittivity $\epsilon_r(r)$ is given by the Cole-Cole equation as

$$\epsilon_r(r) = \epsilon_\infty(r) + \sum_{m=1}^{4} \frac{\Delta\epsilon_m(r)}{1 + (i\omega\tau_m(r))^{(1-\alpha_m(r))}} + \frac{\sigma_j(r)}{i\omega\epsilon_0}. \tag{3.26}$$

Here, the parameters $\epsilon_\infty(r), \Delta\epsilon_m(r), \sigma_j(r), \alpha_m(r), \tau_m(r)$ such that $\epsilon_r(r)$ fits the experimental measurements of Gabriel *et al* [8] can be referred from the IT'IS website [95].

Inside each layer $i \in \{0, 1, 2, 3, 4\}$ (i.e., air, skin, fat, muscle and bone), the complex conductivity $\sigma(r)$ is assumed to be constant. Thus, $\sigma(r) = \sigma_i$, if $r \in i^{th}$ layer. Let the potentials in tissue layer with complex conductivity σ_i be denoted by V_i, $\forall i \in \{0, 1, 2, 3, 4\}$. Current induced in each tissue layer creates potential distribution and also affects the potential distribution of exterior layers. Thus, the net potential distribution is the sum of of the interior and exterior potentials. Therefore, the potential V_i is given by

$$V_i(\lambda_1, \lambda_2, \lambda_3) = \sum_{n=0}^{\infty} \sum_{p=1}^{2n+1} A^i_{(n,p)} \mathbb{E}^p_n(\lambda_1, \lambda_2, \lambda_3) + \sum_{n=0}^{\infty} \sum_{p=1}^{2n+1} B^i_{(n,p)} \mathbb{F}^p_n(\lambda_1, \lambda_2, \lambda_3), \alpha^i_1 \leq \lambda_1 \leq \alpha^{i-1}_1. \tag{3.27}$$

where $A^i_{(n,p)}$ and $B^i_{(n,p)}$ are the coefficients of the n^{th} degree and p^{th} order terms, respectively, of the interior and exterior potential distribution of the i^{th} tissue layer. The values α^i_1 denote the major semi-axis length of the i^{th} ellipsoidal interface. The boundary conditions at an interface between the i^{th} and $(i+1)^{th}$ tissue layer with conductivities σ_i, $\sigma_{(i+1)}$ and potentials V_i, $V_{(i+1)}$ respectively, are defined as

$$\sigma_i \nabla V_i(\mathbf{r}).e_n = \sigma_{(i+1)} \nabla V_{(i+1)}(\mathbf{r}).e_n, \mathbf{r} \in \Omega^{(i+1)}_i \tag{3.28}$$

$$V_i(\mathbf{r}) = V_{(i+1)}(\mathbf{r}), \mathbf{r} \in \Omega^{(i+1)}_i \tag{3.29}$$

where e_n is the unit vector normal to the interface and $\mathbf{r}$ is a point on the surface $\Omega^{(i+1)}_i$ separating the i^{th} and $(i+1)^{th}$ layer. While (4.6) states continuity of potential, (4.5) states continuity of current density at the interface; it can also

be seen as the inability to pile up charge at the interface. At the outermost interface (i.e., air–skin interface) we have non conducting air on one side and skin tissue with conductivity σ_1 on the other; hence, (4.5) becomes $\sigma_1 \nabla V_1 . e_n = 0$. This further implies the signal is confined to within the body. Furthermore, from the fact that potential vanishes at infinity, we have $\lim_{\mathbf{r}\to\infty} V_0(\mathbf{r}) = 0$.

Note that all but the third layer (muscle layer) do not contain any source. Hence (4.4) applies to all the layers except $i = 3$. Beginning from the exterior (air layer), the potential will only have the exterior form (i.e., $A^0_{(n.p)} = 0$). Thus,

$$V_0(\lambda_1, \lambda_2, \lambda_3) = \sum_{n=0}^{\infty} \sum_{p=1}^{2n+1} B^0_{(n,p)} \mathbb{F}^p_n(\lambda_1, \lambda_2, \lambda_3) \tag{3.30}$$

for $\lambda_1 \geq \alpha^0_1$. The muscle layer contains the source, thus the potential expression includes the homogenous interior potential and the particular solution of the Poisson's equation. Denoting the particular solution by V_p, the potential distribution in the muscle tissue layer, i.e., $\alpha^3_1 \leq \lambda_1 \leq \alpha^2_1$, is then given by

$$V_3(\lambda_1, \lambda_2, \lambda_3) = V_p + \sum_{n=0}^{\infty} \sum_{p=1}^{2n+1} A^3_{(n,p)} \mathbb{E}^p_n(\lambda_1, \lambda_2, \lambda_3) \tag{3.31}$$

Let $\mathbf{r}_0$ be a vector from origin to the point where the current dipole $\mathfrak{M}$ is acting on. Then, the particular solution of the Poisson's equation for the potential, V_p, at any point referenced by vector $\mathbf{r}$ from the origin is given by [118],[125], [127]

$$V_p(\mathbf{r}) = -\frac{1}{4\pi\sigma_3} \mathfrak{M} \cdot \nabla_{\mathbf{r}_0} \frac{1}{|\mathbf{r} - \mathbf{r}_0|} \tag{3.32}$$

where the operation $\nabla_{\mathbf{r}_0}$ is the gradient with respect to $\mathbf{r}_0$. Now, let us replace the term $\frac{1}{|\mathbf{r}-\mathbf{r}_0|}$ with its ellipsoidal expansion;

$$\frac{1}{|\mathbf{r}-\mathbf{r}_0|} = \sum_{n=0}^{\infty}\sum_{p=1}^{2n+1} \frac{4\pi}{2n+1}\frac{1}{\gamma_n^p}\mathbb{E}_n^p(\lambda_{1_0},\lambda_{2_0},\lambda_{3_0})\mathbb{F}_n^p(\lambda_1,\lambda_2,\lambda_3) \tag{3.33}$$

where $(\lambda_{1_0},\lambda_{2_0},\lambda_{3_0})$ are ellipsoidal coordinates representing the point referenced by $\mathbf{r}_0$. Substituting (3.33) into (3.32) and (3.32) into (3.31), we have

$$\begin{aligned} V_3(\lambda_1,\lambda_2,\lambda_3) &= \sum_{n=0}^{\infty}\sum_{p=1}^{2n+1} A_{(n,p)}^3\mathbb{E}_n^p(\lambda_1,\lambda_2,\lambda_3) \\ &+ \sum_{n=0}^{\infty}\sum_{p=1}^{2n+1} \frac{\mathfrak{M}\cdot\nabla_{\mathbf{r}_0}\mathbb{E}_n^p(\lambda_{1_0},\lambda_{2_0},\lambda_{3_0})}{(2n+1)\sigma_3\gamma_n^p}\mathbb{F}_n^p(\lambda_1,\lambda_2,\lambda_3). \end{aligned} \tag{3.34}$$

Thus, equating (3.34) with (4.4) for $i=3$, we can see that the value of $B_{(n,p)}^3$ is given by

$$B_{(n,p)}^3 = \frac{\mathfrak{M}\cdot\nabla_{\mathbf{r}_0}\mathbb{E}_n^p(\lambda_{1_0},\lambda_{2_0},\lambda_{3_0})}{(2n+1)\sigma_3\gamma_n^p}. \tag{3.35}$$

Applying the orthogonality property of ellipsoidal harmonics (3.25) and boundary conditions (4.5) and (4.6) into (3.30) and (3.31) at the four interfaces of Fig. 3.2, we have the following system of linear equations for each $i\in\{0,1,2,3\}$

$$A_{(n,p)}^i - A_{(n,p)}^{i+1} = (2n+1)I_n^p(\alpha_1^i)[B_{(n,p)}^{i+1} - B_{(n,p)}^i], \tag{3.36}$$

$$\begin{aligned} \sigma_i A_{(n,p)}^i - \sigma_{i+1}A_{(n,p)}^{i+1} &= (2n+1)\left[I_n^p(\alpha_1^i) - \frac{1}{C_{(n,p)}^i}\right] \\ &\times \left(\sigma_{i+1}B_{(n,p)}^{i+1} - \sigma_i B_{(n,p)}^i\right). \end{aligned} \tag{3.37}$$

where $C_{(n,p)}^i = E_n^p(\alpha_1^i)E_n^{p'}(\alpha_1^i)\alpha_2^i\alpha_3^i$ with $E_n^{p'}(\alpha_1^i)$ as the derivative of $E_n^p(\lambda_1)$ computed at $\lambda_1=\alpha_1^i$. Here, α_1^i is the major semi-axis length, and α_2^i and α_3^i are the other two semi-axes lengths of the i^{th} ellipsoid shown in Fig. 3.2.

Solving (3.36) and (3.37) with $A^0_{(n,p)} = 0$ and $B^3_{(n,p)}$ as given in (4.7), the remaining coefficients are

$$
\begin{aligned}
B^1_{(n,p)} =& \frac{B^3_{(n,p)}}{\left[\left(1-\frac{\sigma_2}{\sigma_3}\right)Q^p_n C^2_{(n,p)} + \frac{W^p_n}{\sigma_3}\right]},\\
A^1_{(n,p)} =& (2n+1)\left[\frac{1}{C^0_{(n,p)}} - I^p_n(\alpha^0_1)\right]B^1_{(n,p)},\\
B^0_{(n,p)} =& \frac{B^1_{(n,p)}}{C^0_{(n,p)} I^p_n(\alpha^0_1)},\\
A^2_{(n,p)} =& (2n+1)\left[\frac{1}{C^0_{(n,p)}} + I^p_n(\alpha^1_1,\alpha^0_1) - \frac{W^p_n I^p_n(\alpha^1_1)}{\sigma_2}\right]B^1_{(n,p)},\\
B^2_{(n,p)} =& \frac{W^p_n B^1_{(n,p)}}{\sigma_2},\\
A^3_{(n,p)} =& (2n+1)\left[Q^p_n B^1_{(n,p)} - I^p_n(\alpha^2_1)B^3_{(n,p)}\right],\\
B^4_{(n,p)} =& \left(1-\frac{\sigma_3}{\sigma_4}\right)C^3_{(n,p)}\left[Q^p_n B^1_{(n,p)}\right.\\
&\left. + I^p_n(\alpha^3_1,\alpha^2_1)B^3_{(n,p)}\right] + \frac{\sigma_3}{\sigma_4}B^4_{(n,p)},\\
A^4_{(n,p)} =& (2n+1)\left[Q^p_n B^1_{(n,p)}\right.\\
&\left. + I^p_n(\alpha^3_1,\alpha^2_1)B^3_{(n,p)} - I^p_n(\alpha^3_1)B^4_{(n,p)}\right]
\end{aligned}
$$

where

$$
\begin{aligned}
I^p_n(\alpha^i_1,\alpha^j_1) &= I^p_n(\alpha^i_1) - I^p_n(\alpha^j_1), \forall i,j \in \{0,1,2,3\},\\
W^p_n =& (\sigma_2-\sigma_1)C^1_{(n,p)}\left[\frac{1}{C^0_{(n,p)}} + I^p_n(\alpha^1_1,\alpha^0_1)\right] - \sigma_1,\\
Q^p_n =& \left[\frac{1}{C^0_{(n,p)}} + I^p_n(\alpha^1_1,\alpha^0_1) + \frac{W^p_n I^p_n(\alpha^2_1,\alpha^1_1)}{\sigma_2}\right]B^1_{(n,p)}.
\end{aligned}
$$

This completes the derivation of the potential distribution at any point within the arm. The potential difference V_{Rx} sensed at the receiver is then given by

the difference of the potentials at the receiver electrode locations as

$$V_{Rx} = V(r_1') - V(r_2'). \tag{3.38}$$

3.6 Discussion

3.6.1 Potential Distribution at Receiver End

For the sake of discussion flow, the human arm model given in Fig. 3.2 is used to discuss potential distribution and path loss characterisation according to the result in Section 3.5.3. As used in [69], an arm of diameter 43.5 mm is considered. This diameter is associated with the smallest semi-axis length of the overall ellipsoidal model to fit with our model. Tissue thicknesses skin = 1.5 mm, fat = 8.5 mm, muscle = 27.5 mm, bone = 6 mm. Consider a transmitter injecting an rms current of 1 mA with its electrodes spaced by 5 mm located along the major semi-axis of the arm at 6.9 mm into the muscle tissue from the muscle-bone interface. The maximum electric potential developed along the axis of the dipole as a function of radial distance from the center is shown in Fig. 3.3.

From Fig. 3.3 (a), we can see that the potential decreases slowly starting from the transmitter location all the way to the surface of the skin (43.5 mm from the center). Clearly, the potential level is such that a receiver with electrodes on the surface of the skin along the two opposite sides of the current dipole can detect the transmission easily. However, the potential rapidly decreases from the skin surface onwards. The plot of the potential in Fig. 3.3 (b) shows that the potential falls so rapidly that we can safely assume the signal is confined to within the human body and is difficult to detect by an eavesdropping receiver not far from the body surface, suggesting the transmission technique is inherently

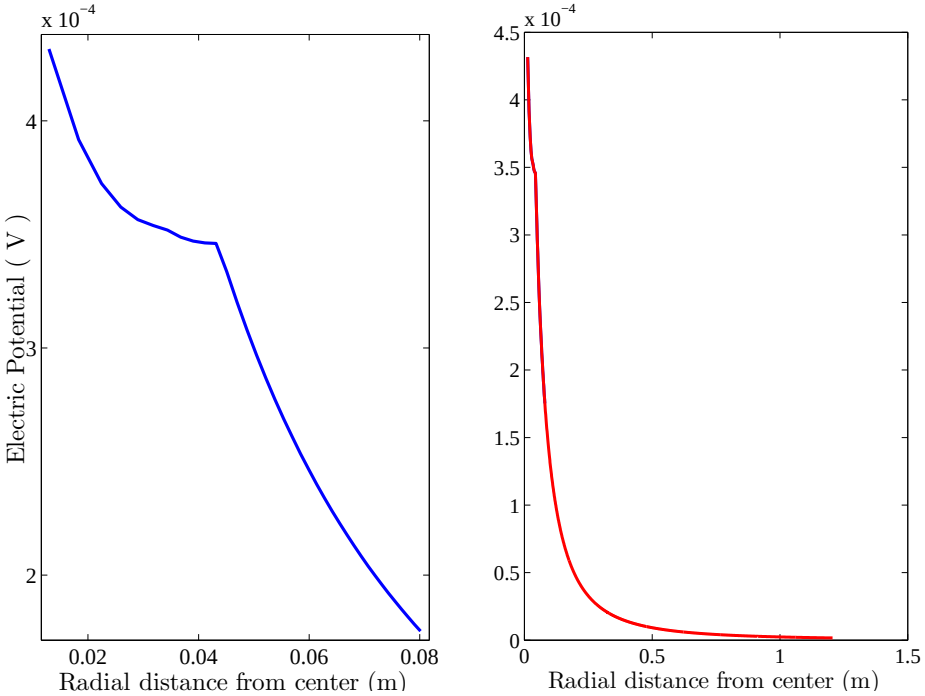

Fig. 3.3 Analytical potential distribution at 600 KHz as a function of communication distance.

secure. In Fig. 3.4, we see that transmissions with lower frequency yield stronger

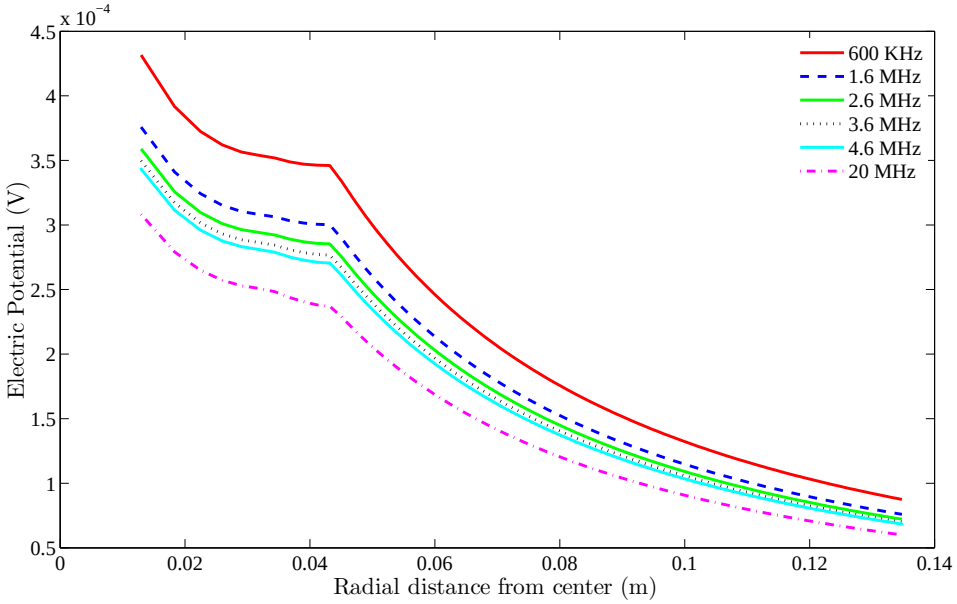

Fig. 3.4 Analytical electric potential distribution at different frequencies

electric potential inside the human body whereas the potential falls off quickly once it leaves the human body.

3.6.2 Path Loss

The path loss is defined as the attenuation of power as the signal travels from the transmitter to the receiver. Here, the received power is normalised to a 50 Ω load as shown in the two port network representation of galvanically coupled implant transceiver in Fig. 3.5. A reference load of 50 Ω is considered to make a just comparison between analytical path loss values and the measured values where our Vector Network Analyser (VNA) (see Section 3.7.1) is calibrated for a 50 Ω termination.

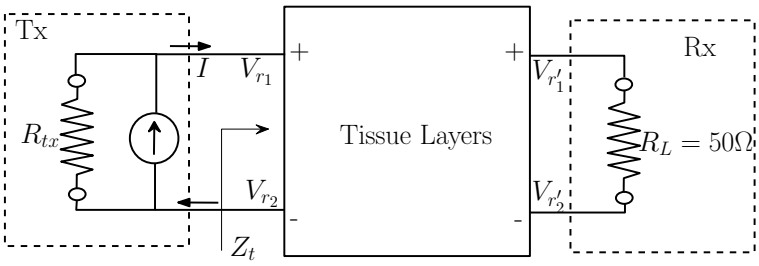

Fig. 3.5 Two port network representation of galvanically coupled implant communication.

In galvanic coupled implant communication, the channel is a direct load connected to the transmitter. Thus, it determines the amount of input power drawn from the transmitter. The transmitter injects the current I and sees an impedance of Z_t building up a potential $V_t = V_{r_1} - V_{r_2}$; using these, we can calculate the power input P_t. Also, using the 50 Ω load and the potential detected at the two electrodes of the receiver we can calculate the received power $P_r = (V_{r_1'} - V_{r_2'})^2/R_L$. Then, the path loss (PL) in dB is calculated as

$$PL = -10 \log \left(\frac{P_r}{P_t} \right). \tag{3.39}$$

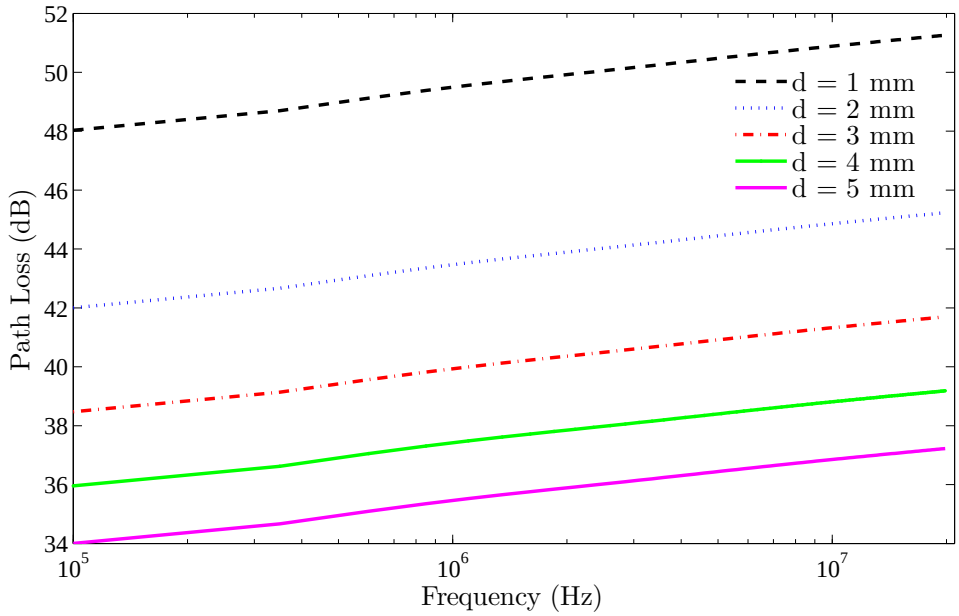

Fig. 3.6 Analytical path loss for various inter-electrode spacing as a function of frequency for the communication scenario considered in Fig. 3.2.

Figure 3.6 shows the plot of path loss for various inter-electrode spacing of the transmitter where the receiver is located with fixed electrode-spacing on the surface of the skin. From this figure, we can see that the path loss increases with frequency. The trend followed by path loss characteristic of galvanic coupled implant communication is different from the in vivo measurements of the surface-to-surface intra-body communication [128]. This is due to the fact that the surface-to-surface communication and the implant-to-surface communications use different channels. In the surface-to-surface, the signal relies on the longitudinal path of the tissue layers where inner layers play a lesser role as frequency increases. However, for implant-to-surface communication, the signal uses the transversal path penetrating all tissue layers all the way up to the skin. The mechanism of how tissue layers affect galvanically coupled implant communication is discussed in Section 3.6.4.

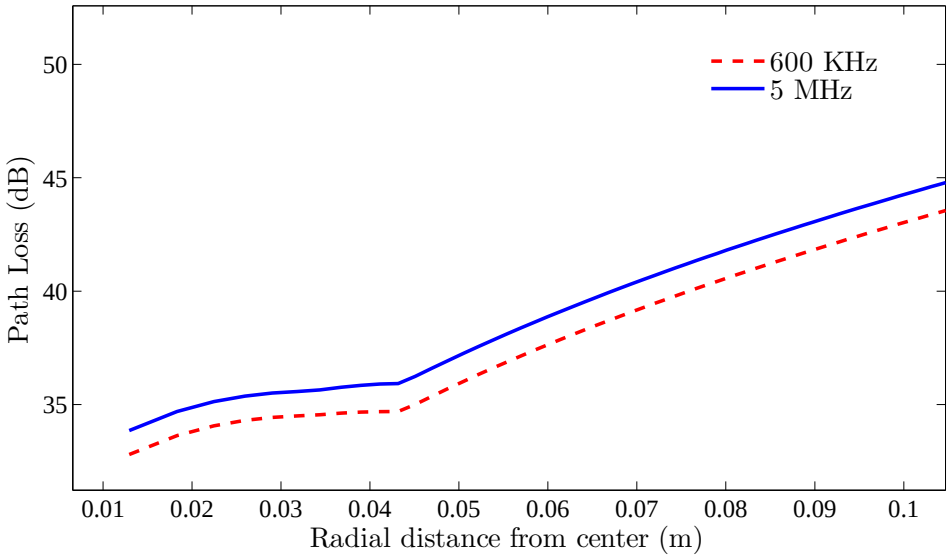

Fig. 3.7 Analytical path loss as a function of separation distance between transmitter and receiver. Here, it can be seen that the path loss increases at a small slope until 0.0435m (i.e., inside the human body) and increases at a high lope after 0.0435m (i.e., outside the human body).

With regards to path loss, yet another important feature of intra-body communication is revealed in Fig. 3.7. Here, we see that path loss stays nearly constant (albeit slightly increasing) when the signal is within the body. However, once the signal leaves the skin at 43.5 mm radial distance, the path loss increases sharply.

3.6.3 Effect of Electrode Spacing: Implant Size

Assuming that the transmitter circuitry can be miniaturised to any size, the determinant factor for implant size is the electrode spacing. According to Fig. 3.6, it can be seen the path loss at the surface decreases by a factor of four when the electrode spacing doubles. Even for the 1 mm electrode spacing (the smallest shown in Fig. 3.6) the path loss for most frequency ranges below 10 MHz is limited to 40 dB range while the smallest side of the path loss for MICS based implants fall within 60 dB range [129].

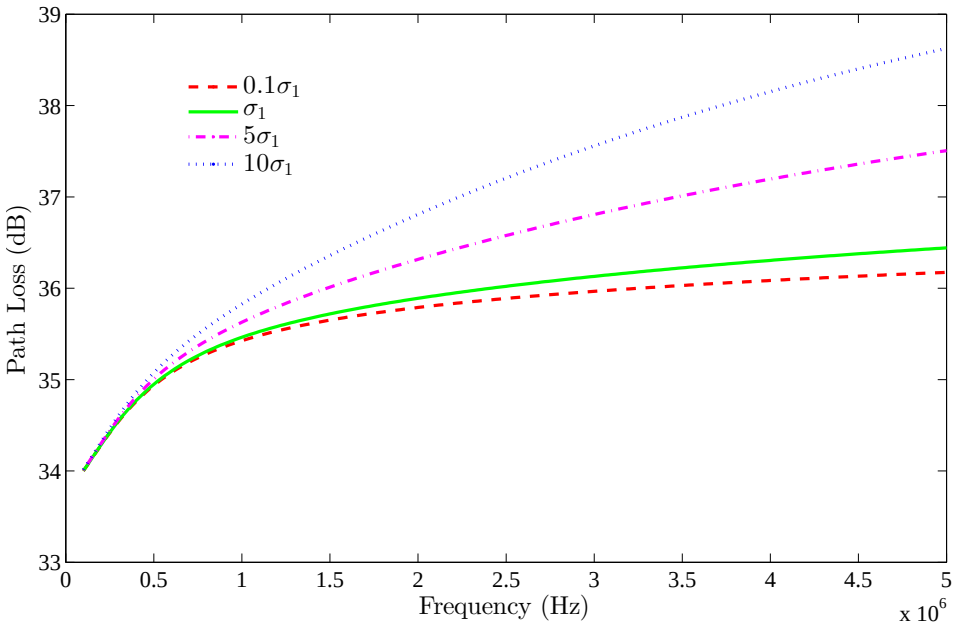

Fig. 3.8 Analytical path loss for various values of conductivity of outer tissue layer. Here, σ_1 is the conductivity of skin.

In fact, frequencies in hundreds of megahertz such as the MICS 402-405 MHz with a bandwidth only of 300 kHz (which could be offered at a much lower frequency) will incur comparatively larger path loss due to the small skin (or penetration) depth (defined in Section 3.6.4) of tissue layers at high frequencies. The determinant parameter in frequency selection is then the bandwidth required for transmission and amount of interference in the frequency band. Another advantage of galvanically coupled implants is that, apart from the electrode spacing requirement, there is no need to use a radiating antenna which significantly influences the size of MICS type implants.

With respect to implant sizes, our results in this chapter and section 2.5.2 of chapter 2 suggest that gc-IBC implants operating at low frequencies offer a high degree of miniaturisation and hence are preferable for implant communication compared to radio wave based RF techniques.

3.6.4 Effect of Tissue Layers

The notion of effect of tissue layers on electromagnetic signals is captured in their thickness(i.e., relative contribution), conductivity and permittivity in frequencies of consideration. Channels that least attenuate electric field are preferable. This can be quantitatively described by skin depth (or penetration depth). Penetration depth, denoted by δ, is defined as the distance at which an electromagnetic field is attenuated by a factor of $\frac{1}{e}$ (where e is the base of natural logarithm) as it passes through a medium of permittivity ϵ, permeability μ and conductivity σ and is given by

$$\delta = \frac{1}{\omega}\left[\frac{\mu\epsilon}{2}\left(\sqrt{1+\left(\frac{\sigma}{\epsilon\omega}\right)^2}-1\right)\right]^{-1/2}. \tag{3.40}$$

where $(\omega = 2\pi f)$ denotes the angular frequency of the signal.

Larger power attenuation (i.e., increased path loss) is associated with smaller the skin depth. From (3.40), with the permittivity and conductivity values shown in Fig. 3.9 and 3.10, the skin depth is a decreasing function of frequency for all the tissues indicated in the figures. In fact, the skin depth is a decreasing function of frequency for all the tissues. Thus, the channel for implant-to-surface communication experiences an increasing path loss with increasing conductivity as shown in Fig. 3.8.

In general, conductivity has an increasing and permittivity has a decreasing trend with frequency. However, different tissues have different rates at which their conductivity increases. Similarly, their permittivities also decrease at different rates. For example, as can be seen in Fig. 3.9, up to 5 MHz the conductivity of skin increases at the highest slope (from the smallest value at lower frequencies) than the rest of the tissues shown while muscle tissue proves to be a highly conductive tissue maintaining a steady conductivity value. On

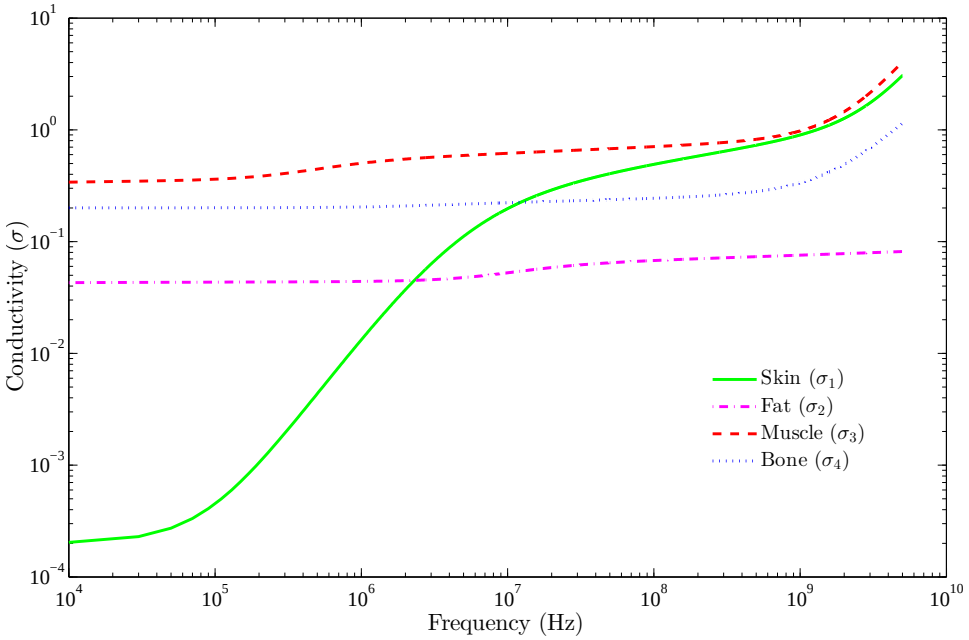

Fig. 3.9 Conductivity as function of frequency for skin, fat, muscle and bone tissues according to (3.26) with coefficients from IT'IS database[95]. Conductivity has an increasing trend with frequency. Here skin is least conducting at low frequencies but its conductivity rises sharply between 100 kHZ and 10 MHz while muscle tissue has the highest conductivity among the tissues shown across the spectrum

the other hand, as can be seen in Fig. 3.10, the permittivity of skin stays steady while the permittivity of muscle tissue decreases (from the highest value at low frequency) at a faster rate for the same frequency range.

With respect to permittivity, the high values associated with muscle tissue strengthen the penetration depth unlike the constant permittivity of skin (up to 20 MHz). From the conductivity perspective, muscle tissue provides a better conductive environment for induced current. Although the least conductive skin seemingly promises longer penetration depth, its effect is overshadowed by its inability of current induction from the electric field.

The competing trends observed here are the conductivity and the penetration depth. Increased conductivity provides stronger conduction current while in-

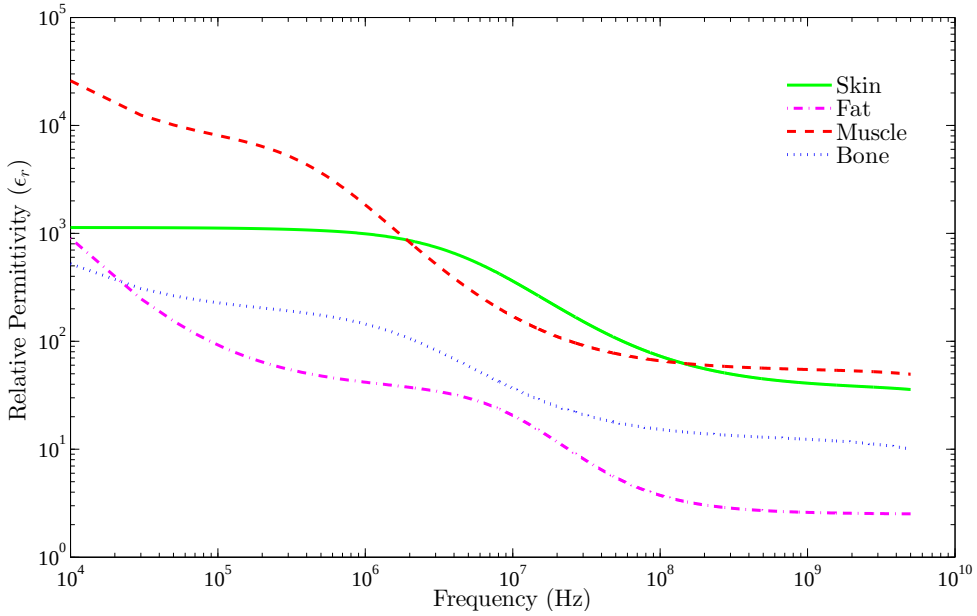

Fig. 3.10 Relative permittivity as function of frequency for skin, fat, muscle and bone tissues according to (3.26) with coefficients from IT'IS database[95]. Here, all tissues shown have decreasing permittivity with muscle tissue having dominant permittivity for most of the spectrum.

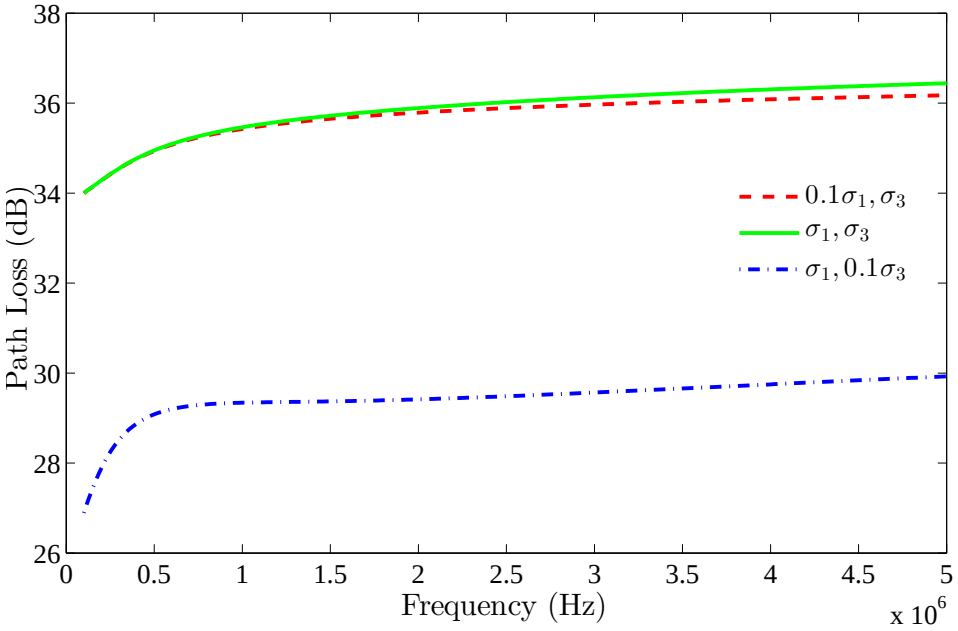

Fig. 3.11 Analytical path loss for different values of conductivity of muscle (σ_3) and skin (σ_1) tissue layers.

creased penetration depth provides stronger induced electric field. However, their effects are different for different tissue layers due to the value of conductivity and varying permittivity profiles with frequency. As seen in Fig. 3.11, the path loss is less sensitive to reduction in conductivity of skin tissue compared to that of muscle tissue.

Although reduced conductivity contributes to reduction in path loss, the channel should have large enough conductivity to enable reliable volume conduction according to (3.7). Thus, there is a trade-off between skin depth and the current conduction capacity of each tissue layer to setup the potential distribution.

The aggregate effect of tissue layers create a total transmitter impedance Z_t. This impedance determines the amount of power imparted into the channel from the transmitter(Fig. 3.12). Thus, it can be seen that the transmit power is a decreasing function of frequency. This is because the the impedance Z_t decreases with increasing frequency. Moreover, tissue thickness constitutes the percentage contribution of each tissue layer in the overall impedance Z_t. The contribution of skin tissue is small since it is the thinnest of all tissue layers; albeit least conductive. Hence, as can be seen in Fig. 3.12, although the conductivity of skin tissue is increased and decreased by an order of magnitude, the amount of power input to the channel is not affected.

However, the case is different for the receiver (i.e., received power). Penetration depth also plays a major role besides the impedance of tissue layers. Thus, as shown in Fig. 3.13, increasing the conductivity of the skin by an order of magnitude, decreases the skin depth significantly; thus, the received power is reduced considerably. This effect is pronounced more at higher frequencies as increasing frequency also further decreases penetration depth. But, decreasing the conductivity of the skin by an order of magnitude results in minimal in-

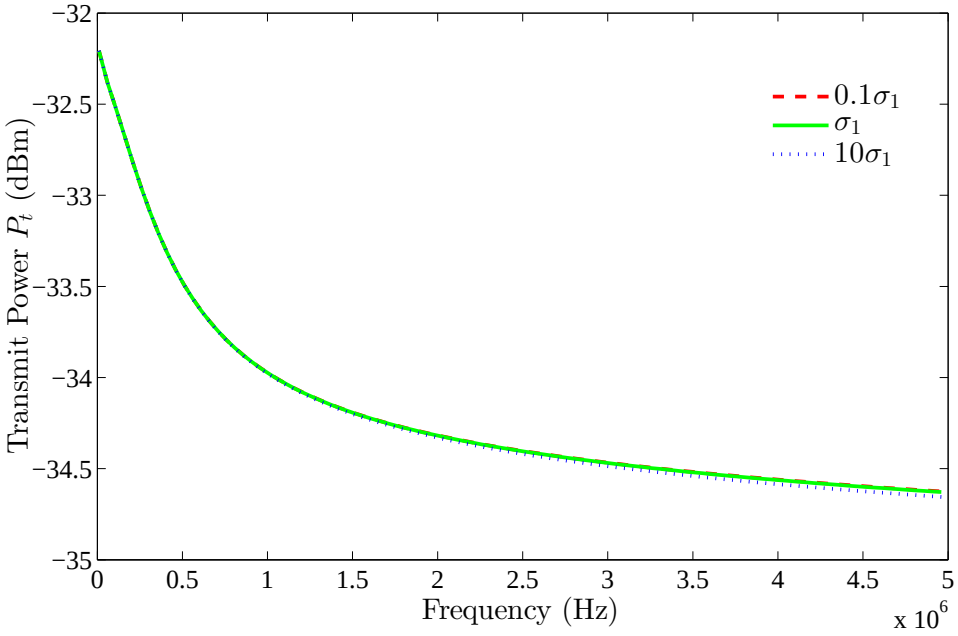

Fig. 3.12 Input power to the channel at the transmitter side for various values of conductivity of skin (σ_1) tissue layer.

crease in received power. This is because the increased skin depth is effectively counter-acted by the increased impedance due to the reduction in conductivity.

In terms of the transmit power, it can be seen that the transmitter imparts -32 to -35 dBm of power which is a fraction of a microwatt. After the channel path loss, the received power is about -63 to -68 dBm Watt of the power as shown in Fig. 3.13. Comparing this with the average receiver sensitivity of the IEEE 802.15.6 standard for HBC receiver which is -92.5 dBmW, we can see that it is larger by more than two orders of magnitude and hence can easily be detected by a receiver that complies with the IEEE 802.15.6 standard.

3.6.5 Potential Ratio and Optimal Frequencies

Generally speaking, the received potential distribution with frequency follows similar trend as the gain (inverse of path loss), i.e., a decrease in the path loss

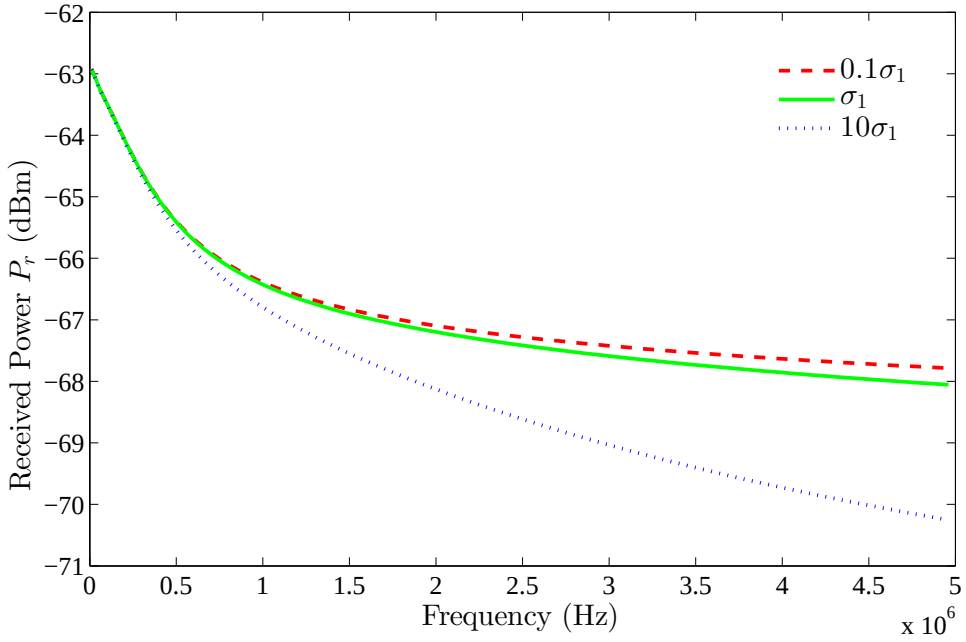

Fig. 3.13 Received power as a function of frequency for different values of conductivities of the skin (σ_1) tissue layer.

implies an increased received potential. However, analysis of the gc-IBC for implant communication in different parts of the body shows that the gain and received potential may take different patterns. The frequency dependent channel impedance determines the amount of input power drawn from the transmitter by the channel. Thus, a channel incurring minimal path loss may be such that it has a small impedance drawing small power from the transmitter is drawn to result in a small potential developed at the receiver side. In other cases, minimal changes in path loss can be associated with considerable change in received potential. These effects are elegantly captured in our model. For example, consider the implant communication setup given in Fig. 3.17. As shown in Table 3.1, increasing brain tissue conductivity by a factor of three than used in Table 3.3, did not change the path loss significantly while the received potential decreased by 35%. Although the conductivity of brain tissue do not vary as much, this is used as an example to show how different tissue layers (in

different parts of the body) with different conductivity profiles affect potential distribution.

Table 3.1 Special case of Path Loss and Potential changes: a case where conductivity of the brain tissue (σ_4) is increased threefold.

Conductivity	Path Loss	Received Potential
σ_4	46.88 dB	89.8 μ V
$3\sigma_4$	46.69 dB	57 μ V

Therefore, the received potential distribution also needs to be studied, besides the path loss, for a abetter characterisation of the channel in gc-IBC implant communication setting unlike radio-wave based transmission. This is mainly because the input power at the transmitter depends on the channel itself. The ratio of receiver to input potential difference follows the trend shown in Fig. 3.14.

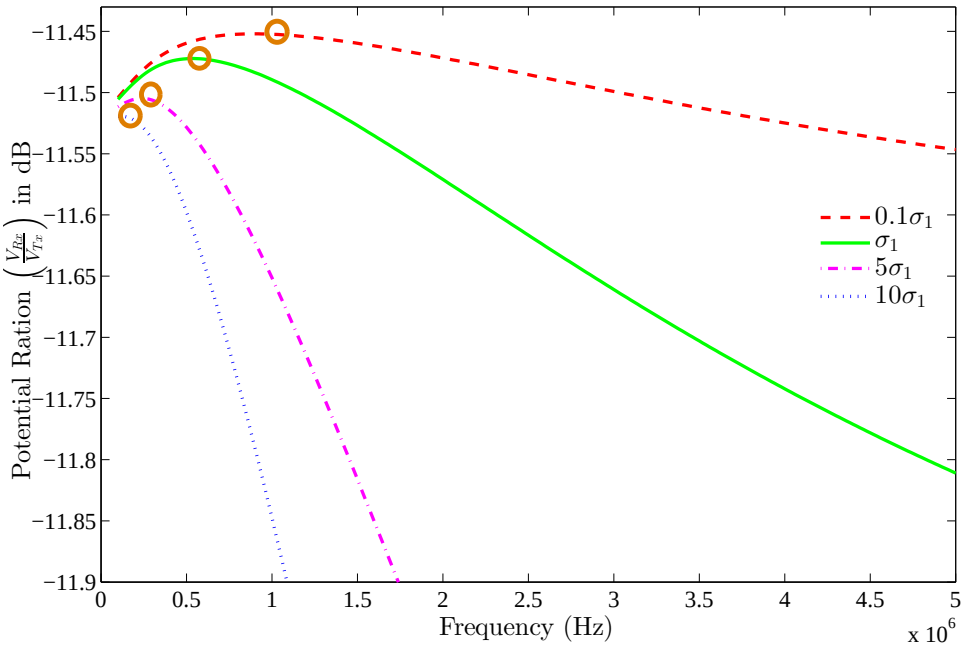

Fig. 3.14 Ratio of received and transmitter potential for different skin conductivity (σ_1). The circled points in the plot indicate the optimum frequencies at which the ratio is maximised.

For a given transmission setting, reception of the maximum possible potential at the receiver can be ensured by maximising the ratio of received potential to input potential at the transmitter. The frequencies where the received potential is maximised are referred to as optimum frequencies (shown circled in Fig. 3.14). These frequencies are dependent on the conductivity and permittivity profiles of the tissue strata. In general, lower conductivity is associate with higher optimal frequency; for example, as can be seen from the figure a reduction in skin conductivity by an order of magnitude moves the optimal frequency to be around 1.1 MHz from 0.6 MHz. This is because the conductivity of skin is increasing with frequency and thus, the conductivity which minimises path loss and impedance shifts to a higher frequency if it decreases by an order of magnitude. Thus, the optimum frequency relies on the body composition and could range between several hundreds of kHz to a few MHz. Although the optimum frequencies are clearly defined, for the example given in the figure the the potential ratio does not change by a large amount in the frequency range below 5 MHz. Thus, the frequency of operation can be increased for higher data rate applications.

3.7 Model Validation Experiment

3.7.1 Experimental Setup

For channel characterisation experiments, the transmitter was fixed at one location and the receiver was moved at various distances relative to the transmitter. Given this, conducting implant communication experiments was a challenging task especially when desired in a multilayered tissue setting. On one hand, use of solid phantoms made it difficult to move the receiver inside a rigid phantom although it enabled us to construct multilayered tissue layer strata. On the other

hand, aqueous phantom solution made it easy to move the transmitter although difficult to construct multilayered tissue layers. Thus, in our experimental validation, we used a homogenous aqueous muscle tissue phantom. Muscle was preferred as it constitutes 2/3 of the total tissue by volume.

Path loss measurements were conducted by transmitting signals through a phantom solution that was prepared to mimic conductivity and permittivity of muscle tissue at 13.56 MHz. The phantom solution recipe is given by Hagmann *et al* [130] as shown in Table 3.2. The aqueous solution was poured into a container as in Fig. 3.15 with dimensions h = 12cm, b =9cm and w= 34 cm (the container approximates the dimensions of a human arm).

Table 3.2 Recipe for aqueous muscle tissue phantom at 13.56 MHz.

Frequency	Percentage of Weight			Properties	
(MHz)	Water	Glycine	NaCl	ϵ_r	σ (S/m)
13.56	79.40	20.00	0.58	145.00	0.60

The experimental rig enabled two degrees of freedom (vertical and horizontal) of movement for receiver electrodes. For a fixed transmitter location, the communication distances between the receiver and transmitter was adjusted vertically and horizontally. In the validation experiment, the transmitter and receiver electrodes were aligned vertically and the vertical distance was adjusted by moving the receiver electrodes up and downwards.

The transmission and reception electrodes were connected to a pair of shielded BNC cables as shown in Fig. 3.15. The electrode spacing at the transmission and reception electrodes was set to be 3 cm. The BNC cables from the transmitter and receiver were connected respectively to the DUT and DET ports of the Vector Network Analyzer (VNA), via a 50 Ohm Balun, for channel path loss measurements. The VNA we used is the Pro miniVNA (miniVNA Pro, Mini Radio Solutions Inc., Poland). In order to remove the effect of common ground

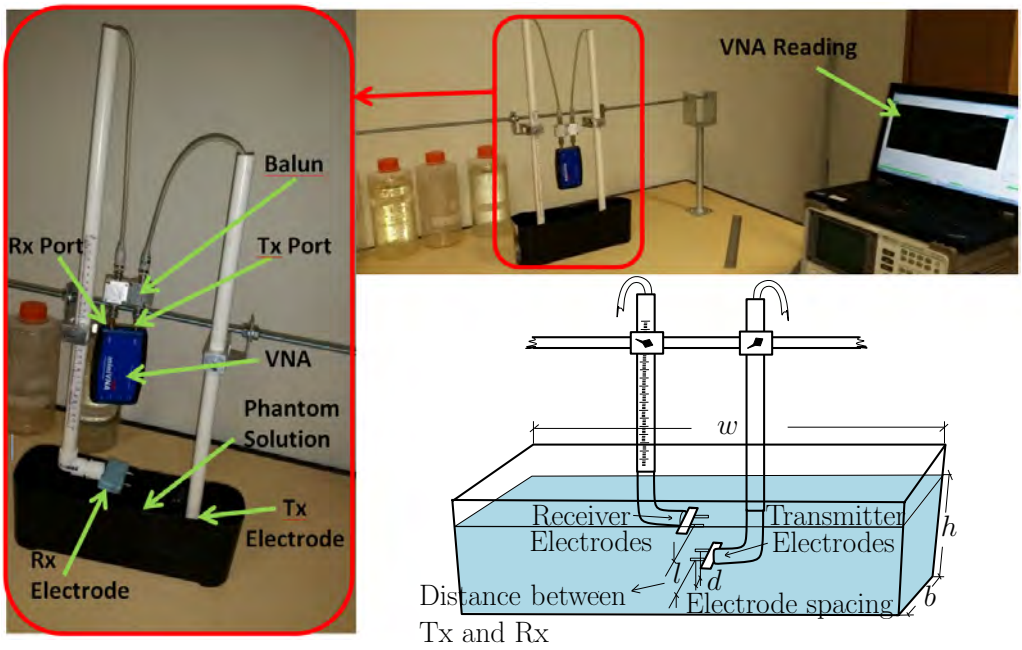

Fig. 3.15 Experimental setup for validation of proposed model. Phantom model setup.

the VNA was wirelessly connected to a battery powered Laptop via BlueTooth. As such, VNA measurements were transferred to the laptop.

3.7.2 Measurement

The transmission electrodes were inserted at a depth of 6.7cm vertically from the outer surface of the phantom solution (i.e., roughly at the center of the 12 cm high phantom solution). With respect to the horizontal direction, transmission and reception electrodes were placed at the middle of the 34 cm long phantom solution. The position of the transmission electrodes was fixed and the reception electrodes were moved vertically up and down to take the path loss readings for each receiver position. The miniVNA sweeps sinusoids with frequencies ranging 100 kHz to 200 MHz and measure the path loss at each frequency. At each relative locations of the receiver 5 transmission gain measurements were taken. Although the path loss readings were for the entire range of 0.1 – 200 MHz,

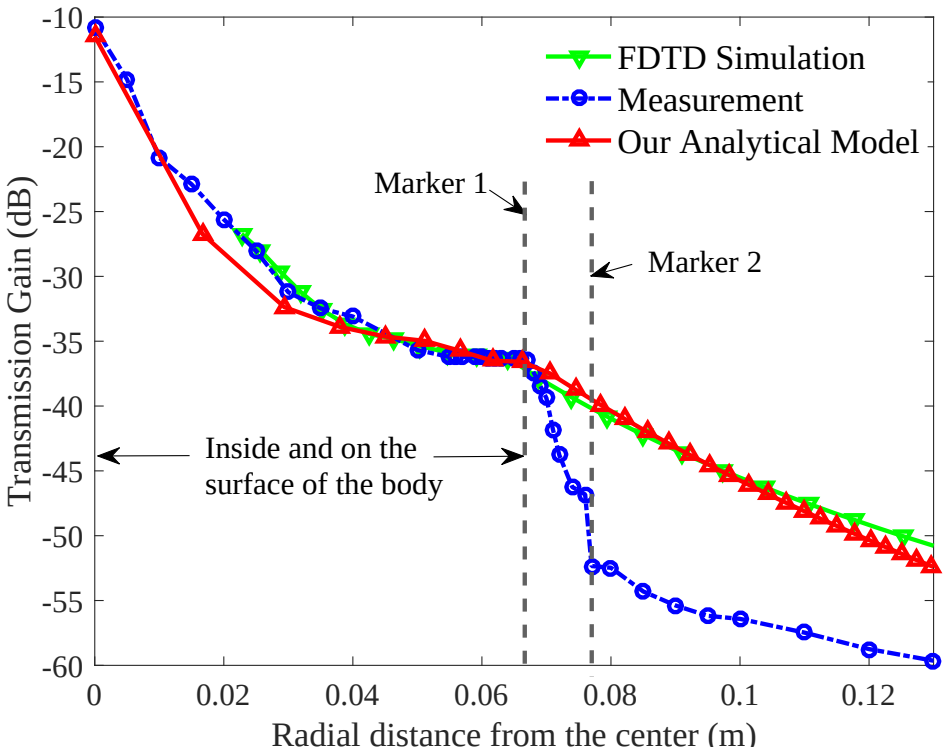

Fig. 3.16 Comparison of our model with measurement and simulation.

we extracted only values for the frequency of 13.67 MHz (since the solution is prepared for this frequency). The path loss in dB is the arithmetic inverse of the transmission gain in dB. The mean value of the readings was then taken as average measured path loss at the considered communication distances as shown in Fig. 3.16.

Finite Difference Time Domain (FDTD) simulations were also carried out using the SMECADx software for the same setting. We considered two settings. In the case of an implant-to-implant setting the receiver is another implanted device inside one of the tissue layers, whereas in the implant-to-surface communication setting, the receiver can either be another implant or mounted on the surface of the skin. From these two settings, the considered region of interest (ROI) is the region inside the human body ranging from the transmitter location up to the the surface of the skin. In the experiment, this region corresponds to a

radial distance of 0 – 6.7 cm from the center (i.e., marker 1 in Fig. 3.16). As can be seen, in the ROI, the proposed analytical model and the FDTD simulation fit the measurement well. Outside our ROI (i.e., outside the surface of the skin), the measured path loss is larger than predicted by our model and the FDTD simulation. After sufficiently large distance (i.e., after marker 2) the path losses follow similar trend.

The measurement discrepancy in the region between marker 1 and marker 2 is believed to be mainly due to the impedance at the electrode contact which is not considered in the proposed model and the FDTD simulation. For capacitive and galvanically coupling electrodes, an insightful study on electrode contact impedance for cases when they are inside media of varying permittivity and conductivity properties is presented in [131]. For receivers within the body tissue, we can see that the electrodes are covered by a conducting tissue where both the conduction and induced currents exist; hence, the contact established is similar to metal-to-electrolyte contact [132, 133]. Therefore, the contact impedance of the electrodes to tissue are comparatively small with respect to the contact impedance outside the body. Thus, the effect of electrode contact impedance on the path loss can be assumed negligible inside the body. This explains the fact that the proposed path loss model fits the measurement in the region of interest (i.e., up to the skin surface). On the contrary, the conduction current vanishes outside the skin surface. Besides, the receiver electrodes are in free space (i.e., non conducting air). Here, the vanishing current makes the contact impedance high and can not be ignored. As the electrodes move away from the skin surface (i.e., away from a relatively more conductive medium), the radius of a sphere of free space surrounding the electrodes increase which makes impedance as an increasing function of distance. Hence, the measured path loss increases at a larger gradient than modeled between vertical marker 1 and maker 2 as shown in in Fig. 3.16. After a far enough distance (i.e., marker 2) the electrode can be

assumed to be inside a sphere of free space with infinite radius and the contact impedance is constant. Thus, after marker 2, the measured path loss roughly takes slower slope as predicted by the FDTD and our model.

3.7.3 Comparison of the Model with Existing Work

Results of the presented model framework were further compared with experimental results reported by Sun *et al* [107]. In [107], a model that employs a simplistic spherical geometry is used and experiment was carried out by implanting a transmitter inside the brain tissue of an anesthetized pig. The transmitter couples a current of 40 μA where the transmitter electrode spacing (i.e., between the anode and cathode electrodes) is set to be 1.4 cm. In their work, they approximated the human head by a sphere of overall radius 7.5 cm with a homogeneous conductivity of 0.45 S·m^{-1}.

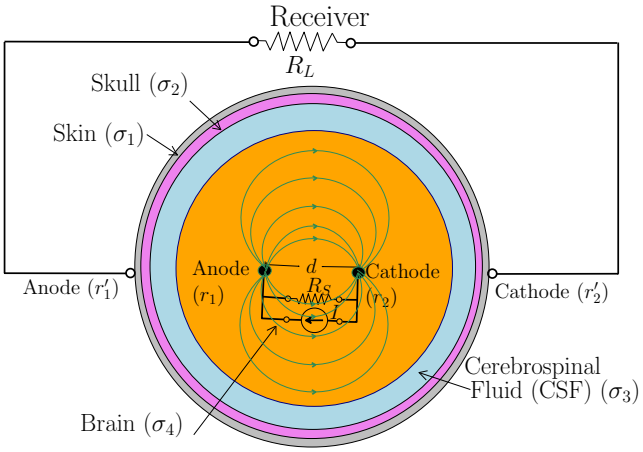

Fig. 3.17 Multilayered ellipsoidal approximation of head.

For the purpose of comparison, our setup was modified to fit the setting given in [107] as shown in Fig. 3.17. The potential distribution were evaluated for the modified setting results were compared with previously reported values in Table 3.3. Here, the electric potential is denoted by V and %Δ denotes the percentage error of the potential calculated in literature in our work using the

measured value given [107] (i.e., *in vivo* measurement on an anesthetised pig) as a reference. For analysis, the complex conductivities of tissues considered (i.e., skin, skull, cerebrospinal fluids and brain tissues) were referred from the IT'IS foundation database[95]. From Table 3.3, it can be seen that our model predicts the measured values with good accuracy and demonstrating that it can be applied to any part of human body (i.e., a limb was considered earlier and now the head).

Table 3.3 Potential difference detected at the receiver

	Homologous sphere [107]	Multilayered sphere [134]	Measured [107]	Our work
V	105 μV	88 μV	90.72 μV	89.8 μV
%Δ	15.74 %	3.00 %	0 %	1.01 %

In summary, our model describes the signal reception in the ROI (i.e., by another implant or a wearable receiver). The fact that electrode contact impedance is large outside the body further strengthens the claim that the IBC signal is confined to within and on the body. Although the region away from the skin is not included in the ROI, inclusion of contact impedance into our model is an interesting problem for future work.

3.8 Conclusion

This chapter presented a novel analytical model framework for implant communication using gc-IBC. The model presents, for the first time, a geometrically versatile solution that can be applied to any part of human body. The model can be used to describe and understand important parameters of the implant communication channel such as the electromagnetic effect of tissue layers, size and depth of the implant on input and received power, path loss, received

potential and potential ratio. The predicted path loss at the surface of the skin for a communication distance of around 6 cm is between 30-40dB in the frequency range of interest which coincides with empirical results previously reported. Our result shows that gc-IBC scheme for implant communication is not only feasible but possesses better path loss characteristics and offers a potentially large degree of miniaturisation. Moreover, different parts of the body have varying number of tissue layers and our analysis provided insight into applying the model to different parts of the body by increasing the number and electromagnetic properties of tissue layers.

Chapter 4

A Hybrid Intrabody Communications for Wireless Cortical Implants

Cortical and deep brain implants are emerging as popular technologies for human-machine interfaces, bionic prostheses, diagnostics and treatment of neurological ailments. These applications require reliable and low power data communication between implants and an external device. While some cortical implants employ inductively coupled data transfer (ic-DT) making use of the physical coils for powering, others are enabled by antenna based radio frequency (RF) centered on 401–406 MHz and around 2.4 GHz. Intrabody communication (IBC) is another emerging technique, for communications in and around the human body, that makes use of the body's lossy dielectric nature. This chapter theoretically compares the efficacy of inductive link and galvanically coupled intrabody communication (gc-IBC) for cortical implants in the frequency range 1–10 MHz with implantation depths up to 7 cm. We propose a hybrid integration of gc-IBC and inductive scheme suitable for implant communications. It is shown here

that, while inductive coupling is preferred for power transfer, gc-IBC has a wide band characteristics compared to ic-DT and 20 dB lower path loss compared to antenna based RF schemes.

4.1 Introduction

Cortical implants are devices surgically implanted in different regions of the cerebral cortex and are equipped with arrays of sensory electrodes to detect bioelectrical signals generated by brain activity (Fig. 4.1). The signals are processed and transmitted to the outside-world via a readout transmitter. Cortical implants that can replace failed sensory function such as vision and hearing are being developed to receive artificially generated stimuli and activate specific regions of the cortex. These applications require reliable and low power data communication between the implanted and external device. Advances in biomedical research and microelectromechanical systems (MEMS) technology have enabled stimulating and sensing devices in addition to locating implantation spots for appropriate applications. However, powering a cortical implant and achieving data transmission from implant to surface and vice versa is still under intense investigation. Most of implants to date are powered via inductive power transfer and in some cases even via wired power transfer [135–139]. In most of these works inductive transfer is also used for data transfer. We refer to the use of inductive link for data transfer as inductively coupled data transfer (ic-DT). Several factors limit its effectiveness for data transfer; for example, it is effective for up to a transmission distance of about 2–3 cm and only offers small bandwidth of a few tens of kilohertz. The MedRadio (401–406 MHz) and the industrial, scientific and medical (ISM) band around 2.4 GHz are also used for implant radio communication powered by different types of antennas [140–142]. The MedRadio and the ISM bands respectively are included as narrow band

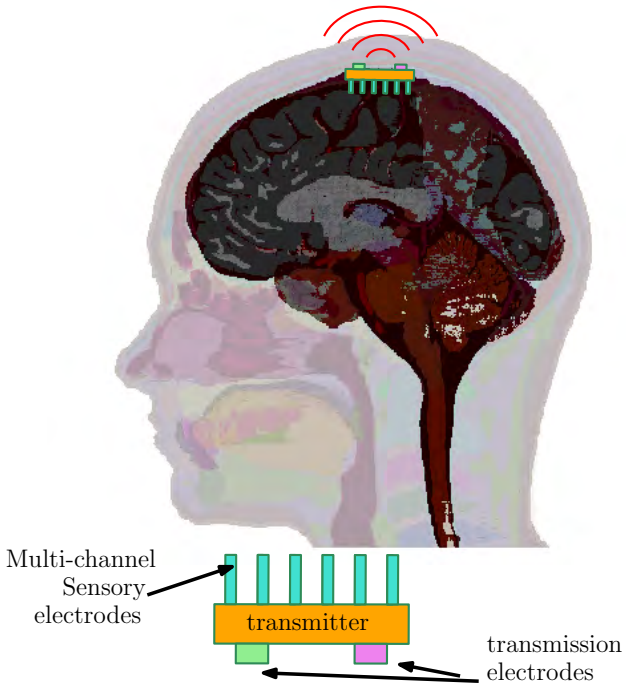

Fig. 4.1 Cortical read-out implant

and ultra wide band specifications of the IEEE 802.15.6 standard designated mainly for implant communication. Antenna based systems are preferred at very high frequencies in order to minimise antenna size. However, high frequency electromagnetic signals suffer high attenuation in the hostile human body environment and hence their penetration depth is small, making them less attractive as communication technique.

It is essential that cortical implants are powered using techniques that minimize the requirement of invasive procedures to replace batteries. As such, it is imperative that the powering mechanism is reliable or that the transmission utilises resources (i.e., power and bandwidth) efficiently. This chapter explores an alternative transmission and reception of electrical signals between the cortical implant and an external device using body-centric communication techniques. The major motivation in this work is to model and analyse the galvanically coupled intrabody communication (gc-IBC), inductively coupled scheme and antenna based RF schemes for powering and data transmission in

cortical implants. To this end, we derived an analytical path loss (PL) model of the inductively coupled scheme as a function, explicitly, of frequency and communication distance for the first time. We also extended the analytical model for gc-IBC, derived in chapter 3, for cortical implant communication. For the case of antenna based schemes, we used path loss models and measurements reported in literature. Our analysis shows that while inductively coupled scheme is a good powering scheme, gc-IBC at a relatively low frequency theoretically offers a better communication alternative for cortical implants with data rates of a few Mbps. In this work, for gc-IBC and ic-DT, we considered the frequency range of 1–10 MHz and 2.4 GHz for antenna enabled RF scheme with a communication distance up to 7 cm which is the average overall radius of the adult human head[107].

This chapter is organised as follows. Section 4.2 outlines the cortical implant setting considered. Section 4.3 and 4.4 derive analytical path loss models, respectively, for inductively coupled and galvanically coupled schemes as functions of frequency and communication distance. The results are discussed in Section 4.5 and our conclusion in Section 4.6.

4.2 Proposed Cortical Implant Communication Scheme

In most cases, cortical implants interface with the cortex via a highly dense array of electrodes for activation of a particular region or sensing bioelectric potentials from that cortex surface as shown in Fig. 4.1. In the case of read-out cortical implants, the transmission unit multiplexes, modulates and transmits the cortex neuron activity signal to the outside world. For cortical stimulation implants,

the device receives processed external stimuli and stimulates the desired cortex region by generating the required electrical pulses at the electrode array.

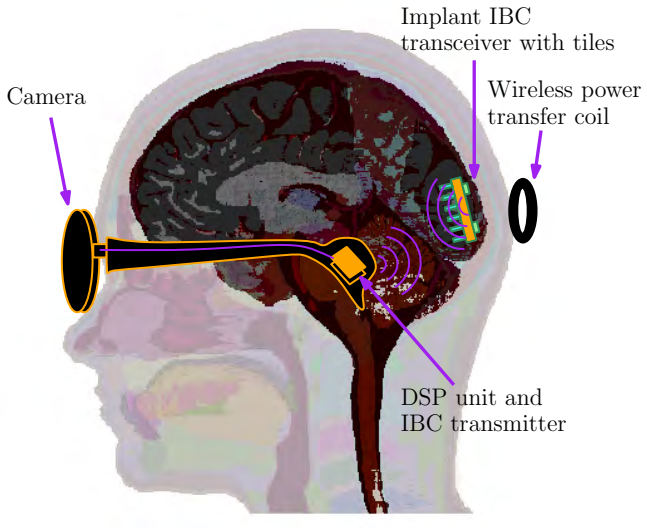

Fig. 4.2 Proposed hybrid cortical implant communications setting for bionic vision

For example, consider the case of the wireless cortical implant for vision restoration e.g. [143, 31, 30]. The authors propose a wired connection of the camera unit and a pocket digital signal processor (DSP) to an inductively coupled wireless data and power transfer unit mounted above pia mater (back of the head). The implant, was 2 cm deep and had 43 channels of stimulating electrodes spaced 1 mm apart. The stimuli were biphasic current signals of up to 100 μA generated at each electrode with two current sources and a 5 bit digital-to-analog convertor (DAC) according to the transmitted features from the pocket processor. Data from the pocket processor is combined at a rate of 100 kbps modulated by a 5 MHz carrier. Here the carrier is used to transfer the power signal. The receiver detects and rectifies the carrier to power itself the demodulate the envelope signal. Although the bandwidth of this signal is small enough to be transmitted using ic-DT, narrow band inductive link (when also designed for power transfer) would struggle to accommodate the actual wide band data requirements of bionic vision implants.

Considering a typical resolution of the human eye at around 1–2 million pixels, stimulation using an array of only 43 electrodes could be considered small [143]. Thus, for example, using about 200 electrodes to increase resolution will see the data rate increased from 100 kbps to about 500 kbps. In this case, the modulation index is reduced and the data rate is considerably high to be amplitude modulated onto a 5 MHz carrier. Thus, a wide band channel is required; however, due to the fact that the transmission via inductive coupling introduces a highly selective narrow band characteristics (especially when designed to minimise path loss at the carrier frequency) not to mention the fading already introduced by the human body as a wireless channel.

In this chapter, we propose a modified version of this bionic vision implant, as shown in Fig. 4.2, that uses IBC surface to implant communication in addition to the inductive link. While the use of coils for inductive power transfer is essential to keep the implant powered from outside across a distance of 2 cm, its use for data transfer is bandwidth limited by the fact that the coils are designed for a fixed resonant frequency. The resonant frequency is chosen mainly based on the intended band of operation and component sizes. In fact, different resonance frequencies have been used for inductive power and data transfer; for example, 1 MHz [47], 24 MHz [49], 5 and 10 MHz [48]. In the following sections we analyse and compare the inductive coupled, galvanically coupled and antenna based RF schemes for power and data transfer.

4.3 Analysis of Inductive Power and data Transfer for Cortical Implants

Consider the primary and the secondary coils for the inductive link as shown in Fig. 4.3 (a). Here the the primary coil is on the surface of the human body

integrated with the transmitter while the secondary coil is implanted as part of the receiver. The separation between the transmitter and receiver is the distance between primary and secondary coils, denoted by d. Without loss of generality, let the circular primary and secondary coils have radii of r and $r-\ell$ respectively where ℓ is the thickness of the coils (i.e., the secondary coil can pass through the primary for analysis of the coupling coefficient). For simplicity of analysis, consider the number of turns in both coils to be similar denoted by N. The inductance of the primary and secondary, L_1 and L_2, respectively are given by

$$L_1 = \frac{\mu_0 \mu_r \pi r^2 N^2}{\ell}, \quad \text{and} \quad L_2 = \frac{\mu_0 \mu_r \pi (r-\ell)^2 N^2}{\ell}. \tag{4.1}$$

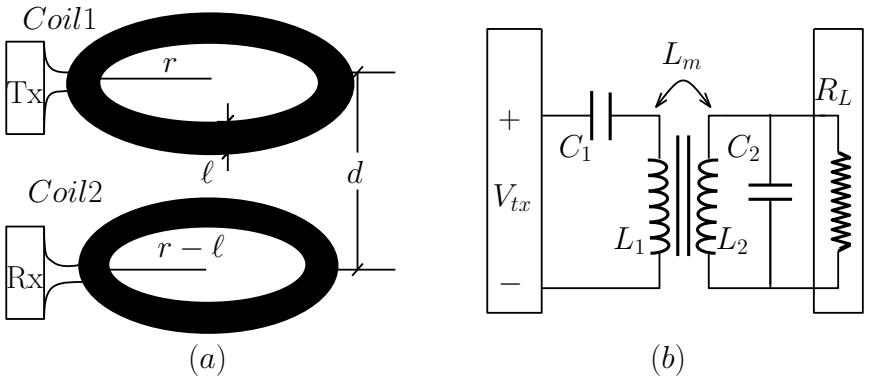

Fig. 4.3 (a) Coil pair used for inductive link. (b) The series-parallel (SP) topology circuitry

Following a similar analysis as [144], we have calculated the mutual inductance L_M as a function of d through elliptical integrals resulting in

$$\begin{aligned} L_m =& \mu_0 \mu_r N^2 \sqrt{(2r-\ell)^+ d^2} \\ & \times \left[\frac{2r^2 - 2r\ell + \ell^2 + d^2}{(2r-\ell)^2 + d^2} \mathcal{I}_e^1(x) - \mathcal{I}_e^2(x) \right] \end{aligned} \tag{4.2}$$

where μ_0 is permeability of the free space 1.26×10^{-6} m kg s^{-2} A^{-2}; μ_r is relative permeability of the tissues between the coils which is equal to unity for all

tissues considered [95]. $\mathcal{I}_e^2(x)$ and $\mathcal{I}_e^2(x)$ are elliptical integrals of 1^{st} and 2^{nd} kind respectively for $x = \sqrt{4r(r-\ell)/[(2r-\ell)^2+d^2]}$. These elliptical integrals, for the problem at hand, can be well approximated by their series expansion up to 2^{nd} order as experimentally demonstrated in [144]. The mutual inductance is due to the coupling coefficient $\mathcal{K}$ between the coils given by $\mathcal{K} = L_m/\sqrt{L_1 L_2}$. We further normalised the coupling coefficient such that $\mathcal{K}|_{d=0} = 1$. Substituting the series expansion of the elliptic integrals and normalising $\mathcal{K}$, gives the mutual inductance as

$$L_m \approx \frac{\mu_0 \mu_r \pi r \ell (r-\ell)(2r-\ell) N^2}{(\ell^2+d^2)\sqrt{(2r-\ell)^2+d^2}} \tag{4.3}$$

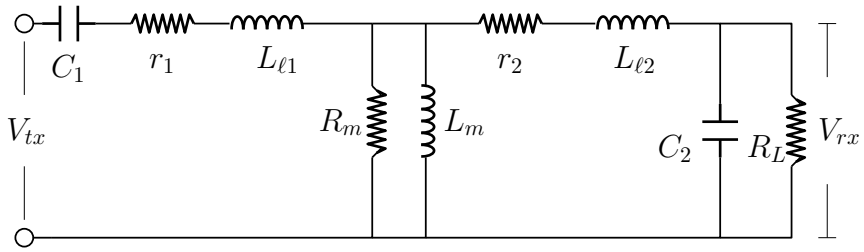

Fig. 4.4 Equivalent SP circuit model for the inductive link.

The series-parallel (SP) topology in Fig. 4.3 (b) is considered for the inductive link analysis. Equivalent circuit for the SP setting is given in Fig. 4.4 where r_1 and r_2 are resistances of the primary and secondary coils respectively, R_m is the magnetising resistance [145]. $L_{\ell 1}$ and $L_{\ell 2}$ are leakage inductances of the primary and secondary coils respectively and are given by $L_{\ell 1} = (1-\mathcal{K})L_1$ and $L_{\ell 2} = (1-\mathcal{K})L_2$. R_L is the load resistance which is assumed to be 50 Ω for the purpose of path loss calculations. Without loss of generality, a uniform load of 50 Ω is used across all schemes considered. Analysing the equivalent circuit of the setting, the path loss for the inductively coupled systems, denoted by PL_{ic},

as a function of frequency and transmission distance is given by

$$PL_{ic}(f,d) = 20\log\left|\frac{-f^2 4\pi^2 C_1 L_m R_L[R_m(R_L+r_2)]}{(1+\frac{jf}{p_0})(\mathcal{M}_1(f,d))(\mathcal{M}_2(f,d))}\right|$$

where

$$\mathcal{M}_1(f,d) = 1 + j\frac{2\psi_1(d)}{f_1}f - \frac{f^2}{f_1^2},$$
$$\mathcal{M}_2(f,d) = 1 + j\frac{2\psi_2(d)}{f_2}f - \frac{f^2}{f_2^2},$$
$$p_0 = R_m(1/L_{\ell 1} + 1/L_{\ell 2} + 1/L_m)/(2\pi),$$
$$\psi_1(d) = \pi r_1 C_1 f_1,\ f_1 = \frac{1}{2\pi}\sqrt{\frac{1}{C_1(L_{\ell 1}+L_m)}},$$
$$\psi_1(d) = \pi R_L C_2 f_2,\ f_2 = \frac{1}{2\pi}\sqrt{\frac{1+r_2/R_L}{C_2(L_{\ell 2}+L_m||L_1)}}.$$

Figure 4.5 shows the calculated path loss for the inductively coupled scheme as a function of frequency and transmission distance. The setting analysed here is for a resonant frequency of 2 MHz (chosen similar with the gc-IBC see Section 4.4) by choosing values $C_1 = 1.4$ nF, $C_2 = 1.4$ nF, coils such that $N = 8$, $r_1 = 0.72\ \Omega, r_2 = 0.72\ \Omega, R_m = 10\ \Omega, \ell = 2$ mm, $r = 6$ mm, and $R_L = 50\ \Omega$. The area and the thickness of the system is selected to be close to the implant dimensions used in [30].

In this setting, the path loss is an increasing function of the transmission distance as expected. The minimum path loss is at the resonant frequency around which power and data transfer is set up. At resonance, the path loss varies from less than 10 dB at lower end of the transmission distance up to around 60 dB at a distance of 7 cm. Impedance mismatch outside the resonant frequency causes the path loss to increase. As such the inductively coupled scheme is a highly frequency selective scheme.

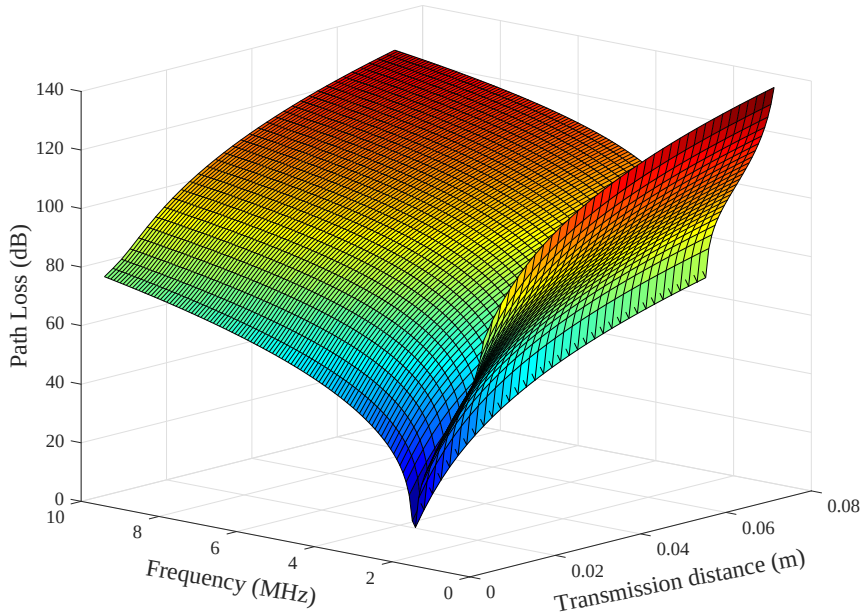

Fig. 4.5 Path loss for an inductively coupled scheme as a function of frequency and transmission distance. Resonance at 2 MHz and path loss increases with transmission distance.

4.4 Analysis of Galvanically Coupled Cortical Implant

In this section, the analytical path loss for the galvaically coupled IBC scheme, specifically for cortical implant, is derived. The implant transmitter shown in Fig. 4.6 injects differential signal using its two electrodes. To calculate the path loss we considered the six major layers of the human head from the outer to the inner parts of the brain, vis Skin, Fat, Muscle, Skull, Cerebrospinal Fluid (CSF), Brain white and grey mater. The conductivity and permittivity of the white and grey mater are approximately similar and hence combined to a single layer for simplicity of analysis. The different layers of the brain were approximated by ellipsoidal geometry as per the framework proposed in chapter 3. We extended our validated analytical model given in [13], to derive the potential distribution for a cortical implant attached inside the brain. Let the potentials in i^{th} tissue

layer with complex conductivity σ_i be denoted by V_i, $\forall i \in \{0,1,2,3,4,5,6\}$ as shown in Fig. 4.6. The conductivity and permittivity of tissues considered can be found in [95]. Under electro-quasi static conditions, the potential distribution V_i at each tissue layer is the sum of of the interior and exterior potentials computed as

$$V_i(\lambda_1,\lambda_2,\lambda_3) = \sum_{n=0}^{\infty}\sum_{p=1}^{2n+1} A^i_{(n,p)}\mathbb{E}^p_n(\lambda_1,\lambda_2,\lambda_3) + \sum_{n=0}^{\infty}\sum_{p=1}^{2n+1} B^i_{(n,p)}\mathbb{F}^p_n(\lambda_1,\lambda_2,\lambda_3), \alpha^i_1 \leq \lambda_1 \leq \alpha^{i-1}_1 \tag{4.4}$$

where $\mathbb{E}^p_n$ and $\mathbb{F}^p_n$ are the products, respectively, of Lamé's functions of first

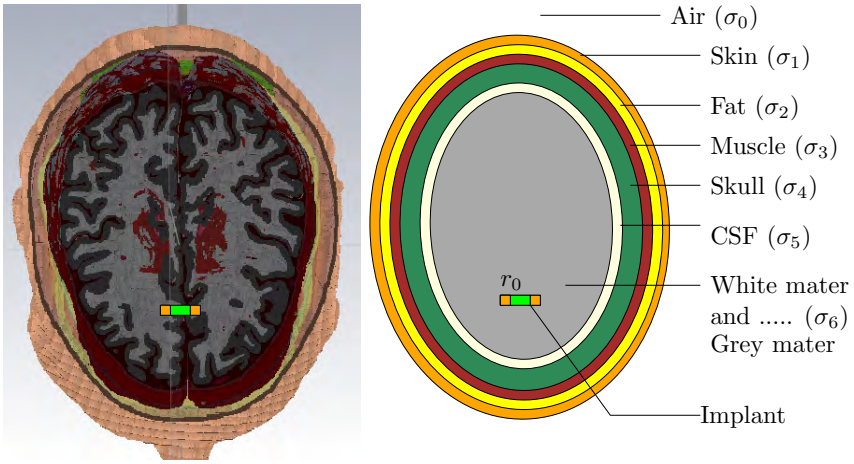

Fig. 4.6 Six-layered ellipsoidal approximation of the human head.

and second kind in the three ellipsoidal coordinates λ_1, λ_2 and λ_3. $A^i_{(n,p)}$ and $B^i_{(n,p)}$ are the coefficients of the n^{th} degree and p^{th} order terms, respectively, of the interior and exterior potential distribution of the i^{th} tissue layer. The values α^i_1 denote the major semi-axis length of the i^{th} ellipsoidal interface. The boundary conditions at an interface between the i^{th} and $(i+1)^{th}$ tissue layer

with conductivities σ_i, $\sigma_{(i+1)}$ and potentials V_i, $V_{(i+1)}$ respectively, are defined as

$$\sigma_i \nabla V_i(\mathbf{r}).e_n = \sigma_{(i+1)} \nabla V_{(i+1)}(\mathbf{r}).e_n, \mathbf{r} \in \Omega_i^{(i+1)} \tag{4.5}$$

$$V_i(\mathbf{r}) = V_{(i+1)}(\mathbf{r}), \mathbf{r} \in \Omega_i^{(i+1)} \tag{4.6}$$

where e_n is the unit vector normal to the interface and $\mathbf{r}$ is a point on the surface $\Omega_i^{(i+1)}$ separating the i^{th} and $(i+1)^{th}$ layer. While (4.6) states continuity of potential, (4.5) states continuity of current density at the interface. Here, $A^0_{(n,p)} = 0$ since the external layer is non conducting air (i.e., with $\sigma_0 = 0$) and $B^6_{(n,p)}$ is derived as,

$$B^6_{(n,p)} = \frac{\mathfrak{M} \cdot \nabla_{\mathbf{r}_0} \mathbb{E}^p_n(\lambda_{1_0}, \lambda_{2_0}, \lambda_{3_0})}{(2n+1)\sigma_6 \gamma^p_n}. \tag{4.7}$$

where $\mathfrak{M}$ is the dipole moment of the transmitter electrodes at locations r_1 and r_2, and $\mathbf{r}_0$ is the vector pointing mid-way between the transmitter electrodes located at $(\lambda_{1_0}, \lambda_{2_0}, \lambda_{3_0})$. Here, γ^p_n is the orthogonality normalisation constants given in [13]. Applying the boundary conditions (4.5) and (4.6), and substituting (4.7) into (4.4), the remaining coefficients are

$$B^1_{(n,p)} = \frac{\sigma_6 B^6_{(n,p)}}{Z^p_n},$$

$$B^0_{(n,p)} = \frac{B^1_{(n,p)}}{C^0_{(n,p)} I^p_n(\alpha^0_1)},$$

$$B^2_{(n,p)} = \frac{U^p_n B^1_{(n,p)}}{\sigma_2},$$

$$B^3_{(n,p)} = \frac{W^p_n B^1_{(n,p)}}{\sigma_3},$$

$$B^4_{(n,p)} = \frac{X^p_n B^1_{(n,p)}}{\sigma_4},$$

$$B^5_{(n,p)} = \frac{Y^p_n B^1_{(n,p)}}{\sigma_5},$$

$$A^1_{(n,p)} = (2n+1)\Big[\frac{1}{C^0_{(n,p)}} - I^p_n(\alpha^0_1)\Big]B^1_{(n,p)},$$
$$A^2_{(n,p)} = (2n+1)\Big[\frac{-I^p_n(\alpha^1_1)U^p_n}{\sigma_2} + \frac{\sigma_1 - U^p_n}{C^1_{(n,p)}(\sigma_1-\sigma_2)}\Big]B^1_{(n,p)},$$

$$A^3_{(n,p)} = (2n+1)\Big[\frac{-I^p_n(\alpha^2_1)W^p_n}{\sigma_3} + \frac{U^p_n - W^p_n}{C^2_{(n,p)}(\sigma_2-\sigma_3)}\Big]B^1_{(n,p)},$$
$$A^4_{(n,p)} = (2n+1)\Big[\frac{-I^p_n(\alpha^3_1)X^p_n}{\sigma_4} + \frac{W^p_n - X^p_n}{C^3_{(n,p)}(\sigma_3-\sigma_4)}\Big]B^1_{(n,p)},$$

$$A^5_{(n,p)} = (2n+1)\Big[\frac{-I^p_n(\alpha^4_1)Y^p_n}{\sigma_5} + \frac{X^p_n - Y^p_n}{C^4_{(n,p)}(\sigma_4-\sigma_5)}\Big]B^1_{(n,p)},$$
$$A^6_{(n,p)} = (2n+1)\Big[\frac{-I^p_n(\alpha^5_1)Z^p_n}{\sigma_6} + \frac{Y^p_n - Z^p_n}{C^5_{(n,p)}(\sigma_5-\sigma_6)}\Big]B^1_{(n,p)},$$

where

$$I^p_n(\alpha^i_1,\alpha^j_1) = I^p_n(\alpha^i_1) - I^p_n(\alpha^j_1), \forall i,j \in \{0,1,2,3,4,5,6\},$$
$$U^p_n = (\sigma_1-\sigma_2)C^1_{(n,p)}\Big[\frac{-1}{C^0_{(n,p)}} - I^p_n(\alpha^1_1,\alpha^0_1) + \frac{\sigma_1}{C^1_{(n,p)}(\sigma_1-\sigma_2)}\Big],$$

$$W^p_n = (\sigma_2-\sigma_3)C^2_{(n,p)}\Big[\frac{U^p_n}{C^2_{(n,p)}(\sigma_2-\sigma_3)} + \frac{U^p_n - \sigma_1}{C^1_{(n,p)}(\sigma_1-\sigma_2)} - \frac{W^p_n I^p_n(\alpha^2_1,\alpha^1_1)}{\sigma_2}\Big],$$
$$X^p_n = (\sigma_3-\sigma_4)C^3_{(n,p)}\Big[\frac{W^p_n}{C^3_{(n,p)}(\sigma_3-\sigma_4)} + \frac{W^p_n - W^p_n}{C^2_{(n,p)}(\sigma_2-\sigma_3)} - \frac{W^p_n I^p_n(\alpha^3_1,\alpha^2_1)}{\sigma_3}\Big],$$

$$Y_n^p = (\sigma_4 - \sigma_5)C_{(n,p)}^4\Big[\frac{X_n^p}{C_{(n,p)}^4(\sigma_4 - \sigma_5)} + \frac{X_n^p - V_n^p}{C_{(n,p)}^3(\sigma_3 - \sigma_4)} - \frac{X_n^p I_n^p(\alpha_1^4, \alpha_1^3)}{\sigma_4}\Big],$$

$$Z_n^p = (\sigma_5 - \sigma_6)C_{(n,p)}^5\Big[\frac{Y_n^p}{C_{(n,p)}^5(\sigma_5 - \sigma_6)} + \frac{Y_n^p - X_n^p}{C_{(n,p)}^4(\sigma_4 - \sigma_5)} - \frac{Y_n^p I_n^p(\alpha_1^5, \alpha_1^4)}{\sigma_5}\Big].$$

For receiver electrodes located at r_1' and r_2', the potential difference V_{Rx} is

$$V_{rx} = V(r_1') - V(r_2') \tag{4.8}$$

where the electrode potentials, $V(r_1')$ and $V(r_2')$ are obtained by evaluating (4.4) at points r_1' and r_2' with $A_{(n,p)}^i$ and $B_{(n,p)}^i$ as given above.

For a receiver impedance R_L, the received power $P_{rx} = V_{rx}^2/R_L$. The transmit power of $P_{tx} = V_{tx}^2/R_i$ where V_{tx} is the potential difference at the transmit electrodes and R_i the transmitter impedance added to the impedance of the tissues seen by the transmitter. The path loss for the galvanically coupled IBC is given by $PL_{gc} = 10\log|P_{tx}/P_{rx}|$ with R_L normalised to 50 Ω.

4.5 Simulation Results

The analytical model for gc-IBC, presented here is validated by simulating the setting in CST (Computer Simulation Technology, Darmstadt, Germany). We used the electro quasi-static solver for an implant placed on the surface of the cortex with an electrode spacing (between anode and cathode of transmitter) of 20 mm in the setting shown in Fig. 4.6. Fig. 4.7 shows the potential distribution from the CST simulation. The comparison of the measured path loss (using a homogeneous phantom solution) with this analytical model and the CST

simulation are given in Fig. 4.8. It can be seen that the analytical model given in this work is a good fit to the CST simulation of the gc-IBC implant scenario. The analytical model has the advantage that researchers and designers can quickly study the effect of the different layers of tissue thicknesses and properties by changing the simulation parameters. Unlike the CST simulation, which also takes a lot of computational time and resources (3 hours for a quad core PC with core i7 processor, 16 GB RAM and Nvidia GeForce 940MX GPU), analytical model of the channel could also be used as a reference in some adaptive receiver processing in estimation of the channel.

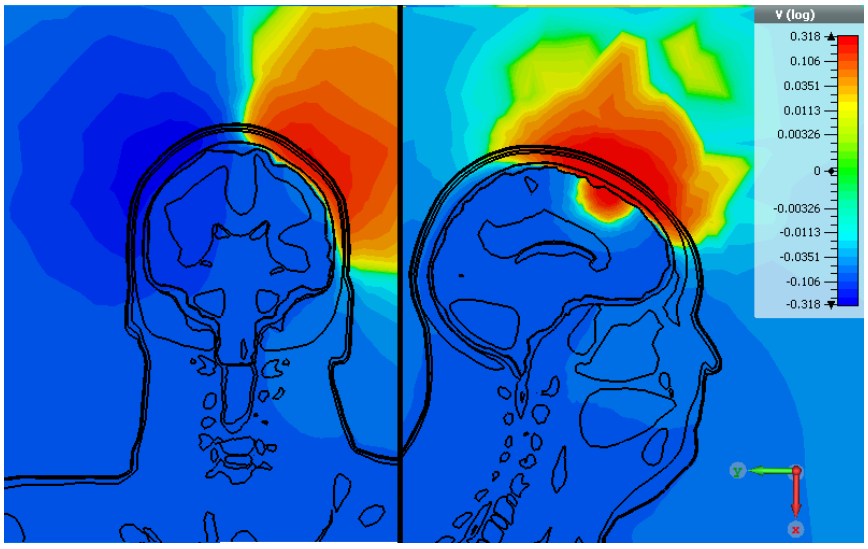

Fig. 4.7 Simulated potential distribution for a gc-IBC cortical read-out implant. Left - frontal view and right - side view

The analytical model for the ic-DT uses the coupling coefficient as a function of transmission distance. The work [144] experimentally validated the coupling coefficient as function of distance between the coils and hence the path loss model for the ic-DT is indirectly validated. In fact, this work even further adjusted the variation between measurement and analytical model of the coupling coefficient given in [144]. In addition to the inductive coupled and galvanic coupled schemes, this chapter also refers to antenna enabled radio communications in the ISM and medRadio bands. There is a rich amount of literature on path loss modeling,

measurement and simulation of the later schemes. Thus, we used one of the results (which is similar to what is often reported) given in [146], for comparison.

4.5.1 Path loss and potential distribution

The comparisons given in Fig. 4.8 present the variation of the path loss as a function of communication distance. In addition to the validation of the analytical model with simulation and experimental results, this plot compares the path loss performance of the three schemes - antenna enabled wireless radio at 2.4 GHz (ISM band), inductively and galvanically coupled schemes at 2 MHz.

Note the difference between wireless radio and the gc-IBC. The slopes at which both path losses increase with distance are close; this indicates both schemes experience similar shadowing when using the log-normal model. However, there is a significant difference of 20 dB between the two performances. As such the gc-IBC channel requires about two orders of magnitude less gain at the receiver for similar transmit power; hence, gc-IBC scheme requires less power. This further complements the simple design requirements and miniaturise-ability of gc-IBC implants. The main reason for higher path loss of antenna based schemes is that the considered tissues have decreasing permittivity and increasing conductivity with frequency such that the penetration (skin) depth is smaller for higher frequencies. On the other hand, for the later, miniaturising antenna size of radio frequency implants require the use of very high frequencies such as the ISM and MedRadio bands.

Now, let us compare the ic-DT and gc-IBC schemes. At resonance, the inductively coupled scheme has the lowest path loss of all. However, it rises at a high rate. Although, under the given setting, the PL for inductively coupled starts more than 20 dB lower than that of gc-IBC, they cross over at

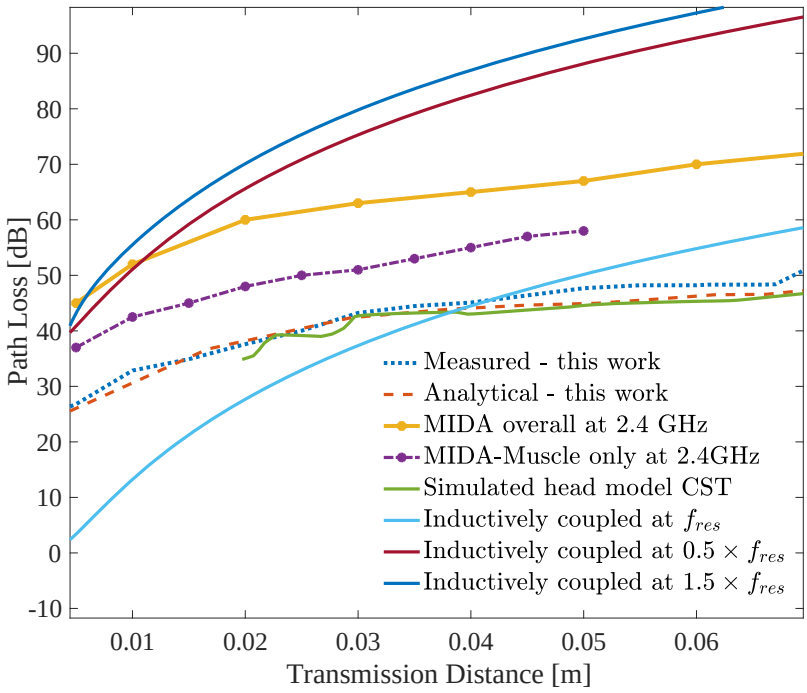

Fig. 4.8 Path loss as a function of transmission distance for various implant communication mechanisms. The multimodal imaging-based detailed anatomical (MIDA) computer model by IT'IS foundation is used [95]. Path loss for the inductive scheme is the lowest at the resonance frequency f_{res} compared to path losses at $0.5 \times f_{res}$ and $2 \times f_{res}$.

a transmission distance of 3 – 4 cm. Thus, inductively coupled schemes are only reliable for small transmission distances. Another observation to note is at frequencies as high as $1.5 \times f_{res}$ and as low as $0.5 \times f_{res}$, the impedance mismatch in the inductive link is so high that the path loss is higher than all the other schemes considered.

Although we used a 2 MHz resonance frequency for the inductive link in most of our discussion, Fig. 4.9 shows that different resonance frequencies selected (i.e., 2, 3, 4 and 5 MHz) provide similar bandwidth when designed for different resonances. Hence, our discussion also applies to ic-DT schemes other than those with resonance frequency of 2 MHz.

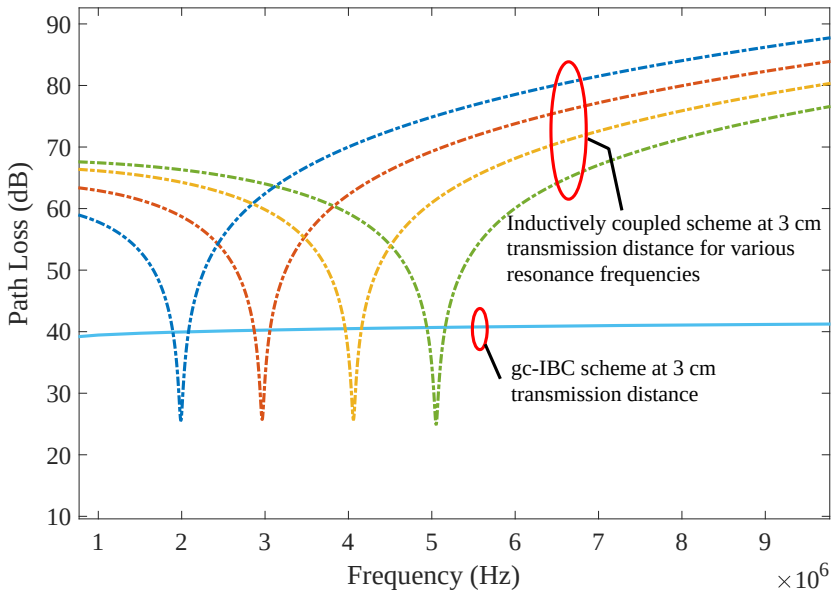

Fig. 4.9 Path losses for gc-IBC scheme and ic-DT at resonance frequencies of 2,3,4 and 5 MHz at a transmission distance of 3 cm.

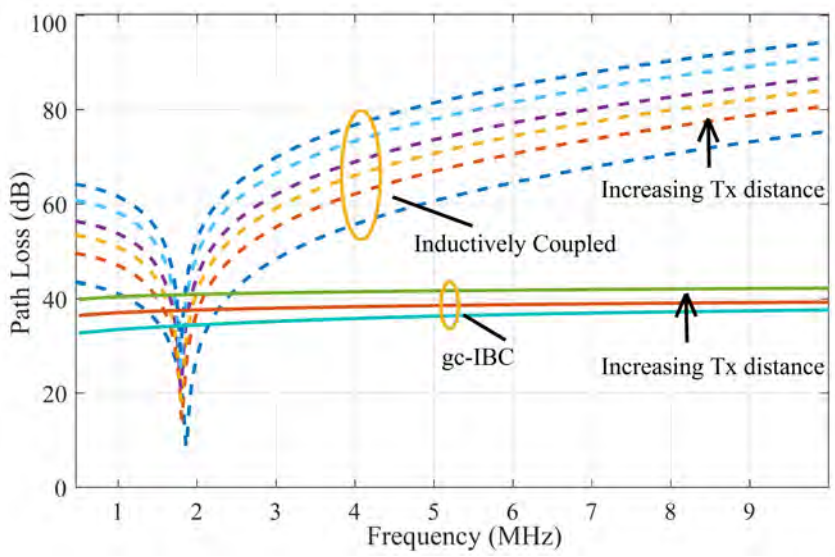

Fig. 4.10 Calculated path loss comparison of ic-DT and gc-IBC schemes in the frequency domain for different communication distances.

4.5.2 Path Loss and Bandwidth

Another important consideration is the slope of the channel PL within the intended band of transmission. The gc-IBC channel has an increasing PL with

frequency. However, as can be seen from Fig. 4.10, the high selectivity of the inductive channel makes the gc-IBC channel appear relatively wide band. At resonance, the coil pairs considered provide 10 and 20 dB path loss at a distance, respectively, of 1 and 2 cm. This performance justifies the application of inductive coupling as a power transfer scheme where the power signal is confined to a narrow band or sinusoidal at a single oscillation frequency. From Fig. 4.10 it can also be seen that the inductive scheme's path loss only a few tens of kilohertz away from the resonant frequency is at least 10 dB higher than the gc-IBC path loss. The difference observed is as high as 50 dB for frequencies about five times the resonance frequencies.

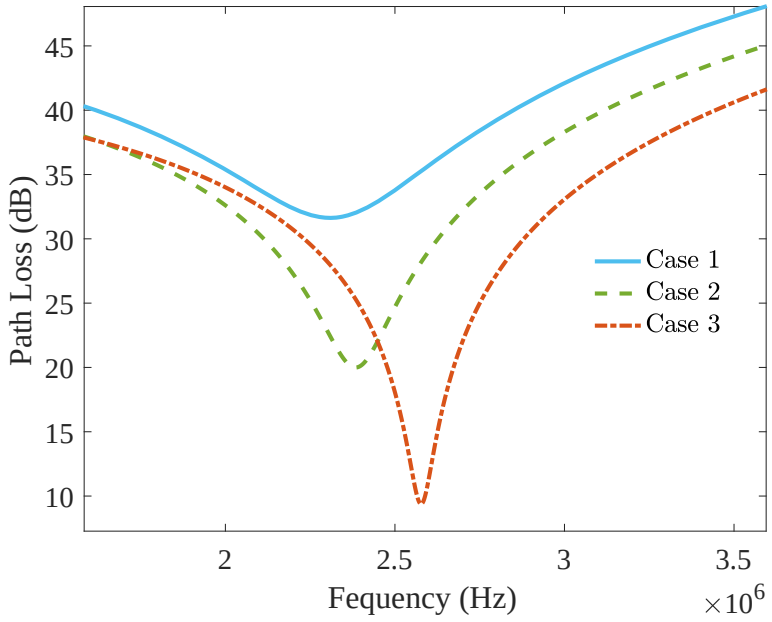

Fig. 4.11 Path loss – bandwidth relationship in the case an inductively coupled scheme is used for data transfer. Case 1 : r = 2 mm, C1 = C2= 20 nF , Case 2 : r = 3.5 mm, C1 = C2= 6.6 nF , Case 3 : r = 6 mm, C1 = C2= 2 nF.

However, many inductively coupled implant schemes employ the use of the scheme both for data and power transfer. This is done by, for example, amplitude modulating the single frequency power carrying signal with a digital data signal to be transmitted. The scheme could be achieved as long as the digital data

transmitted adds only a small bandwidth that can fit the bandwidth of the inductive channel. For example, consider case 3 shown in Fig. 4.11, the inductive coupling channel only accommodates a bandwidth of 60 kHz at a minimum path loss of about 10 dB. In most cases these implants are required for signals with larger bandwidths. Thus, if we try to use inductive coupling with a bandwidth of 155 kHz as in case 2, the minimum PL would be 20 dB. This simply means that the coupled power in case 2 is an order of magnitude lower than what it could have been for case 1. Hence, increasing bandwidth by a factor of 2.5 requires a power coupling reduction of 10 fold. If we select a bandwidth of 450 kHz (i.e., higher than the 300 kHz for the MedRadio case), as in case 1, the minimum PL is about 32 dB which is more than two orders of magnitude sacrifice in the power coupling ratio by deteriorating the PL even worse with distance. This makes it impossible for inductively coupled transceivers to utilise communication schemes such as spread spectrum to be able to communicate under the noise floor thus further reduce the power of the signal needed to be transmitted.

These results suggest that gc-IBC is suited to wider band data transmission while ic-DT scheme is suited to power transfer. Thus, a hybrid system consisting of gc-IBC (for data) and the inductive coupled scheme (for power) could achieve a better performance without introducing further complexity if applied to existing schemes that use inductive coupling both for data and power transfer.

4.5.3 Human Safety and Compliance Assessment

The safety of our gc-IBC implant communication was assessed based on the standards set by the International Commission on Non-Ionising Radiation Protection (ICNIRP) [70]. According to the ICNIRP, for general public exposure, the maximum restrictions of current density, electric field and Specific Absorbtion Rate (SAR), for head and trunk, for the considered range of frequency (1–10

MHz) are given as follows; current density $\leq f/500$ mA m^{-2}, Electric field ≤ 87 $f^{-1/2}$ Vm^{-1} and Localised SAR (averaged over 10 g) ≤ 2 W kg^{-1} where f is the frequency.

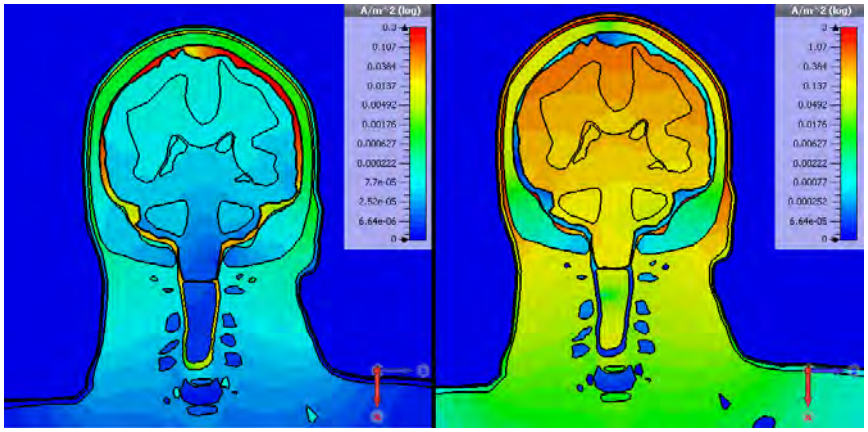

Fig. 4.12 Simulated current density for a gc-IBC cortical read-out implant. Left - displacement current and right - conduction current

The MedRadio standard limits the maximum transmit power to -16 dBm (25 μW) of equivalent radiated power (ERP). To be in-line with the MedRadio standard, the transmit power of the implant was set at -20dBm for the purpose of safety assessment using CST simulations. For this setting, the current density and electric field distribution, simulated for $f = 2$ MHz and electrode spacing of 20 mm, were shown in Figs. 4.12 and 4.13 respectively.

It was observed that, the displacement current is larger than the conduction current by more than an order of magnitude. However, the reverse was found inside the CSF layer. This is mainly because CSF is the most conductive tissue of the human head with a conductivity of about 2 S m^{-1} at 2 MHz. The maximum current density (conduction and displacement combined) is approximately 1.5 Am^{-2} and is smaller than the restriction imposed by the ICNIRP guideline. For this implant on the surface of the cerebral cortex, the electric field distribution is shown in Fig. 4.13. Here, the less conductive tissues exterior to the CSF offer larger penetration depth than the inner tissues. The maximum electric

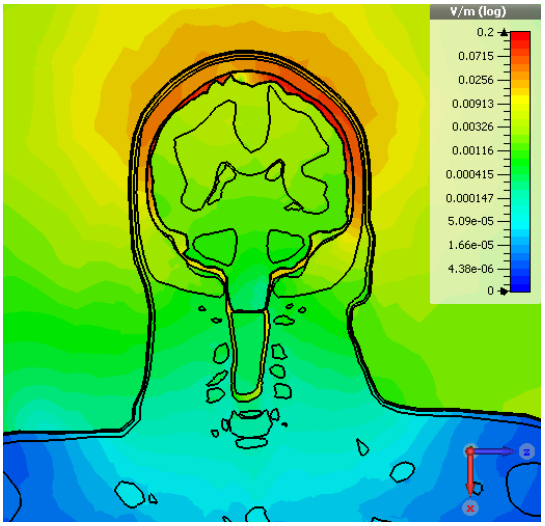

Fig. 4.13 Simulated Electric field distribution for a gc-IBC cortical read-out implant

field for this case is 0.15 V m^{-1} which is negligible compared to the maximum restriction by ICNIRP of 38.9 V m^{-1} for the given setting. With a reference of 1 W transmit power, the maximum value of SAR averaged over 10 g of head tissue is 2.04 W kg^{-1}. Hence, when normalised to the -20 dBm transmit power, this SAR value is also negligibly small compared to the maximum set by ICNIRP of 2 W kg^{-1}. This suggests that our proposed gc-IBC is a safe communication link for cortical implants since it meets the ICNIRP requirements.

4.6 Conclusion

In this chapter we have analysed and compared three technologies for cortical implant communication - the inductive link for data (ic-DT) and power transfer, the gc-IBC and RF antenna based implant communication schemes. From our results, it can be concluded that the inductive coupling is reliable for short range power transfer which suits cortical implants as implantation depths of 2-3 cm. However, despite its popular use, our simulation shows that inductive coupling

is less suitable for applications such as bionic vision that may require about 500 kbps to 1 Mbps when implemented with 200 to 400 electrodes for high resolution vision restoration. We proposed and showed that the gc-IBC offers more wideband channel with less path loss than the ic-DT and RF antenna coupled schemes. We also proposed gc-IBC to be combined with the existing inductively powered implants without introducing a major change in size and design. We have also evaluated the ICNIRP compliance of a gc-IBC cortical implant communication scheme and demonstrated electromagnetic safety.

Chapter 5

Design and Implementation of Integrated Sensor Intrabody Implant Transceiver

This chapter presents the design and implementation of an integrated sensor transmitter and receiver for galvanically coupled intra-body communication (gc-IBC) implant setting. The presented transmitter and receiver were designed with two main objectives. To integrate existing capacitive sensors in a simplified way to minimise component count and hence power consumption, and as a useful test bench to assess the noise characteristics of the channel. A common variable capacitance range of 0-50 pF (as used in most glucose sensors) was considered as a transmit message. A direct sequence spread spectrum (DSSS) with a binary phase shift keying (BPSK) scheme was used to provide noise robustness and multiuser capability. The digital end of the transmitter was implemented in Cypress's programable system on chip (PSoC) and the receiver digital end was implemented in Xilinx Spartan 6 field programmable gate array (FPGA). The

prototype transceiver presented here was designed as a low cost and modularised such that various coding and modulation schemes can be tested.

5.1 Introduction

Continuous monitoring of vital signs using implanted medical devices (IMDs) enables timely medical intervention. This is crucial especially for patients with highly prevalent chronic diseases such as diabetes. Periodic monitoring of blood glucose level (BGL) using external devices puts patients in discomfort. This is due to the fact that they have to first of all remember their scheduled blood glucose level tests and interrupt their daily routines to conduct procedures that require sampling their blood and conducting tests using their BGL monitoring kits. Thus, BGL monitoring is limited to a few number of times per day. However, glucose level is best monitored continuously with an implanted sensor than an intermittent external blood glucose level (BGL) monitor [147]. There are several sensors in use for external BGL detection that are often capacitive sensors with typical values ranging from 0-50 pF [148]. Thus, this applications and many other capacitive sensing applications existing sensors can be integrated into transmitters in a manner that minimises component and power consumption.

Several implant transceivers have been designed in previous works. For example, a generic antenna based radio frequency (RF) implant transceiver in the medical implant communication services (MICS) band was designed by Bradley [45]. This transceiver has a raw data rate of up to 800 kbps and is used in commercial applications. In [14] an ultrasonic read-out transmitter was designed using on-off keying (OOK) and amplitude shift keying (ASK) modulation schemes. Transceivers with high data rate of up to 50 Mbps technique that use optical communication have been presented in [17]. This transceiver employs a near infrared signal of wavelength 860 nm with 4 mW power consumption to cover

a transdermal transmission length of 4 mm. However, the human body incurs a high path loss at such high frequencies. Besides most vital sign monitoring such as BGMs, oximeters and artificial prosthetics such as cochlear implants require a data rate of less than a few hundred kbps. Thus, a low frequency transmission scheme offering low path loss is a good alternative for power efficient transmission.

To this end, intrabody communication based on electric field communication such as galvanically and capacitively coupled transmissions have been investigated to offer low path loss profiles for body confined communications. Following Zimmerman's[58] and Handa's [105] work in 1995 and 1997 respectively, several capacitively and galvanically intrabody transceivers have been designed with various modulation schemes and spectrum use. However, most of these transceivers are designed and characterised for on-body communications. As clearly shown from the models in our previous work [13], galvanically coupled IBC provides a comparatively low path loss than antenna based radio transmissions in the MICS band in 402–405 MHz. This suggests they may be more useful in the implant setting.

In this chapter we present a design and implementation of transceiver that employs galvanically coupled intrabody communication (gc-IBC) with the integrated sensor. The objective of this work was to provide a prototype to demonstrate the use of this scheme for implanted sensor readout transmission for the first time and also to characterise the noise in the channel. The rest of the chapter is organised as follows; Section 5.2 presents the design and implementation of the transmitter system. In this section the sensing unit, modulation techniques used and implementation of the digital end are discussed. Section 5.4 presents the receiver analog end design and implementation. Section 5.5 presents implementation of the receiver digital end. Our conclusion is given in Section 5.6.

5.2 Transmitter System Design

The proposed transmitter design uses capacitance changes to encode signals which are then transmitted via galvanically coupled IBC (gc-IBC) transmission. In addition to providing minimised transmitter complexity, the proposed transmitter is also a prototype to assess the gc-IBC implant communication channel noise for the first time. The input signal for the transmitter is the capacitance denoted by C_{sensor} of the sensor varying from 0 – 50 pF [148].

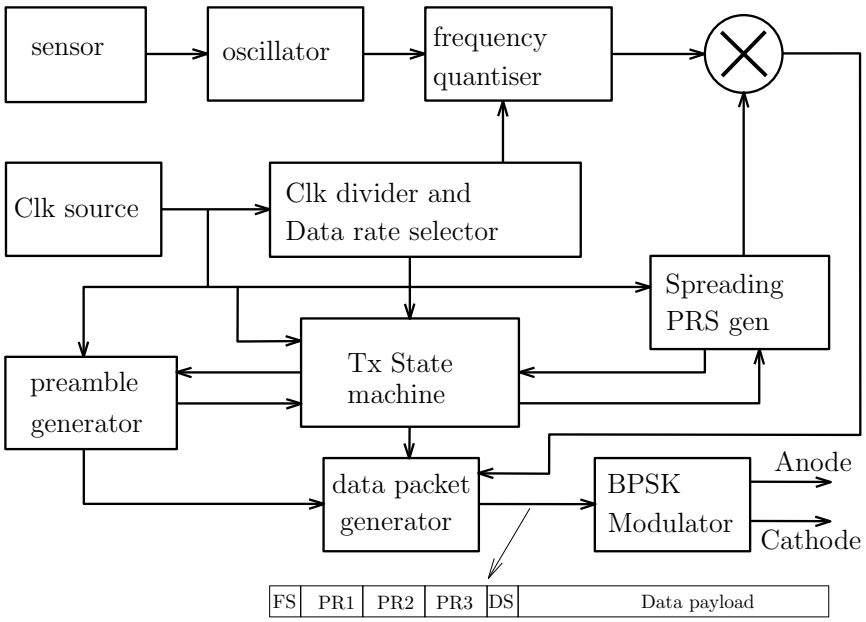

Fig. 5.1 Proposed gc-IBC transmitter block diagram. Here Clk denotes the clock signal, PRS denotes the pseudo random sequence and BPSK denotes the binary phase shift keying modulation scheme.

For noise robustness and multiuser capability a Direct Sequence Spread Spectrum (DSSS) scheme was employed. A chip rate of $f_c = 4$ MHz was used. The block diagram of the transmitter is given in Fig. 5.1. A voltage controlled oscillator (VCO) was formed by integrating the sensor capacitor into a ring oscillator. The frequency of the resulting signal was frequency quantised according to the selected bit rate and processing gain (number of chips per bit) by the clock divider and rate selector block. The spreading pseudo

random sequence (PRS) generator produces the sequence needed to spread the data. The preamble generator generates three copies of the preamble to embed user specific codes for multiuser communication and to aid the clock and data recovery block of the receiver for synchronisation. The transmitter state machine coordinates the different states of the transmitter such as start of the preamble, each generation of preamble, start of the data and the data itself and performs setting and resetting operations to ensure proper packet contents are generated for transmission through the anode and cathode electrodes. The packet structure is shown in Fig. 5.2. A frame start marker (FS) bit and following three copies of 32 bit preamble sequences (PR1, PR2 and PR3) were used to embed device identity and aiding the re-synchronisation of data. After the preambles, there is a data start marker (DS) bit followed by a payload of 1024 data bits.

FS	PR1	PR2	PR3	DS	Data payload

Fig. 5.2 transmitted packet structure. Here FS denotes the frame start followed by the consecutive preamble sequences denoted by PR1, PR2 and PR3. The data start sequence is denoted by DS followed by the transmitted payload.

5.2.1 The Sensing Unit

The capacitive sensor was integrated in the oscillator as shown in Fig. 5.3 to generate V_{sensor} with variable frequency proportional to C_{sensor}. The output of

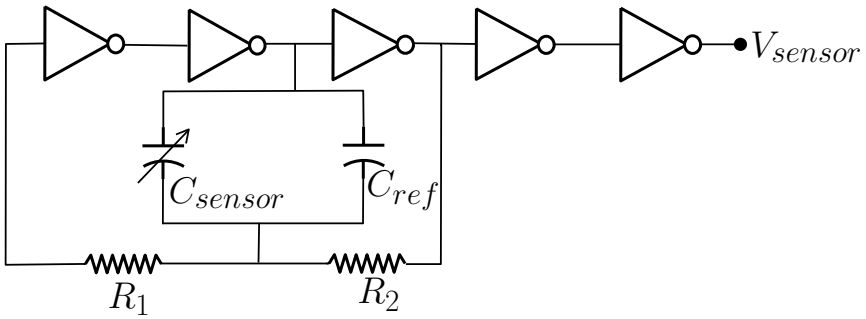

Fig. 5.3 Integrated sensor oscillator

the oscillator is a rectangular wave of instantaneous frequency given by

$$f_s = \frac{1}{2R_1(C_{ref} + C_{sensor})\left(\frac{\alpha R_2}{R_1+R_2} + \beta\right)} \tag{5.1}$$

where $\alpha = 0.715$ and $\beta = 1.224$ are constants associated with the propagation delay of the inverters. The oscillator is designed with $R_1 = 51\ k\Omega$, $R_2 = 51\ k\Omega$ and $C_{ref} = 100$ pF to produce frequency range from 40 kHz – 60 kHz for corresponding capacitance variance of 0–50pF.

The digital base band signal was generated by quantising the frequency of the signal to the nearest integral multiple of $1/T_b$ where T_b is the bit desired period as shown in Fig. 5.4. The quantisation error is captured by a random variable $\Delta\tau = \{\Delta\tau_1, \Delta\tau_2, ..., \Delta\tau_n\}$ which is uniformly distributed in the set $[-\frac{T_b}{2}, \frac{T_b}{2}]$. The mean value $< \Delta\tau > = 0$ suggests that the quantisation process does not affect the average frequency of the sensor which is often the case for intermittent sensory systems such as glucose sensors. Here, sensing is done periodically; for example, once every minute or every hour. However, if we consider instantaneous reading, the worst case scenario is when the error $\Delta\tau = T_b/2$. Denoting the instantaneous period of the signal by $T_s = 1/f_s$, the accuracy of the quantised frequency η is given by

$$\eta = \frac{T_s - 0.5T_b}{T_s} 100\%. \tag{5.2}$$

Now, the chip period $T_c = 1/f_c = 0.25\ \mu$s and let N denote the number of chips per bit such that $T_b = NT_c$. The processing gain N and the measurement accuracy are related by

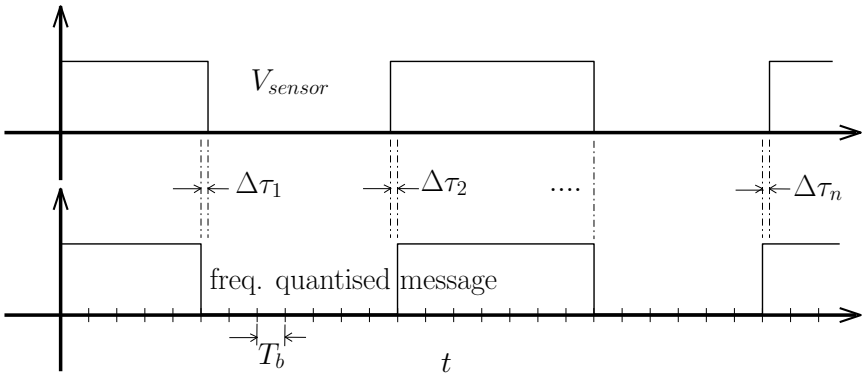

Fig. 5.4 Frequency quantisation of the digital baseband sensor signal. The high and low signals are quantised to the nearest bit width T_b and the corresponding quantisation errors at each transition are denoted by $\Delta\tau_i$.

$$\eta = \frac{T_s - 0.5NT_c}{T_s}100\%. \tag{5.3}$$

The error in frequency Δf is thus given by

$$\Delta f = \frac{f_s^2 NT_c}{2 + f_s NT_c}. \tag{5.4}$$

The quantity actually transmitted is the capacitance value. Thus, the accuracy of the measurement is given by

$$\eta_c = (1 - \frac{\Delta C}{C_{sensor}})100\%. \tag{5.5}$$

$$= \Big[1 - \frac{\Delta f}{(\Delta f + f_s)(1 + 3.1624 f_s R_1 C_{ref})}\Big]100\%. \tag{5.6}$$

The trade-off for increased processing gain was attained as a result of reduced worst case scenario measurement accuracy, i.e., for N = 1,2,4 and 8, the measurement accuracies are 99.61%, 99.22%, 98.45% and 96.7% respectively.

5.2.2 Modulation

The implementation of the transmitter and receiver were modularised such that various types of modulation and coding schemes could be used. In the current implementation, the modulation techniques used were the binary phase shift keying (BPSK) over a direct sequence spread spectrum (DSSS) signal. Although, error control coding schemes could be inserted to improve error performance, we used the un-coded BPSK signal transmission over DSSS to evaluate the raw performance of the system.

Direct Sequence Spread Spectrum (DSSS) : is a spread spectrum technique that is used to spread the bandwidth of a narrow band signal so that the signal power is distributed over a wide band and has a strong immunity against interference and noise. In DSSS, the spreading is achieved by multiplying a PRS and the digital baseband signal as shown in Fig. 5.5. The PRS sequence was then generated. Detailed implementation of the PRS sequence is given in Section 5.2.5.

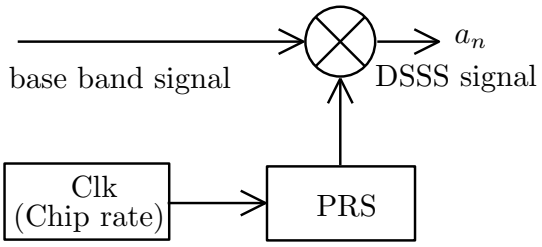

Fig. 5.5 Direct sequence spread spectrum modulation

Binary phase shift keying (BPSK): is a modulation scheme with two phases to represent binary '1' and binary '0'. To minimise detection error over a noisy channel, the digit representing phases used are separated by 180^o. Hence, applying the Gram-Schmidt orthogonalisation procedure, the transmit signal constellation was formed by orthogonal basis functions $\phi_1(t)$ and $\phi_2(t)$. Signals $s_1(t) = \phi_1(t) - \phi_2(t)$ and $s_2(t) = -\phi_1(t) + \phi_2(t)$ are then used to represent '0'

and '1' respectively. These signals are shown in the signal constellation diagram shown in Fig. 5.6.

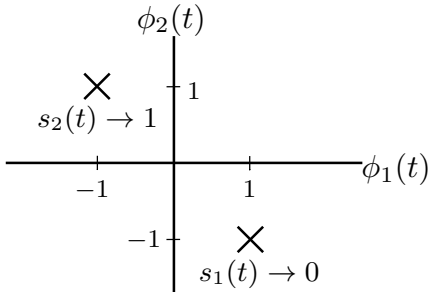

Fig. 5.6 BPSK orthogonal signal constellation.

The more generalised form of the orthogonal basis functions are $\phi_1(t) = \sqrt{\frac{2}{T}}\cos(\frac{2\pi t}{T} + \frac{\pi}{4})$ and $\phi_2(t) = \sqrt{\frac{2}{T}}\cos(\frac{2\pi t}{T} - \frac{\pi}{4})$ where T is the period of the carrier signal. The BPSK encoding signals are then $s_1(t) = -\frac{2}{\sqrt{T}}\sin(\frac{2\pi t}{T})$ and $s_2(t) = \frac{2}{\sqrt{T}}\sin(\frac{2\pi t}{T})$. In general, a pass band BPSK signal is generated at a frequency much larger than the baseband signal is used as shown in Fig. 5.7. However this technique requires a use of local oscillators at the transmitter that are in sync with the receiver side local oscillators. Thus, in addition to the clock data recovery, the receiver is also required to have a carrier synchronisation capability.

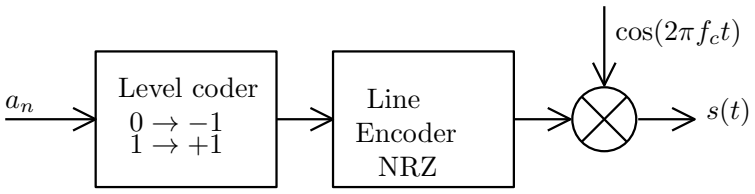

Fig. 5.7 Block diagram for a generalised BPSK modulation.

Thus, we looked for a different technique that can perform the BPSK signalling at the chip rate for the DSSS modulation. Here, a special case of BPSK signalling that makes use of Manchester coding can be used with a relatively easy implementation. In this case, the orthogonal basis functions are given by

$$\phi_1(t) = \begin{cases} \sqrt{\frac{2}{T}} & , \ t \in [0, \frac{T}{2}). \\ 0 & , \ t \in [\frac{T}{2}, T). \end{cases} \tag{5.7}$$

and

$$\phi_2(t) = \begin{cases} 0 & , \ t \in [0, \frac{T}{2}). \\ \sqrt{\frac{2}{T}} & , \ t \in [\frac{T}{2}, T). \end{cases} \tag{5.8}$$

The BPSK signals $s_1(t)$ and $s_2(t)$ are generated as

$$s_1(t) = \phi_1(t) - \phi_2(t). \tag{5.9}$$

$$= \begin{cases} \sqrt{\frac{2}{T}} & , \ t \in [0, \frac{T}{2}). \\ -\sqrt{\frac{2}{T}} & , \ t \in [\frac{T}{2}, T). \end{cases} \tag{5.10}$$

and

$$s_2(t) = -\phi_1(t) + \phi_2(t). \tag{5.11}$$

$$= \begin{cases} -\sqrt{\frac{2}{T}} & , \ t \in [0, \frac{T}{2}). \\ \sqrt{\frac{2}{T}} & , \ t \in [\frac{T}{2}, T). \end{cases} \tag{5.12}$$

The BPSK signalling in Fig. 5.7 is modified and is implemented as shown in Fig. 5.8

In this implementation, the pass band signal was generated by the DSSS modulation and the BPSK was applied on top of the DSSS using it as a

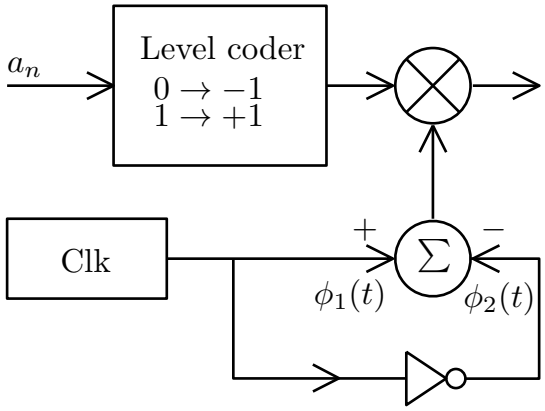

Fig. 5.8 Manchester code based BPSK modulation used.

baseband signal. Thus, to minimise complexity, Manchester line code was used to implement BPSK signalling.

5.2.3 Implementation of transmitter Digital End

The digital end of the transmitter was implemented in Cypress's Programable System on Chip (PSoC), specifically on a PSoC 3 CY8C3245PVI-150. In this section we present resources provided by the PSoC chip and detailed implementation of the digital end of the transmitter.

Overview of PSoC resources for Transmitter Implementation

PSoC chips consist of reconfigurable analog and digital units suitable for power efficient, cost effective and flexible rapid prototyping. The analog blocks include components such as operational amplifiers, trans-impedance amplifier, comparators, ADCs and DACs. The digital part contains 16-24 universal digital blocks (UDB) that are mainly composed of programmable logic devices (PLDs), datapaths (DP) and control logics for clock, reset and status. The UDBs are ca-

pable of realising functionalities such as cyclic redundancy check (CRC), Pseudo random sequence generators, quadrature decoders and gate-level logic functions. UDBs and their contents can be combined using the digital system interconnect (DSI) bus.

We chose the programmable system on chip PSoC for implementation because it offers cost effective and rapid prototyping capabilities. It consists of blocks beyond just a microcontroller. These chips are designed to integrate high performance reconfigurable analog primitives and digital sub systems beyond just a microcontroller. The digital sub system is divided into an array of UDBs that can implement complex programable logic devices. Each UDB consists of two programable logic devices (PLDs), a datapath (DP) and control logics for clock, reset and status. There are a total of 20 UDBs in PSoC3 and these can be interconnected or chained to implement complicated digital systems.

Programable Logic Device (PLD): each programable logic device is an aggregate of AND, OR and NOT gates and Flip-Flops (FF) arranged to have twelve arrays of inputs that feed across eight product terms (PTs) as shown in Fig. 5.9. The product terms 'TC' reference the input term true 'T' logic and its complement 'C' (NOT gated) respectively. The product terms are vertically ANDed into four arrays of horizontally OR gated logic. There are a total of 96 PTs and four 4 arrays of eight input OR gates that can realise various combination of sum-of-products type combinatorial logic of twelve inputs. The outputs of the OR gates are the results stored in macrocelles referenced by MCx. Macrocells consists mainly of flip-flops.

PLDs are the primary structures used in PSoC chips to implement complex PLDs (CPLDs). Implementation of PLDs or transfer of PLDs from another CPLD system such as FPGAs is carried out by using the VeriLog hardware description codes using the PSoC Creator development IDE dedicated for product

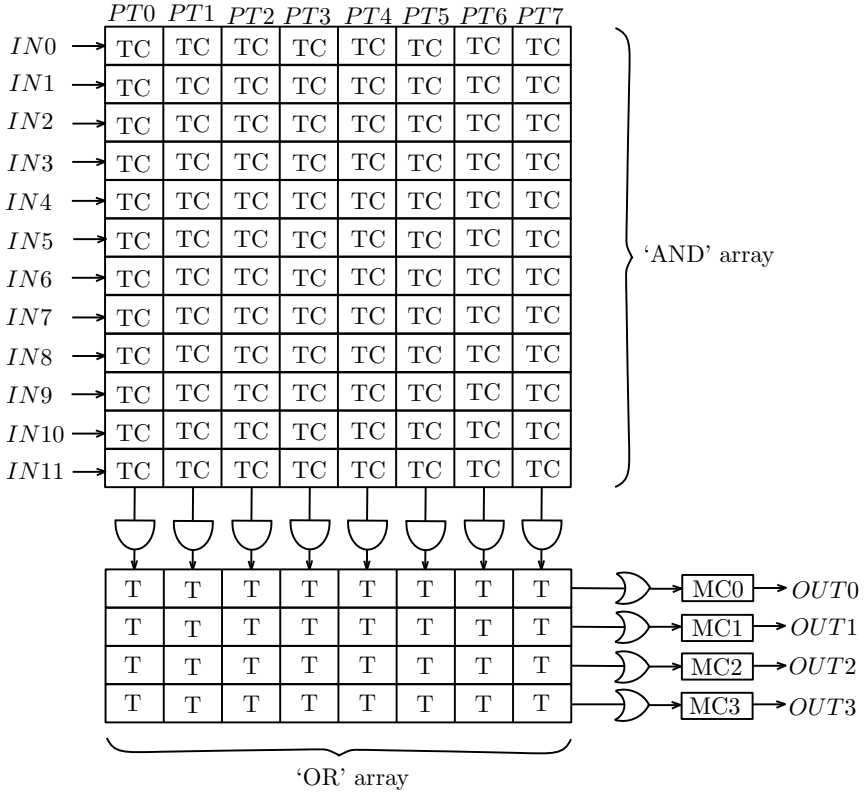

Fig. 5.9 PLD structure. There are a total of 12 inputs connected via arrays of AND gates. The inputs feed 8 product terms. The product terms are collected using the 4 arrays of OR gates. results are stored in macrocells (MCs) that contain flip-flops and other combinational logics.

PSoC based development by Cypress Company. The PSoC3 we used contains a total of 40 PLDs in its 20 UDBs that can be daisy-chained. Thus, PLD alone can handle a total of 240 inputs, 160 Macrocells and 320 PT arrays that can be used independently or interconnected via the digital system interconnect (DSI)to realise complex combinatorial logic. The PLD is used to realise the transmitter state machine and combinatorial logic to derive the preamble and PRS generators. Although PSoC3 chip provides many PLD cells, it can realise far fewer logic compared to field programable gate array (FPGA). However, PSoC3 has datapaths with dedicated arithmetic logic unit (ALU) that can implement complex functions such as adding, subtracting and shifting for efficient use of components. Therefore we use the Datapath (DP) in combination with PLDs for

implementing the entire digital end of the transmitter. Unlike the receiver, the transmitter has low complexity and can be realised entirely out of the PSoC chip with proper combination of DPs and PLDs. In fact, since the FPGA consumes comparatively large power; this makes PSoC a better candidate for low power consumption and rapid prototyping realisation of the transmitter.

Datapath (DP): The center piece of the PSoC datapath is an 8 bit ALU that is capable of primitive operations such as OR, AND, XOR, increment, decrement and shift. The datapath also has segments that can generate conditions such as compare, zero detect and one detect, Using combination of these operations we can realise a number of complex peripherals such as counters, PRS generators and preamble generators that would consume a lot of resources if PLDs were to be used. In fact, using the PLDs alone, it is difficult to realise our entire transmitter in a single PSoC chip. As shown in Fig. 5.10, the DP is equipped with two 32 bit first in first out (FIFO) registers F0 and F1 to pass inputs and outputs to and from the datapath. At each instruction cycle, a byte of data in F0 and F1 can be fetched by the two data registers (D0 and D1) simultaneously or directly by the accumulators (A0 and A1).

State machine and packet generation

The transmitter state machine is the component of the transmitter designed to coordinate the preamble generator, the PRS generator and their driver circuits to ensure the generation of desired packet structure. It accepts the terminal counts of the preamble generators and the PRS generator as inputs and enables the driving circuits of the current state. We implemented the state machine using the Verilog hardware description language shown in the code listing *Listing Appendix* C.1. The PSoC creator was used to build and synthesise it using PLDs.

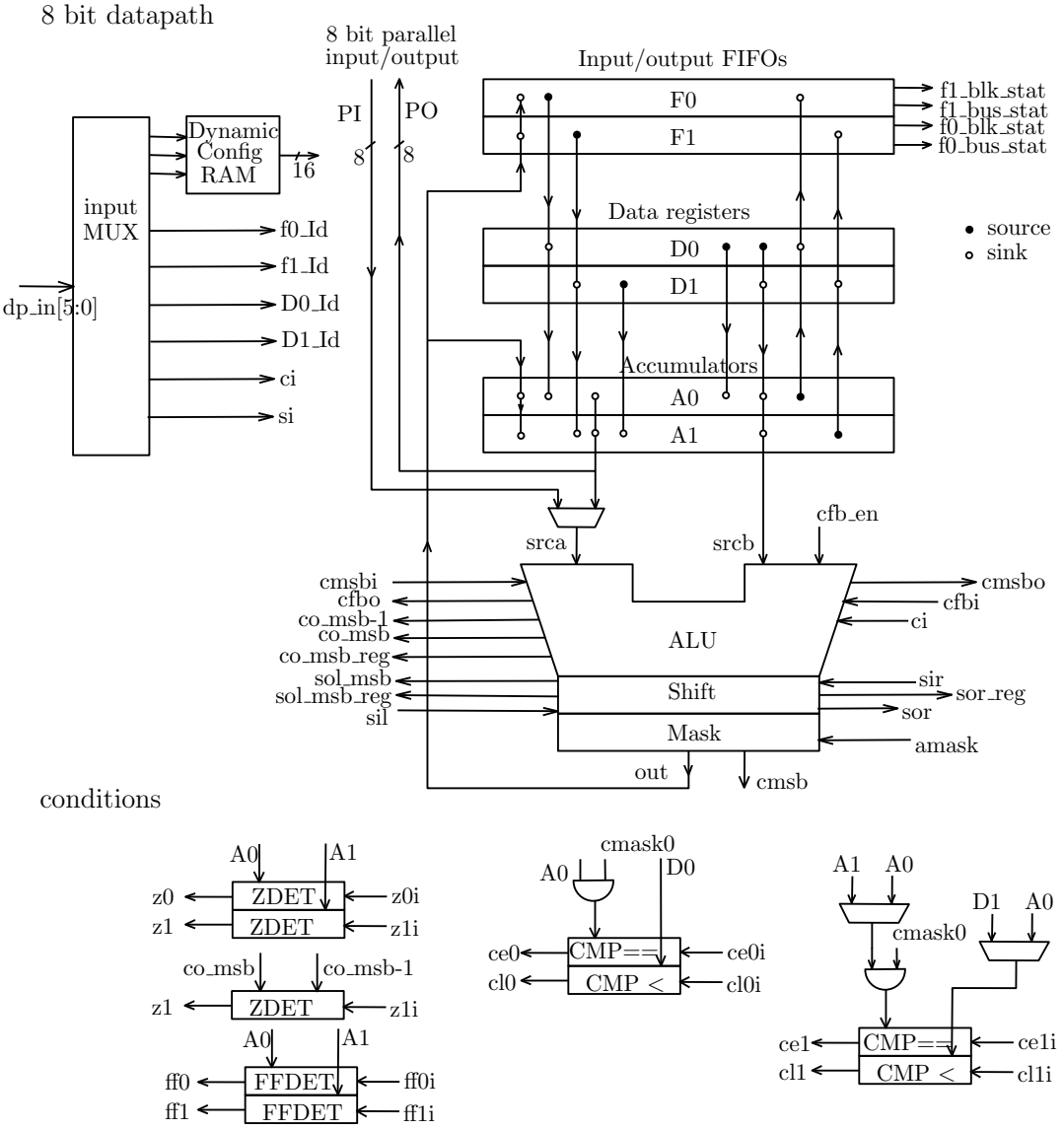

Fig. 5.10 PLD structure. There are a total of 12 inputs connected via arrays of AND gates. The inputs feed 8 product terms. The product terms are collected using the 4 arrays of OR gates. results are stored in macrocells (MCs) that contain flip-flops and other combinational logics.

5.2.4 Digital Clocks and Data Rate Selection

Clock Resources: the internal main oscillator (IMO) is the main resource for the clock. It can generate discrete clocks at 3,6,12,24,48 and 62 MHz. Other clock signals than those generated by the IMO can be generated using the phase locked

loop (PLL) of the PSoC3. The phase locked loop can generate desired clock frequencies from any of the IMO or external clocks up to a multiplication faction $\frac{N}{D}$ where N and D are integers such that $N \in \{4, 5, .., 256\}$ and $D \in \{1, 2, .., 16\}$. For each clock resource, this gives rise to options from a quarter up to 256 times the clock frequency. Clock resources other than the IMO include the MHz-range external crystal oscillator, 32.768-kHz external crystal oscillator and internal low speed oscillator (ILO).

We required two synchronised clocks for the implementation of the transmitter. The master clock is the 4 MHz clock generated from the IMO using the PLL. This clock is associated with the chip rate. The second is the clock that sets the data rate. This is decided by the data rate selector. For example in the case of a 4 bits per chip, the sensor message was frequency quantised using a 1 MHz clock.

5.2.5 Preamble and PRS generation

The preamble and PRS sequences were generated using polynomials and linear shift operations to optimise resources. We used three preambles of length 31 bits denoted PR1, PR2 and PR3. We used a degree 5 primitive polynomial $x^5 + x^4 + x^3 + x^2 + 1$ to span preamble bits PR1 using a seed value of "111111". Sequence PR2 is generated by inverting PR1 and PR3 is same as PR1; this combination maximises use of a single polynomial to generate three preambles. Thus a total of 94 bits including the preamble start bit were generated.

For the pseudo random sequence, we designed a gold code generator using two degree 8 primitive polynomials $x^8 + x^6 + x^5 + x^4 + 1$ and $x^8 + x^4 + x^3 + x^2 + 1$ implemented as shown in Fig. 5.11 both using a seed value of "00000001" to span a PRS sequence of period 255. The PRS sequence generated has a good autocorrelation property as shown in Fig. 5.13

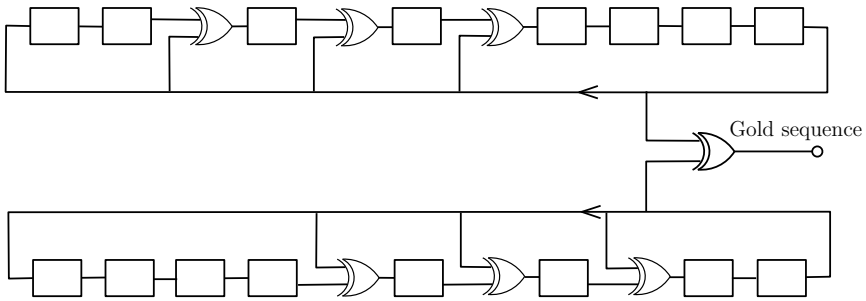

Fig. 5.11 Galois LFSR implementation of the PRS generator

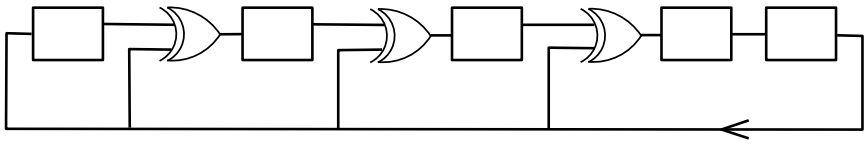

Fig. 5.12 Galois LFSR implementation of the preamble generator

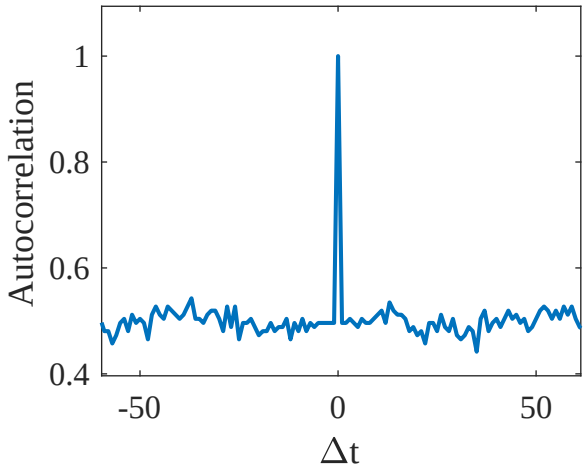

Fig. 5.13 Autocorrelation property of the PRS generated

Both the preamble and the PRS sequences were generated using datapaths of the PSoC3. As shown in Fig. 5.14, the polynomials coefficients were stored into the data registers (D0) and the seed values were stored in the accumulator (A0) register. since the maximum degree chosen is 8, single datapaths were used to generate the sequences and no chaining of UDBs is required; as such the implementation of the the preamble was done in a component efficient manner. For generation of the PRS sequence, the shift input (SI) shown in Fig. 5.14 was tied to a zero logic so that the feedback (FB) signal is fed back to the LSB side

of the accumulator register. In fact these were set using the configuration RAM (CFGRAM) that can handle a maximum of eight instructions. For the preamble sequence with only five degrees, the LSB can be specified that the feedback is tapped from the fifth bit of the accumulator. Other settings such as chaining can also be set using the datapath configuration tool.

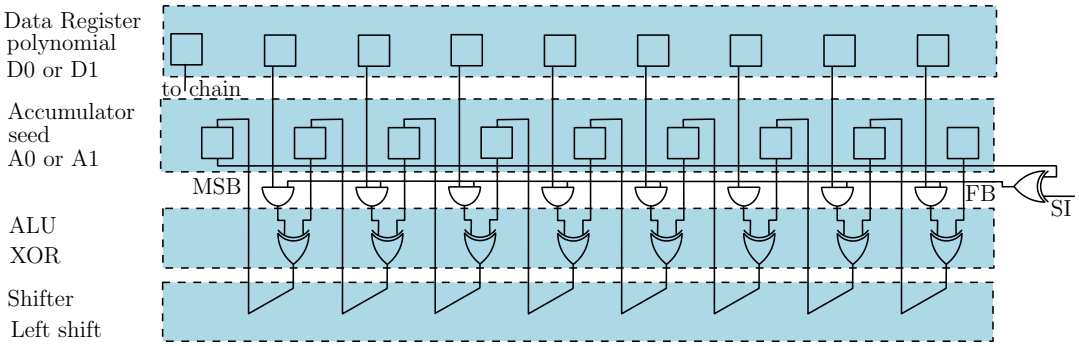

Fig. 5.14 Usage of the datapath structure to implement PRS generation. Polynomial coefficients are loaded into the data register (D0 or D1) and the seed value isloaded into the accumulator (A0 or A1). The ALU is set to perform the XOR function each cycle.

5.2.6 The Complete Transmitter Unit

The complete analog and digital circuitry of the transmitter implementation is shown in Fig. 5.15.

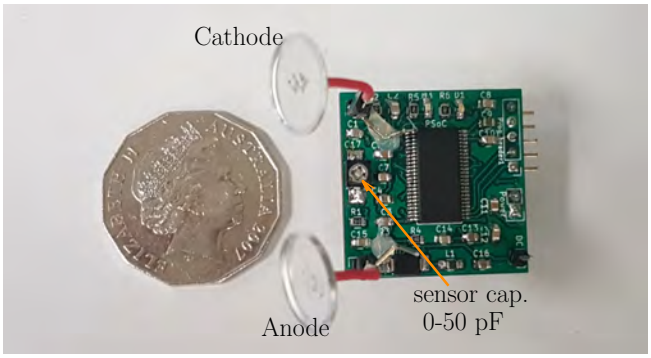

Fig. 5.15 Transmitter circuit - comparison of size.

The block diagram shown in Fig. 5.1 is implemented as shown in Fig. 5.16. We implemented the PSoC transmitter to be supplied by a DC voltage of 0.5–3.7 V. A power supply of 3.3 V battery was used. At the output of the transmitter, the impedance between the electrodes was measured to be 600 Ω. With an average differential voltage of 0.75 V across electrodes, the average transmitted power was 0.936 mW coupling a current of 1.3 mA (less than the 10 mA maximum current limit set by ICNIRP guideline [70]). The PSoC chip offers a rapid prototyping and most of its unused blocks need to be turned off for lower power consumption. This is a good indication that an application specific IC (ASIC) for the transmitter would consume a low power. The advantage of using PSoC for the transmitter is that in addition to quick application specific prototyping, the digital end of the transmitter can be reprogrammed to test different coding and modulation schemes. Besides, PSoC 3 handles signals up to 67 MHz which is sufficiently large for galvanically and capacitively coupled IBC signals.

The output of the binary phase shift keying (BPSK) modulator was processed such that the output signal and its inverted copy are sent to the anode and the cathode electrodes for differential galvanic coupling of the signal into the human body. This way, the differential output coupled to the channel will have maximal differential signal while suppressing the common mode noise.

The noise introduced by the gc-IBC channel was assumed to be additive white gaussian noise (AWGN). In the case that the noise is sightly coloured, the despreading at the receiver whitens the channel noise. Hence the analysis and channel simulation we used is that of a DSSS signal under AWGN channel.

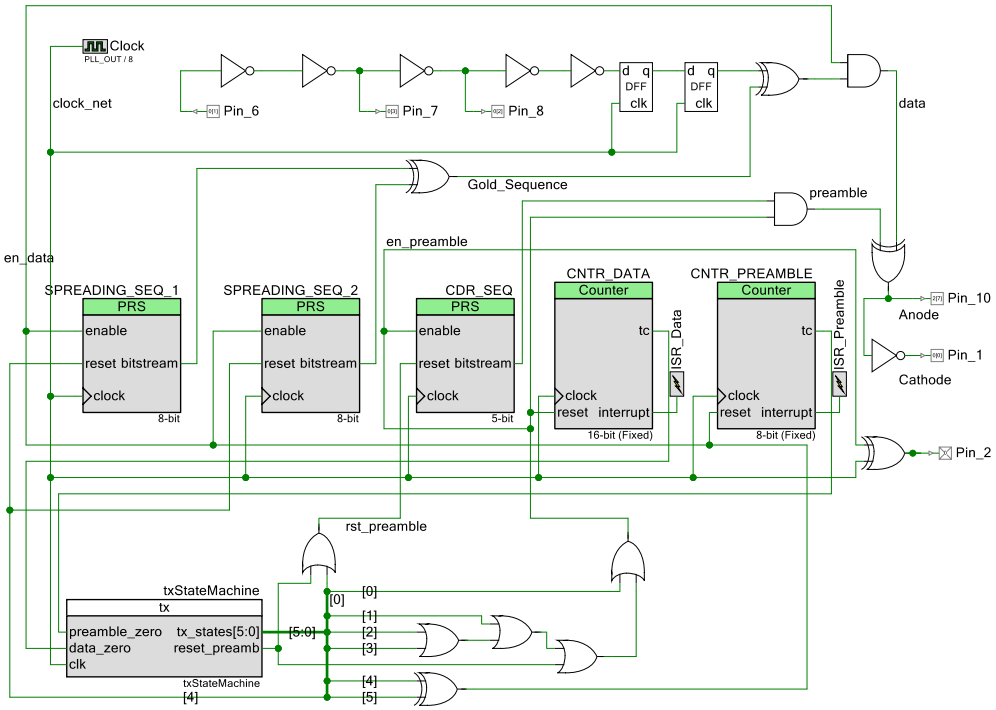

Fig. 5.16 Transmitter digital end PSoC implementation

5.3 Receiver Design and Implementation

The receiver was designed to differentially detect signals received from the anode and cathode electrodes. The overall block diagram of the receiver is shown in Fig. 5.17. The noise added in the channel was limited using band limiting filters and then differentially amplified by the instrumentation amplifier designed with a worst case scenario common mode rejection ratio (CMRR) of 78 dB. The analog front end circuit is shown in Fig. 5.18 This is one of the advantages of a galvanically coupled reception where the common mode noise is removed in the first stages of reception and the remaining noise the differential noise the signal faces as it propagates within the human body. Common mode noise is mainly due to environmental noises and interferences external to the channel.

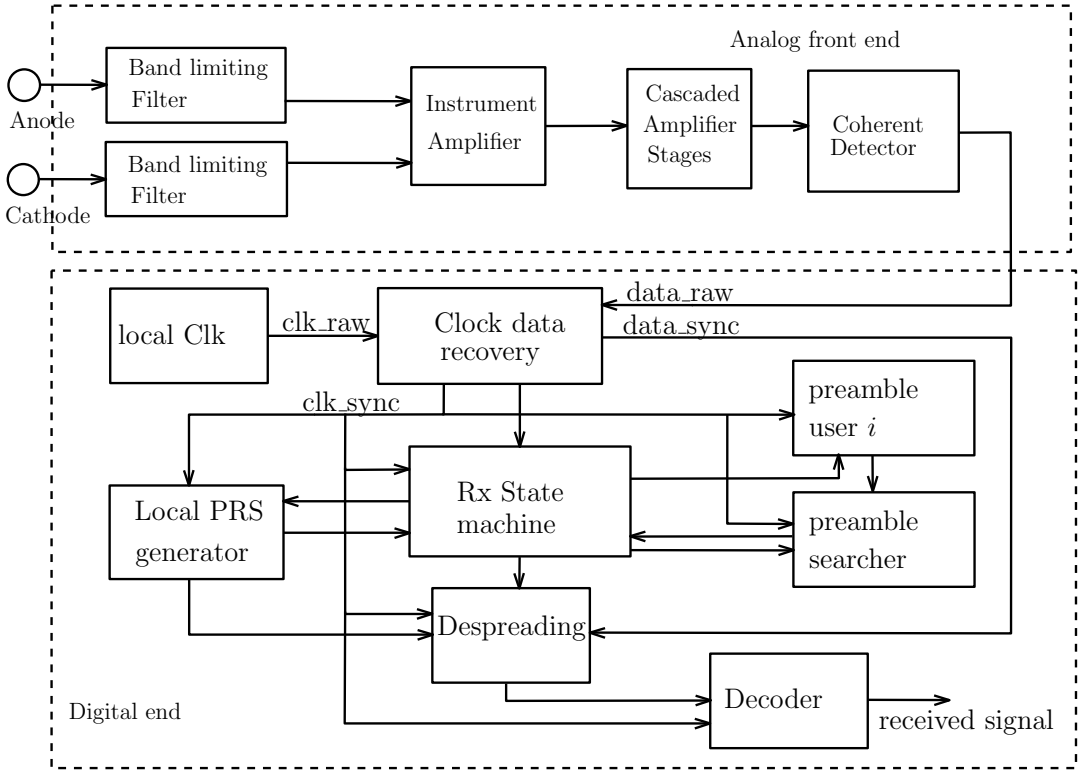

Fig. 5.17 Receiver analog front end block diagram.

The digital end of the receiver was fully implemented on a Xilinx Spartan 6 LX9 field-programable gate array (FPGA). The blocks shown in Fig. 5.17 include clock data recovery (CDR), local PRS and preamble generators, preamble tracker, receiver state machine and detector. Here with the DSSS receiver the detected signal at the chip rate was spread by the PRS signal generated locally to despread the original signal. Thus, the power spectral density of the band limited noise is spread by the despreading operation at the receiver.

5.4 Receiver Analog End

As shown in chapters 3 and 4, the gc-IBC channel incurs a path loss of 40-45 dB for implant-to-surface transmission distance of 7-10 cm [13]. Hence, the received signal has a power ranging from -74.1 to -79.1 dBW for a transmit power of -34.1

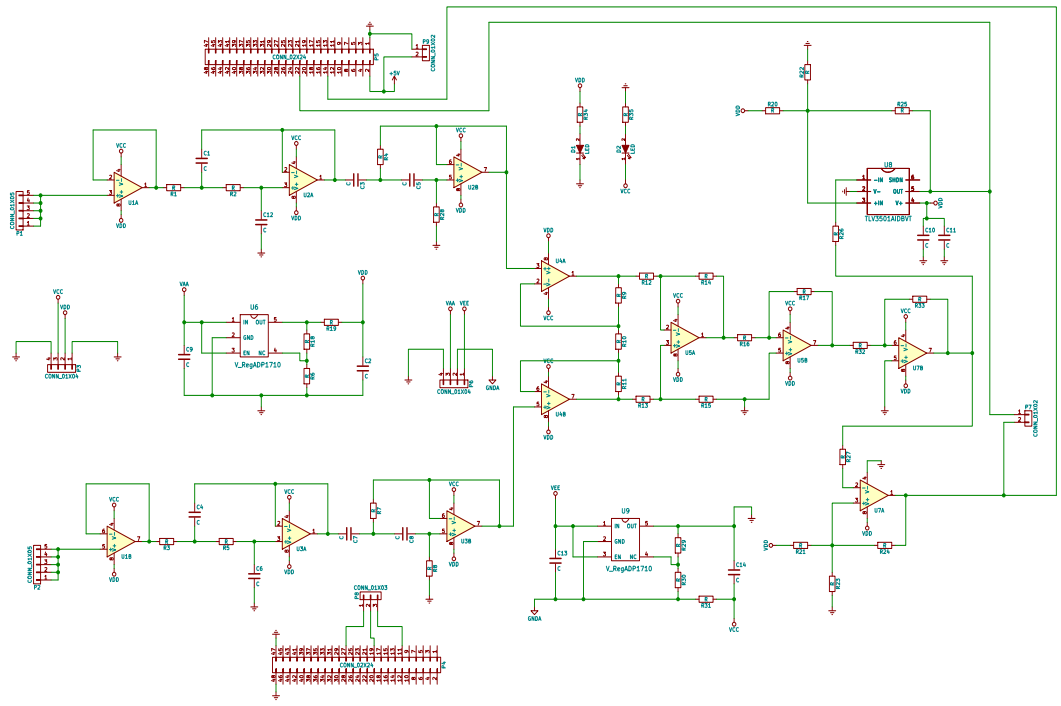

Fig. 5.18 Receiver analog end circuit diagram.

dBW. The instrument amplifier combined with the cascaded amplifier stages were designed to provide a differential gain of 48 dB (slightly higher gain than required to compensate the largest attenuation). The received signal then was passed through coherent BPSK detector to reconstruct the transmitted digital signal.

5.4.1 Band Limiting Filters

The first stage of the receiver analog front end is a bandpass filter designed to band limit the additive channel noise the receiver picks up. This filter is a bandpass filter designed to fit in the null-to-null spectrum of the main lobe. Extending the bandwidth to include secondary lobes would increase the information content by including higher harmonics. However, this would also

increase the noise bandwidth of the noise added by the channel. As shown in Fig. 6.5, the null-to-null bandwidth of the main lobe is twice the chip rate (i.e., 8 MHz). Thus, we designed the bandpass filter to have a bandwidth of 8 MHz.

The filter was desired to be low noise and linear which means it needs to have a maximally flat response in the pass band to avoid ripples that would insert non-linearity to the system in the pass band. The Butterworth filter provides such a flat pass band. For flexible implementation of the high pass and low pass slopes, we implemented the filter as a fourth order bandpass filter by cascading second order high pass and low pass butterworth filters with band transition slopes of 40 db/decade and -40 db/decade respectively. This was found to sufficiently fit the main lobe null-to-null band as show later in this section. If higher orders were required the elliptic filters could be used to reduce component count.

Before the band limiting filter a buffer (shown in the first section of Fig. 5.19) was used to separate the electrode contact from the filter input to avoid the contact impedance affecting the cut off frequency of the filter.

Although it does not matter which filter comes first, the low pass section of the filter is first presented (following the buffer) and the high pass section is given next in our implementation as shown in Fig. 5.19.

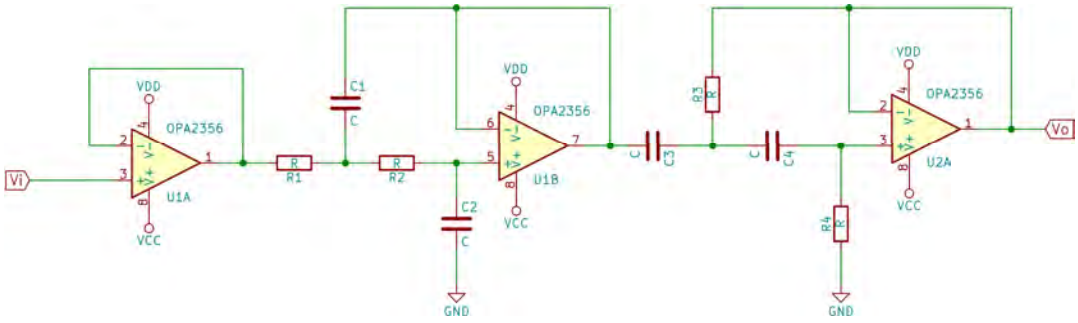

Fig. 5.19 Receiver analog end

In general, the Butterworth filter of order n has a frequency response of the form given by

$$|H(j\omega)| = \frac{1}{\sqrt{1+\varepsilon^2\left(\frac{\omega}{\omega_o}\right)^{2n}}} \tag{5.13}$$

where ω_0 is the cut off frequency and ε is used to determine the maximum pass band gain with respect to the cut off frequency. We set the pass band gain to unity and the cut off frequency at -3dB. This requirement sets $\varepsilon = 1$ as followed in most Butterworth filter designs. We set the cut off at $\omega_L = 2\pi\frac{1}{T_c}$ and the stop band transition to include two side lobes (i.e., the stop band frequency $\omega_S = 2\pi\frac{3}{T_c}$) with a stop band attenuation of -20 dB to determine the order of the filter we require. thus, the stop band attenuation is given by

$$\frac{1}{10} = \frac{1}{\sqrt{1+\left(\frac{\omega_S}{\omega_L}\right)^{2n}}} \tag{5.14}$$

$$\frac{1}{10} = \frac{1}{\sqrt{1+\left(\frac{2\pi\frac{3}{T_c}}{2\pi\frac{1}{T_c}}\right)^{2n}}} \tag{5.15}$$

$$\rightarrow n = 2.09. \tag{5.16}$$

Thus a second order filter was sufficient to provide the required stop band transition. To design for the components, the Sallen-Key implementation of the second order low pass filter was used (the middle section of Fig. 5.19) with the second order transfer function of the form

$$H_{LP}(j\omega) = \frac{\omega_L^2}{-\omega^2 + j2\alpha\omega + \omega_L^2} \tag{5.17}$$

$$= \frac{1}{-C_1C_2R_1R_2\omega^2 + jC_2(R_1+R_2)\omega + 1} \tag{5.18}$$

where

$$\alpha = \frac{1}{2C_1}\Big(\frac{1}{R_1} + \frac{1}{R_1}\Big) \tag{5.19}$$

$$\omega_L = \frac{1}{\sqrt{C_1 C_2 R_1 R_2}} \tag{5.20}$$

Here, the quality factor of the filter is given by $Q_L = \frac{\omega_L}{2\alpha} = \frac{\sqrt{R_1 R_2 C_1 C_2}}{C_2(R_1+R_2)}$.

Similarly the high pass section of the filter with the cut off frequency ω_H is given by second order transfer function given by

$$H_{HP}(j\omega) = \frac{-\omega^2}{-\omega^2 + j2\alpha\omega + \omega_H^2} \tag{5.21}$$

$$= \frac{-\omega^2 C_3 C_4 R_3 R_4}{-C_3 C_4 R_3 R_4 \omega^2 + jR_3(C_3 + C_4)\omega + 1} \tag{5.22}$$

such that

$$\omega_H = \frac{1}{\sqrt{C_3 C_4 R_3 R_4}} \tag{5.23}$$

the quality factor of the filter is given by $Q_H = \frac{\sqrt{R_3 R_4 C_3 C_4}}{R_3(C_3+C_4)}$.

Choosing the quality factors $Q_L = Q_H = 0.5$ to avoid overshot around the filter edges, the following table summarises the component values used in the implementation.

5.4.2 Differential Signal Amplification

The receiver signal was galvanically coupled using the anode and cathode electrodes. After both channel were band limited, they needed to be differentially amplified to remove the common mode noise that had been added by from the surrounding environment. For this we designed an instrumentation amplifier

Item No.	Variable Name	Value	Tolerance
1	R_1	120 Ω	1 %
2	R_2	120 Ω	1 %
3	R_3	1 $k\Omega$	1 %
4	R_4	1 $k\Omega$	1 %
5	C_1	0.1 nF	1 %
6	C_2	0.1 nF	1 %
7	C_3	10 nF	1 %
8	C_4	10 nF	1 %
9	OpAmp	OPA2356	UGBW = 200 MHz SR = 300 V/μs CMRR = 80 dB

Table 5.1 Summary of components designed for limiting filter. Here, UGBW ≅ Unity Gain Bandwidth, SR ≅ Slew rate, CMRR ≅ Common mode rejection ratio.

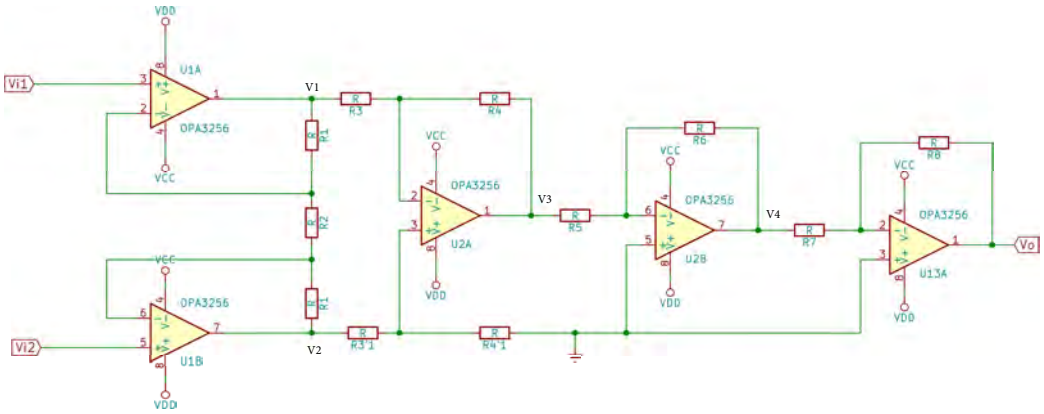

Fig. 5.20 Instrumentation amplifier and cascaded gain stages

with cascaded gain stages shown in Fig. 5.20. The overall differential gain is 48 dB (256 in linear scale). However, this is a large gain to concentrate in just one amplification stage to utilise the gain bandwidth product efficiently. Thus, the gain was divided into four stages of gain 4.

The input signals from the two electrodes are denoted by V_{i1} and V_{i2}. The desired received signal is the differential input

$$V_{di} = V_{i1} - V_{i1}. \tag{5.24}$$

However due the surrounding noise and interference there is also a common mode input

$$V_{cmi} = \frac{V_{i1} + V_{i1}}{2}. \tag{5.25}$$

Analysis of stages is given below.

Stage 1: input stage of amplifier

The outputs of this stage are V_1 and V_2 and are calculated as

$$V_1 = V_{i1} + \frac{R_1}{R_2}\big(V_{i1} - V_{i2}\big) \tag{5.26}$$

$$V_2 = V_{i2} + \frac{R_1}{R_2}\big(V_{i2} - V_{i1}\big) \tag{5.27}$$

Here the common mode and differential outputs of this stage, V_{cm1} and V_{d1} respectively are given by

$$V_{cm1} = \frac{V_1 + V_2}{2} \tag{5.28}$$

$$= \frac{V_{i1} + V_{i2}}{2} = V_{cmi} \tag{5.29}$$

$$V_{d1} = V_1 - V_2 \tag{5.30}$$

$$= \Big(1 + \frac{2R_1}{R_2}\Big)\big(V_{i1} - V_{i2}\big) = \Big(1 + \frac{2R_1}{R_2}\Big)V_{di}. \tag{5.31}$$

Thus, the common mode gain $A_{cm1} = \frac{V_{cm1}}{V_{cmi}} = 1$ and the differential gain A_{d1} are given by

$$A_{cm1} = \frac{V_{cm1}}{V_{cmi}} \tag{5.32}$$

$$= 1 \tag{5.33}$$

$$A_{d1} = \frac{V_{d1}}{V_{di}} \tag{5.34}$$

$$= 1 + \frac{2R_1}{R_2}. \tag{5.35}$$

This stage was designed to have a differential gain of 4 as stated above. Thus R_1 and R_2 are designed to have values $R_2 = 1k\Omega$, $R_1 = 1k\Omega$ to satisfy the differential gain given in (5.35).

The common node rejection ratio (CMRR) of the input stage denoted $CMRR_1$ is given by

$$CMRR_1 = 20\log\left(\frac{A_{d1}}{A_{cm1}}\right) \tag{5.36}$$

$$= 20\log\left[1 + \frac{2R_1}{R_2}\right] \tag{5.37}$$

Stage 2: differential amplifier stage

For this stage, the common mode gain A_{cm2} and the differential gain A_{d2} are given by

$$A_{cm2} = \frac{V_3}{V_{cm1}} \tag{5.38}$$

$$= \Big(\frac{1}{R_3'/R_4' + 1}\Big)\Big(1 - \frac{R_4}{R_3}\frac{R_3'}{R_4'}\Big) \tag{5.39}$$

$$A_{d2} = \frac{V_3}{V_{d1}} \tag{5.40}$$

$$= \Big(\frac{R_4}{2R_3}\Big)\Big(1 + \frac{R_3'/R_4' + 1}{R_3'/R_4' + 1}\Big). \tag{5.41}$$

This stage was also designed to have a differential gain of 4. We used component values $R_3 = R_3' = 2k\Omega$ and $R_4 = R_4' = 8.2k\Omega$ to satisfy the differential gain requirement.

The common node rejection ratio (CMRR) of the differential amplifier stage denoted by $CMRR_2$ is given by

$$CMRR_2 = 20\log\Big(\frac{A_{d2}}{A_{cm2}}\Big) \tag{5.42}$$

$$= 20\log\Bigg[\frac{\Big(\frac{R_4}{2R_3}\Big)\Big(1 + \frac{R_3'/R_4'+1}{R_3'/R_4'+1}\Big)}{\Big(\frac{1}{R_3'/R_4'+1}\Big)\Big(1 - \frac{R_4}{R_3}\frac{R_3'}{R_4'}\Big)}\Bigg] \tag{5.43}$$

The component values that maximise the $CMRR_2$ are such that the ratios $\frac{R_3}{R_4} = \frac{R_3'}{R_4'}$. Thus we set $R_3 = R_3'$ and $R_4 = R_4'$. In this case, the common mode gain $A_{cm2} = 0$ and hence the $CMRR_2 = \infty$. However, due to resistor tolerances these resistor pairs may not be perfectly matched. If we denote the resistor tolerance by Δ_R and is similar across all resistors, the worst case $CMRR_2$ (i.e., the smallest achievable value) can be calculated when

$$R_3 = R_{3n}(1 + \Delta_R) \tag{5.44}$$

$$R_4 = R_{4n}(1 + \Delta_R) \tag{5.45}$$

$$R_3' = R_{3n}(1 - \Delta_R) \tag{5.46}$$

$$R_4' = R_{4n}(1 - \Delta_R) \tag{5.47}$$

where R_{3n} and R_{4n} are the nominal resistance values. Substituting (5.44) – (5.47) into (5.43), the lowes CMRR is bounded by

$$CMRR_2 \geq 20\log\left[\left(\frac{R_{4n}}{R_{3n}}\right)\frac{1 + \frac{R_{3n}}{2R_{4n}}\left(\frac{1+\Delta_R}{1-\Delta_R} + \frac{1-\Delta_R}{1+\Delta_R}\right)}{\frac{1+\Delta_R}{1-\Delta_R} - \frac{1-\Delta_R}{1+\Delta_R}}\right] \tag{5.48}$$

$$\geq 20\log\left[\frac{\frac{R_{4n}}{R_{3n}}(1 - \Delta_R) + (1 + \Delta_R)}{4\Delta_R}\right]. \tag{5.49}$$

Stages 3 and 4 : Cascaded gain stages

Following the instrumentation amplifier stage, the signal was further amplified by two cascaded inverting amplifiers each with a gain of 4. The gains A_3 and A_4 of the subsequent stages are given by

$$A_3 = -\frac{R_6}{R_5} \tag{5.50}$$

$$A_4 = -\frac{R_8}{R_7}. \tag{5.51}$$

Component values $R_5 = R_7 = 2k\Omega$ and $R_6 = R_8 = 8.2k\Omega$ achieve the gain requirements.

In our design we used resistors of 1% tolerance. Hence, $\Delta_R = 0.01$. Combining both stages, the net common mode rejection ratio of the instrumentation amplifier denoted simply by $CMRR$ section is given by

$$CMRR \geq 20 \log \left(\frac{A_{d1} A_{d2} A_3 A_4}{A_{cm1} A_{cm2}} \right) \tag{5.52}$$

$$\geq 20 \log \left[\left(1 + \frac{2R_1}{R_2} \right) \left(\frac{\frac{R_{4n}}{R_{3n}}(1 - \Delta_R) + (1 + \Delta_R)}{4\Delta_R} \right) \left(\frac{R_6}{R_5} \right) \left(\frac{R_8}{R_7} \right) \right]. \tag{5.53}$$

Now, substituting the component tolerance and values the worst case scenario CMRR is calculated as

$$CMRR \geq 20 \log \left[\left(1 + \frac{2 \times 1.5}{1} \right) \left(\frac{\frac{8.2}{2.0}(1 - 0.01) + (1 + 0.01)}{4 \times 0.01} \right) \left(\frac{8.2}{2.0} \right)^2 \right] \tag{5.54}$$

$$\geq 78 \text{ dB}. \tag{5.55}$$

Thus, ideally this analog front end of the receiver was designed with an infinite CMRR. Although the CMRR degrades due to component tolerances, it is greater than 78 dB. The overall differential gain using the normalised components shown in Table 5.2 is 48.8 dB.

The analog end is powered using 3.7 V lithium ion batteries mounted in the space between the analog and digital ends. The analog front end consumes much of the receiver power mainly due to the amplification sages.

Item No.	Variable Name	Value	Tolerance
1	R_1	1.5 $k\Omega$	1 %
2	R_2	1.0 $k\Omega$	1 %
3	R_3	2.0 $k\Omega$	1 %
4	R_4	8.2 $k\Omega$	1 %
5	R_3	2.0 $k\Omega$	1 %
6	R_4	8.2 $k\Omega$	1 %
7	R_5	2.0 $k\Omega$	1 %
8	R_6	8.2 $k\Omega$	1 %
9	R_7	2.0 $k\Omega$	1 %
10	R_8	8.2 $k\Omega$	1 %
11	OpAmp	OPA2356	UGBW = 200 MHz SR = 300 V/μs CMRR = 80 dB

Table 5.2 Summary of components designed for amplifier stages. Here, UGBW ≅ Unity Gain Bandwidth, SR ≅ Slew rate, CMRR ≅ Common mode rejection ratio.

5.5 Receiver Digital End Implementation

The digital end of the receiver was designed and implemented on Xilinx Sparan6 LX9 FPGA. The complete register transfer level (RTL) of the digital front end is complex and not shown here; however, the top level of the modular implementation is shown in Fig. 5.21. The digital end receives the processed discrete signal from the analog front end. The crucial component of the digital end is clock and data synchronisation. Once the local clock is synchronised with the incoming data, the generated local clock was used to drive the receiver components. The preamble generator recreates the preamble sequence generated by the transmitter and the preamble searcher tracks the preamble from the data coordinated by the state machine. The state machine is the central block that coordinates all other blocks to decode the frame data from the packet structure shown in Fig. 5.2. When the preamble is detected the state machine instructs the PRS generator to reset and generate the desired sequence where both the data and the locally generated PRS are input to the demodulating blocks. The

implementation details of each block with the corresponding codes are discussed in the following sections.

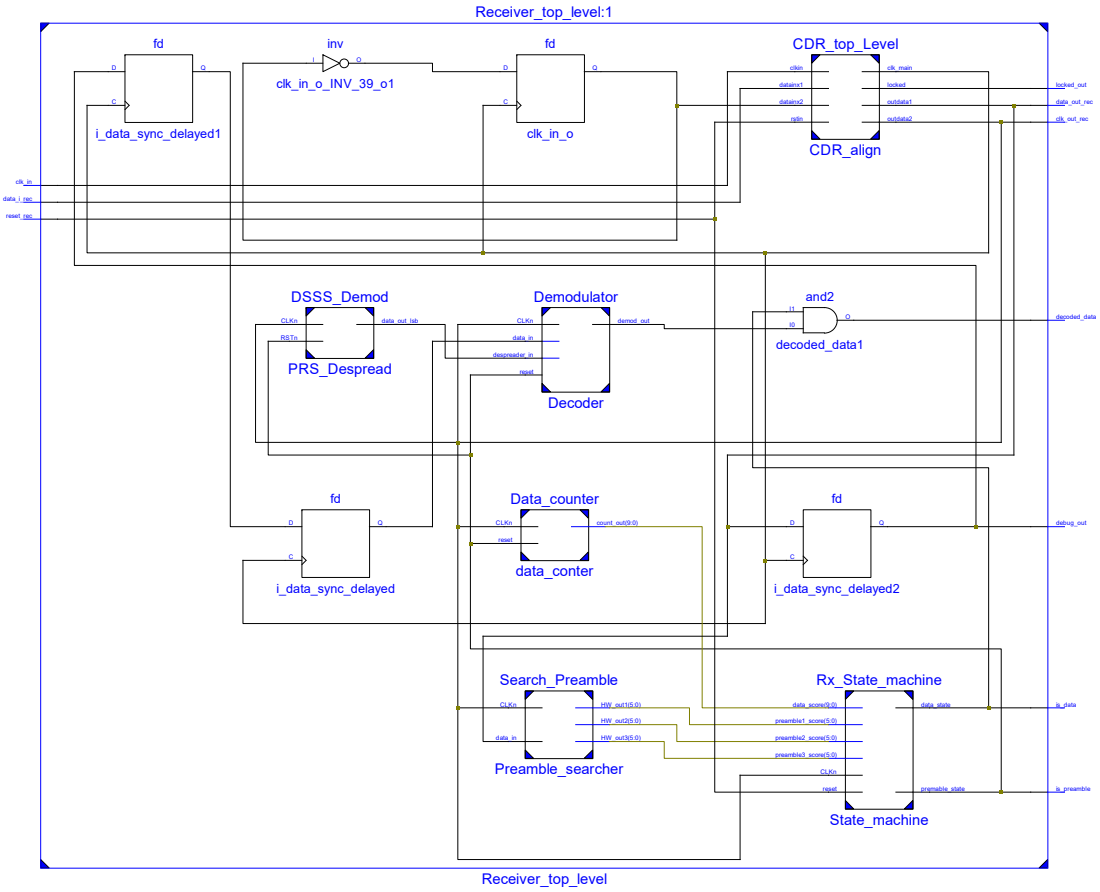

Fig. 5.21 Receiver digital end top level RTL diagram

The entire digital implementation was coded using the VHDL hardware description language. Our implementation follows a modular architecture where each block were implemented and tested individually and are tied together through the receiver top level VHDL code given in the code listing *Listing.* C.2. We used the Xilinx ISE tool to create, build and synthesise the receiver FPGA implementation. The register transfer logic (RTL) given in Fig. 5.21 the synthesis output of the receiver top level VHDL code. There are many advantages of implementing the receiver in a modular manner. First, each block was implemented and tested (with their corresponding test benches) individually.

Second, additional blocks such as error control coding techniques could be implemented and inserted or existing blocks could be modified or bypassed easily without affecting other blocks as seen in *Listing Appendix* C.2.

5.5.1 Clock and Data Recovery

The transmitted signal was modulated at a chip rate of 4 MHz. Thus, at the receiver, a local clock of 4 MHz was generated using phase locked loop (PLL) from the 32 kHz clock provided by Spartan6 FPGA. This clock and the output of the analog end were used as inputs to the clock and data recovery (CDR) block. The CDR block over samples the incoming signal with the local clock at 0^o,90^o,180^o and 270^o with a logic that effectively runs at 16 MHz. We used the Xilinx ISE design tool to design and simulate the digital front end.

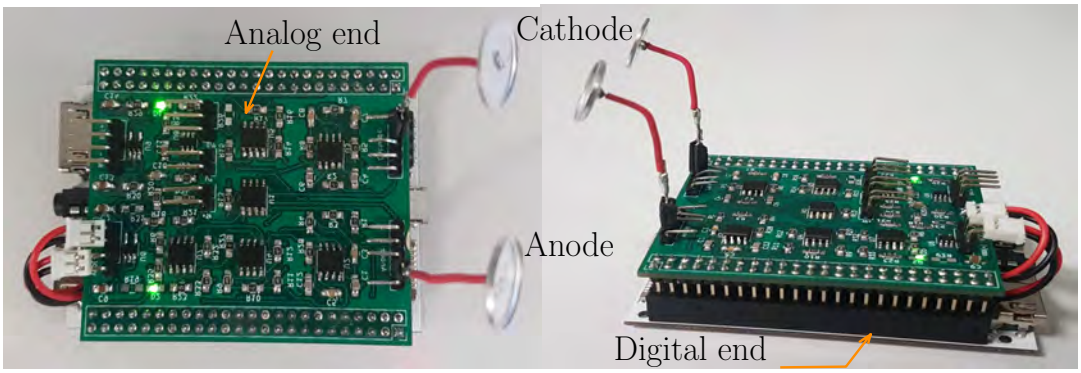

Fig. 5.22 Receiver circuit

The clock domain selection logic circuit is shown in Fig. 5.23. This logic circuit is also used in the Xilinx application note 225. The top level implementation of the clock and data recovery is presented in *Listing Appendix* C.3.

If AAP = BBP = CCP = DDP = 1 or AAN = BBN = CCN = DDN = 1 then clock domain Clk 0^o would be the first to detect the edge. Thus, to maximise noise margin we sample the data mid way and use Clk 180^o. If AAP = 1 and BBP = CCP = DDP = 0 or AAN = 1 and BBN = CCN = DDN = 0

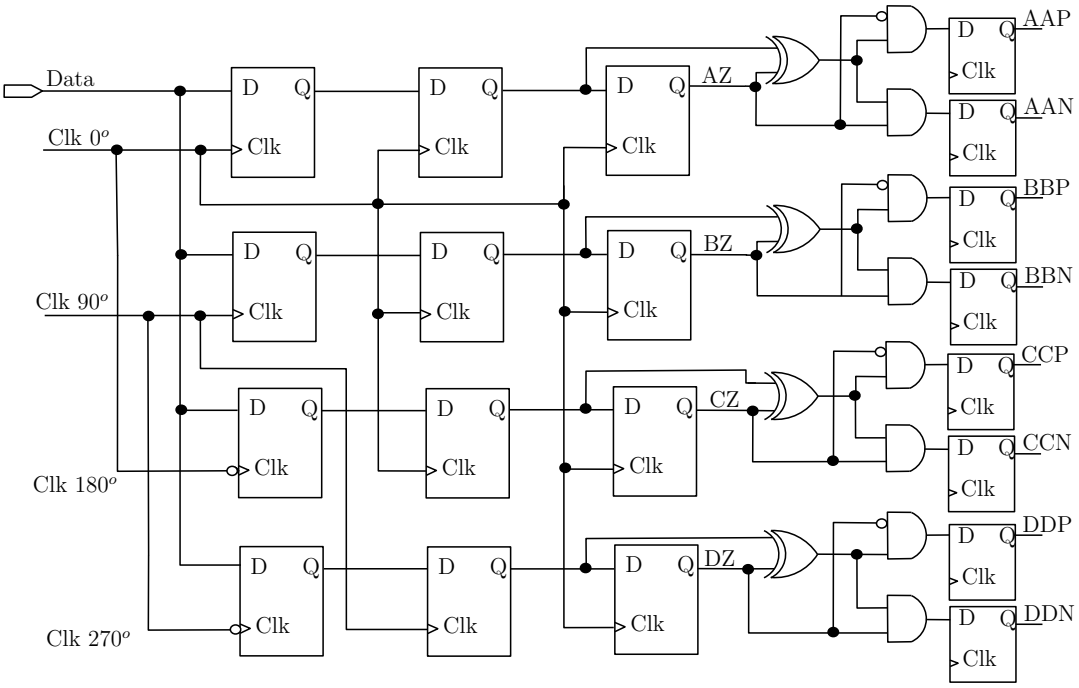

Fig. 5.23 CDR Circuit. Here the data is sampled by four clocks spaced 90ô away from each other. AZ, BZ, CZ and DZ are the stable samples and are inputs to the edge detection and clock domain selection logic. AAP, BBP,CCP and DDP correspond to the positive edges while AAN, BBN, CCN and DDN correspond to the negative edge.

then Clk 90^o would be the first to detect the edge and we use Clk 270^o. If AAP = BBP = 1 and CCP = DDP = 0 or AAN = BBN = 1 and CCN = DDN = 0 then Clk 180^o would be the first to detect the edge and we use Clk 0^o. If AAP = BBP = CCP = 1 and DDP = 0 or AAN = BBN = CCN = 1 and DDN = 0 then Clk 270^o would be the first to detect the edge and we use Clk 90^o.

Based on the data edge detected the clock is selected from any of the four alternatives. The timing jitter could be such that the synchroniser may require to wrap from 270^o to 0^o or 0^o to 270^o (depending on whether the local clock is faster or slower than the transmitter clock) which effectively incurs in a loss of one clock cycle in the data. This is adverse in the sense that despreading the data causes error starting from the bit the wrapping occurred. Thus we used a variable length shift register of up to 64 bits to move backward and forward by up

to 32 bits either way. Based on the edge detected if a transition from 0^o to 270^o is required the shift register is delayed by one bit and if a transition from 270^o to 0^o is detected the shift register is moved forward by a bit to avoid duplicate sampling of the same bit twice. Since 1024 information chips are transmitted between preambles and the next payload is realigned for synchronisation, the probability of filling up the 32 bit shift on either side is small. Our detailed implementation of the CDR synchroniser is presented in *Listing Appendix* C.4.

5.5.2 Local PRS generator

We designed the local PRS signal to be spanned by implementing gold code sequence using the two degree 8 primitive polynomials $x^8 + x^6 + x^5 + x^4 + 1$ and $x^8 + x^4 + x^3 + x^2 + 1$. The VHDL implementation is given in *Listing Appendix* C.5.

5.5.3 Local Preamble Generator and Preamble Tracking

The preamble sequence can be locally generated using two methods. It can be generated by implementing the polynomial $x^5+x^4+x^3+x^2+1$ at the receiver side using linear feedback shift registers (LFSR) in a similar manner as the PRS sequence. However, each sequence spanned by a five degree polynomial are easily enumerable since they are composed only of 31 bits. Thus the second method of generating the three parts of the preamble sequence is to hard code the 31 bit sequences. Hence values `Preamble_seq1 <= "01111100100110000101101010000111";` `Preamble_seq2 <= "10000011011001111010010101111000";` and `Preamble_seq3 <= "01111100100110000101101010000111";` are hard coded in the preamble searcher module. For a multiuser implementation, it is recommended to implement the local preamble using the LFSR and use lookup tables to store

the different seeds used for each device to span the different sequences. In our implementation, since the prototype was required to be used with a single user, both techniques were equally valid. In our implementation, while we generated the PRS by implementing the polynomials using LFSR, we hard coded the preamble sequences as the preamble sequences are only 31 bits long.

The preamble searcher or tracker module was designed to run with every data bit received to search for the preamble in the received sequence. As detailed in *Listing Appendix* C.6, it populates the received serial data into a running 96 bit shift register buffer. It then computes the Hamming distance with the locally generated preamble for the i^th user (only one user in this case). This was done by first XORing these bits with the locally generated preamble and computing the Hamming weight of the resulting sequence.

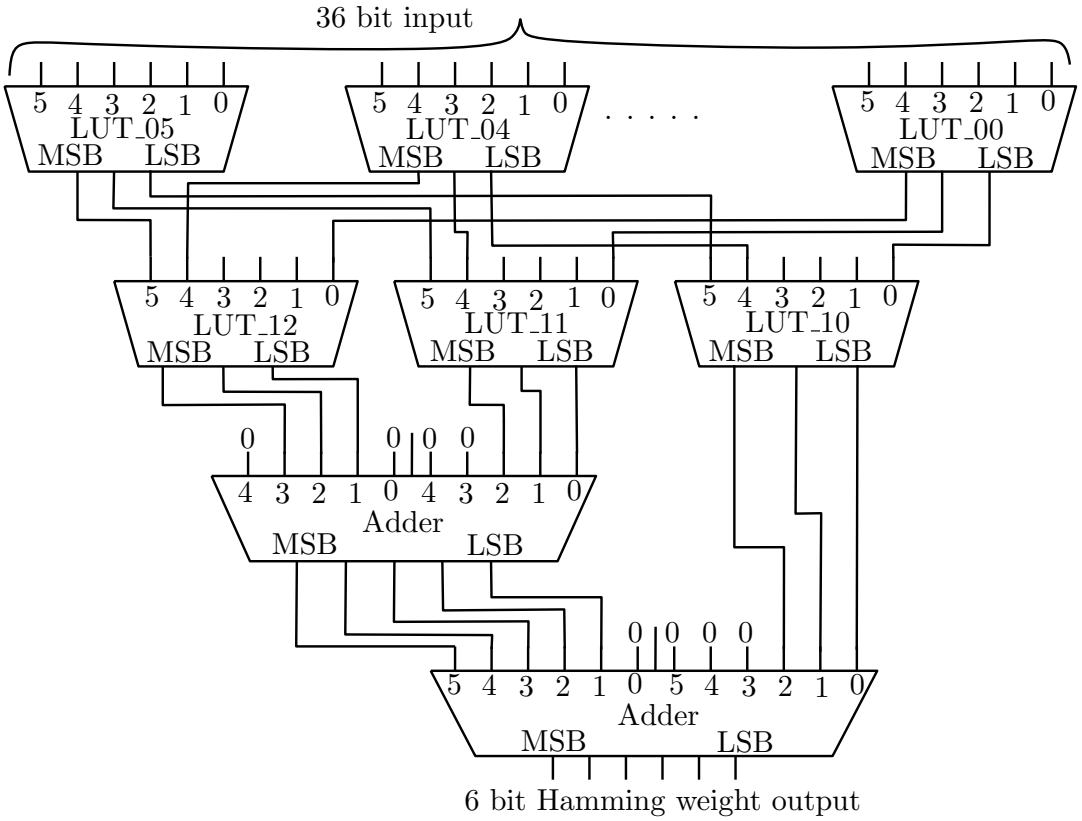

Fig. 5.24 Hamming weight calculator in 4 propagation delays [149]

Computing the Hamming weight using the naive way of counting the number of '1's in the sequence is a costly implementation as it requires several clock cycles comparable to the sequence length. This long propagation delay of such Hamming weight calculator for long sequences is often detrimental to the signal timing. Thus, we used a 36 bit Hamming weight calculator proposed by Sklyarov *et al* [149] and also used in Taylor [150] shown in Fig. 5.24 in only four propagation delays. To use this, the 32 bits of the each preamble XOred with the corresponding incoming sequence were passed to the 36 bit Hamming wight calculator by zero padding the remaining 4 bits.

Thus, the buffer in the preamble searcher module passes the 36 bits corresponding to each preamble to the Hamming weight calculator given in *Listing Appendix* C.7 by zero padding the other 4 bits. The maximum Hamming weight of the a 36 bit sequence can be stored in a 6 bit register as the output of the Hamming weight calculator. The three arrays of 6 bit outputs of the preamble searcher given in *Listing Appendix* C.6 are `HW_out1, HW_out2` and `HW_out3` are thus the hamming distances of the data with the preambles at any given instant of time.

5.5.4 Receiver State Machine

Once the local clock was synchronised with the received digital data, each packet was detected and decoded to obtain the recovered signal transmitted by the transmitter. The module that plays a central role in the signal recovery is the receiver state machine. This module was driven by the central receiver clock signal and accepts `preamble1_score, preamble2_score, preamble3_score` and `data_score` as inputs. The VHDL implementation of the receiver is given in *Listing Appendix* C.8. Here the signals `preamble1_score, preamble2_score` and `preamble3_score` represent the Hamming distances of the received data

with the locally generated preamble sequences and are tied with the outputs of the preamble searchers module. Thus, the receiver state machine evaluates these scores and decides if the preamble state is detected. Following this detection comes the data state and the state machine set the `preamble1_state` signal low to reset and re-initialise the local PRS generator and demodulation modules, and once the data state is finished (i.e., 1024 bits of data are detected) then the state machine sets `data_state` signal low.

5.5.5 Despreading and Recovering Transmit Signal

Once the synchronised clock and data were obtained, the receiver state machine manages the states and coordinates operation of the local PRS generator, preamble generator and despreader to generate the decoded message.

5.5.6 Test Bench to Simulate Receiver Digital End

Test benches were created to simulate and test each of the modules of receiver digital end before they are integrated into the top level architecture. These test benches were also used to check the effect of any change done at later stage. Although, we have implemented the test benches for each module, the receiver top level module test bench is presented here. The code listing given in *Listing Appendix* C.9 shows the VHDL implementation of the receiver top level test bench.

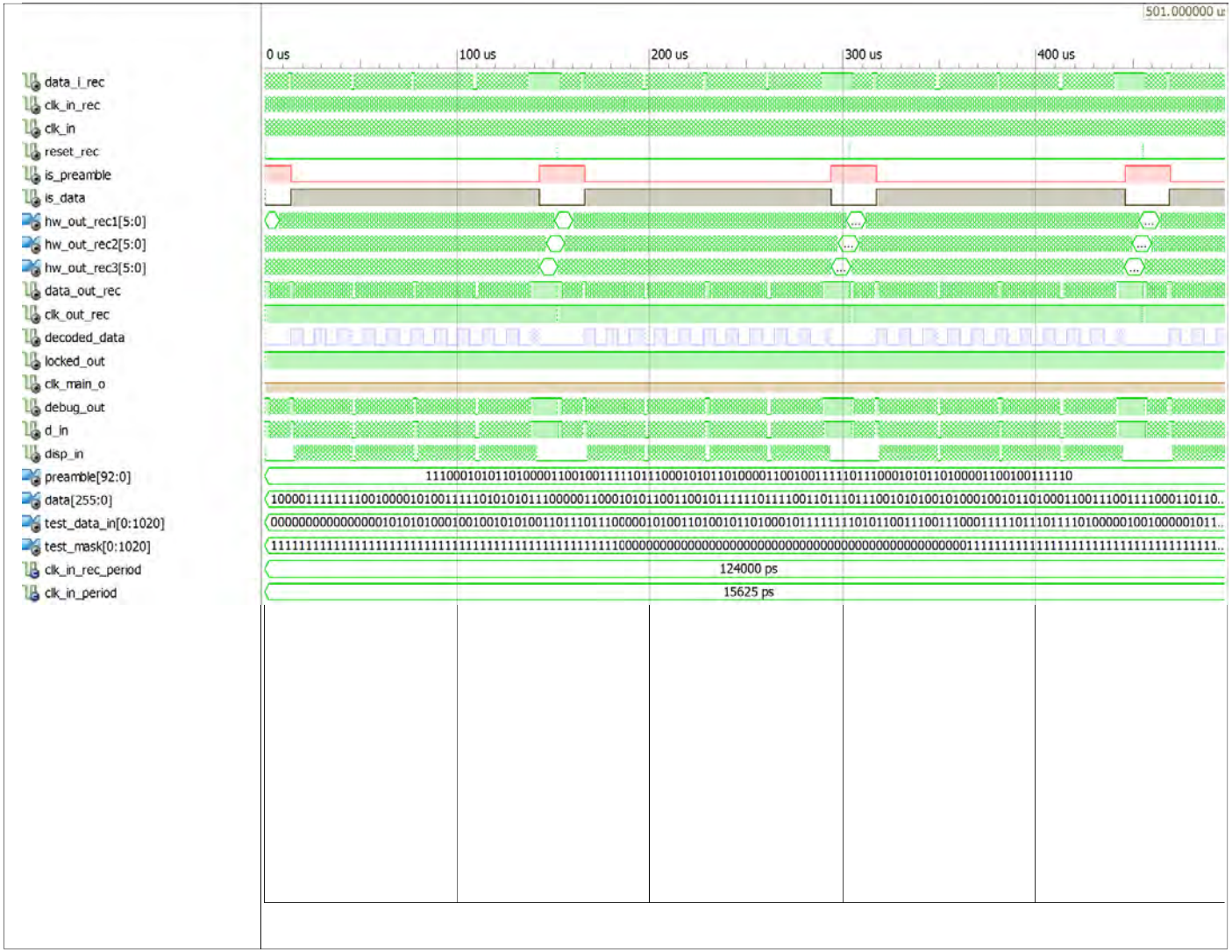

Fig. 5.25 Simulation of the receiver top level architecture. The final decoded data is marked in light blue and as can be seen is a clean reconstruction of the quantised sensor signal discussed in the sensing unit section. Signals representing preamble state and data states of the packet are indicated by red and black colors respectively. The rest of the signals are input and intermediate signals to the receiver digital end.

The simulation of the operation of the receiver using the test bench showed a successful reception and decoding on the generated signal. Signals at various stages in the test bench are shown in Fig. 5.25. In the test bench we derived our test data at a clock that was slightly drifted from the 4 MHz chip rate. Our simulation and experiments show that the CDR module was capable of tracking the input data from the analog end well; for clock drifts less than 2 %, signal recovery was possible with small clock error. In the unlikely case of the system losing track of the input, the system was designed to reset and regain synchronisation once the next preamble is detected.

5.6 Conclusion

In this chapter we have presented design, implementation and characterisation of a sensor integrated galvanically coupled transmitter and receiver. A capacitive sensor represented by a variable capacitor with capacitance range of 0–50 pF was used as a signal source. The sensor was integrated into an oscillator and a minimalist digital data generation is presented. Implant transmitter that galvanically coupled signal to the human body and receiver systems that differentially detects the signal received was implemented. The transmitter system was implemented using Cypress's programmable system on chip (PSoC). Our implementation of the digital end was modularised and carefully designed (effective usage of PLDs and Datapaths in combination) to fit into the PSoC 3 chip. The chip is unique in that it is low cost and allows a rapid prototyping digital and analog systems. The digital end of the receiver was implemented using Xilinx's Spartan 6 FPGA which was powerful enough to handle the entire receiver logic at the desired frequency of operation. The modularised implementation of both the transmitter and receiver ensures a great flexibility in testing out and comparing different modulation and coding schemes. Evaluation of the results,

noise characterisation and prototype performance will be presented in the next chapter to demonstrate the feasibility of the gc-IBC implant communication.

Chapter 6

Performance Evaluation and Noise Characterisation of Intrabody Implant Transceiver

This chapter presents performance evaluation and noise characterisation of the galvanically coupled implant transceiver prototype described in the previous chapter (chapter 5). In order to test the communications in an implant setting, an experimental rig was built. The experimental setup was designed to enable movement of the receiver in three axes with respect to a fixed transmitter location. Both the receiver and the transmitter are inserted into a phantom solution that mimics the electromagnetic properties of human muscle tissue. For the characterisation experiment, the receiver was modified to include transmission and error detection. The channel noise is assumed to be an additive white gaussian noise (AWGN) and analytical bit error rate (BER) performance of the transceiver as a function of the signal to noise ratio (SNR) is computed and verified with simulation of the system. Experiments to characterise the BER as a function of relative distance between the transmitter and receiver

were conducted. These BER characterisations were also used to derive the relationship of the SNR with a transmitter distance. Finally, the power spectral density (PSD) of the noise signal was determined to quantify the channel noise for various depth of implantation.

6.1 Introduction

While the path loss modelling and experimental characterisation of intrabody communications (although mainly for surface-to-surface communication) has been conducted in various works (see chapter 3), investigation to identify the type and quantity of noise introduced by the channel still requires further development. In fact, works such as [151–154] have attempted to identify noise sources as thermal noise and electrode contact noise (also modelled as thermal noise at high frequencies) which are generally of gaussian nature. Bio-electrical signals generated with in the human body are below 10 kHz and do not contribute to the noise added in the MHz frequency range. Assuming the dominant noise source is thermal and taking into account the human body's homeostasis, the noise process could be approximated as stationary gaussian process. Thus, the well known tools for additive white gaussian noise could be used to preliminarily quantify channel noise.

Compared to through-the-air type traditional wireless transceivers, assessing implant transceivers for intrabody communication poses significant challenge. This is mainly due to inconvenience of mounting and moving implants in an experimental setting. Most experiments conducted to characterise implanted medical devices (IMDs) use a form of a replacement of the human body. These are often either porcine meat [155], or phantom bodies [67]. Some phantom bodies are solid [156]. The solid phantoms are convenient to implement layered tissue structured with defined shapes to mimic an actual human body part. Solid

phantoms can also be used to asses surface to surface intrabody communication. However, they are not preferred for assessing implant communication since moving the receiver relative to the transmitter is difficult through a rigid body. Thus, liquid/aqueous phantom solutions are used in cases where transmission of an implant to an on-body and implanted receiver at varying distance from the transmitter [13]. In this characterisation, we used a liquid phantom solution prepared to mimic the permittivity and conductivity of muscle tissue.

Another issue often raised in characterisation experiments is that experiments are not repeatable due to variability in measurement setups which was in detail reviewed in [69]. Thus, we developed a mechatronic rig where the transmitter is mounted on the fixed stand and the receiver is mounted on a movable stand. The movable stand is controlled to move in three axes.

The rest of the chapter is organised as follows. Section 6.2 presents the experimental setup used. Section 6.3 evaluates the performance of the transmission and characterises the channel noise where the AWGN communication channel model of the system is given in subsection 6.3.1 and experimental and simulation results are discussed in subsection 6.3.2. Our conclusion is given in Section 6.4.

6.2 Experimental Setup

For measurements and performance characterisation of the presented system we used the experimental setup shown in Fig. 6.1. We constructed a rig that moves the receiver in three axes with respect to the transmitter, albeit we used only two axes for these experiments. The rig is motorised and is controlled by a Matlab graphical user interface on the laptop (in the left side) for calibration and operation. Both the transmitter and the receiver were enclosed inside IP67 water proof cases and fixed to the vertical stands. The receiver and transmitter

electrodes are connected through IP67 water proof cable glands as shown in Fig. 6.2. Inputs, outputs and reset terminals of the receiver are collected and passed through a water proof link for external measurement and bit error rate display system.

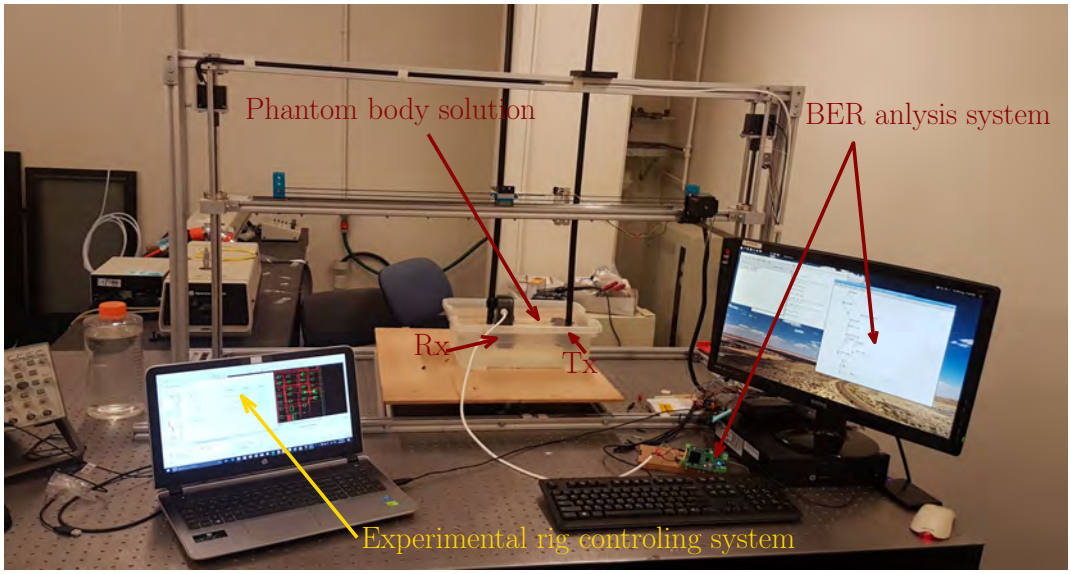

Fig. 6.1 Mechatronic rig for transmitter receiver measurements in phantom body

Fig. 6.2 Water proof IP67 encased receiver (left) and transmitter (right)

A bath is field with phantom solution that mimics the electromagnetic characteristics (i.e., permittivity and conductivity) of the muscle tissue that we prepared according to recipes given in [130] and shown in Table 6.2. The recipe provided is such that solutions at other frequencies could be prepared by linearly extrapolating the concentration of the ingredients.

Frequency	Percentage of Weight			Properties	
(MHz)	Water	Glycine	NaCl	ϵ_r	σ (S/m)
13.56	79.40	20.00	0.58	145.00	0.60
27.12	88.50	11.00	0.49	112.00	0.60
40.68	93.50	6.00	0.52	97.00	0.70

Table 6.1 Recipe for aqueous muscle tissue phantom.

6.3 Performance evaluation and noise characterisation

Using the experimental setup, this section explores two important aspects of the proposed implant communication system. First we evaluate the bit error rate (BER) verses signal to noise ratio (SNR) of the communication. This is done by mathematically analysing and simulating the system followed by experimental measurements of the BER as a function of communication distance. This measurement is an essential step to calculate the SNR of the channel as a function of distance. Since we know the transmitted power and the channel path loss, the SNR verses distance curve translates to noise power spectral density (PSD) as a function of distance.

6.3.1 AWGN Communication Channel Model of the System

The simplified physical layer communication scheme used in this work is shown in Fig. 6.3. The received signal $r(t)$ can be expressed as

$$r(t) = s(t) * h(t) + n(t) \tag{6.1}$$

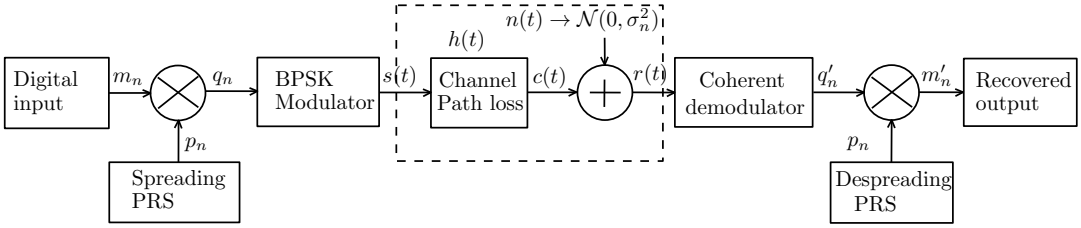

Fig. 6.3 communication channel model

The channel transfer function $h(t)$ is due to the path loss introduced by the human body. This transfer function for implant communication varies with frequency and communication distance as shown in [13].

A sample of the noise corrupted received signal picked up by the electrodes, band limited signal and the detected signals normalised to unity amplitude are shown in Fig. 6.4.

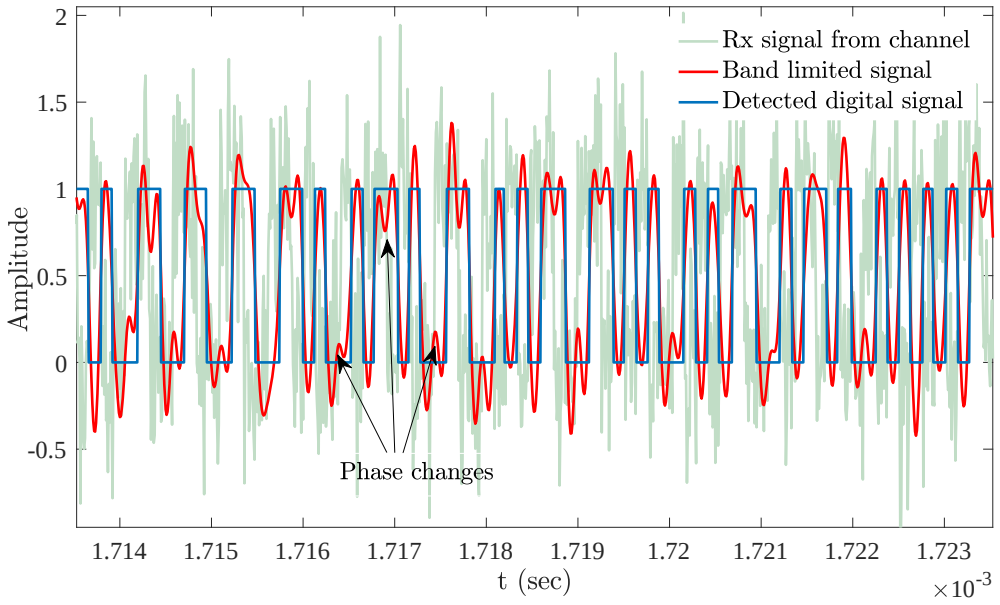

Fig. 6.4 Signals normalised to unity amplitude

The noise signal $n(t)$ is assumed to be and AWGN distributed as $\mathcal{N}(0, \sigma_n^2)$ where σ_n^2 is the variance of the noise process. AWGN has a flat power spectral density of $N_o = \frac{\sigma^2}{2}$ over the entire spectrum. Each chip has an average chip energy $E_c = \frac{A^2 T_c}{2}$ where A is the amplitude of the line waveform and T_c is the chip period. From these, the chip error probability as a function of $\frac{E_c}{N_o}$ is given by

$$p_c = Q\left(\sqrt{\frac{2E_c}{N_o}}\right). \tag{6.2}$$

Thus for a spreading factor of M, the bit error rate (BER) p_b is a binomial distribution of p_c when the bit is decoded by majority voting. It is given by

$$p_b = \sum_{i=M/2}^{M} p_c^i (1 - p_c)^{M-i}. \tag{6.3}$$

The power spectral density (PSD) of the received signal is shown in Fig. 6.5. Here we can see that the signal at the input of the receiver maintains similar spreaded power of the transmitted signal except with a nearly constant noise floor. This roughly confirms our assumption that the noise is AWGN.

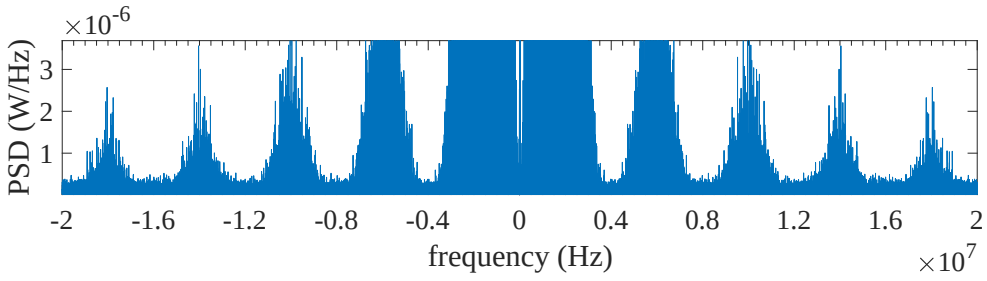

Fig. 6.5 Power spectral density of signal the receiver input

6.3.2 Experimental and Simulation Results Discussion

The presented system was simulated and compared with theoretical BPSK modulated DSSS with respect to BER as a function of SNR (i.e., $\frac{E_b}{N_o}$) is shown in Fig. 6.6. The comparison was done for different spreading factors. As shown the given system follows the theoretical performance closely. Hence, this can be related with BER as a function transmission distance to evaluate the SNR as function of distance to characterise channel noise.

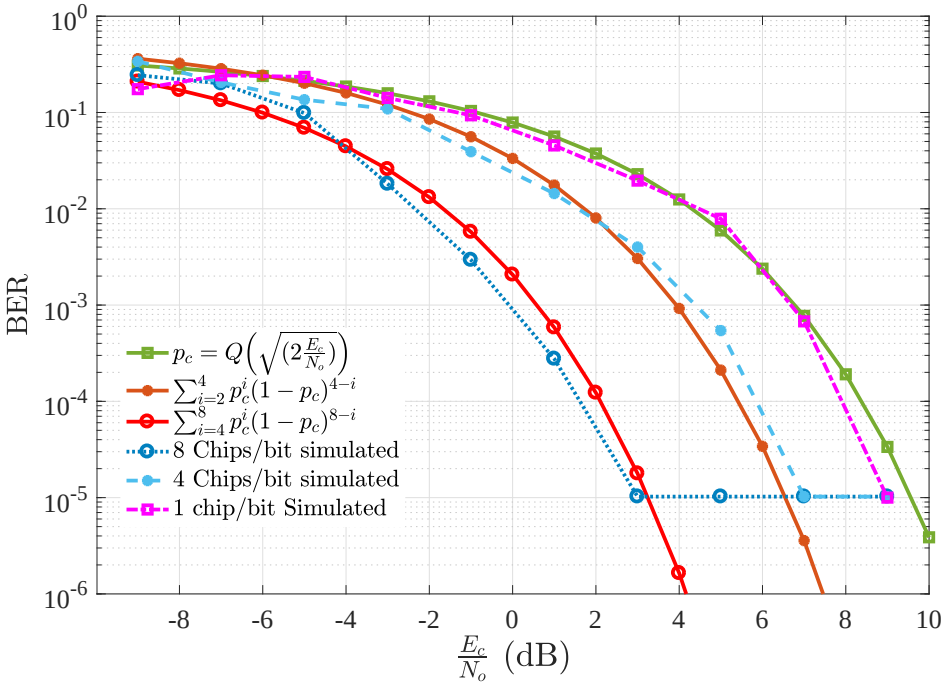

Fig. 6.6 Simulated BER performance of the the transceiver

Measurement of BER requires long sequence of data and repeated experiment. For this purpose the receiver was modified to include an error detection system. The error count and the data counts were registered using 32 bit long registers (i.e., capable of counting 4.295×10^9 that do not fill up for 30 minutes per single measurement and sufficiently large for an error floor of 10^{-6}). These error and data counts were intermittently sent out to the BER calculator program

implemented in the PC on the right side of Fig. 6.1. For every transmission distance set, the error and data counts were reset five times. Averaging this values the BER was measured by varying the transmission distance and is presented in Fig. 6.7.

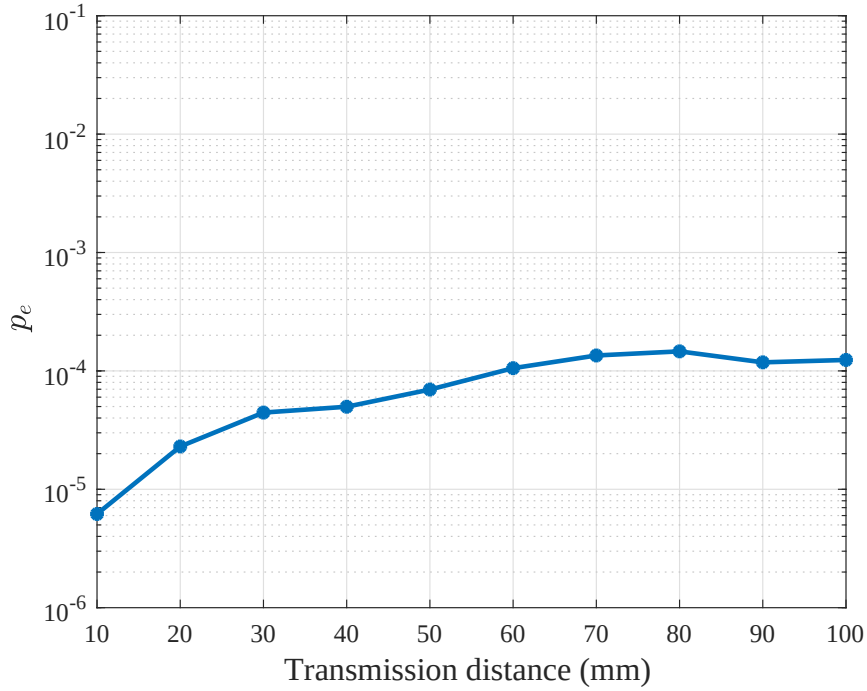

Fig. 6.7 BER verses transmission distance

Using equation (6.3) and the measurements in Fig. 6.7, the SNR can be expressed as a function of distance and the relationship is plotted as shown in Fig. 6.8.

The mean received energy of the signal $E_r = E_c P_L$ where P_L is the path loss as a function of distance analytically computed in our pervious work [13]. Thus, the received signal will have signal to noise energy ratio of $\frac{E_r}{N_o}$. Relating these with the SNR plot in Fig. 6.8, the noise spectral density N_o can be estimated and is shown in Fig. 6.9. This shows that the noise spectral density of the AWGN introduced by the channel is also nearly flat as a function of transmission

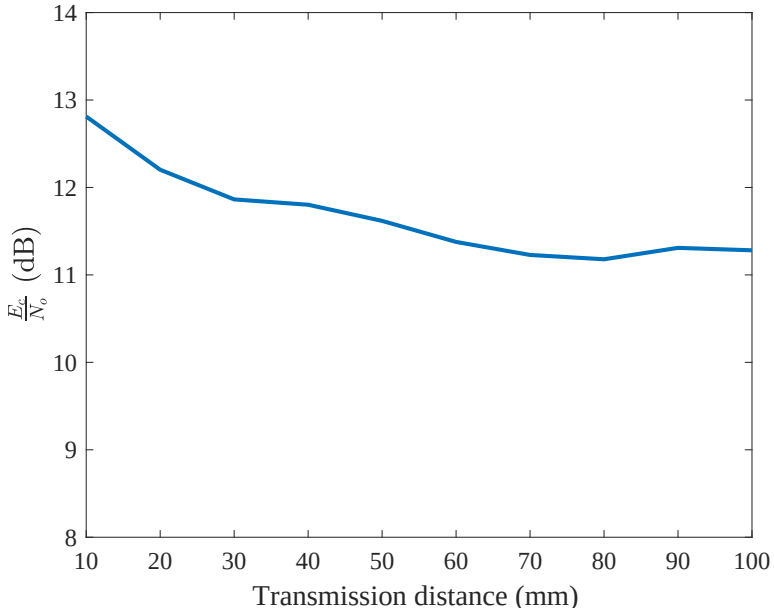

Fig. 6.8 SNR verses transmission distance

distance, albeit smaller for short distances. The average value of the noise power spectral density was measured to be -118 dBWatt/Hz.

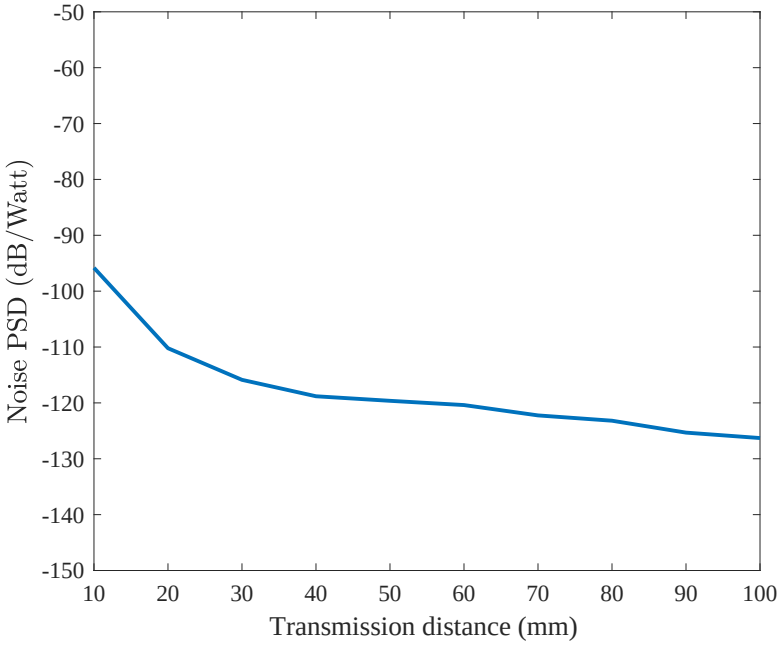

Fig. 6.9 PSD verses transmission distance

6.4 Conclusion

In this chapter we have presented design, implementation and characterisation of a sensor integrated galvanically coupled transmitter and receiver. A capacitive sensor represented by a variable capacitance of value 0–50 pF was used as a signal source. The sensor was integrated into an oscillator and a minimalist digital data generation was presented. implant transmitter that galvanically coupled signal to the human body and receiver systems that differentially detects the signal received is implemented. Evaluation of the performance the prototype system presented here demonstrates the practical feasibility of galvanically coupled implant communication. This work also characterised SNR as a function of transmission distance which is a crucial parameter for improved future receiver designs. The channel noise is characterised as AWGN with an average PSD of -118 dbWatt/Hz.

Chapter 7

Conclusion and Future Work

7.1 Thesis Review

While bio-sensing technologies and medical diagnostics have advanced, the capability of regulatory, therapeutic and diagnostic readout implanted devices has not developed as fast. Implants give a real-time and hence better information of physiological states. The demand for ubiquitous and minimally invasive communication of implanted and on-body sensors is on the rise as a result of the increasing prevalence of chronic disease and rising aging population. Besides, it is also demanded in other areas such as athletic performance monitoring and defence applications that require long term fatigue assessment and assistive technology for prosthetic limbs. Although antenna based electromagnetic wave propagation and inductively coupled data transmission have been extensively explored for implant communication, transmission techniques that require low power consumption and long term IMD powering regimes are still open problems. This thesis contributed to the research gaps by exploring alternative implant communication techniques using gc-IBC mechanisms. The thesis presented a number of significant contributions. We began by critically reviewing progresses and

challenges of existing implant communication technologies. Then we investigated a novel electromagnetic analytic framework for modeling galvanically coupled implant communication with the human body as channel. This model allowed us to accurately estimate and analyse the human body channel without requiring complex numerical computations such as the finite difference time domain (FDTD) analysis. We proposed a hybrid scheme for implant communication, especially for the case of cortical implants. We then moved beyond modeling and experimental validation to design, implement and characterise a galvanically coupled implant transceiver. The detailed conclusions and contributions in each chapter are summarised in the following.

In Chapter 2, we have reviewed progresses and challenges in communication and applications of implanted medical devices. Today, IMDs are used in several diagnostic, therapeutic and assitive technologies in health-care and professional sports. Existing implant communication technologies are predominantly based on antenna baesed electromagnetic wave propagation and inductivelly coupled links. Uncoordinated progresses have been standardised as MICS in 1999 which was later upgraded to MedRadio services in 2009. Recently, the IEEE 802.15.6 standard was also released in 2012 to include non radiating body coupled communications that use the human body as a channel at lower frequencies than MedRadio. These standards has aided the research community and industries like Medtronic and Zarlink to design and develop IMDs with compatible communications circuitry. Although, coordinated efforts led to advancement in IMD technology, there are still challenges for the research community to address. These include, reliable and sustainable power sources, implant miniaturisation, bio-compatibility and human safety. As a result, emerging technologies such as galvanically coupled, ultrasonic, optical and molecular intrabody communications are being investigated. With further advancements and the soaring demand for IMDs, implants per user are envisioned to be interconnected via

a wireless network for reliable data transmission to and from the patient to physicians and family even far away. Besides, advancements in the big data analysis can be exploited by compiling data from various patients over time to aid in medical research.

In Chapter 3 we have presented a novel analytical model framework for implant communication using gc-IBC. The model framework presents, for the first time, a geometrically versatile solution that can be applied to any part of human body. The model can be used to describe and understand important parameters of the implant communication channel such as the electromagnetic effect of tissue layers, size and depth of the implant on input and received power, path loss, received potential and potential ratio. The predicted path loss at the surface of the skin for a communication distance of around 6 cm is between 30-40dB in the frequency range of interest which coincides with empirical results previously reported. Our result shows that gc-IBC scheme for implant communication is not only feasible but possesses better path loss characteristics and offers a potentially large degree of miniaturisation. Moreover, different parts of the body have varying number of tissue layers and our analysis provided insight into applying the model to different parts of the body by increasing the number and electromagnetic properties of tissue layers.

Chapter 4 presented our analyses and comparisons of three technologies for cortical implant communication - the inductive link for data and power transfer, the gc-IBC and RF antenna based implant communication schemes. From our results, it can be concluded that inductive coupling is reliable for short range power transfer which suits cortical implants at subdermal implantation depth of 2-3 cm. However, despite its popular use, inductive coupling is not appropriate for applications such as bionic vision that may require about 500 kbps to 1 Mbps data rates when implemented with 200 to 400 electrodes for high resolution vision restoration. For such cases, our simulations have shown that the gc-IBC

to be more reliable than the ic-DT and RF antenna coupled schemes. Finally, we proposed gc-IBC to be combined with the existing inductively powered implants with out introducing a major change in size and design. We also evaluated the international commission on non ionising radiation protection (ICNIRP) compliance of a gc-IBC cortical implant communication scheme and demonstrated the technique is safe.

This chapter presented a novel analytical model framework for implant communication using gc-IBC. The model presents, for the first time, a geometrically versatile solution that can be applied to any part of human body. The model can be used to describe and understand important parameters of the implant communication channel such as the electromagnetic effect of tissue layers, size and depth of the implant on input and received power, path loss, received potential and potential ratio. The predicted path loss at the surface of the skin for a communication distance of around 6 cm is between 30-40dB in the frequency range of interest which coincides with empirical results previously reported. Our result shows that gc-IBC scheme for implant communication is not only feasible but possesses better path loss characteristics and offers a potentially large degree of miniaturisation. Moreover, different parts of the body have varying number of tissue layers and our analysis provided insight into applying the model to different parts of the body by increasing the number and electromagnetic properties of tissue layers.

Chapter 5 we have presented design, implementation and characterisation of a sensor integrated galvanically coupled transmitter and receiver. A capacitive sensor represented by a variable capacitance of value 0–50 pF is used as a data source. The sensor is integrated into an oscillator and a minimalist digital data generation is presented. implant transmitter that galvanically coupled signal to the human body and receiver systems that differentially detects the signal received is implemented. The transmitter system is implemented using Cypress's

programmable system on chip (PSoC). Our implementation of the digital end was modularised and carefully designed (effective usage of PLDs and Datapaths in combination) to fit into the PSoC 3 chip. The chip is unique in that it is low cost and allows a rapid prototyping digital and analog systems. The digital end of the receiver is implemented using Xilinx's Spartan 6 FPGA which was powerful enough to handle the entire receiver logic at the desired frequency of operation. The modularised implementation of both the transmitter and receiver ensures a great flexibility for testing and comparing different modulation and coding schemes.

Chapter 6 presented evaluation of the performance the prototype system presented here demonstrates the practical feasibility of galvanically coupled implant communication. This work also characterised SNR as a function of transmission distance which is a crucial parameter for improved future receiver designs. The channel noise is characterised as AWGN with an average PSD of -118 dbWatt/Hz.

7.2 Future Work

This thesis presented a novel foundation for analytical modeling and practical implementation of implant communication using the human body as a channel for implant communication. Though this thesis achieved its original aims, it has also opened up several issues for further research listed in the following.

- The analytical model presented is unified in the sense that it can be applied to implants in any part of the body. Thus, different implantation scenarios in other limbs can be modeled by extending the current work.

- The path loss model in this work could be combined with further experiments to estimate channel fading. It can also be extended to assess adaptive channel estimation for implants. The model also aids in calculating the channel capacity of the gc-IBC scheme.
- Comparative analysis of existing and emerging intrabody communication technologies such as molecular communication, antenna based RF, gc-IBC, inductively coupled data transmission, ultrasonic communication, optical implant communication shows that these technologies are mostly complementary to each other; albeit, competing in some cases. This presents an opportunity for future research to explore variety of hybrid communication schemes to enable communication of the molecular domain inside the body with the outside world.
- Miniaturisation of the transceiver presented and various electrode geometry and arrangement could be assessed for practical application.
- Hardware architecture, security and multiple access requirements could be explored to develop a detailed protocol stack.
- Different source and channel codes could be tested for improved error correction and transceiver performance.

7.3 Conclusion

In summary, this thesis has investigated galvanically coupled intrabody communication as a new form of implant communications technique. A novel electromagnetic analytic framework for modeling galvanically coupled implant communication with the human body as channel is presented. A hybrid scheme for implant communication, especially for the case of cortical implants is presented. A prototype gc-IBC implant transceiver is designed, implemented and

characterised. Finally, we highlighted future research questions that surfaced as a result of the thesis findings.

Appendix A

Lamé's functions of First kind E_n^p

Lamé's functions $E_n^p(\rho)$ for degree $n \leq 3$ and order $p \in \{1, 2, .., 2n+1\}$ where $h_j, \forall j \in \{1, 2, 3\}$ are semi-axis distances are given as follows

$$
\begin{aligned}
E_0^1(\rho) &= 1, \\
E_1^1(\rho) &= \rho, \\
E_1^2(\rho) &= \sqrt{|\rho^2 - h_3^2|},
\end{aligned}
$$

$$
\begin{aligned}
E_1^3(\rho) &= \sqrt{|\rho^2 - h_2^2|}, \\
E_2^1(\rho) &= \rho^2 - \frac{1}{3}\Big[(h_3^2 + h_2^2) - \sqrt{(h_3^2 + h_2^2)^2 - 3h_3^2 h_2^2}\Big], \\
E_2^2(\rho) &= \rho^2 - \frac{1}{3}\Big[(h_3^2 + h_2^2) + \sqrt{(h_3^2 + h_2^2)^2 - 3h_3^2 h_2^2}\Big],
\end{aligned}
$$

$$
\begin{aligned}
E_2^3(\rho) &= \rho\sqrt{|\rho^2 - h_3^2|}, \\
E_2^4(\rho) &= \rho\sqrt{|\rho^2 - h_2^2|},
\end{aligned}
$$

$$E_2^5(\rho) = \sqrt{|(\rho^2 - h_3^2)(\rho^2 - h_2^2)|},$$
$$E_3^1(\rho) = \rho^3 - \frac{\rho}{5}\Big[2(h_3^2 + h_2^2) - \sqrt{4(h_3^2 + h_2^2)^2 - 15h_3^2h_2^2}\Big],$$
$$E_3^2(\rho) = \rho^3 - \frac{\rho}{5}\Big[2(h_3^2 + h_2^2) + \sqrt{4(h_3^2 + h_2^2)^2 - 15h_3^2h_2^2}\Big],$$

$$E_3^3(\rho) = \sqrt{|\rho^2 - h_3^2|}$$
$$\times \Big(\rho^2 - \frac{1}{5}\Big[h_3^2 + 2h_2^2 - \sqrt{(h_3^2 + 2h_2^2)^2 - 5h_3^2h_2^2}\Big]\Big),$$

$$E_3^4(\rho) = \sqrt{|\rho^2 - h_3^2|}$$
$$\times \Big(\rho^2 - \frac{1}{5}\Big[h_3^2 + 2h_2^2 + \sqrt{(h_3^2 + 2h_2^2)^2 - 5h_3^2h_2^2}\Big]\Big),$$
$$E_3^5(\rho) = \sqrt{|\rho^2 - h_2^2|}$$
$$\times \Big(\rho^2 - \frac{1}{5}\Big[2h_3^2 + h_2^2 - \sqrt{(2h_3^2 + h_2^2)^2 - 5h_3^2h_2^2}\Big]\Big),$$

$$E_3^6(\rho) = \sqrt{|\rho^2 - h_2^2|}$$
$$\times \Big(\rho^2 - \frac{1}{5}\Big[2h_3^2 + h_2^2 + \sqrt{(2h_3^2 + h_2^2)^2 - 5h_3^2h_2^2}\Big]\Big),$$
$$E_3^7(\rho) = \rho\sqrt{|(\rho^2 - h_3^2)(\rho^2 - h_2^2)|}.$$

Appendix B

Orthogonality Normalisation constants γ_n^p

Normalisation constants γ_n^p for degree $n \leq 3$, order $p \in \{1, 2, .., 2n+1\}$ and semi-axis distances h_j are given as

$$\gamma_0^1 = 4\pi,$$
$$\gamma_1^1 = \frac{4\pi h_3^2 h_2^2}{3},$$

$$\gamma_1^2 = \frac{4\pi h_3^2 (h_2^2 - h_3^2)}{3},$$
$$\gamma_1^3 = \frac{4\pi h_3^2 (h_3^2 - h_3^2)}{3},$$

$$\gamma_2^1 = \frac{16\pi}{405}\Big[2h_3^8 + 2h_2^8 - 4h_3^6 h_2^2 - 4h_3^2 h_2^6 + 6h_3^2 h_2^4 + \sqrt{h_3^4 + h_2^4 - h_3^2 h_2^2}(-2h_3^6 - 2h_2^6 + 3h_3^4 h_2^2 + 3h_3^2 h_2^4)\Big],$$

$$\gamma_2^2 = \frac{16\pi}{405}\Big[2h_3^8 + 2h_2^8 - 4h_3^6h_2^2 - 4h_3^2h_2^6 + 6h_3^2h_2^4 - \sqrt{h_3^4 + h_2^4 - h_3^2h_2^2}(-2h_3^6 - 2h_2^6 + 3h_3^4h_2^2 + 3h_3^2h_2^4)\Big],$$

$$\gamma_2^3 = \frac{4\pi h_3^4h_2^2(h_2^2 - h_3^2)}{15},\ \gamma_2^4 = \frac{4\pi h_3^2h_2^4(h_2^2 - h_3^2)}{15},$$

$$\gamma_2^5 = \frac{4\pi h_3^2h_2^2(h_2^2 - h_3^2)^2}{15},$$

$$\gamma_3^1 = \frac{16\pi h_3^2h_2^2}{13125}\Big[16h_3^8 + 16h_2^8 - 36h_3^6h_2^2 - 36h_3^2h_2^6 + 46h_3^4h_2^4 + \sqrt{4h_3^2 + 4h_2^4 - 7h_3^2h_2^2}(-8h_3^6 - 8h_2^6 + 11h_3^4h_2^2 + 11h_3^2h_2^4)\Big],$$

$$\gamma_3^2 = \frac{16\pi h_3^2h_2^2}{13125}\Big[16h_3^8 + 16h_2^8 - 36h_3^6h_2^2 - 36h_3^2h_2^6 + 46h_3^4h_2^4 + \sqrt{4h_3^2 + 4h_2^4 - 7h_3^2h_2^2}(8h_3^6 + 8h_2^6 - 11h_3^4h_2^2 - 11h_3^2h_2^4)\Big],$$

$$\gamma_3^3 = \frac{16\pi h_3^2h_1^2}{13125}\Big[6h_3^8 + 16h_2^8 - 12h_3^6h_2^2 - 28h_3^2h_2^6 + 34h_3^4h_2^4 + \sqrt{h_3^4 + 4h_2^4 - h_3^2h_2^2}(-6h_3^6 - 8h_2^6 + 9h_3^4h_2^2 + 13h_3^2h_2^4)\Big],$$

$$\gamma_3^4 = \frac{16\pi h_3^2h_1^2}{13125}\Big[6h_3^8 + 16h_2^8 - 12h_3^6h_2^2 - 28h_3^2h_2^6 + 34h_3^4h_2^4 + \sqrt{h_3^4 + 4h_2^4 - h_3^2h_2^2}(6h_3^6 + 8h_2^6 - 9h_3^4h_2^2 - 13h_3^2h_2^4)\Big],$$

$$\gamma_3^5 = \frac{16\pi h_3^2h_1^2}{13125}\Big[16h_3^8 + 6h_2^8 - 28h_3^6h_2^2 - 12h_3^2h_2^6 + 34h_3^4h_2^4 + \sqrt{4h_3^2 + h_2^4 - h_3^2h_2^2}(-8h_3^6 - 6h_2^6 + 13h_3^4h_2^2 + 9h_3^2h_2^4)\Big],$$

$$\gamma_3^6 = \frac{16\pi h_3^2 h_1^2}{13125}\Big[16h_3^8 + 6h_2^8 - 28h_3^6h_2^2 - 12h_3^2h_2^6 + 34h_3^4h_2^4 + \sqrt{4h_3^2 + h_2^4 - h_3^2h_2^2}(8h_3^6 + 6h_2^6 - 13h_3^4h_2^2 - 9h_3^2h_2^4)\Big],$$

$$\gamma_3^7 = \frac{4\pi h_3^4 h_2^4 h_1^4}{105}.$$

Appendix C

Transceiver Hardware Implementation Code Listing

C.1 Verilog Implementation of Transmitter State Machine Operation

Listing C.1 Code listing showing the transmitter state machine operation

```
`include "cypress.v"

module tx (
        input wire preamble_zero,
        input wire data_zero,
        input wire clk,
        output reg reset_preamb,
        output wire [6:0] tx_states);

    localparam
    STATE_PREAMBLE_START    = 0,
    STATE_PREAMBLE1         = 1,
```

```
STATE_PREAMBLE2          = 2,
STATE_PREAMBLE3          = 3,
STATE_DATA_START         = 4,
STATE_DATA               = 5,
STATE_PREAMBLE2P         = 6,
STATE_PREAMBLE3P         = 7;


localparam
PACKET_DATA_SZ      = 1024,
PACKET_PREAMB_SZ    = 32;

reg [2:0] state, state_i;
//initial state = STATE_PREAMBLE_START;

assign tx_states[0] = (state==STATE_PREAMBLE_START);
assign tx_states[1] = (state==STATE_PREAMBLE1);
assign tx_states[2] = (state==STATE_PREAMBLE2);
assign tx_states[3] = (state==STATE_PREAMBLE3);
assign tx_states[4] = (state==STATE_DATA_START);
assign tx_states[5] = (state==STATE_DATA);

wire [7:0] control;
wire [7:0] status;


assign status[5:0] = tx_states;
assign status[7:6] = 2'b00;

cy_psoc3_control #(.cy_force_order(`TRUE)) ctrl (
    .control(control)
);

cy_psoc3_status #(  .cy_force_order(`TRUE),
                    .cy_md_select(8'b00000000)) stat (
```

```
    .reset(1'b0),
    .clock(clk),
    .status(status)
);

always @(control or state or preamble_zero or data_zero)
   begin : next_state_proc
state_i <= state;

case (state)
    STATE_PREAMBLE_START: begin
        if (control[0] == 1) begin
             reset_preamb = 1'b1;
             state_i <= STATE_PREAMBLE1;
        end
    end


    STATE_PREAMBLE1: begin
        reset_preamb = 1'b0;
        if (preamble_zero == 1) begin
            reset_preamb = 1'b1;
            state_i <= STATE_PREAMBLE2;
        end
    end

    STATE_PREAMBLE2: begin
        reset_preamb = 1'b0;
        if (preamble_zero==1) begin
            reset_preamb = 1'b1;
            state_i <= STATE_PREAMBLE3;
        end
    end
```

```
        STATE_PREAMBLE3: begin
            reset_preamb = 1'b0;
            if (preamble_zero==1) begin
                reset_preamb = 1'b0;
                state_i <= STATE_DATA_START;
            end
        end


        STATE_DATA_START: begin
            reset_preamb = 1'b0;
            state_i <= STATE_DATA;
        end

        STATE_DATA: begin
            if (data_zero == 1) begin
                reset_preamb = 1'b1;
                state_i <=     STATE_PREAMBLE1;//
                   STATE_PREAMBLE_START; //
            end
        end

        default:
            state_i <= STATE_PREAMBLE_START;

    endcase
    end /* next_state_proc */

    always @(posedge clk) begin : counter_proc
        state <= state_i;
        //reset_preamb <= reset_preamb_i;
    end /* counter_proc */

endmodule
```

C.2 Top Level Modular Implementation of the Receiver Digital End in VHDL

Listing C.2 Code listing showing the top level modular implementation of the receiver digital end

```
%\begin{minted}{vhdl}
library IEEE;
use IEEE.STD_LOGIC_1164.ALL;


entity Receiver_top_level is
Port ( data_i_rec: in  STD_LOGIC;
    clk_in_rec   : in  STD_LOGIC;
    data_out_rec : inout  STD_LOGIC;
    clk_out_rec  : inout  STD_LOGIC;
    clk_in       : in  STD_LOGIC;
    reset_rec    : in  STD_LOGIC;
    is_preamble  : inout  STD_LOGIC;
    is_data      : inout  STD_LOGIC;
    decoded_data : out  STD_LOGIC;
    locked_out   : out  STD_LOGIC;
    debug_out    : out  STD_LOGIC;
    HW_out_rec1  : inout  STD_LOGIC_VECTOR (5 downto 0);
    HW_out_rec2  : inout  STD_LOGIC_VECTOR (5 downto 0);
    HW_out_rec3  : inout  STD_LOGIC_VECTOR (5 downto 0));
end Receiver_top_level;

architecture top_level_Arch of Receiver_top_level is


component CDR_top_Level
  Port ( clkin          : in  STD_LOGIC;
    rstin       : in  STD_LOGIC;
    datainx1    : in  STD_LOGIC;
```

```
    datainx2    : in  STD_LOGIC;
    locked      : out  STD_LOGIC;
    clk_main    : out  STD_LOGIC;
    outdata1    : out  STD_LOGIC;
    outdata2    : out  STD_LOGIC);
end component;

component Ser2Par_HW
  Port ( data_in : in  STD_LOGIC;
    CLKn : in  STD_LOGIC;
    --HW_in : inout  STD_LOGIC_VECTOR (35 downto 0);
    HW_out1 : inout  STD_LOGIC_VECTOR (5 downto 0);
    HW_out2 : inout  STD_LOGIC_VECTOR (5 downto 0);
    HW_out3 : inout  STD_LOGIC_VECTOR (5 downto 0));
end component;

component Despreading_lfsr
  Port ( CLKn : in  STD_LOGIC;
    RSTn : in  STD_LOGIC;
    --data_out : out  STD_LOGIC_VECTOR (6 downto 0));
    data_out_lsb : out  STD_LOGIC);
end component;

component Rx_State_machine
  Port ( CLKn : in  STD_LOGIC;
    reset : in  STD_LOGIC;
    preamble1_score : in  STD_LOGIC_VECTOR (5 downto 0);
    preamble2_score : in  STD_LOGIC_VECTOR (5 downto 0);
    preamble3_score : in  STD_LOGIC_VECTOR (5 downto 0);
    data_score          : in  STD_LOGIC_VECTOR (9 downto 0);
    premable_state      : out  STD_LOGIC;
    data_state          : out  STD_LOGIC);
end component;

component Demodulator is
```

```
  Port ( CLKn : in  STD_LOGIC;
    reset : in  STD_LOGIC;
    data_in : in  STD_LOGIC;
    despreader_in : in  STD_LOGIC;
    demod_out : inout  STD_LOGIC);
end component;

component Data_counter is
  Port ( CLKn : in  STD_LOGIC;
    reset : in  STD_LOGIC;
    count_out : out  STD_LOGIC_VECTOR (9 downto 0));
end component;

component small_preamb is
  Port ( CLKn : in  STD_LOGIC;
    data_in : in  STD_LOGIC;
    data_out : inout  STD_LOGIC);
end component;

signal clk_in_rec_1 : STD_LOGIC;
signal i_data_unsync : STD_LOGIC; -- added for debug

signal clk_rec_i : STD_LOGIC;
signal clk_rec : STD_LOGIC;
signal locked_in : STD_LOGIC := '0';
signal i_data_sync : STD_LOGIC;
signal i_data_sync2 : STD_LOGIC;
signal reset_preamb: STD_LOGIC;
signal reset_data : STD_LOGIC;
signal premable_state_i : STD_LOGIC;
signal data_state_i : STD_LOGIC;
signal decoder_prs : STD_LOGIC;
signal decoded_data_i : STD_LOGIC;
signal data_count_out :  STD_LOGIC_VECTOR (9 downto 0);
signal clk_main : STD_LOGIC;
```

```
signal clk_main_o : STD_LOGIC;
--signal data_out_rec_i : inout  STD_LOGIC;
--signal clk_out_rec : inout  STD_LOGIC;

signal i_data_sync_delayed : STD_LOGIC;
signal i_data_sync_delayed1 : STD_LOGIC;
signal i_data_sync_delayed2 : STD_LOGIC;
signal i_data_sync_delayed3 : STD_LOGIC;
signal premable_state_delayed : STD_LOGIC;
signal data_out_small_preamb : STD_LOGIC;
signal rst_CDR_i: std_logic;
--signal is_preamble_i : std_logic := (others => '0');

signal data_test_out :  STD_LOGIC_VECTOR (4 downto 0) := (others
    => '0');
signal clk_in_o : STD_LOGIC :='0';

begin
CDR_reseter: entity work.reset_CDR
  Port map( CLKn=> clk_in_rec_1,
    reset       => reset_rec,
    rst_CDR     => rst_CDR_i,
    count_out   => open);


CDR_align : component CDR_top_Level
  port map( clkin => clk_in,
     rstin      => reset_rec,
     datainx1   => data_i_rec,
     datainx2   => clk_in_o,
     locked     => locked_in,
     clk_main   => clk_main,
     outdata1   => i_data_sync,
     outdata2   => clk_rec);
```

```
Preamble_searcher : component Ser2Par_HW
  Port map( data_in     => i_data_sync,
    CLKn        => clk_in_rec_1,
    HW_out1     => HW_out_rec1,
    HW_out2     => HW_out_rec2,
    HW_out3     => HW_out_rec3);

PRS_gen : component Despreading_lfsr
 Port map( CLKn     => clk_in_rec_1,
    RSTn            => premable_state_i,
    data_out_lsb    => decoder_prs);

State_machine : component Rx_State_machine
  Port map( CLKn    => clk_in_rec_1,
    reset           => reset_rec,
    preamble1_score => HW_out_rec1,
    preamble2_score => HW_out_rec2,
    preamble3_score => HW_out_rec3,
    data_score      => data_count_out,
    premable_state  => premable_state_i,
    data_state      => data_state_i);

Decoder: component Demodulator
  Port map( CLKn        => clk_in_rec_1,
    reset           => premable_state_i,
    data_in             => i_data_sync_delayed,
    despreader_in       => decoder_prs,
    demod_out           => decoded_data_i);


data_conter: component Data_counter
  Port map( CLKn        => clk_in_rec_1,
    reset       => premable_state_i,
    count_out   => data_count_out);
```

```
small_preamb_1 : component small_preamb
  Port map( CLKn=>      clk_in_rec_1,
    data_in     =>      i_data_sync_delayed,
    data_out    =>      data_out_small_preamb);


decoded_data    <= decoded_data_i and data_state_i;
is_preamble     <= premable_state_i;
is_data         <= data_state_i;
clk_in_rec_1    <= clk_rec;--clk_in_o;
i_data_unsync   <= data_i_rec;
data_out_rec    <= i_data_sync;
locked_out      <= locked_in;
clk_main_o      <= clk_main;

debug_proc1 : process(clk_main) is
begin
        if clk_main'event and clk_main ='1' then
                clk_in_o <= not clk_in_o;
        end if;
end process;

debug_proc : process(clk_main_o) is
begin
   clk_out_rec  <= clk_rec;
        if clk_main_o'event and clk_main_o ='1' then
        i_data_sync_delayed2    <= i_data_sync;
        --i_data_sync_delayed2  <= i_data_sync_delayed3;
        i_data_sync_delayed1    <= i_data_sync_delayed2;
        i_data_sync_delayed     <= i_data_sync_delayed1;
        premable_state_delayed  <= premable_state_i;
        debug_out                               <= data_out_rec;
        data_test_out(0) <= i_data_sync;
        data_test_out(1) <= data_test_out(0);
        data_test_out(2) <= data_test_out(1);
```

```
        data_test_out(3) <= data_test_out(2);
        data_test_out(4) <= data_test_out(3);
        end if;
end process;
end top_level_Arch;
%\end{minted}
```

C.3 Top Level Modular Implementation of Clock Data Recovery and Data Synchroniser at the Receiver Digital End in VHDL

Listing C.3 Code listing showing the top level modular implementation of clock data recovery and data synchroniser at the receiver digital end

```
library IEEE;
use IEEE.STD_LOGIC_1164.ALL;
library unisim ;
use unisim.vcomponents.all ;

entity CDR_top_Level is
  Port ( clkin : in  STD_LOGIC;
    rstin : in  STD_LOGIC;
    datainx1 : in  STD_LOGIC;
    datainx2 : in  STD_LOGIC;
    locked : out  STD_LOGIC;
    clk_main : out  STD_LOGIC;
    outdata1 : out  STD_LOGIC;
    outdata2 : out  STD_LOGIC);
end CDR_top_Level;

architecture CDR_top_Level_arch of CDR_top_Level is

component sync_master_v2 port (
        clk             : in std_logic ;-- clock input
        clk90           : in std_logic ;-- clock 90 input
        datain1         : in std_logic ;-- data inputs
        datain2         : in std_logic ;-- data inputs
        rst             : in std_logic ;-- reset input
        useaout         : out std_logic ;-- useA output for
           cascade
```

```
        usebout          : out std_logic ;-- useB output for
           cascade
        usecout          : out std_logic ;-- useC output for
           cascade
        usedout          : out std_logic ;-- useD output for
           cascade
        ctrlout          : out std_logic_vector(1 downto 0) ;--
           ctrl outputs for cascade
        sdataout1        : out std_logic;
        sdataout2        : out std_logic);-- data out
end component;


signal clk               : std_logic;
signal clkdcm            : std_logic;
signal clkint            : std_logic;
signal clk90             : std_logic;
signal clk90dcm          : std_logic;
signal outdataint1       : std_logic ;
signal outdataint2       : std_logic;
signal ctrl              : std_logic_vector(1 downto 0) ;
signal usea              : std_logic;
signal useb              : std_logic;
signal usec              : std_logic;
signal used              : std_logic;
signal clkfbout :std_logic;

begin
pll_base_inst : PLL_BASE
  generic map
   (BANDWIDTH            => "OPTIMIZED",
    CLK_FEEDBACK         => "CLKFBOUT",
    COMPENSATION         => "INTERNAL",
    DIVCLK_DIVIDE        => 1,
    CLKFBOUT_MULT        => 13,
```

```
    CLKFBOUT_PHASE       => 0.000,
    CLKOUT0_DIVIDE       => 52,--104,
    CLKOUT0_PHASE        => 0.000,
    CLKOUT0_DUTY_CYCLE   => 0.500,
    CLKOUT1_DIVIDE       => 52,--104,
    CLKOUT1_PHASE        => 90.000,
    CLKOUT1_DUTY_CYCLE   => 0.500,
    CLKIN_PERIOD         => 31.250,
    REF_JITTER           => 0.010)
  port map
    -- Output clocks
   (CLKFBOUT            => clkfbout,
    CLKOUT0             => clkdcm,
    CLKOUT1             => clk90dcm,
    CLKOUT2             => open,
    CLKOUT3             => open,
    CLKOUT4             => open,
    CLKOUT5             => open,
    -- Status and control signals
    LOCKED              => LOCKED,
    RST                 => '0',
    -- Input clock control
    CLKFBIN             => clkfbout,
    CLKIN               => clkint);


ibufg1 : ibufg port map(i => clkin, o => clkint );

bufg1 : bufg port map(i => clkdcm, o => clk );

bufg2 : bufg port map(i => clk90dcm, o => clk90 );


CDR_sync1: entity work.CDR_sync
 Port map( clk_in       => clk, --clk_rec, ----
```

```
    clk_in_90           => clk90,--premable_state_delayed,--
    reset                           => rstin,
    data_in                 => datainx1,
    data_out                => outdataint1              );

CDR_sync2: entity work.CDR_sync
  Port map( clk_in              => clk, --clk_rec, ----
    clk_in_90           => clk90,--premable_state_delayed,--
    reset                           => rstin,
    data_in                 => datainx2,
    data_out                => outdataint2              );

process (clk, rstin)
        begin
                if rstin = '1' then
                        outdata1 <= '0';
                        outdata2 <= '0';--<= (others => '0' ) ;
                elsif clk'event and clk = '1' then
                        outdata1 <= outdataint1 ;
                        outdata2 <= outdataint2 ;
                end if ;
        end process ;
        clk_main <= clk;
end CDR_top_Level_arch;
```

C.4 Detailed Implementation of CDR Synchroniser at the Receiver Digital End in VHDL

Listing C.4 Code listing showing the detailed implementation of CDR synchroniser at the receiver digital end

```
library ieee;
use ieee.std_logic_1164.all;
use ieee.numeric_std.all;


use work.bits.all;

entity CDR_Sync is
        port (
                clk_in, reset : in std_logic;
                clk_in_90 : in std_logic;
                data_in : in std_logic;
                data_out : out std_logic);
end CDR_Sync;

architecture CDR_Sync_arch of CDR_Sync is

    constant CYC_BUFF_SZ : natural := 64;

    signal clk_in_180 : std_logic;
    signal clk_in_270 : std_logic;

    signal data_in_0    : std_logic_vector (1 downto 0);
    signal data_in_90   : std_logic_vector (1 downto 0);
    signal data_in_180  : std_logic_vector (1 downto 0);
    signal data_in_270  : std_logic_vector (1 downto 0);
```

```
    signal AA_cycle     : std_logic_vector (CYC_BUFF_SZ-1 downto
        0);
    signal BB_cycle     : std_logic_vector (CYC_BUFF_SZ-1 downto
        0);
    signal CC_cycle     : std_logic_vector (CYC_BUFF_SZ-1 downto
        0);
    signal DD_cycle     : std_logic_vector (CYC_BUFF_SZ-1 downto
        0);

    signal AA_n, AA_p : std_logic;
    signal BB_n, BB_p : std_logic;
    signal CC_n, CC_p : std_logic;
    signal DD_n, DD_p : std_logic;

    signal use_0, use_0_latch : std_logic;
    signal use_90, use_90_latch : std_logic;
    signal use_180, use_180_latch : std_logic;
    signal use_270, use_270_latch : std_logic;

    signal previous_shift : std_logic;
    signal delay_time : unsigned (bits_for_val(CYC_BUFF_SZ-1)-1
       downto 0);

    signal delay_data_in_0 : std_logic_vector (1 downto 0);
    signal delay_data_in_90 : std_logic_vector (1 downto 0);
    signal delay_data_in_180 : std_logic_vector (1 downto 0);
    signal delay_data_in_270 : std_logic_vector (1 downto 0);


begin

    clk_in_180 <= not clk_in;
    clk_in_270 <= not clk_in_90;

    -- Oversample input signal using 4 phases of clk_in
```

```
sample_0 : process(clk_in) begin
    if clk_in'event and clk_in = '1' then
        data_in_0(0) <= data_in;
        -- Resample onto clk_in
        data_in_0(1) <= data_in_0(0);
        data_in_90(1) <= data_in_90(0);
        data_in_180(1) <= data_in_180(0);
    end if;
end process sample_0;

sample_90 : process(clk_in_90) begin
    if clk_in_90'event and clk_in_90 = '1' then
        data_in_90(0) <= data_in;
        data_in_270(1) <= data_in_270(0);
    end if;
end process sample_90;

sample_180 : process(clk_in_180) begin
    if clk_in_180'event and clk_in_180 = '1' then
        data_in_180(0) <= data_in;
    end if;
end process sample_180;

sample_270 : process(clk_in_270) begin
    if clk_in_270'event and clk_in_270 = '1' then
        data_in_270(0) <= data_in;
    end if;
end process sample_270;

wrap_delay : process (clk_in) begin
    if clk_in'event and clk_in = '1' then
        AA_cycle <= concat_bit(AA_cycle, data_in_0(1));
        BB_cycle <= concat_bit(BB_cycle, data_in_90(1));
        CC_cycle <= concat_bit(CC_cycle, data_in_180(1));
        DD_cycle <= concat_bit(DD_cycle, data_in_270(1));
```

```
    end if;
end process wrap_delay;

delay_data_in_0(0) <=AA_cycle(to_integer(delay_time));
delay_data_in_90(0) <=BB_cycle(to_integer(delay_time));
delay_data_in_180(0) <=CC_cycle(to_integer(delay_time));
delay_data_in_270(0) <=DD_cycle(to_integer(delay_time));

edge_store : process(clk_in) begin
    if clk_in'event and clk_in = '1' then
        delay_data_in_0(1) <= delay_data_in_0(0);
        delay_data_in_90(1) <= delay_data_in_90(0);
        delay_data_in_180(1) <= delay_data_in_180(0);
        delay_data_in_270(1) <= delay_data_in_270(0);
    end if;
end process edge_store;

find_edge : process(clk_in) begin
    if clk_in'event and clk_in = '1' then
       AA_p <= (delay_data_in_0(1)   xor delay_data_in_0(0))
                  and delay_data_in_0(0);
   BB_p <= (delay_data_in_90(1)  xor delay_data_in_90(0))
      and delay_data_in_90(0);
   CC_p <= (delay_data_in_180(1) xor delay_data_in_180(0))
      and delay_data_in_180(0);
   DD_p <= (delay_data_in_270(1) xor delay_data_in_270(0))
      and delay_data_in_270(0);
       AA_n <= (delay_data_in_0(1)   xor delay_data_in_0(0))
                  and not delay_data_in_0(0);
   BB_n <= (delay_data_in_90(1)  xor delay_data_in_90(0))
      and not delay_data_in_90(0);
   CC_n <= (delay_data_in_180(1) xor delay_data_in_180(0))
      and not delay_data_in_180(0);
   DD_n <= delay_data_in_270(1) xor delay_data_in_270(0))
      and not delay_data_in_270(0);
```

```
    end if;
end process find_edge;

phase_picker : process(clk_in) begin
    if clk_in'event and clk_in = '1' then
        use_0   <= (AA_p and BB_p and not CC_p and not DD_p)
            or
                   (AA_n and  BB_n and not CC_n and not DD_n
                      );
    use_90  <= (AA_p and BB_p and CC_p and not DD_p) or
                   (AA_n and BB_n and CC_n and not DD_n);
    use_180 <= (AA_p and BB_p and CC_p and DD_p) or
                   (AA_n and BB_n and CC_n and DD_n);
    use_270 <= (AA_p and not BB_p and not CC_p and not DD_p)
        or
                   (AA_n and not BB_n and not CC_n and not
                      DD_n);
    end if;
end process phase_picker;

phase_latch : process(clk_in) begin
    if clk_in'event and clk_in = '1' then
        if reset = '1' then
            use_0_latch <= '0';
            use_90_latch <= '0';
            use_180_latch <= '0';
            use_270_latch <= '0';

        elsif ((use_0 and not use_180_latch) or
            (use_90 and not use_270_latch) or
            (use_180 and not use_0_latch) or
            (use_270 and not use_90_latch)) = '1' then

            use_0_latch <= use_0;
            use_90_latch <= use_90;
```

```
                use_180_latch <= use_180;
                use_270_latch <= use_270;
            end if;
        end if;
    end process phase_latch;


    cycle_detect : process(clk_in, reset) begin
        if clk_in'event and clk_in = '1' then
            if reset = '1' then
                delay_time <= to_unsigned(CYC_BUFF_SZ/2,
                    delay_time'length);

            elsif (use_270_latch and use_0) = '1' then
                previous_shift <= '0';
                delay_time <= delay_time - 1;

            elsif (use_0_latch and use_270) = '1' then
                previous_shift <= '1';
                delay_time <= delay_time + 1;

            end if;
        end if;
    end process cycle_detect;

    data_out <= (delay_data_in_0(0)   and use_0_latch) or
                (delay_data_in_90(0)  and use_90_latch) or
                (delay_data_in_180(0) and use_180_latch) or
                (delay_data_in_270(0) and use_270_latch);

end CDR_Sync_arch;
```

C.5 VHDL Implementation of Local Despreading PRS Generation at the Receiver Digital End

Listing C.5 Code listing showing implementation of local despreading PRS generation at the receiver digital end

```
library IEEE;
use IEEE.STD_LOGIC_1164.ALL;

entity Despreading_lfsr is
    Port ( CLKn : in  STD_LOGIC;
           RSTn : in  STD_LOGIC;
           --data_out : inout  STD_LOGIC_VECTOR (7 downto 0):=
              "00000000";
                          data_out_lsb: out STD_LOGIC);
end Despreading_lfsr;

architecture Behavioral of Despreading_lfsr is


component DFlipFlop
Port (  CLKn : in std_logic;
         RSTn : in std_logic;
         D : in std_logic;
         Q : out std_logic);
end component;


signal data_reg1 : std_logic_vector(7 downto 0) := "00000001";
signal data_reg2 : std_logic_vector(7 downto 0) := "00000001";

signal tap_reg : std_logic_vector(7 downto 0) ;
```

```
signal tap_data1 : std_logic;--_vector(0 downto 0) ;
signal tap_data2 : std_logic;--_vector(0 downto 0) ;
signal data_out :  STD_LOGIC_VECTOR (7 downto 0) := "11111111";

begin
 process(CLKn,RSTn) is
   begin
                tap_data1 <= ( data_reg1(1) xor data_reg1(2) xor
                    data_reg1(3) xor data_reg1(7)); -- X^8 + X
                   ^6 + X^5 + X^4 + 1
                tap_data2 <= ( data_reg2(3) xor data_reg2(4) xor
                    data_reg2(5) xor data_reg2(7)); -- X^8 + X
                   ^4 + X^3 + X^2 + 1
  end process;


  stage0: DFlipFlop
        port map(CLKn, RSTn, tap_data1, data_reg1(0));
  stage1: DFlipFlop
        port map(CLKn, RSTn, tap_data2, data_reg2(0));

  g0:for i in 0 to 6 generate
                stageN1: DFlipFlop port map(CLKn, RSTn,
                   data_reg1(i), data_reg1(i+1));
  end generate;

  g1:for i in 0 to 6 generate
                stageN2: DFlipFlop port map(CLKn, RSTn,
                   data_reg2(i), data_reg2(i+1));
  end generate;

  data_out <= data_reg1 xor data_reg2;
  data_out_lsb <= data_out(7);

end Behavioral;
```

C.6 VHDL Implementation of the Preamble Tracker at the Receiver Digital End

Listing C.6 Code listing showing implementation of the preamble tracker at the receiver digital end

```
library IEEE;
use IEEE.STD_LOGIC_1164.ALL;
use IEEE.NUMERIC_STD.ALL;
use IEEE.STD_LOGIC_UNSIGNED.ALL;



entity Search_Preamble is
  Port ( data_in : in  STD_LOGIC;
    CLKn : in  STD_LOGIC;
    HW_out1 : inout  STD_LOGIC_VECTOR (5 downto 0);
    HW_out2 : inout  STD_LOGIC_VECTOR (5 downto 0);
    HW_out3 : inout  STD_LOGIC_VECTOR (5 downto 0)
);
end Search_Preamble; --Ser2Par_HW;

architecture Behavioral of Search_Preamble is

component Shift_reg96
  port( data2shift : in  STD_LOGIC;
        CLKn : in  STD_LOGIC;
        shiftOut : inout  STD_LOGIC_VECTOR (92 downto 0));
end component;

component HW_CHAIN
  port( CLKn : in  STD_LOGIC;
    i_data_m : in  STD_LOGIC_VECTOR (35 downto 0);
    o_data_m : inout  STD_LOGIC_VECTOR (5 downto 0));
end component;
```

```
component xor_32_clked
  port( CLKn : in  STD_LOGIC;
    data_in1 : in  STD_LOGIC_VECTOR(30 downto 0);
    data_in2 : in  STD_LOGIC_VECTOR(30 downto 0);
    data_out : inout  STD_LOGIC_VECTOR(30 downto 0));
end component;

signal shift_reg_data : STD_LOGIC_VECTOR(92 downto 0)  := (
   others => '0');
signal shift_reg_out1 : STD_LOGIC_VECTOR(30 downto 0)  := (
   others => '0');
signal shift_reg_out2 : STD_LOGIC_VECTOR(30 downto 0)  := (
   others => '0');
signal shift_reg_out3 : STD_LOGIC_VECTOR(30 downto 0)  := (
   others => '0');
signal Preamble_seq1 :  STD_LOGIC_VECTOR(30 downto 0);-- :=
   "01110001010110100001100100111110";
signal Preamble_seq2 :  STD_LOGIC_VECTOR(30 downto 0);-- :=
   "10001110101001011110011011000001";
signal Preamble_seq3 :  STD_LOGIC_VECTOR(30 downto 0);-- :=
   "01110001010110100001100100111110";

signal HW_out1_i :   STD_LOGIC_VECTOR (5 downto 0):= (others =>
   '0');
signal HW_out2_i :   STD_LOGIC_VECTOR (5 downto 0):= (others =>
   '0');
signal HW_out3_i :   STD_LOGIC_VECTOR (5 downto 0):= (others =>
   '0');

signal HW_in1 : STD_LOGIC_VECTOR(35 downto 0) := (others => '0')
   ; --:= "000000000000000000000000000000000000";
signal HW_in3 : STD_LOGIC_VECTOR(35 downto 0) := (others => '0')
   ; -- := "000000000000000000000000000000000000";
```

```
signal HW_in2 : STD_LOGIC_VECTOR(35 downto 0) := (others => '0')
   ; --:= "000000000000000000000000000000000000";


begin

 Preamble_seq1 <= "011111001001100001011010100011 1";
 Preamble_seq2 <= "100000110110011111010010101110 00";
 Preamble_seq3 <= "011111001001100001011010100011 1";

 HW_in1(35 downto 31) <= "00000";
 HW_in2(35 downto 31) <= "00000";
 HW_in3(35 downto 31) <= "00000";

 shift_reg_out1 <= shift_reg_data(30 downto 0);
 shift_reg_out2 <= shift_reg_data(61 downto 31);
 shift_reg_out3 <= shift_reg_data(92 downto 62);



 Shift_reg96_1: Shift_reg96
   port map( data2shift => data_in,
     CLKn => CLKn,
     shiftOut => shift_reg_data);

 HW_CHAIN_1: HW_CHAIN
     port map( CLKn => CLKn,
        i_data_m => HW_in1,
         o_data_m => HW_out1_i);

 HW_CHAIN_2: HW_CHAIN
     port map( CLKn => CLKn,
         i_data_m => HW_in2,
         o_data_m => HW_out2_i);

 HW_CHAIN_3: HW_CHAIN
```

```
    port map( CLKn => CLKn,
        i_data_m => HW_in3,
        o_data_m => HW_out3_i);


xor31_1: xor_32_clked
    port map(  CLKn => CLKn,
       data_in1 => shift_reg_out1,
       data_in2 => Preamble_seq1,
       data_out => HW_in1(30 downto 0));
xor31_2: xor_32_clked
    port map(  CLKn => CLKn,
       data_in1 => shift_reg_out2,
       data_in2 => Preamble_seq2,
       data_out => HW_in2(30 downto 0));

xor31_3: xor_32_clked
    port map(  CLKn => CLKn,
       data_in1 => shift_reg_out3,
       data_in2 => Preamble_seq3,
       data_out => HW_in3(30 downto 0));

state_sync_proc: process(CLKn) is
    begin
       if CLKn'event and CLKn ='1' then
                       HW_out1 <= HW_out1_i;
                       HW_out2 <= HW_out2_i;
                       HW_out3 <= HW_out3_i;
       end if;
    end process;-- state_sync_proc

end Behavioral;
```

C.7 Lookup Table Based VHDL Implementation the Hamming Weight Calculator in only Four Clock Cycles

Listing C.7 Lookup table based implementation the Hamming weight calculator in only four clock cycles

```
library IEEE;
use IEEE.STD_LOGIC_1164.ALL;
use IEEE.NUMERIC_STD.ALL;
use IEEE.STD_LOGIC_UNSIGNED.ALL;

entity HW_CHAIN is
  Port (  CLKn : in  STD_LOGIC;
    i_data_m : in  STD_LOGIC_VECTOR (35 downto 0);
    o_data_m : inout  STD_LOGIC_VECTOR (5 downto 0)--;
    );
end HW_CHAIN;

architecture Behavioral of HW_CHAIN is

        signal o_data1   : STD_LOGIC_VECTOR (2 downto 0);
        signal o_data2   : STD_LOGIC_VECTOR (2 downto 0);
        signal o_data3   : STD_LOGIC_VECTOR (2 downto 0);
        signal o_data4   : STD_LOGIC_VECTOR (2 downto 0);
        signal o_data5   : STD_LOGIC_VECTOR (2 downto 0);
        signal o_data6   : STD_LOGIC_VECTOR (2 downto 0);

        signal i_data12   : STD_LOGIC_VECTOR (5 downto 0);
        signal i_data11   : STD_LOGIC_VECTOR (5 downto 0);
        signal i_data10   : STD_LOGIC_VECTOR (5 downto 0);

   signal o_data12   : STD_LOGIC_VECTOR (2 downto 0);
```

```
        signal o_data11   : STD_LOGIC_VECTOR (2 downto 0);
        signal o_data10   : STD_LOGIC_VECTOR (2 downto 0);

-------------------------------------------------------
---- Translate vector to bits (3 bits)----------------

   signal o_gndd   : STD_LOGIC;
   signal o_gndd1   : STD_LOGIC;
   signal o_gndd2   : STD_LOGIC;

   signal o_data00   : STD_LOGIC;
   signal o_data01  : STD_LOGIC;
   signal o_data02   : STD_LOGIC;

   signal o_data60   : STD_LOGIC;
   signal o_data61  : STD_LOGIC;
   signal o_data62   : STD_LOGIC;

   signal o_data20   : STD_LOGIC;
   signal o_data21  : STD_LOGIC;
   signal o_data22   : STD_LOGIC;

   signal o_data30   : STD_LOGIC;
   signal o_data31  : STD_LOGIC;
   signal o_data32   : STD_LOGIC;

   signal o_data40   : STD_LOGIC;
   signal o_data41  : STD_LOGIC;
   signal o_data42   : STD_LOGIC;

   signal o_data50   : STD_LOGIC;
   signal o_data51  : STD_LOGIC;
   signal o_data52   : STD_LOGIC;

   -- second stage LUT o/p
```

```
    signal o_data70   : STD_LOGIC;
    signal o_data71   : STD_LOGIC;
    signal o_data72   : STD_LOGIC;

    signal o_data80   : STD_LOGIC;
    signal o_data81   : STD_LOGIC;
    signal o_data82   : STD_LOGIC;

    signal o_data90   : STD_LOGIC;
    signal o_data91   : STD_LOGIC;
    signal o_data92   : STD_LOGIC;

    -- Adder stages
    signal i_sum11   : STD_LOGIC_VECTOR (4 downto 0);
    signal i_sum12   : STD_LOGIC_VECTOR (4 downto 0);

    signal i_sum21   : STD_LOGIC_VECTOR (5 downto 0);
    signal i_sum22   : STD_LOGIC_VECTOR (5 downto 0);

------------------------------------------------------------
-------  instantiate components  --------------------------
component LUT6_HW
  port( CLKn : in  STD_LOGIC;
    i_data : in  STD_LOGIC_VECTOR (5 downto 0);
    --o_data : inout  STD_LOGIC_VECTOR (2 downto 0);
    o_data000 : out  STD_LOGIC;
    o_data111 : out  STD_LOGIC;
    o_data222 : out  STD_LOGIC);
end component;


signal sum_a : unsigned(4 downto 0);
signal sum_b : unsigned(5 downto 0);
------------------------------------------------------------
```

```
begin

        o_gndd <='0';
        o_gndd1 <='0';
        o_gndd2 <='0';

-- First stage LUTs
LUT6H_1: LUT6_HW
  port map(     CLKn => CLKn,
        i_data => i_data_m(35 downto 30),
        o_data000 => o_data00,
        o_data111 => o_data01,
        o_data222 => o_data02
        );
LUT6H_2: LUT6_HW
  port map(     CLKn => CLKn,
        i_data => i_data_m(29 downto 24),
        o_data000 => o_data60,
        o_data111 => o_data61,
        o_data222 => o_data62
        );
LUT6H_3: LUT6_HW
  port map(     CLKn => CLKn,
        i_data => i_data_m(23 downto 18),
        o_data000 => o_data20,
        o_data111 => o_data21,
        o_data222 => o_data22
        );
LUT6H_4: LUT6_HW
  port map(     CLKn => CLKn,
        i_data => i_data_m(17 downto 12),
        o_data000 => o_data30,
        o_data111 => o_data31,
        o_data222 => o_data32
        );
```

```
LUT6H_5: LUT6_HW
  port map(     CLKn => CLKn,
        i_data => i_data_m(11 downto 6),
        o_data000 => o_data40,
        o_data111 => o_data41,
        o_data222 => o_data42
        );
LUT6H_6: LUT6_HW
  port map(     CLKn => CLKn,
        i_data => i_data_m(5 downto 0),
        o_data000 => o_data50,
        o_data111 => o_data51,
        o_data222 => o_data52
        );


-- inputs to LUT10,LUT11 and LUT12 respectively


-- second stage LUTs
LUT6H_12: LUT6_HW
  port map(     CLKn => CLKn,
        i_data => i_data12,
        o_data000 => o_data70,
        o_data111 => o_data71,
        o_data222 => o_data72
        );
LUT6H_11: LUT6_HW
  port map(     CLKn => CLKn,
        i_data => i_data11,
        o_data000 => o_data80,
        o_data111 => o_data81,
        o_data222 => o_data82
);
LUT6H_10: LUT6_HW
```

```
  port map(     CLKn => CLKn,
        i_data => i_data10,
        o_data000 => o_data90,
        o_data111 => o_data91,
        o_data222 => o_data92
);

 process(i_data_m) is
  begin
--        if CLKn'event and CLKn = '0' then

    i_data10 <= (o_data00 & o_data60 & o_data20 & o_data30 &
       o_data40 & o_data50);
      i_data11 <= (o_data01 & o_data61 & o_data21 & o_data31 &
         o_data41 & o_data51);
    i_data12 <= (o_data02 & o_data62 & o_data22 & o_data32 &
       o_data42 & o_data52);


-- Compiling 1st operand        for the first adder -- from
   LUT21 x4
        i_sum11(0) <= o_gndd;
        i_sum11(1) <= o_gndd;
        i_sum11(2) <= o_data70;
        i_sum11(3) <= o_data71;
        i_sum11(4) <= o_data72;

-- Compiling  2nd operand       for the first adder -- from
   LUT11 x 2
        i_sum12(0) <= o_gndd2;
        i_sum12(1) <= o_data80;
        i_sum12(2) <= o_data81;
        i_sum12(3) <= o_data82;
        i_sum12(4) <= o_gndd2;
```

```
        SUM1_ADDER5bit: sum_a <= unsigned(i_sum11) + unsigned(
           i_sum12);

-- Compiling  1nd operand       for the second adder -- from
   Adder1

        i_sum21(0) <= sum_a(0);
        i_sum21(1) <= sum_a(1);
        i_sum21(2) <= sum_a(2);
        i_sum21(3) <= sum_a(3);
        i_sum21(4) <= sum_a(4);
        i_sum21(5) <= o_gndd1;

-- Compiling  2nd operand       for the second adder -- from
   LUT10 x 1
        i_sum22(0) <= o_data90;
        i_sum22(1) <= o_data91;
        i_sum22(2) <= o_data92;
        i_sum22(3) <= o_gndd1;
        i_sum22(4) <= o_gndd1;
        i_sum22(5) <= o_gndd1;

        SUM2_ADDER6bit : sum_b <= unsigned(i_sum21) + unsigned(
           i_sum22);
        o_data_m <= std_logic_vector(sum_b);
end process;
end Behavioral;
```

C.8 VHDL Implementation of the Receiver State Machine

Listing C.8 VHDL implementation of the receiver state machine.

```
library IEEE;
use IEEE.STD_LOGIC_1164.ALL;
use IEEE.NUMERIC_STD.ALL;
use IEEE.STD_LOGIC_UNSIGNED.ALL;


entity Rx_State_machine is
  Port ( CLKn           : in  STD_LOGIC;
    reset                    : in  STD_LOGIC;
    preamble1_score : in  STD_LOGIC_VECTOR (5 downto 0);
    preamble2_score : in  STD_LOGIC_VECTOR (5 downto 0);
    preamble3_score : in  STD_LOGIC_VECTOR (5 downto 0);
    data_score          : in  STD_LOGIC_VECTOR (9 downto 0);
    premable_state      : out  STD_LOGIC;
    data_state          : out  STD_LOGIC);
end Rx_State_machine;

architecture Behavioral of Rx_State_machine is

    signal STATE_PREAMBLE       : STD_LOGIC;
    signal STATE_DATA           : STD_LOGIC;
    signal preamble_found       : STD_LOGIC;
    signal data_ended       : STD_LOGIC;


    signal preamble1_score1 :   STD_LOGIC_VECTOR (5 downto 0);
    signal preamble2_score1 :   STD_LOGIC_VECTOR (5 downto 0);
    signal premable3_score1 :   STD_LOGIC_VECTOR (5 downto 0);
```

```
    TYPE State_type IS (START_PREAMBLE, PREMBLE, START_DATA,
       DATA);
    SIGNAL State : State_Type;
    SIGNAL State_i : State_Type;


begin

next_state_proc: process(CLKn, reset) is
 begin
    If (reset = '1') then            -- Upon reset, set the
       state to A
        State <= START_PREAMBLE;

    elsif CLKn'event and CLKn ='1' then -- rising_edge(clock)
       THEN
          case State is
                when START_PREAMBLE =>
                  --if P='1' then
                        State <= PREMBLE;
                        data_state <= '0';
                        premable_state <='1';
                  --end if;
                when PREMBLE =>
                  if preamble_found='1' then
                        State <= START_DATA;
                        data_state <= '1';
                        premable_state <='1';
                  end if;
                when START_DATA =>
                  --if P='1' then
                        State <= DATA;
                        data_state <= '1';
                        premable_state <='0';
                  --end if;
```

```
                when DATA=>
                  if data_ended ='1' then
                        State <= START_PREAMBLE;
                        data_state <= '0';
                  end if;
                when others =>
                  State <= START_PREAMBLE;
                  premable_state <='0';
          end case;
    end if;
  end process;
-- next_state_proc

state_sync_proc: process(CLKn) is
        begin
                if CLKn'event and CLKn ='1' then
                                State_i <= State;
                end if;
        end process;
-- state_sync_proc

preamble_checker_proc: process(CLKn) is
  begin
        if CLKn'event and CLKn ='1' then
          if preamble1_score(3) = '0' and  preamble1_score(4) =
              '0' then
                if preamble2_score(3) = '0' and  preamble2_score
                   (4) = '0' then
                  if preamble3_score(3) = '0' and
                     preamble3_score(4) = '0' then
                        preamble_found <= '1';
                        --data_ended <= '0';
                  else
                        preamble_found <= '0';
                  end if;
```

```
                else
                        preamble_found <= '0';
                end if;
          else
                preamble_found <= '0';
          end if;
        end if;
  end process;
-- preamble_checker_proc


data_score_checker_proc: process(CLKn) is
  begin
    if CLKn'event and CLKn ='1' then
        if data_score = "1111111111" then
                data_ended <= '1';
        else
                data_ended <= '0';
        end if;
    end if;
  end process;
-- data_score_checker_proc


end Behavioral;
```

C.9 VHDL Implementation of the Test Bench to Test the Receiver Top Level Architecture

Listing C.9 VHDL implementation of the test bench to test the receiver top level architecture.

```
LIBRARY ieee;
USE ieee.std_logic_1164.ALL;

ENTITY Rceiver_top_level_tb IS
END Rceiver_top_level_tb;

ARCHITECTURE behavior OF Rceiver_top_level_tb IS

    -- Component Declaration for the Unit Under Test (UUT)

    COMPONENT Receiver_top_level
    PORT(
         data_i_rec : IN  std_logic;
         clk_in_rec : IN  std_logic;
                 data_out_rec : inout  STD_LOGIC;
                 clk_out_rec : inout  STD_LOGIC;
         clk_in : IN  std_logic;
         reset_rec : IN  std_logic;
                 is_preamble : INOUT  std_logic;
                 is_data : INOUT  std_logic;
                 d_in : out  STD_LOGIC;
         disp_in : out  STD_LOGIC;
         decoded_data : OUT  std_logic;
                 locked_out : out  STD_LOGIC;
                 debug_out      : out  STD_LOGIC;
         HW_out_rec1 : INOUT  std_logic_vector(5 downto 0);
         HW_out_rec2 : INOUT  std_logic_vector(5 downto 0);
         HW_out_rec3 : INOUT  std_logic_vector(5 downto 0)
        );
    END COMPONENT;


   --Inputs
   signal data_i_rec : std_logic := '0';
   signal clk_in_rec : std_logic := '0';
   signal clk_in : std_logic := '0';
   signal reset_rec : std_logic := '0';
   signal is_preamble : std_logic := '0';
   signal is_data : std_logic := '0';

        --BiDirs
   signal HW_out_rec1 : std_logic_vector(5 downto 0);
   signal HW_out_rec2 : std_logic_vector(5 downto 0);
   signal HW_out_rec3 : std_logic_vector(5 downto 0);
        signal data_out_rec :   STD_LOGIC;
```

```
   signal clk_out_rec :   STD_LOGIC;
        --Outputs
   signal decoded_data : std_logic;
        signal locked_out : STD_LOGIC;
        signal clk_main_o : STD_LOGIC;
        signal debug_out  : STD_LOGIC;
   -- Clock period definitions
   constant clk_in_rec_period : time := 124 ns;
   constant clk_in_period : time := 31.25/2.0*1 ns;

   signal d_in :   STD_LOGIC;
   signal disp_in :   STD_LOGIC;


signal preamble : std_logic_vector(92 downto 0) :=
   "11100010101101000011001000 ....... 001100100111110";
signal data: std_logic_vector(255 downto 0) :=
   "10000111111110010000101001111101010101110000011000101
. . . 10000001110100100011100010000000101100011110 1";

signal test_data_in : std_logic_vector(0 to 1020) :=
   "00000000000000001010101000100100101010011011101110000010100110100 1

. . . 11000000000000000";
signal test_mask : std_logic_vector(0 to 1020) :=
   "11111111111111111111111111111111111111111111111111000000000000000 0

. . . 1111111111111111";

  BEGIN
        -- Instantiate the Unit Under Test (UUT)
   uut: Receiver_top_level PORT MAP (
          data_i_rec => data_i_rec,
          clk_in_rec => clk_in_rec,
          data_out_rec => data_out_rec,
          clk_out_rec => clk_out_rec,
          clk_in => clk_in,
          reset_rec => reset_rec,
          is_preamble => is_preamble,
          is_data => is_data,
          locked_out => locked_out,
                  d_in => d_in,
          disp_in => disp_in,
                  decoded_data => decoded_data,
                  debug_out => debug_out,
          HW_out_rec1 => HW_out_rec1,
          HW_out_rec2 => HW_out_rec2,
          HW_out_rec3 => HW_out_rec3
        );

   -- Clock process definitions

   clk_in_process :process
   begin
                clk_in          <= '0';
                clk_in_rec      <= '0';
                wait for clk_in_period/2;
                clk_in          <= '1';
```

```
            clk_in_rec      <= '1';
            wait for clk_in_period/2;
end process;

-- Stimulus process
stim_proc: process
begin
   -- hold reset state for 100 ns.

   wait for 100 ns;
            reset_rec <= '1';
            wait for 100 ns;
            reset_rec <= '0';
            wait for 1000 ns;

            for i in 92 downto 0 loop
                    data_i_rec <= preamble(i);
                    wait for clk_in_rec_period;
            end loop;

            for i in 0 to 254 loop
                    data_i_rec <= test_data_in(i+3) xor
                       test_mask(i+3);
                    wait for clk_in_rec_period;
            end loop;

            for i in 0 to 254 loop
                    data_i_rec <= test_data_in(i+255) xor
                       test_mask(i+255);
                    wait for clk_in_rec_period;
            end loop;

            for i in 0 to 254 loop
                    data_i_rec <= test_data_in(i+510) xor
                       test_mask(i+510);
                    wait for clk_in_rec_period;
            end loop;

            for i in 0 to 254 loop
                    data_i_rec <= test_data_in(i+765) xor
                       test_mask(i+765);
                    wait for clk_in_rec_period;
            end loop;

 for i in 92 downto 0 loop
            data_i_rec <= preamble(i);
                    wait for clk_in_rec_period;
            end loop;

            for i in 0 to 254 loop
                    data_i_rec <= test_data_in(i+2);
                    wait for clk_in_rec_period;
            end loop;

            for i in 0 to 254 loop
                    data_i_rec <= not(test_data_in(i+255));
                    --clk_in_rec <= data(i);
                    wait for clk_in_rec_period;
```

```
                end loop;

                for i in 0 to 254 loop
                        data_i_rec <= test_data_in(i+510);
                        wait for clk_in_rec_period;
                end loop;

                for i in 0 to 254 loop
                        data_i_rec <= not(test_data_in(i+765));
                        wait for clk_in_rec_period;
                end loop;

                wait for clk_in_rec_period*100;

   end process;

END;
```

References

[1] Asimina Kiourti and Konstantina S Nikita. A review of in-body biotelemetry devices: implantables, ingestibles, and injectables. *IEEE Transactions on Biomedical Engineering*, 2017.

[2] Kateryna Bazaka and Mohan V Jacob. Implantable devices: issues and challenges. *Electronics*, 2(1):1–34, 2012.

[3] John E Ferguson and A David Redish. Wireless communication with implanted medical devices using the conductive properties of the body. *Expert review of medical devices*, 8(4):427–433, 2011.

[4] Bradley Wilsmore and James Leitch. Remote monitoring of medical devices in australia. *The Medical Journal of Australia*, 206(2):62–63, 2017.

[5] Anders J Johansson. Wireless communication with medical implants: Antennas and propagation. In *PhD thesis, Lund University, Sweden*, June 2004.

[6] Shuang Zhang, Yuping Qin, Jiangming Kuang, Peng Un Mak, Sio Hang Pun, Mang I Va, and Yihe Liu. Development and prospect of implantable intra-body communication technology. In *Journal of Computers*, volume 9, pages 463–473, 2014.

[7] Assefa K Teshome, Behailu Kibret, and Daniel TH Lai. Wireless implant communications using the human body. In *Encyclopedia of Information Science and Technology, Fourth Edition*, pages 6319–6334. IGI Global, 2018.

[8] Sami Gabriel, RW Lau, and Camelia Gabriel. The dielectric properties of biological tissues: Iii. parametric models for the dielectric spectrum of tissues. *Physics in medicine and biology*, 41(11):2271, 1996.

[9] Suman Pandey, Pawan K Tiwari, and Tae-Young Byun. Integration of bio-sensing with information and communication to provide improved health-care services. In *Embedded and Multimedia Computing Technology and Service*, pages 509–516. Springer, 2012.

[10] Gregg Jørgen Suaning and Nigel H Lovell. Cmos neurostimulation asic with 100 channels, scaleable output, and bidirectional radio-frequency telemetry. *IEEE Transactions on Biomedical Engineering*, 48(2):248–260, 2001.

[11] James D Weiland and Mark S Humayun. A biomimetic retinal stimulating array. *IEEE engineering in medicine and biology magazine*, 24(5):14–21, 2005.

[12] European Telecommunication Standard Institute (ETSI). Electromagnetic compatibility and radio spectrum matters (ERM); short range devices (SRD); ultra low power active medical implants (ULP-AMI) and peripherals (ULP-AMI-P) operating in the frequency range 402 MHz to 405 MHz; part 1: Technical characteristics and test methods. In *European Standard (Telecommunications series)*, volume V1.3.1, 2009.

[13] Assefa K Teshome, Behailu Kibret, and Daniel TH Lai. Galvanically coupled intrabody communications for medical implants: A unified analytic model. *IEEE Transactions on Antennas and Propagation*, 64(7):2989–3002, 2016.

[14] F Mazzilli and C Dehollain. 184 μw ultrasonic on–off keying/amplitude-shift keying demodulator for downlink communication in deep implanted medical devices. *Electronics Letters*, 52(7):502–504, 2016.

[15] G Enrico Santagati and Tommaso Melodia. Experimental evaluation of impulsive ultrasonic intra-body communications for implantable biomedical devices. *IEEE Transactions on Mobile Computing*, 16(2):367–380, 2017.

[16] Joseph L. Abita and Wolfger Schneider. Transdermal optical communications. *Johns Hopkins APL Techn. Dig.*, 25(3):261–268, 2004.

[17] Manuel Faria, Luis Nero Alves, and Paulo Sérgio de Brito André. Transdermal optical communications. *Visible Light Communications: Theory and Applications*, page 309, 2017.

[18] Muhammad Mujeeb-U-Rahman, Dvin Adalian, Chieh-Feng Chang, and Axel Scherer. Optical power transfer and communication methods for wireless implantable sensing platforms. *Journal of biomedical optics*, 20(9):095012–095012, 2015.

[19] Derya Malak and Ozgur B Akan. A communication theoretical analysis of synaptic multiple-access channel in hippocampal-cortical neurons. *IEEE Trans. Commun.*, 61(6):2457–2467, 2013.

[20] Ozgur B Akan, Hamideh Ramezani, Tooba Khan, Naveed A Abbasi, and Murat Kuscu. Fundamentals of molecular information and communication science. *Proceedings of the IEEE*, 105(2):306–318, 2017.

[21] Eren Balevi and Ozgur B Akan. A physical channel model for nanoscale neuro-spike communications. *IEEE Trans. Commun.*, 61(3):1178–1187, 2013.

[22] Yuechuan Yu, Tram Nguyen, Prashant Tathireddy, Darrin J Young, and Shad Roundy. Wireless hydrogel-based glucose sensor for future implantable applications. In *SENSORS, 2016 IEEE*, pages 1–3. IEEE, 2016.

[23] Brian K Rivera, Shan K Naidu, Kamal Subramanian, Matthew Joseph, Huagang Hou, Nadeem Khan, Harold M Swartz, and Periannan Kuppusamy. Real-time, in vivo determination of dynamic changes in lung and heart tissue oxygenation using epr oximetry. *Advances in experimental medicine and biology*, 812:81, 2014.

[24] Pingping Gou, Nadine D Kraut, Ian M Feigel, Hao Bai, Gregory J Morgan, Yanan Chen, Yifan Tang, Kara Bocan, Joshua Stachel, Lee Berger, et al. Carbon nanotube chemiresistor for wireless ph sensing. *Scientific reports*, 4, 2014.

[25] Rangarajan Jegadeesan, Sudip Nag, Kush Agarwal, Nitish V Thakor, and Yong-Xin Guo. Enabling wireless powering and telemetry for peripheral nerve implants. *IEEE journal of biomedical and health informatics*, 19(3):958–970, 2015.

[26] Simon Little, Alex Pogosyan, Spencer Neal, Baltazar Zavala, Ludvic Zrinzo, Marwan Hariz, Thomas Foltynie, Patricia Limousin, Keyoumars Ashkan, James FitzGerald, et al. Adaptive deep brain stimulation in advanced parkinson disease. *Annals of neurology*, 74(3):449–457, 2013.

[27] Fan-Gang Zeng, Stephen Rebscher, William Harrison, Xiaoan Sun, and Haihong Feng. Cochlear implants: system design, integration, and evaluation. *IEEE reviews in biomedical engineering*, 1:115–142, 2008.

[28] Marcus Yip, Rui Jin, Hideko Heidi Nakajima, Konstantina M Stankovic, and Anantha P Chandrakasan. A fully-implantable cochlear implant soc with piezoelectric middle-ear sensor and arbitrary waveform neural stimulation. *IEEE journal of solid-state circuits*, 50(1):214–229, 2015.

[29] William F House. Cochlear implants. *Annals of Otology, Rhinology & Laryngology*, 85(3_suppl):3–3, 1976.

[30] Arthur James Lowery, Jeffrey V Rosenfeld, Marcello GP Rosa, Emma Brunton, Ramesh Rajan, Collette Mann, Mark Armstrong, Anand Mohan, Horace Josh, Lindsay Kleeman, et al. Monash vision group's gennaris cortical implant for vision restoration. In *Artificial Vision*, pages 215–225. Springer, 2017.

[31] Philip M Lewis, Helen M Ackland, Arthur J Lowery, and Jeffrey V Rosenfeld. Restoration of vision in blind individuals using bionic devices: a review with a focus on cortical visual prostheses. *Brain research*, 1595:51–73, 2015.

[32] Fabien Lotte and Cuntai Guan. Regularizing common spatial patterns to improve bci designs: unified theory and new algorithms. *IEEE Transactions on biomedical Engineering*, 58(2):355–362, 2011.

[33] Ruchi Warty, Mohammad-Reza Tofighi, Usmah Kawoos, and Arye Rosen. Characterization of implantable antennas for intracranial pressure monitoring: Reflection by and transmission through a scalp phantom. *IEEE Transactions on Microwave Theory and Techniques*, 56(10):2366–2376, 2008.

[34] Usmah Kawoos, Xu Meng, Mohammad-Reza Tofighi, and Arye Rosen. Too much pressure: Wireless intracranial pressure monitoring and its applica-

tion in traumatic brain injuries. *IEEE Microwave Magazine*, 16(2):39–53, 2015.

[35] Erik Johannessen, Olga Krushinitskaya, Andrey Sokolov, Philipp Häfliger, Arno Hoogerwerf, Christian Hinderling, Kari Kautio, Jaakko Lenkkeri, Esko Strömmer, Vasily Kondratyev, et al. Toward an injectable continuous osmotic glucose sensor. *Journal of diabetes science and technology*, 4(4):882–892, 2010.

[36] Elham Moradi, Toni Björninen, Lauri Sydänheimo, Jose M Carmena, Jan M Rabaey, and Leena Ukkonen. Measurement of wireless link for brain–machine interface systems using human-head equivalent liquid. *IEEE Antennas and Wireless Propagation Letters*, 12:1307–1310, 2013.

[37] Stephan Reichelt, Jens Fiala, Armin Werber, Katharina Forster, Claudia Heilmann, Rolf Klemm, and Hans Zappe. Development of an implantable pulse oximeter. *IEEE transactions on Biomedical Engineering*, 55(2):581–588, 2008.

[38] SR Goldstein, JI Peterson, and RV Fitzgerald. A miniature fiber optic ph sensor for physiological use. *Journal of biomechanical engineering*, 102(2):141–146, 1980.

[39] Dorin Panescu. An imaging pill for gastrointestinal endoscopy. *IEEE Engineering in Medicine and Biology magazine*, 24(4):12–14, 2005.

[40] Douglas B Shire, Shawn K Kelly, Jinghua Chen, Patrick Doyle, Marcus D Gingerich, Stuart F Cogan, William A Drohan, Oscar Mendoza, Luke Theogarajan, John L Wyatt, et al. Development and implantation of a minimally invasive wireless subretinal neurostimulator. *IEEE Transactions on Biomedical Engineering*, 56(10):2502–2511, 2009.

[41] Thomas Abell, Richard McCallum, Michael Hocking, Kenneth Koch, Hasse Abrahamsson, Isabelle LeBlanc, Greger Lindberg, Jan Konturek, Thomas Nowak, Eammon MM Quigley, et al. Gastric electrical stimulation for medically refractory gastroparesis. *Gastroenterology*, 125(2):421–428, 2003.

[42] Benjamin B Yellen, Zachary G Forbes, Derek S Halverson, Gregory Fridman, Kenneth A Barbee, Michael Chorny, Robert Levy, and Gary Friedman. Targeted drug delivery to magnetic implants for therapeutic appli-

cations. *Journal of Magnetism and Magnetic Materials*, 293(1):647–654, 2005.

[43] Huseyin S. Savci, Ahmet Sula, Zheng Wang, Numan S. Dogan, and Ercument Arvas. Mics transceivers: Regulatory standards and applications. In *Proceedings of IEEE SoutheastCon*, pages 179–182, Apr 2005.

[44] IEEE Computer Society. Ieee standard for local and metropolitan area network: Part 15.6 wireless body area networks. Feb 2012.

[45] Peter D. Bradley. An ultra low power, high performance medical implant communication system (mics) transceiver for implantable devices. In *IEEE Biomedical Circuits and Systems (BioCAS)*, pages 158–162, 2006.

[46] Behailu Kibret, Assefa K. Teshome, and Daniel TH Lai. Characterizing the human body as a monopole antenna. *IEEE Trans. Antennas Propag.*, 63(10):4384–4392, 2015.

[47] Guoxing Wang, Wentai Liu, Mohanasankar Sivaprakasam, and Gurhan Alper Kendir. Design and analysis of an adaptive transcutaneous power telemetry for biomedical implants. *IEEE Transactions on Circuits and Systems I: Regular Papers*, 52(10):2109–2117, 2005.

[48] Maysam Ghovanloo and Khalil Najafi. A wideband frequency-shift keying wireless link for inductively powered biomedical implants. *IEEE Transactions on Circuits and Systems I: Regular Papers*, 51(12):2374–2383, 2004.

[49] Jose L Bohorquez, Anantha P Chandrakasan, and Joel L Dawson. A 350 μw cmos msk transmitter and 400 μw ook super-regenerative receiver for medical implant communications. *IEEE Journal of Solid-State Circuits*, 44(4):1248–1259, 2009.

[50] Wentai Liu, Mohanasankar Sivaprakasam, Guoxing Wang, Mingcui Zhou, John Granacki, Jeffrey LaCoss, and Jack Wills. Implantable biomimetic microelectronic systems design. *IEEE engineering in medicine and biology magazine*, 24(5):66–74, 2005.

[51] Louis Hyunsuk Jung, P Byrnes-Preston, Roland Hessler, Torsten Lehmann, GJ Suaning, and Nigel H Lovell. A dual band wireless power and fsk data

telemetry for biomedical implants. In *Engineering in Medicine and Biology Society, 2007. EMBS 2007. 29th Annual International Conference of the IEEE*, pages 6596–6599. IEEE, 2007.

[52] Eyal Margalit, Mauricio Maia, James D Weiland, Robert J Greenberg, Gildo Y Fujii, Gustavo Torres, Duke V Piyathaisere, Thomas M O'Hearn, Wentai Liu, Gianluca Lazzi, et al. Retinal prosthesis for the blind. *Survey of ophthalmology*, 47(4):335–356, 2002.

[53] Guillaume Simard, Mohamad Sawan, and Daniel Massicotte. High-speed oqpsk and efficient power transfer through inductive link for biomedical implants. *IEEE Transactions on biomedical circuits and systems*, 4(3):192–200, 2010.

[54] Maysam Ghovanloo and Suresh Atluri. A wide-band power-efficient inductive wireless link for implantable microelectronic devices using multiple carriers. *IEEE Transactions on Circuits and Systems I: Regular Papers*, 54(10):2211–2221, 2007.

[55] Yasuhiro Take, Hiroki Matsutani, Daisuke Sasaki, Michihiro Koibuchi, Tadahiro Kuroda, and Hideharu Amano. 3d noc with inductive-coupling links for building-block sips. *IEEE Transactions on Computers*, 63(3):748–763, 2014.

[56] Takahiro Kagami, Hiroki Matsutani, Michihiro Koibuchi, Yasuhiro Take, Tadahiro Kuroda, and Hideharu Amano. Efficient 3-d bus architectures for inductive-coupling thruchip interfaces. *IEEE Transactions on Very Large Scale Integration (VLSI) Systems*, 24(2):493–506, 2016.

[57] Burhan Gulbahar. Theoretical analysis of magneto-inductive thz wireless communications and power transfer with multi-layer graphene nano-coils. *IEEE Transactions on Molecular, Biological and Multi-Scale Communications*, 3(1):60–70, 2017.

[58] T. G. Zimmerman. Personal area networks (PAN): nearfield intra-body communication. In *IBM Syst.*, volume 35, pages 609–617, MA, USA, Apr. 1996.

[59] M. Gray. Physical limits of intra-body signalling. In *Master thesis, Massachusetts Institute of Technology*, pages 1–49, 1997.

[60] M. Shinagawa, M. Fukumoto, and K. Ochiai. A near-field-sensing transceiver for intra-body communication based on the electro-optic effect. In *IEEE Trans. Instrum. Meas.*, volume 53, pages 1533–1538, 2004.

[61] K. Fujii, M. Takahashi, and K. Ito. Electric field distributions of wearable devices using the human body as a transmission channel. In *IEEE Trans. on Antennas and Propagation*, volume 55, pages 2080–2087, 2007.

[62] N. Cho, J. Yoo, and S. J. Song. The human body characteristics as a signal transmission medium for intra-body communication. In *IEEE Trans. on Microwave Theory and Techniques*, volume 55, pages 1080–1086, 2007.

[63] Handa T, Shoji S, Ike S, Takeda S, and Sekiguchi T. A very low-power consumption wireless ECG monitoring system using body as a signal transmission medium. In *Int. Solid State Sensor Actuator Conf.*, pages 1003–1006, 1997.

[64] D. P. Lindsey, E. L. McKee, and M. L. Hull. A new technique for transmission of signals from implantable transducers. In *IEEE Trans. Biomed. Eng.*, volume 45, pages 614–619, 1998.

[65] K. Hachisuka, Y. Terauchi, and Y. Kishi. Simplified circuit modeling and fabrication of intra-body communication devices. In *Sensors and Actuators*, pages 322–330, 2006.

[66] Y.Song, Q.Hao, K.Zhang, M.Wang, Y.F.Chu, and B.Z.Kang. The simulation method of the galvanic coupling intrabody communication with different signal transmission paths. In *IEEE Trans. Instrum. Meas.*, volume 4, pages 1257–1266, 2011.

[67] M. S. Wegmuller. Intra-body communication (IBC) for biomedical sensor networks. In *Ph.D. Thesis, ETH*, Switzerland, 2007.

[68] Marc Simon Wegmueller, Sonja Huclova, Juerg Froehlich, Michael Oberle, Norbert Felber, Niels Kuster, and Wolfgang Fichtner. Galvanic coupling enabling wireless implant communications. *IEEE Trans. Instrum. Meas.*, 58(8):2618–2625, 2009.

[69] M Amparo Callejon, Javier Reina-Tosina, David Naranjo-Hernández, and Laura M Roa. Galvanic coupling transmission in intrabody communication:

A finite element approach. *IEEE Trans. Biomed. Eng.*, 61(3):775–783, 2014.

[70] International Commission on Non-Ionizing Radiation Protection (ICNIRP). Guidance for limiting exposure to time-varying electric, magnetic, and electromagnetic fields (up to 300 GHz). In *Health Physics*, volume 74, pages 494–522, Apr 1998.

[71] Ian F Akyildiz, Fernando Brunetti, and Cristina Blázquez. Nanonetworks: A new communication paradigm. *Computer Networks*, 52(12):2260–2279, 2008.

[72] Laura Galluccio, Sergio Palazzo, and G Enrico Santagati. Characterization of molecular communications among implantable biomedical neuro-inspired nanodevices. *Nano Communication Networks*, 4(2):53–64, 2013.

[73] Derya Malak and Ozgur Akan. Communication theoretical understanding of intra-body nervous nanonetworks. *IEEE Communications Magazine*, 52(4):129–135, 2014.

[74] Wireless for implantable medical devices. http://www.microsemi.com/products/ultra-low-power-wireless/implantable-medical-transceivers/zl70102.

[75] N. Cho, J. Bae, and H. J. Yoo. A 10.8mw, body channel communication/MICS dual-band transceiver for a unified body sensor network controller. In *IEEE ISSCC Dig. Tech. Papers*, Feb 2009.

[76] Jagdish Pandey and Brian Otis. A sub-100uw mics/ism band transmitter based on injection-locking and frequency multiplication. In *IEEE Journal of Solid-State Circuits (JSCC)*, volume 46, pages 1–34, May 2013.

[77] Kateryna Bazaka and Mohan V. Jacob. Implantable devices: Issues and challenges. In *Electronics*, volume 2, pages 1–34, 2013.

[78] Dwight Reynolds, Gabor Z Duray, Razali Omar, Kyoko Soejima, Petr Neuzil, Shu Zhang, Calambur Narasimhan, Clemens Steinwender, Josep Brugada, Michael Lloyd, et al. A leadless intracardiac transcatheter pacing system. *New England Journal of Medicine*, 374(6):533–541, 2016.

[79] Michael Catrysse, Bart Hermans, and Robert Puers. An inductive power system with integrated bi-directional data-transmission. *Sensors and Actuators A: Physical*, 115(2):221–229, 2004.

[80] John S Ho, Alexander J Yeh, Evgenios Neofytou, Sanghoek Kim, Yuji Tanabe, Bhagat Patlolla, Ramin E Beygui, and Ada SY Poon. Wireless power transfer to deep-tissue microimplants. *Proceedings of the National Academy of Sciences*, 111(22):7974–7979, 2014.

[81] Andreas Christ, Mark G Douglas, John M Roman, Emily B Cooper, Alanson P Sample, Benjamin H Waters, Joshua R Smith, and Niels Kuster. Evaluation of wireless resonant power transfer systems with human electromagnetic exposure limits. *IEEE Transactions on Electromagnetic compatibility*, 55(2):265–274, 2013.

[82] Elham Moradi, Sara Amendola, Toni Björninen, Lauri Sydänheimo, Jose M Carmena, Jan M Rabaey, and Leena Ukkonen. Backscattering neural tags for wireless brain-machine interface systems. *IEEE Transactions on Antennas and Propagation*, 63(2):719–726, 2015.

[83] Canan Dagdeviren, Byung Duk Yang, Yewang Su, Phat L Tran, Pauline Joe, Eric Anderson, Jing Xia, Vijay Doraiswamy, Behrooz Dehdashti, Xue Feng, et al. Conformal piezoelectric energy harvesting and storage from motions of the heart, lung, and diaphragm. *Proceedings of the National Academy of Sciences*, 111(5):1927–1932, 2014.

[84] Paul D Mitcheson, Eric M Yeatman, G Kondala Rao, Andrew S Holmes, and Tim C Green. Energy harvesting from human and machine motion for wireless electronic devices. *Proceedings of the IEEE*, 96(9):1457–1486, 2008.

[85] Steven R Anton and Henry A Sodano. A review of power harvesting using piezoelectric materials (2003–2006). *Smart materials and Structures*, 16(3):R1, 2007.

[86] Qingyun Ma. *A low-power analog-signal-processing-unit for wirelessly-powered implantable recording system.* The University of Alabama at Birmingham, 2015.

[87] Benjamin J Hansen, Ying Liu, Rusen Yang, and Zhong Lin Wang. Hybrid nanogenerator for concurrently harvesting biomechanical and biochemical energy. *ACS nano*, 4(7):3647–3652, 2010.

[88] Jacopo Olivo, Sandro Carrara, and Giovanni De Micheli. Energy harvesting and remote powering for implantable biosensors. *IEEE Sensors Journal*, 11(7):1573–1586, 2011.

[89] Francesco Merli, Léandre Bolomey, Jean-François Zurcher, Giancarlo Corradini, Eric Meurville, and Anja K Skrivervik. Design, realization and measurements of a miniature antenna for implantable wireless communication systems. *IEEE Transactions on Antennas and Propagation*, 59(10):3544–3555, 2011.

[90] Asimina Kiourti and Konstantina S Nikita. A review of implantable patch antennas for biomedical telemetry: Challenges and solutions [wireless corner]. *IEEE Antennas and Propagation Magazine*, 54(3):210–228, 2012.

[91] Mehmet R Yuce and Tharaka Dissanayake. Easy-to-swallow antenna and propagation. *IEEE Microwave Magazine*, 14(4):74–82, 2013.

[92] Olive H Murphy, Christopher N McLeod, Manoraj Navaratnarajah, Magdi Yacoub, and Christofer Toumazou. A pseudo-normal-mode helical antenna for use with deeply implanted wireless sensors. *IEEE Transactions on Antennas and Propagation*, 60(2):1135–1139, 2012.

[93] Soheil Hashemi and Jalil Rashed-Mohassel. Miniaturization of dual band implantable antennas. *Microwave and Optical Technology Letters*, 59(1):36–40, 2017.

[94] M. Amparo Callejón, Javier Reina-Tosina, David Naranjo-Hernández, and Laura M. Roa. Galvanic coupling transmission in intrabody communication: A finite element approach. In *IEEE Transaction on Biomedical Engineering*, volume 61, pages 775–783, 2014.

[95] IT'IS Foundation. "Tissue Properties Database V2.3''. Thermal and dielectric properties V2.3(Excel).xls, February 2013.

[96] Svetlana A Shabalovskaya. Surface, corrosion and biocompatibility aspects of nitinol as an implant material. *Bio-medical materials and engineering*, 12(1):69–109, 2002.

[97] Pichitpong Soontornpipit, Cynthia M Furse, and You Chung Chung. Miniaturized biocompatible microstrip antenna using genetic algorithm. *IEEE Transactions on Antennas and Propagation*, 53(6):1939–1945, 2005.

[98] Bin Liu, Eric Kim, Anika Meggo, Sachin Gandhi, Hao Luo, Srinivas Kallakuri, Yong Xu, and Jinsheng Zhang. Enhanced biocompatibility of neural probes by integrating microstructures and delivering anti-inflammatory agents via microfluidic channels. *Journal of Neural Engineering*, 14(2):026008, 2017.

[99] Michel M Maharbiz, Rikky Muller, Elad Alon, Jan M Rabaey, and Jose M Carmena. Reliable next-generation cortical interfaces for chronic brain–machine interfaces and neuroscience. *Proceedings of the IEEE*, 105(1):73–82, 2017.

[100] Yun Jung Heo and Shoji Takeuchi. Towards smart tattoos: Implantable biosensors for continuous glucose monitoring. *Advanced healthcare materials*, 2(1):43–56, 2013.

[101] S Hanna. Regulations and standards for wireless medical applications. In *Proceedings of the 3rd international symposium on medical information and communication technology*, pages 23–26, 2009.

[102] Mahammad A Hannan, Saad M Abbas, Salina A Samad, and Aini Hussain. Modulation techniques for biomedical implanted devices and their challenges. *Sensors*, 12(1):297–319, 2011.

[103] Mahammad A Hannan, Saad Mutashar, Salina A Samad, and Aini Hussain. Energy harvesting for the implantable biomedical devices: issues and challenges. *Biomed. Eng. Online*, 13, 2014.

[104] IEEE Standards Association and others. IEEE standard for local and metropolitan area networks-part 15.6: wireless body area networks. *IEEE Std*, 802(6), 2012.

[105] Takashi Handa, Shuichi Shoji, Shinichi Ike, Sunao Takeda, and Tetsushi Sekiguchi. A very low-power consumption wireless ECG monitoring system using body as a signal transmission medium. In *International Conference on Solid State Sensors and Actuators, 1997. TRANSDUCERS'97 Chicago.*, volume 2, pages 1003–1006. IEEE, 1997.

[106] Derek P Lindsey, Eric L McKee, Maury L Hull, and Stephen M Howell. A new technique for transmission of signals from implantable transducers. *IEEE Trans. Biomed. Eng.*, 45(5):614–619, 1998.

[107] Mingui Sun, Marlin Mickle, Wei Liang, Qiang Liu, and Robert J Sclabassi. Data communication between brain implants and computer. *IEEE Trans. Neural Syst. Rehabil. Eng.*, 11(2):189–192, 2003.

[108] Mingui Sun, Brian L Wessel, Wei Liang, Paul Roche, Qiang Liu, Marlin Mickle, Robert J Sclabassi, et al. A volume conduction antenna for implantable devices. In *EMBS'03.*, volume 4, pages 3356–3359. IEEE, 2003.

[109] Cynthia M Furse and Andrew Chrysler. A history & future of implantable antennas. In *APSURSI'14*, pages 527–528. IEEE, 2014.

[110] CM Furse, R Harrison, and F Solzbacher. Recent advances in biomedical telemetry. In *ICEAA'07.*, pages 1026–1027. IEEE, 2007.

[111] W Besio and A Prasad. Analysis of skin-electrode impedance using concentric ring electrode. In *EMBS'06. 28th Annual International Conference of the IEEE*, pages 6414–6417. IEEE, 2006.

[112] Keisuke Hachisuka, Yusuke Terauchi, Yoshinori Kishi, Ken Sasaki, Terunao Hirota, Hiroshi Hosaka, Katsuyuki Fujii, Masaharu Takahashi, and Koichi Ito. Simplified circuit modeling and fabrication of intrabody communication devices. *Sensors and actuators A: physical*, 130:322–330, 2006.

[113] Behailu Kibret, MirHojjat Seyedi, Daniel T. H. Lai, and Micheal Faulkner. Investigation of galvanic-coupled intrabody communication using the human body circuit model. In *IEEE J. Biomed. Health Inform*, volume 18, pages 1196–1206, July 2014.

[114] Jordi Agud Ruiz, Jiang Xu, and Shigeru Shimamoto. Propagation characteristics of intra-body communications for body area networks. In *3rd IEEE CCNC 2006.*, volume 1, pages 509–513. IEEE, 2006.

[115] J. Bae, H. Cho, K. Song, H. Lee, and H.-J. Yoo. The signal transmission mechanism on the surface of human body for body channel communication. In *IEEE Trans. Microw. Theory Techn.*, volume 60, pages 582–593, March 2012.

[116] Sio Hang Pun, Yue Ming Gao, PengUn Mak, Mang Vai, Min Du, et al. Quasi-static modeling of human limb for intra-body communications with experiments. *IEEE Trans. Info. Tech. in Biomed.*, 15(6):870–876, 2011.

[117] DJP Dechambre. Computation of ellipsoidal gravity field harmonics for small solar system bodies. *Electrical Engineering-Systems in The University of Michigan*, 2000.

[118] Fotini Kariotou. Electroencephalography in ellipsoidal geometry. *Journal of Math. Analysis and Applications*, 290(1):324–342, 2004.

[119] George Dassios and Fotini Kariotou. Magnetoencephalography in ellipsoidal geometry. *Journal of Math. Physics*, 44(1):220–241, 2003.

[120] Craig E Tenke and Jürgen Kayser. Generator localization by current source density (CSD): implications of volume conduction and field closure at intracranial and scalp resolutions. *Clinical neurophysiology*, 123(12):2328–2345, 2012.

[121] Seward B Rutkove. Introduction to volume conduction. *The clinical neurophysiology primer*, 388:43, 2007.

[122] Robert Plonsey and Dennis B Heppner. Considerations of quasi-stationarity in electrophysiological systems. *The Bulletin of mathematical biophysics*, 29(4):657–664, 1967.

[123] Joachim H Nagel. Biopotential amplifiers. *Bronzino JD: Biomedical engineering hand book, 2nd ed., Springer-Verlag New York*, pages 70–1, 2000.

[124] George Dassios. *Ellipsoidal harmonics: theory and applications*, volume 146. Cambridge University Press, 2012.

[125] David B Geselowitz. On bioelectric potentials in an inhomogeneous volume conductor. *Biophysical journal*, 7(1):1, 1967.

[126] MS Lynn and WP Timlake. Multiple wielandt deflations in the numerical solution of singular integral equations of potential theory. In *Proceedings of the 23rd ACM national conference*, pages 481–484, 1968.

[127] David B Geselowitz. On the theory of the electrocardiogram. *Proceedings of the IEEE*, 77(6):857–876, 1989.

[128] Yong Song, Qun Hao, Kai Zhang, Ming Wang, Yifang Chu, and Bangzhi Kang. The simulation method of the galvanic coupling intrabody communication with different signal transmission paths. *IEEE Trans. Instrum. Meas.*, 60(4):1257–1266, 2011.

[129] Karen Lopez-Linares Roman, Günter Vermeeren, Arno Thielens, Wout Joseph, and Luc Martens. Characterization of path loss and absorption for a wireless radio frequency link between an in-body endoscopy capsule and a receiver outside the body. *EURASIP Journal on Wireless Communications and Networking*, 2014(1):1–10, 2014.

[130] MJ Hagmann, RL Levin, L Calloway, AJ Osborn, and KR Foster. Muscle-equivalent phantom materials for 10-100 MHz. *IEEE Trans. on Microwave Theory and Tech.*, 40(4):760–762, 1992.

[131] Andreas Hördt, Peter Weidelt, and Anita Przyklenk. Contact impedance of grounded and capacitive electrodes. *Geophysical Journal International*, 193(1):187–196, 2013.

[132] LA Geddes and R Roeder. Criteria for the selection of materials for implanted electrodes. *Annals of biomedical engineering*, 31(7):879–890, 2003.

[133] Ilkka Antero Hokajärvi. Electrode contact impedance and biopotential signal quality. *Thesis, Tampere University of Technology, Finland*, 2012.

[134] Mingui Sun. An efficient algorithm for computing multishell spherical volume conductor models in EEG dipole source localization. *IEEE Trans. Biomed. Eng.*, 44(12):1243–1252, 1997.

[135] Kanber Mithat Silay, Catherine Dehollain, and Michel Declercq. Improvement of power efficiency of inductive links for implantable devices. In *Research in Microelectronics and Electronics, 2008. PRIME 2008. Ph. D.*, pages 229–232. IEEE, 2008.

[136] Suresh Atluri and Maysam Ghovanloo. A wideband power-efficient inductive wireless link for implantable microelectronic devices using multiple carriers. In *Circuits and Systems, 2006. ISCAS 2006. Proceedings. 2006 IEEE International Symposium on*, pages 4–pp. IEEE, 2006.

[137] Kanber Mithat Silay, Catherine Dehollain, and Michel Declercq. Inductive power link for a wireless cortical implant with biocompatible packaging. In *Sensors, 2010 IEEE*, pages 94–98. IEEE, 2010.

[138] Christian Sauer, Milutin Stanacevic, Gert Cauwenberghs, and Nitish Thakor. Power harvesting and telemetry in cmos for implanted devices. *IEEE Transactions on Circuits and Systems I: Regular Papers*, 52(12):2605–2613, 2005.

[139] Clemens M Zierhofer and Erwin S Hochmair. Geometric approach for coupling enhancement of magnetically coupled coils. *IEEE transactions on Biomedical Engineering*, 43(7):708–714, 1996.

[140] Sofia Bakogianni and Stavros Koulouridis. An implantable planar dipole antenna for wireless medradio-band biotelemetry devices. *IEEE Antennas and Wireless Propagation Letters*, 15:234–237, 2016.

[141] Hua Li, Yong-Xin Guo, Changrong Liu, Shaoqiu Xiao, and Lin Li. A miniature-implantable antenna for medradio-band biomedical telemetry. *IEEE Antennas and Wireless Propagation Letters*, 14:1176–1179, 2015.

[142] Zhu Duan, Yong-Xin Guo, Minkyu Je, and Dim-Lee Kwong. Design and in vitro test of a differentially fed dual-band implantable antenna operating at mics and ism bands. *IEEE transactions on antennas and propagation*, 62(5):2430–2439, 2014.

[143] Arthur James Lowery. Introducing the monash vision group's cortical prosthesis. In *Image Processing (ICIP), 2013 20th IEEE International Conference on*, pages 1536–1539. IEEE, 2013.

[144] Rafael Mendes Duarte and Gordana Klaric Felic. Analysis of the coupling coefficient in inductive energy transfer systems. *Active and Passive Electronic Components*, 2014, 2014.

[145] Chung-Chuan Hou and Kuei-Yuan Chang. Inductive power transfer systems for bus-stop-powered electric vehicles. *Energies*, 9(7):512, 2016.

[146] Yangzhe Liao, Mark S Leeson, and Matthew D Higgins. A communication link analysis based on biological implant wireless body area networks. *Applied Computational Electromagnetics Society Journal*, 31(6), 2016.

[147] David C Klonoff. The benefits of implanted glucose sensors. *Journal of Diabetes Science and Technology*, 1(6):797–800, 2007.

[148] Ming-Zhi Yang, Ching-Liang Dai, and Cheng-Bei Hung. Fabrication of a glucose sensor with oscillator circuit using cmos-mems technique. *Microelectronic Engineering*, 97:353–356, 2012.

[149] Valery Sklyarov and Iouliia Skliarova. Digital hamming weight and distance analyzers for binary vectors and matrices. *International Journal of Innovative Computing, Information and Control*, 9(12):4825–4849, 2013.

[150] Kim Taylor. A modular transceiver platform for human body communications. *Masters Thesis, Victoria University*, 2016.

[151] Meenupriya Swaminathan, Joan Sebastià Pujol, Gunar Schirner, and Kaushik R Chowdhury. Multi-path 2-port channel characterization for galvanic coupled intra-body communication. In *Proceedings of the 9th International Conference on Body Area Networks*, pages 118–123. ICST (Institute for Computer Sciences, Social-Informatics and Telecommunications Engineering), 2014.

[152] Meenupriya Swaminathan, Ferran Simon Cabrera, Joan Sebastia Pujol, Ufuk Muncuk, Gunar Schirner, and Kaushik R Chowdhury. Multi-path model and sensitivity analysis for galvanic coupled intra-body communication through layered tissue. *IEEE transactions on biomedical circuits and systems*, 10(2):339–351, 2016.

[153] Xi Mei Chen, Peng Un Mak, Sio Hang Pun, Yue Ming Gao, Chan-Tong Lam, Mang I Vai, and Min Du. Study of channel characteristics for galvanic-type intra-body communication based on a transfer function from a quasi-static field model. *Sensors*, 12(12):16433–16450, 2012.

[154] Yuhwai Tseng, Chauchin Su, and Yingchieh Ho. Evaluation and verification of channel transmission characteristics of human body for optimizing data transmission rate in electrostatic-coupling intra body communication system: A comparative analysis. *PloS one*, 11(2):e0148964, 2016.

[155] Yu-Ping Qin, Shuang Zhang, Hai-Yan Liu, Yi-He Liu, You-Zhi Li, Xue Peng, Xiu Ma, Qi-Li Li, and Xuan Huang. Path loss measurement and

channel modeling with muscular tissue characteristics. *The open biomedical engineering journal*, 11:1, 2017.

[156] Katsuyuki Fujii, Koichi Ito, and Shigeru Tajima. A study on the receiving signal level in relation with the location of electrodes for wearable devices using human body as a transmission channel. In *Antennas and Propagation Society International Symposium, 2003. IEEE*, volume 3, pages 1071–1074. IEEE, 2003.

.